Thesis for the degree

Doctor of Philosophy

Higgs Boson Searches at OPAL (LEP), ATLAS (LHC) and ILC

by

Lidija Živković

Submitted to the Scientific Council
of the Weizmann Institute of Science
Rehovot, Israel
April 2006

The work presented in this thesis was carried out under the supervision of Prof. Eilam Gross and Prof. Ehud Duchovni.

Acknowledgments

Many people supported me toward the end of this thesis. I am sincerely tankful to all of them.

To my supervisors, Eilam Gross, who often pushed me beyond and showed me how far I can go, and Ehud Duchovni, who was there whenever I needed help. They taught me everything I know about experimental high energy physics.

To Giora Mikenberg for lot of helpful advices and comments.

To Daniel Lellouch, Lorne Levinson and Vladimir Smakhtin for their help regarding hardware and computing.

To the two postdocs in the group, German Martinez who helped me when I started, and Michael Riveline who assisted me at the crucial moments of my work.

To the fellow students, Amit Klier and Michael Kupper for the assistance in the part of my analysis, and to Peter Renkel and Arie Melamed-Katz for lot of useful discussions.

To Helen Katz and Dan Schrager for the assistance regarding various computer and computing problems.

To the people that helped me with my hardware project, Moshe Sidi, Yafa Gil and Galia Gitliz, and also to all the people from the Mexico building.

To Philip Bechtle for the assistance with the OPAL analysis.

To Klaus Desch, Sven Heinemeyer and Georg Weiglein for the support regarding ILC project.

To Laura Reina and Alexandar Belyaev for the discussions regarding the `H` production at the LHC.

To many members of the ATLAS collaboration, especially to Donatela Cavalli for lot of useful discussions and advices. I also want to thank Michael Heldmann for the help with τ reconstruction, Kamal Benslama who helped me with electron identification, and Kambiz Mahboubi for the Fast Shower. My gratitude to the Higgs conveners: Karl Jakobs, Elzbieta Richter-Was, Fabio Cerutti, Guillaume Unal and Markus Schumacher. I would like to express my thankfulness to Emil Obreshkov for the help regarding ATLAS software.

I also thank my dear friend Ivanka Božović-Jelisavčić and the High Energy Physics group from the Vinča Institute in Belgrade for their support.

I gratefully thank the Benoziyo Center for High Energy Physics for their support of this work. This work was also supported by the Israeli Science, Foundation and by the

Federal Ministry of Education, Science, Research and Technology (BMBF) within the framework of the German-Israeli Project Cooperatin in Future-Oriented Topics (DIP).

This thesis is dedicated to my family. To my husband Saša who was with me all the time. And to my parents, my mother Branka who did not live long enough to see this work, and to my father Miodrag who supported me since I was a little curious girl.

Abstract

An impressive effort was done by the four LEP collaborations in the search for the SM and the MSSM Higgs boson. However, very little attention was paid to the possibility of a CP violating Higgs sector and no significant effort to search for the resulting signatures was carried out. Once the CP state of the neutral Higgs bosons is ill defined, new Higgs boson production and decay channels might be opened. One of them, $e^+e^- \to Z^0 H_2 \to Z^0 H_1 H_1 \to \nu\bar{\nu} b\bar{b} b\bar{b}$ is analyzed in the scope of this thesis. No significant excess of the data over the expected background is found. The results of this channel are combined with the results of other searches for the MSSM Higgs bosons and interpreted in the framework of a model with CP violation at OPAL. It was found that under certain assumptions (CPX scenario) the region $\tan\beta < 2.8$ is excluded at 95% confidence level but no universal mass limit is obtained for either of the Higgs bosons. The combination of the results of the four LEP experiments improves the limit on $\tan\beta$ to 3.3.

The LHC will be complemented by the ILC. In this thesis we consider a scenario where only one Higgs boson is observed by (both) LHC and ILC. We estimate the uncertainties in the indirect determination of the mass of the pseudoscalar Higgs boson, m_A. Taking for the first time all experimental and theoretical uncertainties into account, a determination of M_A with an accuracy of about 20% (30%) seems to be feasible for $M_A = 600$ (800) GeV.

In the main part of this thesis we develop a completely new algorithmic method for τ-lepton identification within the framework of the fast simulation of the ATLAS detector. We have found out that this method is reproducing quite accurately the full detector simulation Tau ID performance (efficiency and rejection).

One of the main goals of the ATLAS experiment is to measure the various Higgs boson couplings as accurate as possible. Such a measurement is mandatory for a full understanding of the Higgs sector. The most challenging measurements of the Higgs boson properties is the determination of the Yukawa coupling to the top quark. We conducted a feasibility study aimed to asses ATLAS sensitivity to this coupling using the the $t\bar{t}H$ channel followed by $H \to \tau^+\tau^-$. The signal events were reconstructed using the full and the fast simulation of the ATLAS detector. It is shown that the two methods are in good agreement and that we can use the fast simulation to complete the analysis. We obtain a significance of 1.6σ for the low luminosity condition (30 fb^{-1}) and $m_H = 120$ GeV, and 2.0σ for the high luminosity condition (300 fb^{-1}) and $m_H = 120$ GeV.

Contents

List of Tables

List of Figures

Chapter 1

Preface

For over two thousand years people have thought about the fundamental particles from which all matter was made, starting with the gradual development of atomic theory, followed by a deeper understanding of the theory of the quantum atom, leading to the recent theory of the Standard Model.

In ancient Greece the concept of the changes in matter due to different internal orderings of indivisible particles was introduced. In the beginning, the four elements, water, air, earth and fire, were recognized as the building blocks of the world. Then, Democritus developed the theory postulating that the universe consisted of empty space and an (almost) infinite number of invisible particles, atoms[1], which were matter constituents, and could differ from each other in form, position, and arrangement [1].

Starting at the end of the 19^{th} century scientists began looking inside the atom discovering its constituents, and managed to describe the forces that governed their mutual interactions. They also found out that light, basically waves, could be described as consisted of energy quanta being the photons. On the other hand, particles could behave as waves, and Quantum Mechanics was born. In the famous miraculous year, 1905, Albert Einstein published five revolutionary papers, one of them proposing the special theory of relativity. Finally, the idea of quantum field theory with quantum fields being the basic ingredients of the universe, and particles being bundles of energy and momentum of the fields emerged. One of the key elements in the triumph of quantum field theory was the development of renormalization theory. It led to the Standard Model, renormalizable quantum field theory, which was triumphantly verified by different experiments from the mid-1970s until today [2, 3].

The Standard Model (SM) describes the elementary particles and their mutual interactions. It is based on the gauge invariant relativistic quantum field theory. However, unbroken gauge theories result in massless vector fields which is in contradiction with observations that the carriers of the weak interaction are very massive. Thus, the gauge symmetry is broken and the particles acquire self energy and hence mass by the interaction

[1] *άτομον* from *ά-non* and *τομον-divisible*

with a background field with non-zero vacuum expectation value - the Higgs field [4].

The Higgs mechanism, i.e. the mechanism of Spontaneous Symmetry Breaking, predicts the existence of a spinless particle, the Higgs boson. It is the only particle of the Standard Model which has not yet been experimentally detected. In the context of the Standard Model, all properties of the Higgs boson apart from its mass are predicted. The mass of the Higgs boson can be constrained to $m_H > 114.4$ GeV from direct searches at LEP [5], and to $m_H \lesssim 200$ GeV from precision measurements [6]. The search for the Higgs boson and the precise measurement of its properties are one of the major experimental goals of modern particle physics.

Even though the Standard Model predictions were confirmed with a great success, it still suffers from several theoretical drawbacks. There are also measurements of cosmological quantities, such as the amount of CP violation necessary for the baryogenesis or the existence of the dark matter, which are not in an agreement with the Standard Model.

One way to overcome the aforementioned problems is the introduction of an additional symmetry between bosons and fermions, Supersymmetry (SUSY) [7]. It introduces many new particles, and enlarges the Higgs sector. In the Minimal Supersymmetrical Standard Model (MSSM), three neutral and two charged Higgs bosons exist. The mass of the lightest Higgs boson within MSSM is bounded to be below ~ 135 GeV [8, 9]. Large amount of the CP violation necessary for the baryogenesis can be explained by introducing CP violation in the Higgs sector of the MSSM.

This thesis concerns with the search for the SM and MSSM Higgs bosons with a CP violating supersymmetric Higgs sector. The search is performed in all major accelerators, namely LEP, the prospective LHC and the proposed ILC machines.

A theoretical introduction to the Standard Model and the Minimal Supersymmetric Standard Model with an emphasis on the Higgs boson is given in Chapter 2.

The OPAL experiment at LEP is described in Chapter 3. We investigated the possible existence of the Higgs boson in a scenario with a CP violation in the Higgs sector of the MSSM. The analysis of the $e^+e^- \to Z^0 H_2 \to Z^0 H_1 H_1 \to \nu\bar{\nu} b\bar{b} b\bar{b}$ is described in section 3.2. This work is a part of three OPAL Notes [10] and contributed to two scientific papers [11, 12].

If only one Higgs boson is found at the Large Hadron Collider (LHC), it would be important to determine its nature. The combined information of mass parameters from the LHC and the International Linear Collider (ILC), and the Higgs-boson branching ratio measurements at the ILC can be used to obtain bounds on the mass of the CP-odd Higgs boson, M_A. Such an analysis is described in Chapter 4. This analysis contributed to [13, 14, 15].

The ATLAS experiment at the LHC, which is expected to start its operation in 2007, is described in Chapter 5. Thin Gap Chambers (TGC) are produced at the Weizmann

Institute. I was involved with the high voltage pulse test system that verifies the integrity of all electrical connections of the TGC units. This work is described in section 5.2.

The Higgs boson, if exists, will be probably found at LHC. For a light Higgs boson, the Branching ratio to τ-lepton pair is the second highest. Different SUSY models also contain events with τ-leptons. Electrons and muons form τ-decays cannot be efficiently discerned from those coming from other sources, and one way to identify a τ-lepton is to observe a jet formed from its hadronic products, i.e. τ_j. We have developed a τ-tagging algorithm for the fast simulation of the ATLAS detector. Section 5.3 [16] describes this algorithm and presents a comparison with the present parametrization based method for τ-tagging in the fast simulation of the detector.

One of the main goals of the ATLAS experiment is to measure various Higgs boson couplings as accurate as possible [17]. Such a measurement is mandatory for a full understanding of the Higgs sector. The most challenging measurements of the Higgs boson properties is the determination of the Yukawa coupling to the top quark. To complement the $t\bar{t}H \rightarrow t\bar{t}b\bar{b}$ channel, which is the most significant in the low Higgs mass region ($m_H \sim 120$ GeV), we introduce a feasibility study of the $t\bar{t}H$ channel with the Higgs decaying to a pair of τ leptons (in section 5.4).

The work presented in this thesis is summarized in Chapter 6.

Chapter 2

Introduction

2.1 The Standard Model and Higgs Mechanism

One of the major physics achievement is the joint description of the electromagnetic, weak and strong interaction by a single theory. The model proposed by Glashow, Salam and Weinberg [2] in the middle sixties, had been extensively tested during the last 35 years. The discovery of neutral weak interactions and the production of intermediate vector bosons ($W^{\pm}$ and Z^0) with the expected properties [18], and the observations of gluon jets [19] confirmed the model. More recent measurements did not find an experimental result that contradicted the Standard Model predictions.

The description of the Standrad model interactions is implemented by a gauge theory based on $SU(3)_C \times SU(2)_L \times U(1)_Y$ symmetry, which is spontaneously broken via the Higgs mechanism. The matter fields, leptons and quarks, are organized in families, with the left-handed fermions belonging to weak isodoublets while the right-handed components transform as weak isosinglets. The vector bosons, $W^{\pm}$, Z^0, γ and gluons, that mediate the interactions are introduced via minimal coupling to the matter fields. An essential ingredient of the model is the scalar potential that is added to the Lagrangian to generate the vector boson and fermion masses in a gauge invariant way, via the Higgs mechanism [4]. A remnant scalar field, the Higgs boson, is part of the physical spectrum. This is the only missing piece of the Standard Model that still awaits experimental confirmation.

There are many references describing the Standard Model. The following brief summary is based on [20].

The Standard Model [2, 3] is defined by the symmetries of the Lagrangian, the representations of the fermions and the bosons, and the pattern of spontaneous symmetry breaking. The symmetry of the Lagrangian is the gauge symmetry:

$$G_{SM} = SU(3)_C \times SU(2)_L \times U(1)_Y. \tag{2.1}$$

There are three fermion generations, each consisting of five representations:

$$Q_{L_i}(3,2)_{+1/6}, u_{R_i}(3,1)_{+2/3}, d_{R_i}(3,1)_{-1/3}, L_{L_i}(1,2)_{-1/2}, l_{R_i}(1,1)_{-1}, \tag{2.2}$$

and a single complex doublet of scalars:

$$\phi(1,2)_{+1/2}. \tag{2.3}$$

The notation means that, for instance, the left-handed quarks, $Q_{L_i}(3,2)_{+1/6}$, are in a triplet of the $SU(3)_C$ group, a doublet of the $SU(2)_L$ group and carry hypercharge $Y = Q_{EM} - T_3 = +1/6$. The index $i = 1,2,3$ denotes the flavor (generation) index. The gauge group is spontaneously broken:

$$G_{SM} \rightarrow SU(3)_C \times U(1)_{EM} \tag{2.4}$$

because the scalar ϕ assumes a non-zero vacuum expectation value (VEV).

The Standard Model Lagrangian is the most general renormalizable Lagrangian that is consistent with the gauge symmetry described by Eq. (2.1). A Lagrangian generally depends on a field Φ and its first derivative $\partial_\mu\Phi$, i.e. $\mathcal{L} = \mathcal{L}(\Phi, \partial_\mu\Phi)$. Φ and $\partial_\mu\Phi$ transform under local gauge transformation as:

$$\begin{aligned} \Phi(x) &\rightarrow e^{i\epsilon_a(x)T_a}\Phi(x), \\ \delta\Phi(x) &= i\epsilon_a(x)T_a\Phi(x), \end{aligned} \tag{2.5}$$

and

$$\begin{aligned} \partial_\mu\Phi(x) &\rightarrow e^{i\epsilon_a(x)T_a}\partial_\mu\Phi(x) + i(\partial_\mu\epsilon_a(x))T_a e^{i\epsilon_a(x)T_a}\Phi(x), \\ \delta\partial_\mu\Phi(x) &= i\epsilon_a(x)T_a\partial_\mu\Phi(x) + i(\partial_\mu\epsilon_a(x))T_a\Phi(x). \end{aligned} \tag{2.6}$$

The kinetic terms of the Lagrangian - $(\partial_\mu\phi(x))^\dagger(\partial_\mu\phi(x))$ for a scalar field and $\bar{\psi}(x)\gamma^\mu\partial\psi(x)$ for a fermion field - are not invariant under this transformation. In order to restore gauge invariance the derivative ∂^μ needs to be replaced with the covariant derivative $\mathcal{D}^\mu$:

$$\mathcal{D}^\mu = \partial^\mu + igT_aA_a^\mu. \tag{2.7}$$

A_a^μ is a vector boson field in the adjoint representation of the gauge group that transforms as

$$\delta A_a^\mu = -f_{abc}\epsilon_b A_c^\mu - \frac{1}{g}\partial^\mu\epsilon_a, \tag{2.8}$$

where f_{abc} are structure constants of a given group. For the Standard Model gauge group,

the covariant derivative $\mathcal{D}^\mu$ is given by

$$\mathcal{D}^\mu = \partial^\mu + ig'YB^\mu + igT_bW_b^\mu + ig_sL_aG_a^\mu, \tag{2.9}$$

where B^μ is the single hypercharge boson, W_b^μ are the three weak interaction bosons, and G_a^μ are the eight gluon fields. Y is the charge of the $U(1)_Y$, T_b's are $SU(2)_L$ generators (represented by the 2×2 Pauli matrices $\frac{1}{2}\tau_b$ for doublets and 0 for singlets), and L_a's are $SU(3)_C$ generators (represented by the 3×3 Gell-Mann matrices $\frac{1}{2}\lambda_a$ for triplets and 0 for singlets).

In that way, the kinetic term for the left-handed quarks Q_L^I is given by

$$\begin{aligned}\mathcal{L}_{kin}(Q_L) &= i\overline{Q_{L_i}^I}\gamma^\mu\mathcal{D}_\mu Q_{L_i}^I,\\ \mathcal{D}_\mu Q_{L_i}^I &= (\partial_\mu + \tfrac{i}{6}g'B_\mu + \tfrac{i}{2}gW_\mu^b\tau_b + \tfrac{i}{2}g_sG_\mu^a\lambda_a)Q_{L_i}^I,\end{aligned} \tag{2.10}$$

and the kinetic term for the scalar doublet is

$$\begin{aligned}\mathcal{L}_{kin}(\phi) &= (\mathcal{D}_\mu\phi(x))^\dagger(\mathcal{D}_\mu\phi(x))\\ \mathcal{D}_\mu\phi &= (\partial_\mu + \tfrac{i}{6}g'B_\mu + \tfrac{i}{2}gW_\mu^b\tau_b)\phi(x).\end{aligned} \tag{2.11}$$

These kinetic terms (including analogous for other fermion representations) define the gauge interactions of the fermions and scalars.

The gauge self-interactions come from

$$\begin{aligned}\mathcal{L}_{kin}(A^\mu) &= -\frac{1}{4}tr(F^{\mu\nu a}F_{a\mu\nu}),\\ F_a^{\mu\nu} &= \partial^\mu A_a^\nu - \partial^\nu A_a^\mu - gf_{abc}A_b^\mu A_c^\nu.\end{aligned} \tag{2.12}$$

For non-Abelian symmetries Eq. (2.12) introduces trilinear and quartic self-couplings, while for Abelian symmetries ($f_{abc}=0$) there are no vector boson self interactions.

The coupling of the scalar field to fermions allows the later to acquire masses without violation of the gauge invariance. The Yukawa interactions are given by

$$-\mathcal{L}_Y = Y_{ij}^d\overline{Q_{L_i}^I}\phi d_{R_j}^I + Y_{ij}^u\overline{Q_{L_i}^I}\tilde{\phi}u_{R_j}^I + Y_{ij}^l\overline{L_{L_i}^I}\phi l_{R_j}^I, \tag{2.13}$$

where

$$\tilde{\phi} = i\tau_2\phi^*. \tag{2.14}$$

The index I indicates that the fermion fields are given in an interaction basis, with no flavor (generation) mixing under the $SU(2)_L$ gauge transformations. The Yukawa couplings are general complex 3×3 matrices. Scalar self-interactions, i.e. the Higgs potential is given by

$$V = -\mu^2\phi^\dagger\phi + \lambda(\phi^\dagger\phi)^2. \tag{2.15}$$

The full Standard Model Lagrangian is then

$$\mathcal{L} = \mathcal{L}_{kin} + \mathcal{L}_Y - V. \tag{2.16}$$

Because of the symmetry of the full Lagrangian, particles do not have masses. This is due to the fact that the mass terms for the fermions, $m\bar{f}_L f_R$, and gauge bosons, $M^2 W^a_\mu W^\mu_a$, are not invariant under the gauge transformations $SU(2)_L \times U(1)_Y$. This contradicts the experimental findings that all Standard Model particles except photons are massive. The most compelling and the simplest solution of the massless particles problem is Spontaneous Symmetry Breaking. The scalar doublet can be written as:

$$\phi = \begin{pmatrix} \phi^+ \\ \phi^0 \end{pmatrix}. \tag{2.17}$$

If the parameter μ in the Higgs Potential (Eq. (2.15)) is positive, the potential (Figure 2.1) has one unstable maximum at $\phi = 0$ and the set of minima at $\phi \neq 0$ that are mapped to each other by the local symmetry group (red line in Figure 2.1). Then, choosing a ground state field (vacuum) spontaneously breaks the symmetry of the Higgs potential.

The Higgs field given by Eq. (2.17) can be expanded around its vacuum expectation value (VEV) $v = \sqrt{\mu^2/\lambda}$:

$$\phi = \frac{1}{\sqrt{2}} \begin{pmatrix} 0 \\ v + h \end{pmatrix}. \tag{2.18}$$

The vacuum expectation value v is related to the Fermi constant:

$$\frac{G_F}{\sqrt{2}} = \frac{1}{2v^2} \Rightarrow v = \left(\sqrt{2} G_F\right)^{-1/2} \approx 246 \text{ GeV}. \tag{2.19}$$

Inserting Eq. (2.18) into the kinetic term for the scalar field $\mathcal{L}_{kin}(\phi)$ (Eq. (2.11)), the vector bosons W^μ_b and B^μ acquire masses:

$$\begin{aligned} &\frac{1}{8} \left| \begin{pmatrix} gW^\mu_3 + g'B^\mu & g(W^\mu_1 - iW^\mu_2) \\ g(W^\mu_1 + iW^\mu_2) & -gW^\mu_3 + g'B^\mu \end{pmatrix} \begin{pmatrix} 0 \\ v \end{pmatrix} \right|^2 \\ &\qquad = \frac{1}{4} g^2 v^2 W^\mu_- W_{\mu+} + \frac{1}{8}(g^2 + g'^2) v^2 Z^\mu Z_\mu, \end{aligned} \tag{2.20}$$

where we defined

$$W^\mu_\pm = \tfrac{1}{\sqrt{2}}(W^\mu_1 \mp W^\mu_2), \tag{2.21}$$

$$Z^\mu = \tfrac{1}{\sqrt{g^2+g'^2}}(gW^\mu_3 - g'B^\mu), \tag{2.22}$$

$$A^\mu = \tfrac{1}{\sqrt{g^2+g'^2}}(g'W^\mu_3 + gB^\mu). \tag{2.23}$$

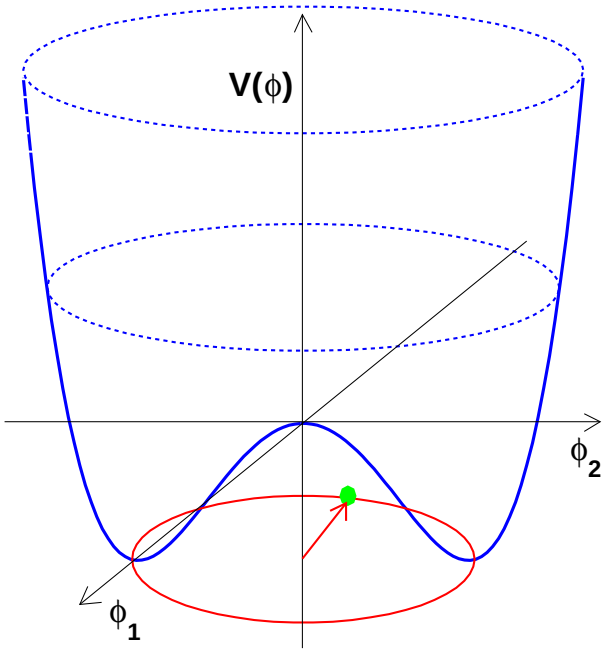

Figure 2.1: *Higgs Potential.*

The weak (Weinberg) mixing angle is defined as

$$\tan\theta_W \equiv \frac{g'}{g}, \tag{2.24}$$

and Eqs. (2.22), (2.23) can be rewritten as:

$$\begin{pmatrix} Z^\mu \\ A^\mu \end{pmatrix} = \begin{pmatrix} \cos\theta_W & -\sin\theta_W \\ \sin\theta_W & \cos\theta_W \end{pmatrix} \begin{pmatrix} W_3^\mu \\ B^\mu \end{pmatrix}. \tag{2.25}$$

Three out of four degrees of freedom of the complex scalar doublet ($\phi^\pm$ and $Im(\phi^0)$) are absorbed ("eaten") by the longitudinal polarization of the massive $W^\pm$ and Z, and only the real neutral scalar field, the physical Higgs boson, is left.

The vector boson masses are:

$$m_W^2 = \frac{1}{4}g^2v^2, \quad m_Z^2 = \frac{1}{4}(g^2+g'^2)v^2, \quad m_A^2 = 0. \tag{2.26}$$

The masslessness of the photon is not a prediction of the SM. It is guaranteed by the exact $U(1)_{EM}$ gauge symmetry.

The ρ-relation,

$$\rho \equiv \frac{m_W^2}{m_Z^2\cos^2\theta_W} \equiv 1 \tag{2.27}$$

is a prediction of all models where the $SU(2)_L \times U(1)_Y \to U(1)_{EM}$ breaking is induced by

scalar singlets or doublets only.

Inserting Eq. (2.18) into the Yukawa term $\mathcal{L}_Y$ (Eq. (2.13)) introduces the fermion mass terms:

$$-\mathcal{L}_M = (M_d)_{ij}\overline{d^I_{L_i}}d^I_{R_j} + (M_u)_{ij}\overline{u^I_{L_i}}u^I_{R_j} + (M_l)_{ij}\overline{l^I_{L_i}}l^I_{R_j}, \tag{2.28}$$

where the fermion mass matrices are defined as:

$$M_f = \frac{v}{\sqrt{2}}Y^f. \tag{2.29}$$

In order to find the mass eigenstates of the fermions, one needs to diagonalize the mass matrices. The transformation between the interaction and the mass basis is done with the unitary matrices V_{fL} and V_{fR}:

$$V_{fL}M_fV^\dagger_{fR} = M_f^{diag} \tag{2.30}$$

implying M_f^{diag} diagonal and real. In the mass basis, the fermion mass can be simply written as:

$$m_f = \frac{v}{\sqrt{2}}g_f, \tag{2.31}$$

where $g_f \equiv V_{fL}Y^fV^\dagger_{fR}$ is the diagonalized Yukawa coupling. The Yukawa couplings are free parameters of the Standard Model and they are determined to a certain accuracy from the measured fermion masses.

The Higgs boson itself acquires mass through self coupling in the Higgs potential $V(\phi)$ (Eq. (2.15)). The Higgs mass at the tree level is

$$m_H^2 = 2\lambda v^2, \tag{2.32}$$

where λ is an independent parameter. m_H can not be predicted by the SM.

At present the Standard Model gives an excellent description of nature. It is a renormalizable quantum field gauge theory with massive fermions and vector gauge bosons. In total, the Standard Model contains 18 free parameters. They are given in Appendix A. The only unknown parameter of the Standard Model is the mass of the Higgs boson.

2.1.1 Decays of the Higgs Boson

The couplings of the Higgs boson to fermions (Figure 2.2) and gauge bosons $V = W, Z$ are set by their masses:

$$\begin{aligned} g_{ffH} &= \frac{m_f\sqrt{2}}{v}, \\ g_{VVH} &= \frac{2m_V^2}{v}. \end{aligned} \tag{2.33}$$

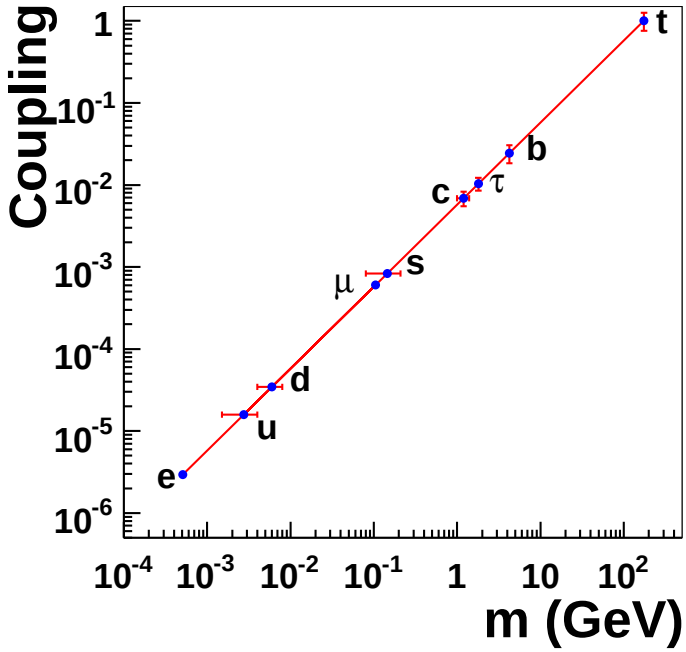

Figure 2.2: *Couplings of the Higgs boson to the fermions as a function of their masses.*

At the Born-level, the decay width of the Higgs boson into a pair of fermions is given by [21, 22]:

$$\Gamma(H \to f\bar{f}) = \frac{N_C G_F}{4\pi\sqrt{2}} m_f^2 m_H \beta_f^3 \propto g_{ffH}^2 \tag{2.34}$$

where

$$N_C = \begin{cases} 1 & \text{leptons;} \\ 3 & \text{quarks;} \end{cases} \tag{2.35}$$

is a color factor, and

$$\beta = \sqrt{1 - 4m_f^2/m_H^2} \tag{2.36}$$

is a phase space factor accounting for the velocity of the fermion in the center-of-mass system. The branching factors are modified by higher-order QCD and electroweak corrections.

The decay width to the pair of vector bosons is given by:

$$\Gamma(H \to VV) = \delta_V \frac{G_F}{16\sqrt{2}\pi} m_H^3 (1 - x_V + \frac{3}{4}x_V^2)\beta_V, \tag{2.37}$$

with

$$\delta_V = \begin{cases} 1 & V = Z; \\ 2 & V = W; \end{cases} \tag{2.38}$$

$$x_V = 4\frac{m_V^2}{m_H^2}, \tag{2.39}$$

and

$$\beta_V = \sqrt{1 - x_V}. \tag{2.40}$$

The decay into a pair of gluons or photons proceeds mainly via top- and bottom-quark loops [21]. If $m_H \ll m_t$, then the partial widths can be approximated by

$$\begin{aligned} \Gamma(H \to gg) &= \frac{G_F \alpha_s^2(m_H^2)}{36\sqrt{2}\pi^3} m_H^3 \left(1 + \left(\frac{95}{4} - \frac{7N_f}{6}\right)\frac{\alpha_s}{\pi}\right), \\ \Gamma(H \to \gamma\gamma) &= \frac{G_F \alpha^2}{128\sqrt{2}\pi^3} m_H^3 \left|\frac{4}{3} N_C e_t^2 - 7\right|^2, \end{aligned} \tag{2.41}$$

where $\alpha = 1/137$ is the electromagnetic fine structure constant, and α_s the strong force constant.

The Standard Model Higgs boson decays are dominated by the heaviest, kinematically accessible particles. Thus, for $m_H \lesssim 135$ GeV, the largest branching ratio is $H \to b\bar{b}$, but other sizable decays are $H \to gg, \tau^+\tau^-, c\bar{c}$ and $WW^{(*)}$. Despite the dominance of only few decay channels, it is important to calculate all decay rates with a high precision. For example, even though $BR(H \to \gamma\gamma)$ is typically $\mathcal{O}(10^{-3})$, it may be the easiest decay mode to observe a light Higgs boson at the LHC because of a very clear signal and an excellent $\gamma\gamma$ mass resolution. As m_H increases, $H \to WW^{(*)}$ and $H \to ZZ^{(*)}$ become the dominant decay modes, even above the $H \to t\bar{t}$ threshold. Figure 2.3 shows the branching fractions of the most important decay channels of the Standard Model Higgs boson [23]. The total decay width of the Higgs boson together with the ATLAS detector resolution is shown in Figure 2.4 [23]. For a mass bellow ~ 150 GeV, the decay width is below 10^{-2} GeV, and is much smaller then the experimental mass resolution. Above 150 GeV, the width grows rapidly, $\Gamma_H \sim m_H^3$.

2.1.2 Mass Bounds on the Standard Model Higgs Boson

2.1.2.1 Bounds from Theory

Besides the generation of the particle masses, the introduction of a new scalar particle was motivated by divergences in the scattering of a longitudinally polarized W bosons in the high energy limit [21, 22]. Without an additional interaction, the cross-section of that process, shown in the first three graphs in Figure 2.5, would diverge and would violate unitarity bounds above $\sqrt{s} = 1.2$ TeV. An interaction with the Higgs boson cancels those divergences. This mechanism would work only if the Higgs boson is not too heavy, otherwise, it would not contribute enough to the scattering amplitude before unitarity is violated. Therefore, the Higgs boson mass should be less than 850 GeV [22].

Stronger bounds on the Higgs boson mass can be derived from the energy scale up to which the Standard Model should be valid without the necessity of introducing the new

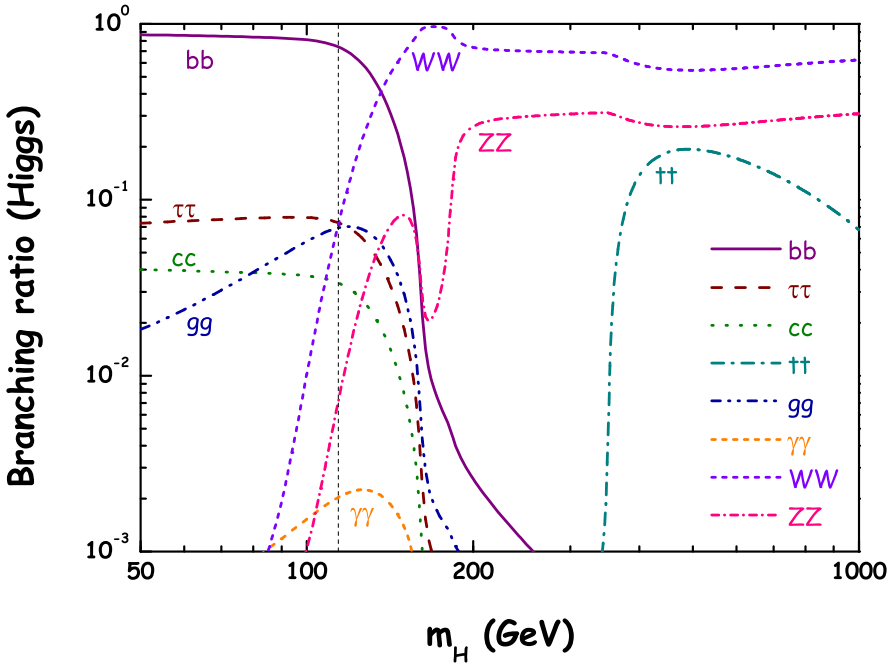

Figure 2.3: *Higgs boson branching ratios calculated with the HDECAY [23] as a function of the m_H.*

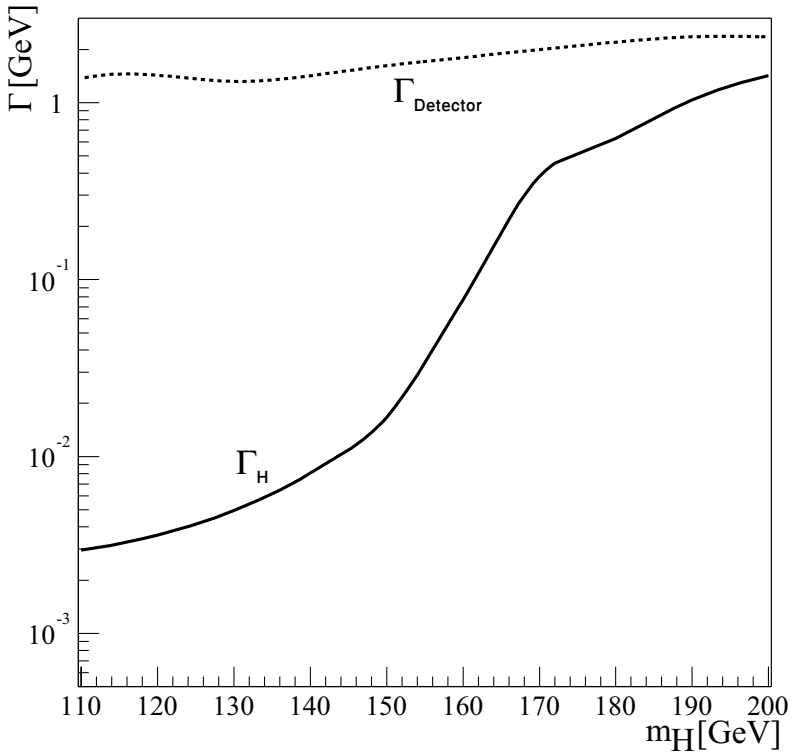

Figure 2.4: *The total width of the Higgs boson together with the detector resolution as a function of the m_H.*

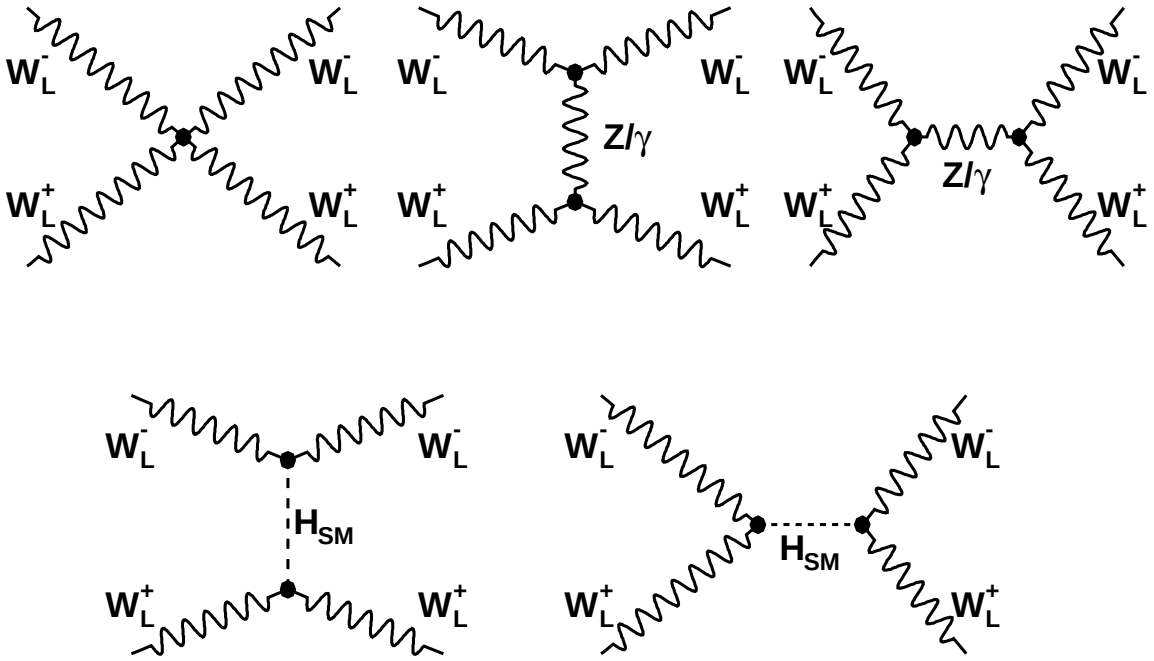

Figure 2.5: *Divergent WW cross-section graphs and their cancellation. The upper three diagrams violate unitarity starting above* $\sqrt{s} \approx 1.2$ *TeV. This unitarity violation is cancelled by the lower two diagrams involving Higgs boson exchange.*

physics [21, 22]. Figure 2.6 shows the dominant diagrams for the Higgs self coupling with the strength λ. If the Higgs boson is light, λ is small and dominant loop contribution to the Higgs potential comes from top loops (λ_t is large due to the large mass of the top quark). As a result of the loop contribution, the λ is reduced. If the Standard Model is valid as an effective theory up to the scale Λ, then these loop contributions have to be summed up until this scale. For the Higgs mechanism to remain valid, the coupling λ must remain positive, otherwise no minimum exists in the potential and no stable spontaneous symmetry breaking occurs. This places a lower bound on λ, hence on m_H, depending on cut-off scale Λ (Figure 2.7).

The energy dependence $\lambda(Q^2)$ can be derived from the renormalization group equations [21, 22]. If λ is large, the Higgs loop dominates over the top loop. Neglecting the graph with a top-quark loop, we can write λ as

$$\lambda(Q^2) = \frac{\lambda(v^2)}{1 - \frac{3\lambda(v^2)}{8\pi^2} \ln \frac{Q^2}{v^2}}. \tag{2.42}$$

For a heavy Higgs boson, λ could grow to infinity (Landau-pole). Requiring that the self coupling λ remains finite for arbitrary values of Q implies $\lambda(v) = 0$. Since $\lambda(v^2) = {m_H}^2/2v^2$, this would result in the non-interacting trivial theory. If, instead, λ is required to be finite only up to a scale Λ_{NP}, where the new physics enters, the mass bound can be

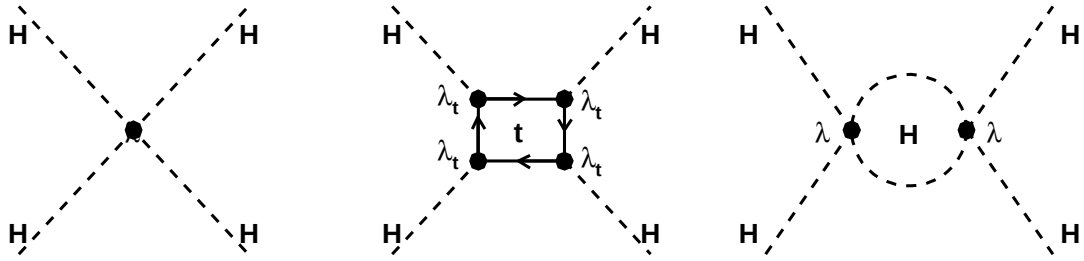

Figure 2.6: *The dominant diagrams for the Higgs boson self coupling.*

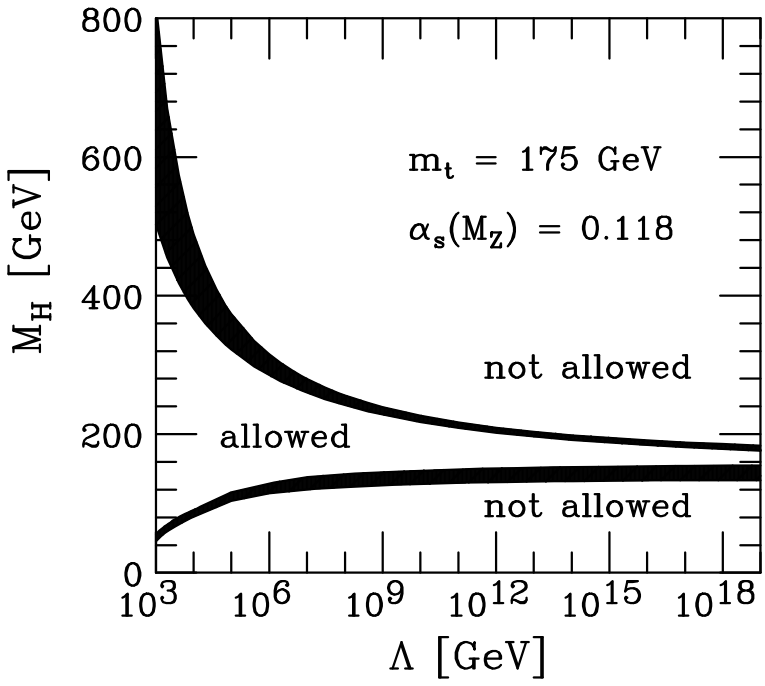

Figure 2.7: *Theoretical bounds on the SM Higgs mass as a function of the cut-off scale. It is assumed that the SM is a valid theory up to the scale* Λ*. The requirement of avoiding a Landau pole provides the upper bound and stability of the vacuum provides the lower bound [24].*

written as

$$m_{H_0}^2 < \frac{8\pi^2 v^2}{3 \ln \Lambda_{NP}^2 / v^2}. \tag{2.43}$$

From Figure 2.7, one can read that if there is no new physics up to the Planck scale ($\Lambda \approx 10^{19}$ GeV), m_H must be $\lesssim 180$ GeV [24].

2.1.2.2 Bounds from the Experiment

Direct searches for the Higgs boson have been conducted at the LEP experiments at CERN. No evidence for a signal was observed in a data from e^+e^- collisions up to the center of mass energies of 209 GeV. An experimental lower bound is set to $m_H > 114.4$ GeV at the 95% confidence level [5].

An indirect measurement of m_H within the Standard Model framework is possible using the precision measurements of the fundamental parameters, e.g., m_Z, Γ_{Z^0}, $m_{W^\pm}$. Such measurements have been performed by several experiments and a global fit to these electroweak observables with the Higgs boson mass as a free parameter sets limits on m_H [6]. The measurement of m_H is corelated with other parameters of the Standard Model, especially with mass of the top quark.

The χ^2 of the electroweak fit[1] is shown in Figure 2.8. The fit yields $m_H = 91^{+45}_{-32}$ GeV, which corresponds to one-sided 95% CL and an upper limit on m_H of 186 GeV including the theoretical uncertainty[2].

2.1.3 Problems of the Standard Model

In spite of the enormous experimental success of the Standard Model, it is believed that it is not the full picture of Nature, rather a low energy effective theory of a more fundamental one. The SM suffers from several obstacles that will be described in the following.

2.1.3.1 Experimental problems

There are experimental evidences that the neutrinos are massive, contrary to the assumptions of the Standard Model [25]. During the past years several neutrino experiments like the SuperKamiokande, K2K, SNO and Kamland [26] have established the presence of neutrino oscillations. This is a clear sign of the neutrino masses, since only massive particles have a time evolution and therefore can oscillate if mass differences between the various neutrino mass eigenstates exist.

[1] The fit is done assuming the latest measurement of the top quark mass $m_t = 172.7 \pm 2.9$ GeV.

[2] These values strongly depend on the mass of the top quark. A shift of 20% in m_H is expected if the measured m_t changes by 3 GeV (about one standard deviation). For instance $m_t = 178$ GeV leads to the best fit at $m_H = 117$ GeV, and an upper limit at $m_H \lesssim 250$ GeV.

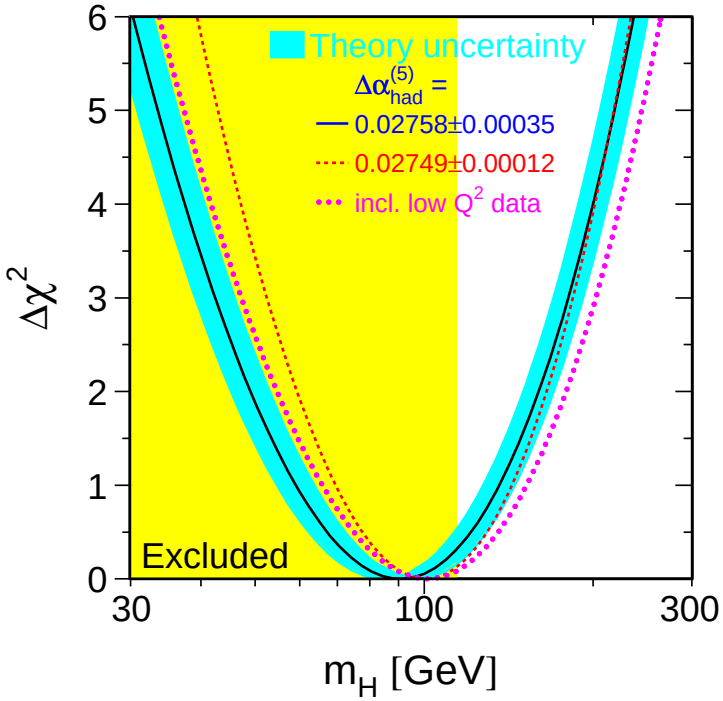

Figure 2.8: $\Delta\chi^2$ *curve as a function of* m_H*. The line is the result of the fit using all data from the LEP experiments. The band represents an estimate of the theoretical error due to missing higher order corrections. The vertical band shows the 95% CL exclusion limit on* m_H *from the direct search. Also shown are the (dashed) curves using a theory-driven evaluation of* $\Delta\alpha^{(5)}_{had}$*, or including the low-*Q^2 *measurements [6].*

The second obstacle came from the creation of the Universe and the cosmological precision measurements. The abundance of the antimatter in the visible Universe and the measured ratio $n_\gamma/n_b \approx 10^9$ [27] places a lower bound on the amount of CP violation, which is one of the three requirements for the creation of the matter-antimatter asymmetry [28]. The Standard Model incorporates CP violation only by the CKM mechanism [29]. The measured CP violation in the Standard Model is smaller by at least eight orders of magnitude then the one needed to generate the cosmologically observed matter-antimatter asymmetry.

Another observation that cannot be explained within the Standard Model is the requirement for dark matter [30]. According to the contemporary measurements, only 5% of the amount of the total energy is stored in an ordinary matter as known by the SM. For the remaining 95% of the energy of the Universe there is no explanation in the SM.

2.1.3.2 Theoretical problems

The dominant contributions to the self-energy of the Higgs boson are shown in Figure 2.9. They are coming from the Higgs itself, fermion and boson loops. If the SM is valid up to an energy scale Λ, then the size of these contributions is $\Delta {m_H}^2 \sim \Lambda^2$. On the other hand

loop corrections to the fermion masses are only subject to the logarithmic divergences, so that the overall correction is of the scale of mass itself and no finetuning problem emerges. For the Higgs boson this means that if the SM is valid up to the Planck scale of $\Lambda_P = 10^{19}$ GeV, then the natural scale of the Higgs boson mass is Λ_P while all other particles have natural mass scales below VEV v. This is the so-called hierarchy problem, which refers to the extremely large splitting of the weak scale and natural cut-of scale, the Planck scale. In order to achieve the necessary Higgs mass range of $m_H < 1$ TeV, an unnatural finetuning with the relative precision of $m_H/\Lambda_P > 10^{16}$ has to be applied. This finetuning is not explained in the context of the SM and it can be solved by extensions of the SM.

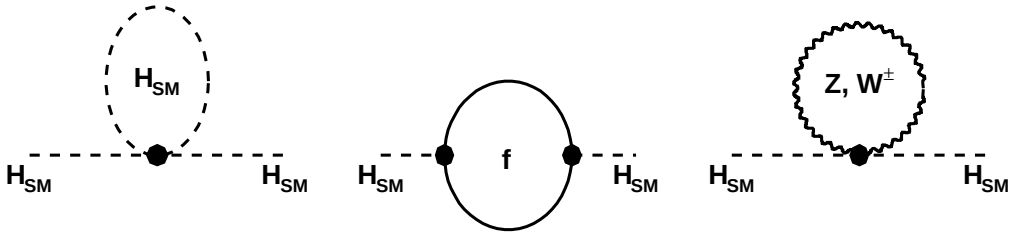

Figure 2.9: *Divergent loop contributions to the Higgs boson mass. The quadratic divergences from these graphs are not cancelled in the SM.*

The Standard Model leaves unexplained why the strong and the electroweak gauge structure is $SU(3)_C \times SU(2)_L \times U(1)_Y$ with different gauge couplings and fermionic quantum numbers whose values are not predicted by the model. There have been lot of efforts to unify the gauge groups and to have only one coupling at the energy scale of *Grand Unification* [31]. This is not possible within the Standard Model because coupling constants do not meet in a single point.

2.2 Extensions to the Standard Model

Some of the problems mentioned above can be solved by introducing the new symmetry which relates bosons to fermions. Under such a symmetry, named Supersymmetry (SUSY), every Standard Model fermion has a bosonic partner, and every Standard Model boson has a fermionic partner [7]. The new supersymmetric particles cannot be identified with the particles from the Standard Model, so SUSY at least doubles the particle content. An additional Higgs doublet together with its supersymmetric partner must be introduced into the supersymmetric extension of the Standard Model [32]. The particle content of the supersymmetric Standard Model is shown in Table 2.1. Physical particles are mass eigenstates, that are mixtures of interaction eigenstates. Thus, the charged Winos $\tilde{W}^{\pm}$

and charged Higgsinos $\tilde{H}^{\pm}$ mix giving rise to two charginos $\chi^{\pm}_{1,2}$, while the neutral Wino $\tilde{W}^3$, Bino $\tilde{B}$ and neutral Higgsinos mix into four neutralinos χ^0_i.

	supermultiplet	F	B	$SU(3)$	$SU(2)$	$U(1)_Y$	$U(1)_{EM}$
quarks	$Q^I_L = \begin{pmatrix} U^I_L \\ D^I_L \end{pmatrix}$	q^I_L	$\tilde{q}^I_L$	3	2	$\frac{1}{6}$	$\begin{pmatrix} \frac{2}{3} \\ -\frac{1}{3} \end{pmatrix}$
	U^I_R	u^I_R	$\tilde{u}^I_R$	$\bar{3}$	1	$-\frac{2}{3}$	$-\frac{2}{3}$
	D^I_R	d^I_R	$\tilde{d}^I_R$	$\bar{3}$	1	$\frac{1}{3}$	$\frac{1}{3}$
leptons	$L^I_L = \begin{pmatrix} N^I_L \\ E^I_L \end{pmatrix}$	l^I_L	$\tilde{l}^I_L$	1	2	$-\frac{1}{2}$	$\begin{pmatrix} 0 \\ -1 \end{pmatrix}$
	E^I_R	e^I_R	$\tilde{e}^I_R$	1	1	1	1
Higgs	$H_d = \begin{pmatrix} H^0_d \\ H^-_d \end{pmatrix}$	$\begin{pmatrix} \tilde{h}^0 \\ \tilde{h}^- \end{pmatrix}$	$\begin{pmatrix} h^0_d \\ h^-_d \end{pmatrix}$	1	2	$-\frac{1}{2}$	$\begin{pmatrix} 0 \\ -1 \end{pmatrix}$
	$H_u = \begin{pmatrix} H^+_u \\ H^0_u \end{pmatrix}$	$\begin{pmatrix} \tilde{h}^+ \\ \tilde{h}^0 \end{pmatrix}$	$\begin{pmatrix} h^+_u \\ h^0_u \end{pmatrix}$	1	2	$\frac{1}{2}$	$\begin{pmatrix} 1 \\ 0 \end{pmatrix}$
gauge bosons	G	$\tilde{G}$	G	8	1	0	0
	W	$\tilde{W}$	W	1	3	0	$(0, \pm 1)$
	B	$\tilde{B}$	B	1	1	0	0

Table 2.1: *The particle content of the supersymmetric Standard Model.*

Since no supersymmetric particle has been observed at the same mass as its SM partner, SUSY has to be either spontaneously or explicitly broken. It has been shown that spontaneously broken supersymmetry ran into phenomenological difficulties [32], so the way out is an explicit breaking of supersymmetry. The terms that break supersymmetry explicitly and generate no quadratic divergences are contained in the soft breaking Lagrangian $\mathcal{L}_{soft}$.

General broken SUSY has a huge parameter space and therefore very limited predictive power. An example of much more constrained version, with less free parameters, is the Minimal Supersymmetric Standard Model (MSSM) [32].

2.2.1 The Higgs sector of the MSSM

As discussed in the previous section, the MSSM contains two doublets of complex Higgs fields:

$$H_1 = \begin{pmatrix} H_1^+ \\ H_1^0 \end{pmatrix}, \quad H_2 = \begin{pmatrix} H_2^0 \\ H_2^- \end{pmatrix}. \tag{2.44}$$

The non-vanishing vacuum expectation values of the neutral components of the two Higgs doublet are chosen to be $(0, v_1)$ and $(v_2, 0)$, respectively. The two vacuum expectation values are related:

$$\tan\beta \equiv \frac{v_2}{v_1}, \quad \text{with } \sqrt{v_1^2 + v_2^2} \approx 246 \text{ GeV}. \tag{2.45}$$

Including the soft-supersymmetry-breaking terms, the MSSM Higgs potential of the two Higgs doublets H_1 and H_2 becomes

$$\begin{aligned} V_{Higgs} = {} & m_{1H}^2|H_1|^2 + m_{2H}^2|H_2|^2 - m_{12}^2(\epsilon_{ij}H_1^i H_2^j + h.c.) \\ & + \frac{1}{8}(g^2 + g'^2)(|H_1|^2 - |H_2|^2)^2 + \frac{1}{2}g^2|H_1^* H_2|^2. \end{aligned} \tag{2.46}$$

where $m_{iH}^2 \equiv |\mu|^2 + m_i^2$ $(i = 1, 2)$, and ϵ_{ij} is the Levi-Civita symbol. The parameters m_i^2 $(i = 1, 2)$ are real and can be either positive or negative. The only place where a phase could show up is the last term which is proportional to $H_1^i H_2^j$, where any CP violating phase can be absorbed in a redefinition of the phases of H_1 and H_2. Thus, the MSSM Higgs potential is invariant under CP transformations at the tree level. The Higgs potential V_{Higgs} contains both soft-SUSY breaking terms - the three mass terms - and SUSY-conserving terms - the two last terms.

The three parameters of the Higgs potential $m_{1H}^2, m_{2H}^2, m_{12}^2$ can be rewritten in terms of the $\tan\beta$ and one physical Higgs mass. The parameter m_{12}^2 is related to the mass of the CP-odd Higgs boson:

$$m_{12}^2 = m_A^2 \sin\beta\cos\beta. \tag{2.47}$$

The parameters m_{1H}^2 and m_{2H}^2 can be determined from the requirement that spontaneous symmetry breaking $SU(2)_L \times U(1)_Y \to U(1)_{EM}$ exists, which yields:

$$\begin{aligned} m_{1H}^2 &= \frac{m_A^2 \tan\beta}{\sin\beta\cos\beta} - \frac{m_Z^2}{2}\cos 2\beta, \\ m_{2H}^2 &= \frac{m_A^2}{\sin\beta\cos\beta\tan\beta} + \frac{m_Z^2}{2}\cos 2\beta. \end{aligned} \tag{2.48}$$

Thus, there are only two free parameters which are chosen to be m_A and $\tan\beta$.

The eight real scalar degrees of freedom (that correspond to two complex Higgs doublets) are three Goldstone bosons absorbed by the $W^\pm$ and Z, and five physical Higgs bosons: neutral CP-even h and H, neutral CP-odd A, and two charged $H^\pm$. At the tree

level, the following masses are obtained:

$$m^2_{h,H} = \frac{1}{2}\left(m^2_A + m^2_Z \pm \sqrt{(m^2_A + m^2_Z)^2 - 4m^2_Z m^2_A cos^2 2\beta}\right) \quad (2.49)$$

$$m^2_{H^\pm} = m^2_W + m^2_A, \quad (2.50)$$

leading to the following bounds at the tree level:

$$\begin{aligned} m_h &\leq m_A, \\ m_h &\leq m|\cos 2\beta| \leq m_Z, \quad \text{with } m \equiv \min(m_Z, m_A), \\ m_H &\geq m_Z, \\ m_{H^\pm} &\geq m_W. \end{aligned} \quad (2.51)$$

Based on these limits the lightest MSSM Higgs boson, the h, was expected to be within the range of LEP. Consequently, LEP was expected to provide a decisive test of the validity of this model. However, radiative corrections for the lightest Higgs boson mass can be large [33]. The upper bound on m_H in the presence of loop-effects can be parametrized by:

$$m^2_h \leq m^2_Z \cos 2\beta + \delta M^2_t + \delta M^2_X. \quad (2.52)$$

The most important correction, δM^2_t, comes from the top quark loops (due to high mass and very strong coupling to the Higgs boson):

$$\delta M^2_t = \frac{3G_F}{\sqrt{2}\pi^2} m^4_{top} \log \frac{m_{\tilde{t_1}} m_{\tilde{t_2}}}{m^2_{top}}. \quad (2.53)$$

The second contribution, δM^2_X originates from loops involving scalar top quarks. It introduces a strong dependence on the squark mixing parameters $X_t = A_t - \mu \cot \beta$ (A_t is stop trilinear coupling [33]):

$$\delta M^2_X = \frac{3G_F}{2\sqrt{2}\pi^2} X_t \left[2g_1(m^2_{\tilde{t_1}}, m^2_{\tilde{t_2}}) + X_t g_2(m^2_{\tilde{t_1}}, m^2_{\tilde{t_2}})\right] \quad (2.54)$$

with

$$g_1(a,b) = \frac{1}{a-b}\log\frac{a}{b} \quad \text{and} \quad g_2(a,b) = \frac{1}{(a-b)^2}\left[2 - \frac{a+b}{a-b}\log\frac{a}{b}\right]. \quad (2.55)$$

With these corrections, an upper bound on the lightest Higgs boson is pushed to $\sim$ 135 GeV [8, 9]. Since the sparticles $\tilde{t_1}$ and $\tilde{t_2}$ are involved in important loop corrections, the Higgs sector cannot be described only by $\tan\beta$ and m_A, as at the tree level. The most important parameters entering at the loop level are:

- M_{SUSY} - the common SUSY breaking scale, to which all squark and slepton mass

parameters $M_{\tilde{Q}}$ are set at the Planck scale;

- μ - the Higgsino mixing parameter;
- M_2 - the $SU(2)_L$ gaugino (Wino) mass parameter. The parameter M_1 is then calculated using the GUT-inspired relation $M_1 = 5/3 \tan^2 \theta_W M_2$, which depends on the unification of the gaugino masses at GUT scale;
- $m_{\tilde{g}}$ - the gluino mass;
- $X_t = A_t - \mu \cot \beta$ - the stop mixing parameter. In most models $A_b = A_t$ is used.

The couplings of the neutral MSSM Higgs boson to the SM particles are $g = g_{SM} f$ with f given in Table 2.2 [22]. They depend on $\tan \beta$, since this determines the relative contribution to the mass generation of the two doublets, and on α, which determines the mixing of the two interaction CP-even neutral eigenstates into the mass eigenstates.

Higgs boson	Fermions		Gauge bosons
	down type	up type	Z,W
h	$\frac{-\sin\alpha}{\cos\beta}$	$\frac{\cos\alpha}{\sin\beta}$	$\sin(\beta-\alpha)$
H	$\frac{\cos\alpha}{\cos\beta}$	$\frac{\sin\alpha}{\sin\beta}$	$\cos(\beta-\alpha)$
A	$\tan\beta$	$\cot\beta$	0

Table 2.2: *The correction factors to the couplings of the neutral MSSM Higgs bosons with respect to the SM couplings of the SM Higgs boson.*

2.2.2 CP violation in the MSSM Higgs sector

The Higgs potential is invariant under CP transformations at the tree level within the MSSM. However, the same radiative corrections that push the mass of the lightest Higgs boson up, introduce CP violation in Higgs sector of the MSSM [34]. In such a case the mass eigenstates are no longer CP eigenstates, instead one introduces H_1, H_2 and H_3, which have mixed CP parities. Since A^0 is not a mass eigenstate anymore, m_{H^+} is used as a parameter instead of m_A. The CP-violation manifests itself in complex phases of the parameters of $\mathcal{L}_{MSSM}$. The most important are $A_{t,b}$ and $m_{\tilde{g}}$.

In general, the CP-violation in the Higgs potential at one-loop level exists if the relation

$$\mathrm{Im}(m_{12}^2 \mu A_{t,b}) \neq 0 \tag{2.56}$$

is satisfied. The phases of m_{12}^2 and μ can be absorbed by redefinition of the fields, thus the only parameter that introduces CP-violation is the phase of $A_{t,b}$. At the two-loop level, the phase of $m_{\tilde{g}}$ also enters as an additional parameter which can provide CP-violation.

The CPV one-loop contributions to the Higgs potential are shown in Figure 2.10. The tree-level quartic coupling of the Higgs potential between the weak Higgs eigenstates h_i is shown in the first diagram (the one on the left), and the loop-effects introducing the trilinear couplings $A_{t,b}$ in the two other diagrams. As a consequence, CP-violation is introduced in the Higgs potential.

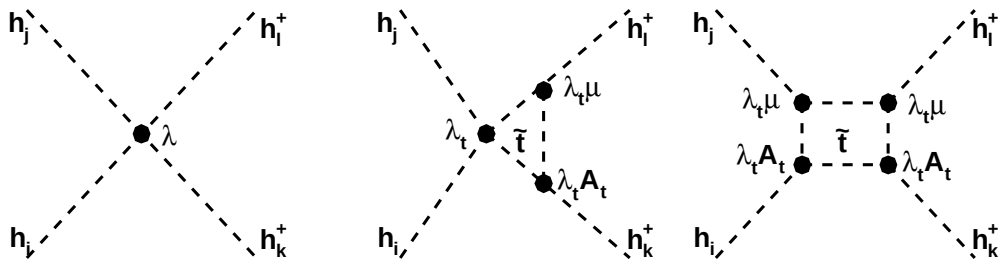

Figure 2.10: *Introduction of CPV effects into the Higgs potential.*

If CP is violated in the Higgs sector, then the Higgs boson mass eigenstates do not have well defined CP parity. The interaction eigenstates a, h_1, h_2 are connected with the mass eigenstates H_1, H_2, H_3 via the general orthogonal matrix O_{ij}

$$\begin{pmatrix} H_1 \\ H_2 \\ H_3 \end{pmatrix} = O_{ij} \begin{pmatrix} a \\ h_1 \\ h_2 \end{pmatrix}, \tag{2.57}$$

with $m_{H_1} < m_{H_2} < m_{H_3}$.

The CP-violating self energy effects give sizeable off-diagonal scalar-pseudoscalar contributions to the general neutral Higgs-boson mass matrix. The CP-violating elements scale qualitatively as [34]:

$$M_{SP}^2 \propto \frac{m_t^4}{v^2} \frac{\mathrm{Im}(\mu A_t)}{32\pi^2 M_{SUSY}^2}. \tag{2.58}$$

Large CPV effects are obtained if the SUSY breaking scale M_{SUSY} is small and the $\mathrm{Im}(\mu A_t)$ is large. Also, large m_t increases the CPV effects.

When choosing the parameters, experimental constrains from electric dipole moment (EDM) measurements of the neutron and the electron have to be fulfilled [35]. However, cancellations among different contributions to the EDM may emerge, so those measurements do not provide universal exclusion in the MSSM parameter space.

The couplings of the Higgs mass eigenstates to the SM bosons are given by

$$g_{H_iZZ} = \cos\beta O_{2i} + \sin\beta O_{3i}, \tag{2.59}$$

$$g_{H_iH_jZ} = O_{1i}(\cos\beta O_{3j} + \sin\beta O_{2j}) - O_{1j}(\cos\beta O_{3i} + \sin\beta O_{2i}), \tag{2.60}$$

and they obey the sum rules

$$\sum_{i=1}^{3} g^2_{H_iZZ} = 1, \tag{2.61}$$

$$g_{H_kZZ} = \frac{1}{2}\sum_{i,j=1}^{3} \epsilon_{ijk} g_{H_iH_jZ}. \tag{2.62}$$

It can be seen that only CP-even weak eigenstates h_1 and h_2 couple to the Z in Higgsstrahlung (Figure 2.11). Since all mass eigenstates are mixtures of all weak eigenstates, it is possible that the lightest Higgs boson contains large portion of CP-odd field. Then it might escape detection at LEP even if its mass is small.

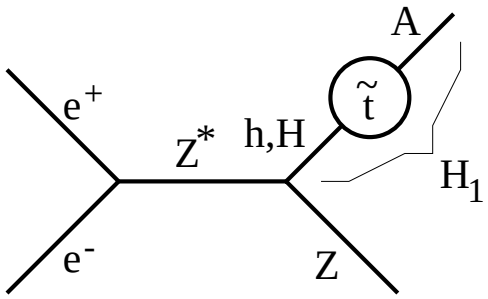

Figure 2.11: *Diagram illustrating the effective coupling of a Higgs mass eigenstate to the Z^0 in Higgsstrahlung. The complete mass eigenstate H_1 is composed of admixtures of h, H and A. Here the h, H and A denote the CP-even and CP-odd weak eigenstates, respectively. Only the CP-even admixtures h and H couple to the Z^0, while the CP-odd A does not. Therefore the coupling of the mass eigenstate is reduced with respect to a CP conserving scenario.*

The important consequence of CP violation is the modification of the top and bottom quark Yukawa couplings through CP-violating vertex effects [34] involving gluinos and higgsinos, as well as top and bottom squarks. Although these effects enter the charged and neutral Higgs-boson masses and couplings formally at the two-loop level, they can still modify the numerical predictions of the masses and couplings in a significant way.

2.3 Introduction to the High Energy Physics Experiment

Modern accelerators are built either as synchrotrons, where particles move on constant radius in a variable magnetic field, or as linear accelerators. High energy experiments are mostly performed using colliders, where the two beams of particles, organized in bunches and moving in opposite directions at high energies, collide in the detector.

Two basic quantities governing the performance of the accelerator are the center of mass energy $\sqrt{s}$, and the luminosity $\mathcal{L}$. The center of mass energy can be either adjusted to produce certain particle resonantly to maximize the number of produced events, or it can be set as high as possible to search for the new phenomena at higher energy scales. The number of produced events N in a time interval Δt depends on the luminosity:

$$N = \sigma \int_{\Delta t} \mathcal{L} dt \tag{2.63}$$

where σ is the cross-section of the given process. On the other hand, the luminosity depends on the machine parameters:

$$\mathcal{L} = \frac{N_{p1} N_{p2} f_b}{4\pi \sigma_x \sigma_y}, \tag{2.64}$$

where N_{p1} and N_{p2} are the numbers of particles in two colliding bunches, f_b is the rate of bunch crossings, and $\sigma_{x,y}$ are transversal beam spot sizes at the interaction point. A way to measure the luminosity is to use well-modeled physical process with a high cross-section, like for instance Bhabha-scattering $e^+e^- \to e^+e^-$ in e^+e^- colliders.

The detectors are placed at the collision points of the beams. Usually, they obey cylindrical symmetry, with the z-axis in the direction of the beam. Their structure is an onion-like, with the subdetectors with different purposes filling subsequent layers. In order to determine the charge and the momentum of the particle, detectors are put into a magnetic field. Starting from the innermost layer, the subdetectors have the following purposes:

- Impact parameter measurement
  The innermost detector layer measures the impact parameter of the trajectories of the charged particles with respect to the reconstructed primary interaction point. This enables the tagging of particles with relatively long lifetime.

- Momentum measurement
  The next detector layer measures the curvature of the trajectories of the charged particles in a magnetic field in order to determine their momentum and charge.

- Particle identification

The energy loss per flight length, $\mathrm{d}E/\mathrm{d}x$, of a charged particle can be used, together with the momentum information, to determine the particle mass and, hence, to identify the particle.

- Energy measurement
  The energy of the particles is measured in the calorimeters. There are two types of calorimeters: electromagnetic (EM) and hadronic (HAD) ones. Electrons, positrons and photons deposit all their energy in the electromagnetic calorimeter. Heavier particles may leave some of their energy in the EM calorimeters (if they are charged), and deposit the remaining energy in hadronic calorimeters.

- Muon Identification
  The outermost detector layer aims at detecting muons, the only interacting particles which are able to cross the calorimeter.

Chapter 3

LEP and OPAL

3.1 Introduction to the Experiment

3.1.1 The LEP Accelerator

The Large Electron Positron Collider (LEP) [36] at CERN started operating in 1989 and was shut down in November 2000. Having a circumference of 27 km, the accelerator was the largest in a world. Beams of electrons and positrons were accelerated, counter-rotated and occasionally interacted at four[1] interaction points where four experiments - ALEPH, DELPHI, L3 and OPAL - were positioned (Figure 3.1).

The LEP tunnel, located ~ 100 m bellow surface, has eight straight sections, where the bunches were accelerated and experiments were situated, and eight curved sections, where bunches were bended to form a ring. The electrons were produced by thermionic emission, then accelerated along an electron linear collider, the LEP Injector Linac (LIL). Some of the electrons were collided with a tungsten target to produce the positrons. The remaining electrons, along with the positrons, were then passed into the Electron Positron Accumulator ring (EPA), where they were accumulated before injection, and, subsequently, into the Proton Synchrotron (PS) to be initially accelerated to a few GeV. Afterward, they were transfered to the Super Proton Synchrotron (SPS) where further acceleration took place and finally they were injected into the LEP ring.

In the phase of LEP 1, from 1989 to 1995 the center of mass energy was around $\sqrt{s} = 91.2$ GeV, which corresponded to the mass of Z boson. The main goal was to accurately measure the properties of the Z boson and compare results with the Standard Model predictions. From 1996, when LEP 2 phase started, the beam energy was gradually increasing. When it exceeded $2m_W$, pair production of the charged gauge bosons became possible, allowing for more tests of the Standard Model. With further increase of energy, the search for the Higgs boson became the most important part of the LEP physics program. During LEP 2 phase, center of mass energy increased up to 209 GeV. Parameters

[1] Actually, there were eight interaction points, but only four were used for the experiments.

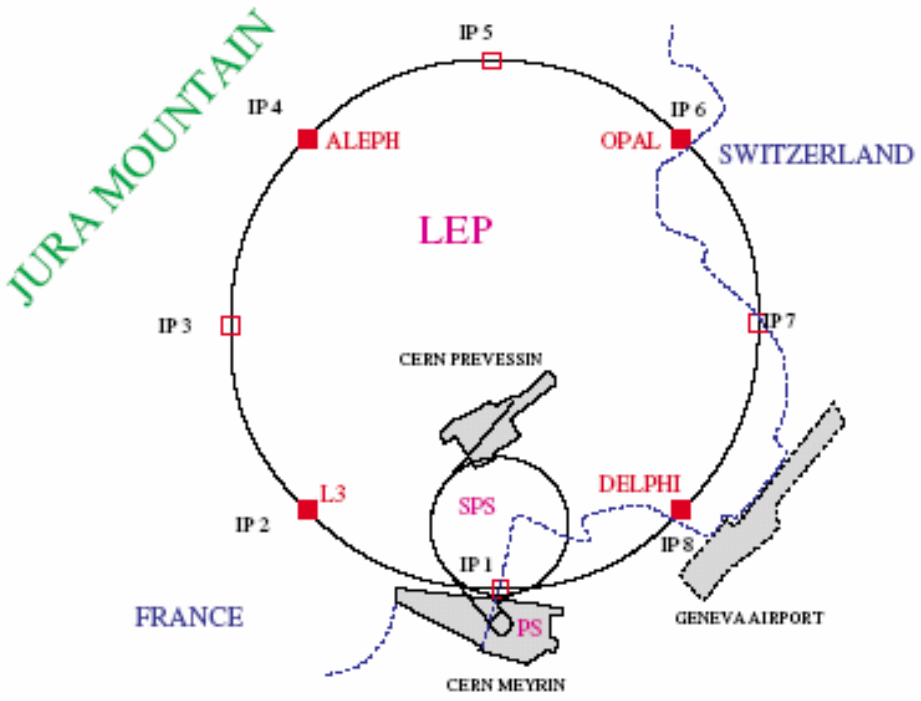

Figure 3.1: *Sketch of the LEP.*

of the LEP are given in a Table 3.1.

One of the main reasons that the LEP program was terminated was that the energy loss due to synchrotron radiation scaled like the fourth power of the beam energy:

$$E_{loss} \sim \frac{1}{r}\left(\frac{E_b}{m}\right)^4, \tag{3.1}$$

where r is the bending radius, E_b the beam energy, and m the particle mass. It was, therefore, impossible to further increase the energy of the machine. In order to avoid this obstructing energy loss one can accelerate heavier particles in the same machine. The natural candidates for such a replacement are protons. It is very difficult to produce large quantities of anti-protons and one is compelled to run two proton beams against each other. The main drawback is that the proton is a composite particle, and the primary interaction ($qq, gq, gg, q\bar{q}, \bar{q}\bar{q}$, and $g\bar{q}$) is accompanied by a hadronic background originating from the parts in the proton that did not participate in the primary interactions. Also, the interacting partons ($q, \bar{q}, g$) carry only part of the initial proton's energy. As an alternative solution to the energy crisis of using heavier particles, one can increase the radius of the accelerator (which is very expensive) or use Linear Colliders with electron beams.

center of mass energy	$\sqrt{s}$	$89 - 209$ GeV
beam spot size	$\sigma_x \times \sigma_y$	$200\ \mu m \times 2.5\ \mu m$
collision frequency	f_b	$22\ \mu s$
Particles per bunch	N	3×10^{11}
Luminosity	$\mathcal{L}$	$10^{31}\text{cm}^{-2}\text{s}^{-1}$
accelerating gradient		up to 7 MV/m

Table 3.1: *Machine parameters of the LEP accelerator.*

3.1.2 The OPAL Detector

The Omni Purpose Apparatus at LEP (OPAL) was one of the four LEP detectors. It had cylindrical symmetry. The interaction point was the origin of the right-handed coordinate system with the z-axis pointing into the flight direction of the e^- beam and x-axis pointing toward the center of the LEP ring. The detector covered $\sim 97\%$ of the solid angle in order to detect as much outgoing particles as possible. The dimensions of the detector were approximately $10 \times 10 \times 12$ m^3. It is shown in Figure 3.2.

The detailed description of the OPAL detector is given in [37], and is introduced in the following.

3.1.2.1 Central Tracking System

The central tracking system (CT) comprised four detectors: the silicon micro-vertex detector (SI), the central vertex detector (CV), the central jet chamber (CJ) and the z-chambers (CZ).

The Silicon-Microvertex detector (SI) The Microvertex detector [38] was constrained to fit in an annular space between the beam pipe with an outer radius of 56.5 mm and the pressure vessel with an inner radius of 80 mm. It consisted of two layers of double-sided silicon microstrip detectors of 18.3 cm length. The inner layer, that consisted of 12 modules, covered $|\cos\theta| < 0.93$, while the outer one, that consisted of 15 modules, covered $|\cos\theta| < 0.89$. On both sides the microvertex detector was covered with strips with 25 μm pitch. On the front side they were oriented in the z direction and they measured a space point in a $r - \phi$ plane. Every second strip was read out and a track point resolution in a $r - \phi$ plane of 15 μm was reached. On the backside, with strips oriented perpendicular to the z axis, only every fourth strip was read out which led to spatial track point resolution in a $r - z$ plane is 24 μm.

The Vertex Chamber (CV) The vertex chamber was a 1 m long cylindrical drift chamber, with an inner radius of 8.8 cm and an outer one of 23.5 cm. A gas mixture of argon (88.2%), methane (9.8%) and isobutane (2.0%) was used. It consisted of two layers

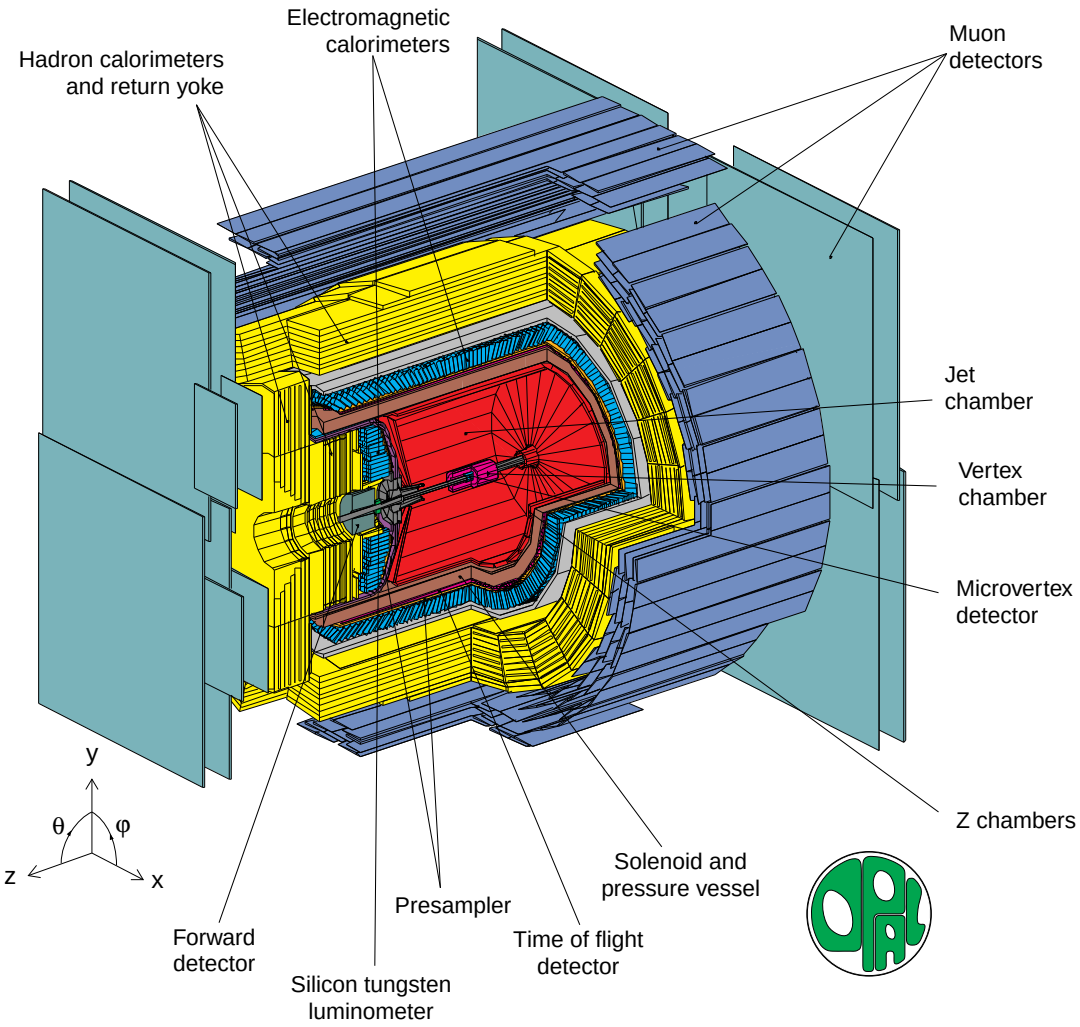

Figure 3.2: *Sketch of the OPAL detector.*

with 36 sectors each. In the inner layer each sector had 12 signal wires parallel to the z direction. The six signal wires of the outer layer were mounted at a stereo angle of 4° with the respect to the z axis, allowing a determination of the z coordinate of the tracks with a precision of 300 μm. The resolution in a $r - \phi$ plane was 50 μm.

The Central Jet Chamber (CJ) The central jet chamber [39] was a 4 m long cylindrical drift chamber, with an inner radius of 25 cm and an outer one of 185 cm and filled with the same gas mixture as vertex chamber. It was designed to combine good space point measurements with the reasonable two-track resolution for an efficient reconstruction of events with high density of tracks (such as jets). It was also capable to identify particles using the $\mathrm{d}E/\mathrm{d}x$ information. The axial magnetic field of 0.435 T provided precision measurement of the momenta of charged particles.

The jet chamber was divided into 24 identical sectors, each containing 159 sense wires along the beam direction. The radial anode wire planes were positioned between two cathode planes. To remove right-left ambiguity, the sense wires were staggered by ± 100 μm

with the respect to the potential wires. The three-dimensional coordinates of charged tracks were recorded based on the wire position, drift time and charge division measurement. Tracks could have been fully measured in the region $43° \leq \theta \leq 157°$.

The z-Chamber (CZ) The z-chambers were arranged to form a cylindrical layer between the jet chamber and the coil. Their purpose was to measure more accurately the z position of charged tracks thus improving the polar angle and momentum resolution. It consisted of 24 drift chambers, each divided into the eight cells of six anode wires which were spanned in the $r-\phi$ plane perpendicular to the jet chamber wires. The z coordinate was measured with a precision of 100 μm.

Combined Performance of the Tracking System The momentum resolution was obtained from the difference between positively and negatively charged muons in $e^+e^- \to \mu^+\mu^-$ events [40]. The resolution obtained from the width of the distributions was improved from $\sigma_p/p^2 = (1.84 \pm 0.09) \cdot 10^{-3}$ GeV^{-1} without CZ hits to $\sigma_p/p^2 = (1.42 \pm 0.01) \cdot 10^{-3}$ GeV^{-1} when the CZ hits were included.

The impact parameter resolutions from $e^+e^- \to \mu^+\mu^-$ events (momenta around 45 GeV) without the silicon micro-vertex detector was about 35 μm in $r-\phi$ and 2 mm (2.7 cm) in z with (without) the CV stereo information. With the SI detector, the resolutions went down to 18 μm (24 μm) in $r-\phi$ (z), as mentioned above.

3.1.2.2 The Time-Of-Flight system (TOF)

The time-of-flight detector was located outside of the pressure vessel and the solenoid coil. It consisted of plastic scintillator strips, read out at both sides of the barrel using photo multipliers. It achieved a time resolution of 300 ps. It was mainly used for triggering and cosmic rejection.

3.1.2.3 The Electromagnetic Calorimeter

The next layer outside the time-of-flight system was the electromagnetic calorimeter (ECAL), which consisted of four subdetectors: the barrel electromagnetic presampler (PB), the barrel electromagnetic calorimeter (EB), the endcap electromagnetic presampler (PE) and the endcap electromagnetic calorimeter (EE). The total coverage of the electromagnetic calorimeter was $|\cos\theta| < 0.98$.

The electromagnetic calorimeter measured the energy and the direction of electrons, positrons and photons with the energies from a few hundreds of MeV up to ~ 100 GeV. It also provided π^0-photon and electron-hadron discrimination.

Barrel Electromagnetic Presampler The presamplers were used to improve energy and position resolution. The barrel electromagnetic presampler (PB) was a cylindrical

detector, located right behind TOF detector. It consisted of 16 chambers, each 3 cm thick and 662.3 cm long, arranged around a cylinder with a radius of 238.8 cm. Each chamber contained two layers of limited streamer tubes. The anode wire in each tube was oriented along the z direction and could provide the z coordinate measurement by charge division. The cathode strips, on either side of the tubes, were oriented at 45° with respect to the wire direction.

The two anodes and four cathodes in each chamber were read out. The cathode strip pitch was 11 mm and the anode pitch was 9.9 mm. The chambers were filled with a gas mixture of n-pentane (32%) and CO_2 (68%).

Barrel Electromagnetic Calorimeter The barrel electromagnetic calorimeter (EB) contained 9440 lead glass blocks (75% PbO). Each block was $\sim 10 \times 10$ cm^2 in area and 37 cm deep (corresponding to 24.6 radiation lengths, X_0, in average), and covered the full azimuthal angle and the polar angle region $|\cos\theta| < 0.82$, at a radius of 2.455 m. The longitudinal axes of the blocks pointed to the interaction point, slightly tilted from a perfectly pointing geometry to prevent particles escaping through the gaps between two blocks. The calorimeter was segmented into 59 blocks in the z direction and 160 blocks in the ϕ direction. The granularity achieved in ϕ corresponded to 40 mrad. The energy deposit in the calorimeter was obtained by measuring the Cherenkov light, emitted by relativistic electrons and positrons in the shower, using a magnetic field resistant phototubes.

Endcap Electromagnetic Presampler The endcap electromagnetic presampler (PE) was an umbrella-shaped arrangement of 32 thin-gap chambers (TGCs) [41] in 16 wedges. It covered polar angle region $0.83 < |\cos\theta| < 0.95$. The chambers overlapping scheme ensured the full coverage of the region. The TGC detectors were thin (1 mm overall thickness) multiwire chambers that operated in a semisaturated mode. Gold-plated tungsten wires, 50 μm in diameter, were used for the anode, operating in a voltage of +3.5 kV. The operating gas was a mixture of n-pentane (45%) and CO_2 (55%). The energy and position were measured by the 18 mm wide cathode strip on both sides of the chamber and the anode wires, with 2 mm pitch, that were read out in groups of four.

Endcap Electromagnetic Calorimeter The endcap electromagnetic calorimeter (EE) consisted of two dome-shaped arrays of 1132 lead-glass (55% PbO) blocks, located behind the endcap presamplers covering the full azimuthal angle in the regions $0.81 < |\cos\theta| < 0.98$. The blocks were 9.2×9.2 cm^2 in area and 52 cm deep (corresponding to $22X_0$, in average). The detector operated in the region of a full magnetic field. The Cherenkov photon detectors (vacuum photodiodes) were designed to operate in an axial magnetic field of 0.45 T.

Combined Performance of the ECAL The average energy resolution of the ECAL system had a constant term of $\sigma_E/E = (1.8 \pm 0.3)\%$ and an energy dependent term

$$\frac{\sigma_E}{E} = \frac{16\%}{\sqrt{E(GeV)}} \tag{3.2}$$

from lead-glass blocks only, which went down to

$$\frac{\sigma_E}{E} = \frac{13\%}{\sqrt{E(GeV)}} \tag{3.3}$$

with the presampler corrections. The noise spectrum was found to be below 300 MeV.

3.1.2.4 The Hadronic Calorimeter

The Hadron Calorimeter (HCAL) consisted of two subdetectors: the barrel and endcap hadron calorimeter (HB), and the pole-tip hadron calorimeter (HP). The total solid angle coverage of the HCAL system was 97%. The iron of the magnet return yoke acted as an absorber for hadronic showers and provided 4 or more hadronic interaction lengths in addition to ~ 2 interaction length in front of it. The sampling calorimeters were made of iron layers interleaved with sensitive planes of detectors. They measured the energy of the strongly interacting particles and assisted in the muon identification. The total hadronic energy was calculated using information from both ECAL and HCAL.

Barrel and Endcap Hadronic Calorimeter The barrel consisted of 9 layers of chambers alternating with 8 layers of iron stabs. It was 1 m thick and was placed at a radius 3.89 m. The slabs were 10 cm thick, with a gap of 25 mm. The barrel was closed at each end by a doughnut shaped endcaps, each comprising 8 layers of chambers and 7 iron slabs, 10 cm thick with 35 mm gap. The polar angle coverage of HB was $|\cos\theta| < 0.91$. The probability of a pion to pass through without an interaction was ~ 0.001.

Pole-Tip Hadron Calorimeter The pole-tip hadron calorimeter extended the polar angle coverage of HB to $0.91 < |\cos\theta| < 0.99$. Each pole-tip contained 160 thin-gap chambers (TGC), organized in 10 layers alternating with 10 iron slabs. The slabs were 80 mm thick with gaps of only 10 mm (to which the 7 mm thick TGCs fitted well). The number of samplings was increased to 10 to improve energy resolution in the forward region.

All TGC chambers were built at the Weizmann Institute of Science in collaboration with Tel Aviv University and the Technion. This was the main contribution of the Israeli group to the OPAL detector.

Combined Performance The energy resolution in the barrel (HB) and endcap was

$$\frac{\sigma_E}{E} = \frac{120\%}{\sqrt{E(GeV)}} \tag{3.4}$$

for isolated particles.
The resolution of the pole-tip hadron calorimeter was:

$$\frac{\sigma_E}{E} = \begin{cases} \frac{100\%}{\sqrt{E(GeV)}} & E < 15\ GeV \\ \frac{120\%}{\sqrt{E(GeV)}} & E > 15\ GeV \end{cases} \tag{3.5}$$

due to leakage of hadrons.

3.1.2.5 The Muon Detectors

The muon detector system contained two subdetectors: the barrel muon detector (MB) and the endcap muon detector (ME). These detectors, placed at the outermost layer of the OPAL detector were designed to identify muons, particularly in the presence of hadrons which would have been absorbed in the yoke.

Barrel Muon Detector The barrel muon detector (MB) comprised 110 drift chambers in four layers covering a cylinder 10 m long, with a radius of 5 m. The wires were spanned parallel to the z direction. The gas mixture was argon (90%) and ethane (10%). Detector covered the angular range $|\cos\theta| < 0.72$ for tracks that traversed at least one layer and $|\cos\theta| < 0.68$ for tracks that traversed all four layers. The drift time information provided the resolution of 1.5 mm in $r-\phi$ plane. The z coordinate was measured by cathode pads with a resolution of 2 mm.

Endcap Muon Detector The two endcap muon detectors (ME) consisted of four layers of limited streamer tubes. The layers were perpendicular to the beam axis. Each endcap contained 12 chambers with two layers of streamer tubes oriented vertically in one layer and horizontally in another. The gas mixture was isobutane (75%) and argon (25%). The cathode strips were read out with a resolution of 1 (3) mm for strips perpendicular (parallel) to the wires. The coverage of the endcap muon detector was $0.67 < |\cos\theta| < 0.985$.

Combined Performance The average identification efficiency was approximately 76% for muons with $E > 3$ GeV in the region $|\cos\theta| < 0.9$. The average probability for a hadron misidentification was 0.8%.

3.1.2.6 The Forward Detectors

The forward detector system consisted of the forward detector (FD) with the gamma catcher (GC), the silicon-tungsten luminometer (SW) and the MIP plug [37, 42, 43]. The FD and SW were designed to measure the luminosity using small-angle Bhabha scattering events and tag electrons from photon-photon ($\gamma\gamma$) interactions. The main applications of the MIP plug were to detect low-angle, high momentum muons, and to tag the two photon processes.

The Forward Detector and Gamma Catcher The forward detector consisted of 35 layers of lead-scintillator sandwich, corresponding to $24X_0$: $4X_0$ in the presampler and $20X_0$ in the main calorimeter. Proportional tube counters, situated between the presampler and the main calorimeter, measured the shower position in θ and ϕ up to an accuracy of 1.3 mrad. The calorimeter was designed to provide shower development information and coarse ϕ position measurement in the polar angle range between 47 and 120 mrad from the beam axis.

The gap between the forward calorimeter and the endcap lead-glass within polar angle range of 142-200 mrad was covered by the gamma catcher (GC), a small electromagnetic calorimeter ($7X_0$ in thickness).

Silicon-Tungsten Luminometer In 1993 the silicon-tungsten luminometer (SW) was additionally installed to cover angular range of 33 mrad to 59 mrad. It consisted of 19 layers of silicon detectors and 18 layers of tungsten absorbers, adding up to a total thickness of $22X_0$. The main purpose was to measure low angle electrons from Bhabha scattering for the luminosity determination.

The MIP Plug The MIP plug covered the polar angle from 43 to 200 mrad, complementing the electromagnetic calorimeters. It consisted of an inner and an outer pair of annular layers, each divided into 8 tile sectors. The outermost layers were separated by 4 mm of lead to reduce the background. The two inner layers were placed on either side of the silicon-tungsten luminometer.

Combined Performance Using the FD and GC, the luminosity was measured with an accuracy of 0.4%. When SW was installed, the accuracy was further improved to 0.14%.

3.1.3 Event Reconstruction

Given the rate of e^+e^- intersections at LEP (once every 22 μs), it would be impossible to store and process all raw data that was detected by the experiment at each bunch crossing. Therefore, only events in which the e^+e^- interaction yielded an intresting

physical process were read out after being selected by the trigger system. The rate of triggered events at LEP was of the order of 10 per second. Once triggered, an event was reconstructed from subdetector raw data: tracks and calorimeter clusters were formed and their four-momenta were obtained.

3.1.3.1 Data Format

The data used in the analysis has undergone several steps of processing. From the raw data of the subdetector readouts, such as wire chamber hits and photomultiplier pulses, algorithms reconstructed central detector tracks, calorimeter clusters, muon tracks, etc. The commonly used Data Summary Tapes (DSTs) made all this information available. For specialized analyses like Higgs boson searches, further processing became necessary. DST tracks and clusters had to pass a number of quality requirements to reduce non-physical effects like beam pipe and gas interactions or electronic noise. Higher level processing included reconstruction of hadronic jets, missing energy, secondary vertices and other variables. Furthermore, particles like photons and leptons, and b-quark jets were identified.

3.1.3.2 Monte Carlo Simulation

A study or a search for a given physical process was done by simulating the signal and its relevant background processes using Monte Carlo (MC) method. In a MC sample, a large number of events was generated using the so called 'generator' with the parameters distributed according to a given physics model. Hadronization of quarks and gluons into stable particles was modelled using the program JETSET [44,45]. The output was a list of the four momenta of all the particles. It included the particles generated by the 'generator' (the tree-level), the intermediate particles that decayed, and the final semi-stable particles that could be detected by the detector.

The final set of stable particles was passed to the simulation of the detector response, including all known hardware effects, inefficiencies, disturbances and mismeasurements that could occur in reality. This was done with the program GOPAL [46]. Finally, all the simulated events were reconstructed with the same algorithms used for the real data.

3.1.3.3 Event Building

Further processing depended on the given physics analysis. The Higgs boson searches were mainly intrested in reconstructing hadronic decay products of Higgs and gauge bosons, and assigning them to their mother particles. Therefore, hadronic jet identification became a central task of those searches.

Before further reconstruction, each event had to fulfill certain quality requirements. Tracks from the central detector had to obey the following conditions:

- A polar angle should satisfy $|\cos\theta| < 0.962$.
- There should be at least 20 hits in the Jet Chamber and more than half the number of possible hits along the track (with respect to the polar angle and the origin of the track).
- A point of the closest approach to beam axis should be within 2.5 cm in transverse plane and 30 cm along z-axis with respect to the interaction point.
- A transverse momentum should be greater than 120 MeV.

Calorimeter clusters had to satisfy:

- Clusters from the electromagnetic calorimeter must consist of at least one lead-glass block in the barrel, and at least two in the endcap.
- The energy of the cluster must be greater than 100 MeV in the barrel and 250 MeV in the endcap.
- Hadronic calorimeter cluster must have an energy of more than 600 MeV in both the barrel and endcap, and more than 2 GeV in the Poletip calorimeter.

For the jet reconstruction, only tracks, ECAL and HCAL clusters were taken into account. Since most charged particles in hadronic events are pions, the energy of tracks was calculated from the momentum measurement in the jet chamber assuming the pion mass. Neutral particles were identified from their energy deposition in the calorimeters. If no track was pointing to the cluster or the energy of the pointing track was significantly lower than the cluster energy, a neutral particle was added to the event [47, 48].

The set of accepted charged and neutral particles was then submitted to a jet algorithm following the DURHAM scheme [49]. The $y_{n+1,n}$ value became a measurement of how similar was the event to n-jet event.

A jet energy and momentum vector were obtained from the four-vector sum over the particles belonging to a jet. Summing all accepted particles of the event, the total energy E_{vis} and the total momentum $\vec{P}_{vis}$ were obtained. Then the missing energy and the missing momentum were defined as

$$\begin{aligned} E_{miss} &= \sqrt{s} - E_{vis} \\ \vec{P}_{miss} &= -\vec{P}_{vis} \end{aligned} \tag{3.6}$$

The visible and the missing mass of an event were calculated through $E^2 = m^2 + |\vec{P}|^2$.

The Thrust value of an events is maximal possible longitudinal projection of the particle momenta onto an axis $\vec{n}$:

$$T = \max_{\vec{n}} \left(\frac{\sum_i |\vec{p_i} \cdot \vec{n}|}{\sum_i |\vec{p_i}|} \right). \tag{3.7}$$

The unit vector $\vec{n}$ that maximizes the sum is called Thrust axis. For a pencil-like events with the two narrow back-to-back jets $\vec{n}$ points to the direction of these jets, and the Thrust value is close to one. The more spherical an event looks, the lower is the Thrust value.

3.1.3.4 b-tagging

An efficient and pure identification of b-jets, i.e. jets originating from b-quarks, was essential for the Higgs searches at LEP, since in the most of the models, Higgs boson in the mass range reachable at LEP preferably decays into a $b\bar{b}$ pair. Long lifetime of bottom quarks of the order of 10^{-12} s and high mass of ~ 5 GeV were exploited to determine which jets originating from b-quarks. At LEP, the decay vertex of a typical b-jet was displaced from the interaction point by a few millimeters. The Silicon-Microvertex detector was designed to resolve such a spatial separation. The second indicator for the b-jets were soft high p_T (with respect to the jet axis) electrons and muons from semileptonic b decays.

The following b-jet tagging techniques were used in OPAL (see [47] and references therein):

1. **Lifetime tagging**
   The lifetime tagging explored the long lifetime of B-hadrons and the high mass of b-quark[2]. An artificial neural network (ANN) was used to identify secondary vertices inside jets. The input quantities were the variables that indicated the existence of the secondary vertices. The output, a likelihood function, was used as a discriminant.

2. **High p_T lepton tagging**
   The semileptonic decay of the b-quark results in a lepton with a relatively high transverse momentum, p_T, with a respect to the jet axis (compared to leptons from the other flavor jets) due to the high mass of b-quark. Using an information about p_T of the lepton with a respect to the jet momentum a likelihood was formed, and then used in the combined B-probability calculation. In only 5.9% of all jets a lepton with a high p_T was found, in which case the lepton tag added a significant amount of sensitivity to the identification of B hadrons.

3. **Jet shape tagging**
   A b-jet has a higher mass and gives rise to higher multiplicity final states than jets from lighter quarks. The ANN that combined various shape-event variables was used as a discriminant.

[2]Because of the high mass, the multiplicity at the B hadron decay vertex is sufficient to identify the secondary vertex inside the jet.

All these variables were evaluated using Monte Carlo simulations and then tested using calibration data at $\sqrt{s} \approx m_Z$. The distributions of the three discriminants were combined using a likelihood method with the three classes of jets considered: b-flavored, c-flavored and light (uds) jets. The final b-tagging discriminant was given by:

$$\mathcal{B}_{jet} = \frac{\prod_{t=\tau,l,s} w_b \cdot f_b^t}{\sum_{q=b,c,uds} \prod_{t=\tau,l,s} w_q \cdot f_q^t} \tag{3.8}$$

where w_q, with $q = b, c, uds$, were the weight factors, and f_q^t were the probability density functions of discriminants for the class q and the tagging technique t: τ - lifetime tag, l - lepton p_T, and s - jet shape. In the missing energy channel[3] that is a subject of the analysis described in this thesis, the high p_T lepton tagging was not used since the background process $W^+W^- \to \nu l q\bar{q}'$, where the lepton remains very close to one of the jets, is significant and can be confused with the signal. Also, all weight factors were set to 1. The performance of the b-tagging algorithm is given in Figure 3.3.

3.1.4 Physics processes

The Standard Model Higgs boson searches at LEP will be briefly introduced in this section. Then we will describe the MSSM Higgs boson processes.

3.1.4.1 The Standard Model Higgs Boson Production

Due to the low mass of the electron, the direct coupling of e^+e^- to the Higgs boson is extremely small, and the direct s-channel production of the Higgs boson at LEP, $e^+e^- \to H^0$ is highly unlikely. Instead, other processes are considered [50]:

- The Higgs-strahlung, where the e^+e^- annihilate into a virtual (off-shell) Z^0 boson, denoted by Z^{*0} ($m_{Z^*} \approx \sqrt{s}$), which then emits Higgs boson to become real (on-shell) Z^0.

- The W^+W^- and Z^0Z^0 fusion, where both the electron and the positron emit W or Z bosons, which then produce a Higgs boson. The W^+W^- fusion process becomes significant near the kinematic limit of the Higgs-strahlung process, while the Z^0Z^0 fusion is suppressed by factor 10 with respect to the W^+W^- fusion process.

For the Higgs boson masses that were accessible at LEP, the $BR(H \to b\bar{b})$ is dominant (75-85%). The other significant decay is to a pair of τ-leptons (7-8%). Other Standard Model Higgs boson decays are experimentally useless as either negligible or it would be impossible to distinguish them from the background.

[3] For the description of the channels see the next section.

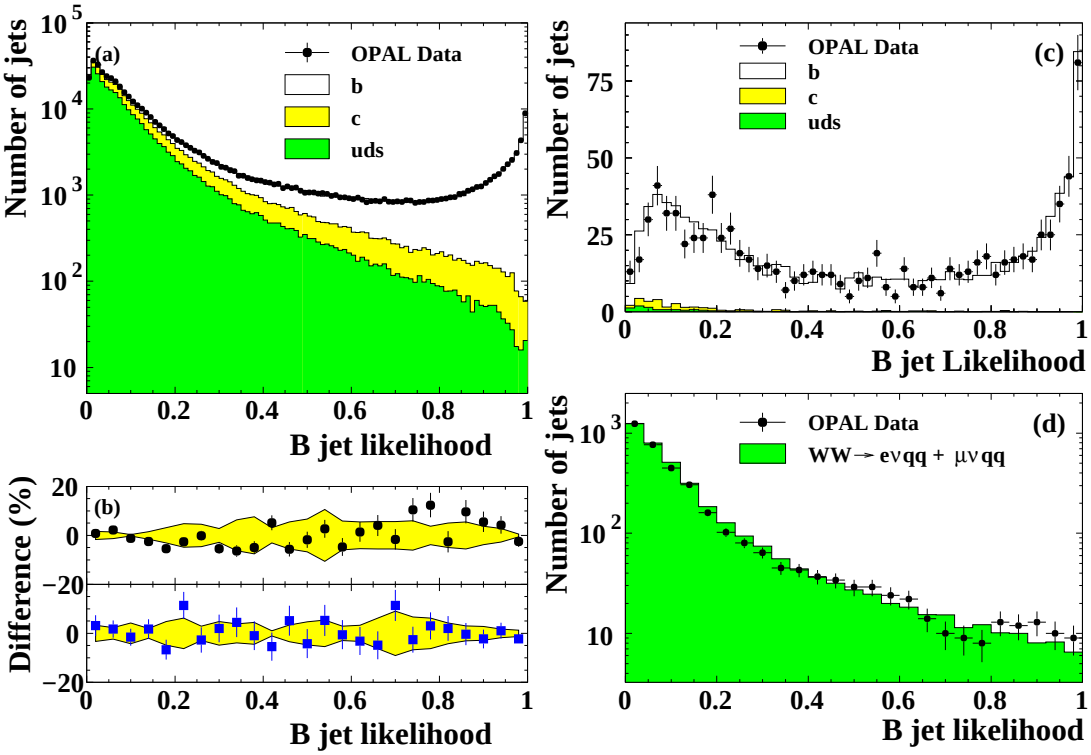

Figure 3.3: *(From [47]) (a) The b-tagging algorithm output $\mathcal{B}$, for all jets in the Z calibration data. (b) The comparison between calibration data and simulation of the b-tag values opposite to an anti-tagged (upper part, dots) and a tagged (lower part, rectangles) b-jet. The shaded bands indicate the systematic uncertainty on the difference. (c) The distribution of $\mathcal{B}$ for high-energy $e^+e^- \to q\bar{q}(\gamma)$ events. One of the jets has been tagged as a b-jet and the $\mathcal{B}$ of the other jet is shown. (d) Distribution of $\mathcal{B}$ for jets in events identified as $e^+e^- \to W^+W^- \to q\bar{q}l\nu$.*

In order to increase the sensitivity for the detection of a Higgs boson signal, the search was divided into four channels, corresponding to final states of the process $e^+e^- \to H^0Z^0$. The main search channels were 4-jet channel ($Hq\bar{q}$), light lepton (electron and muon) channel (He^+e^-, $H\mu^+\mu^-$), τ channel ($H\tau^+\tau^-$, $\tau^+\tau^-q\bar{q}$), and the missing energy channel ($H\nu\bar{\nu}$).

3.1.4.2 The MSSM Higgs Boson Production and Decay

There are several production mechanisms of the neutral Higgs boson within the MSSM. In the CP conserving scenario (CPC), in addition to the Standard Model production processes $e^+e^- \to hZ$, pair production, $e^+e^- \to hA$, is also possible. In a CP-violating (CPV) model, the two main channels, Higgs-strahlung and pair production, are generalized to $e^+e^- \to H_iZ$ and $e^+e^- \to H_iH_j$ ($i \neq j$ due to Bose symmetry, and $i = 1, 2, 3$).

The dominant decay for Higgs boson masses below 130 GeV is usually decay to the

SM fermions, $H \to f\bar{f}$, where fermion is mostly b-quark. The important consequence of CP violation is the modification of the top- and bottom-quark Yukawa couplings through CP-violating vertex effects [34] involving gluinos and higgsinos, as well as top and bottom squarks. Important decay channel that opens in the MSSM is cascade decay $H_2 \to H_1 H_1$, which is dominant whenever is kinematically accessible, i.e. if $2m_{H_1} < m_{H_2}$.

Unlike the Standard Model, the cross section and branching ratios of the MSSM Higgs boson do not depend solely on the mass of the Higgs boson, but also on the MSSM parameters choice. The $\sigma \times BR$ for the processes in the CPV MSSM scenario is shown in Figure 3.4 [12].

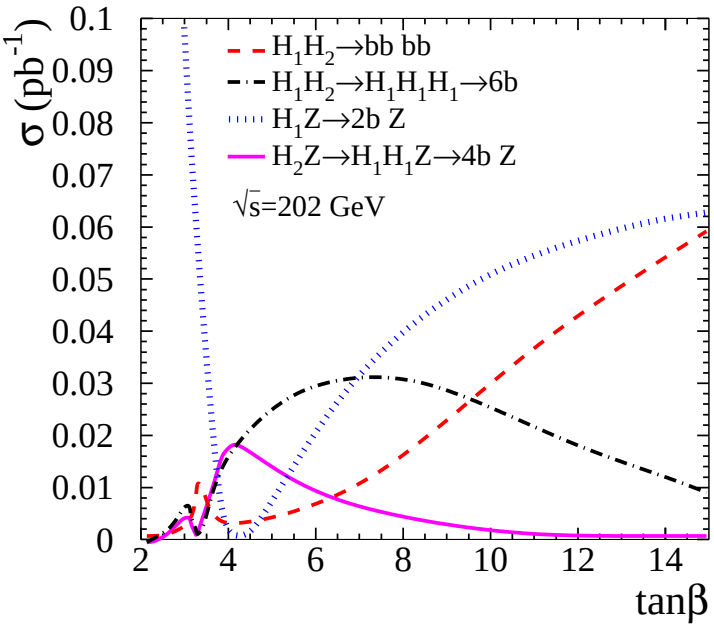

Figure 3.4: *$\sigma \times BR$ for the processes in the CPV MSSM scenario for $\sqrt{s} = 202$ GeV, $m_{H_1} \sim 40$ GeV and $m_{H^+} \sim 120$ GeV [12].*

In the following we will investigate the missing energy channel, i.e. the following processes: $e^+e^- \to Z^0 H_2 \to Z^0 H_1 H_1 \to \nu\bar{\nu} b\bar{b} b\bar{b}$, and $e^+e^- \to Z^0 H_2 \to \nu\bar{\nu} b\bar{b}$.

3.1.4.3 The Standard Model Processes

For the analysis presented in this theses, all Standard Model processes without a Higgs boson are treated as background. The understanding of the background is crucial since its rate at LEP energies can be several order of magnitude larger than the signal processes. The relevant SM background processes are described here:

- Two Photon processes
  Two photons, radiated by the incoming leptons, can interact with each other produc-

ing two or more hadronic jets. If the scattered incoming lepton(s) escapes through the beam pipe or remains only partially detected, the event might fake a signal.

- Two Fermion processes
  The incoming leptons annihilate into a Z^* or γ^*, which then decays into two fermions. Initial state radiation photons, that are preferably emitted in the beam pipe direction and might escape detection faking missing energy, can bring the invariant mass of the $f\bar{f}$ system back to m_Z. Eventhough the invariant mass of the $f\bar{f}$ peaks at m_Z, the tail of the mass distribution is still big enough to make this process one of the dominant backgrounds.

- Four fermion background
  This background contains different type of processes, with Z pair and W pair productions being dominant. Missing energy can be real, originating in decay processes of the Z or W that include ν ($W \to \ell\bar{\nu}_\ell$, $Z \to \nu\nu$), or fake from events with visible particles emitted into the beam pipe or low-efficiency regions of the detector.

3.1.4.4 Data Sets and Generation of the Physics Processes

During the year 2000 about 207 pb^{-1} of luminosity have been recorded by the OPAL detector at the center of mass energies between 199 GeV and 209 GeV. The luminosities collected at different energies are shown in Figure 3.5 (yellow-light).

Signal events were generated using HZHA03 [51] at $\sqrt{s} = 206$ GeV and for the Higgs boson masses $m_{H2} = 100,\ 105,\ 110$ GeV and $m_{H1} = 12 - 53$ GeV (see Table 3.2).

All background processes were generated at the actual center of mass energies. Two-photon events were generated using PHOJET [52] for $\gamma\gamma \to u\bar{u}, d\bar{d}, s\bar{s}$ and PYTHIA [45] for $\gamma\gamma \to c\bar{c}, b\bar{b}$. Two fermion events were mainly simulated with KK2F [53], while four fermion background was modelled with grc4f [54].

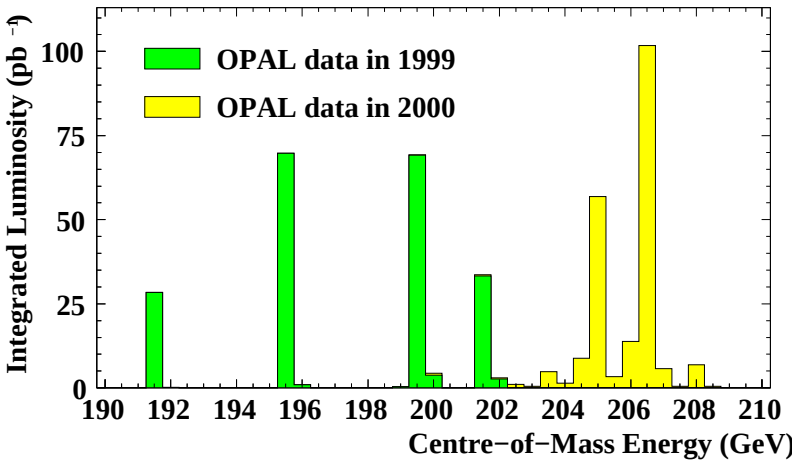

Figure 3.5: *Integrated luminosity collected by OPAL in years 1999 (green-dark) and 2000 (yellow-light) as a function of the center of mass energy.*

m_{H2} (GeV)	m_{H1} (GeV)
100	12
	20
	30
	40
	48
105	12
	20
	30
	40
	50
110	12
	20
	30
	40
	50
	53

Table 3.2: *Generated signals (at $\sqrt{s} = 206$ GeV) for various H_1 and H_2 masses.*

3.2 Search for CPV Higgs at OPAL

The search for the extended Higgs sector of the MSSM is one of the main efforts to test the existence of SUSY. Furthermore, the Standard Model fails to provide enough CP-violation to explain the cosmological matter-antimatter asymmetry [28]. The CP-violating effects in SUSY can help to reduce this crisis. Investigation of the CP-violation in the Higgs sector of the MSSM is the subject of this section.

3.2.1 Motivation

At the tree-level MSSM contains three neutral Higgs bosons with well defined CP-parity. Unlike the SM case, radiative corrections in the MSSM sector are rather big. They push the upper bound on the lightest neutral Higgs boson mass upward to about 135 GeV [8, 9, 33]. However, radiative corrections might also introduce CP violation by loop effects in the interactions between Higgs boson and top and bottom squark [34]. In such a case the neutral Higgs boson mass eigenstates are no longer CP eigenstates, instead one introduces H_1, H_2 and H_3, which have mixed CP parities. Since A^0 is not a mass eigenstate anymore, m_{H^+} is used as a parameter instead of m_A. In such a scenario there are significant regions in the (m_{H^+}, tanβ) plane where the lightest neutral Higgs boson contains large admixture of the CP-odd state A^0. In such a case the H_1 might decouple completely from the Z^0 and evades detection at LEP even if its mass is low.

As a consequence of the second order loop diagrams, the couplings of the Higgs particles to b-quarks are changed, so the $e^+e^- \to H_2Z^0 \to H_1H_1Z^0 \to b\bar{b}b\bar{b}\nu\bar{\nu}$ channel is opened. We concentrate on this channel which is specific for the MSSM Higgs sector with CP-violation (CPV MSSM in the following). In addition, analysis will be applied on SM-like $e^+e^- \to H_2Z^0 \to b\bar{b}\nu\bar{\nu}$. The Feynman diagrams of the two processes are shown in Figure 3.6.

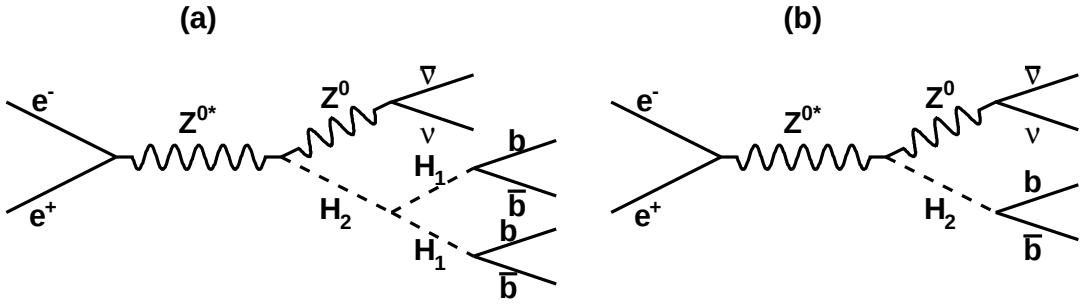

Figure 3.6: *(a)* $e^+e^- \to H_2Z^0 \to H_1H_1Z^0 \to b\bar{b}b\bar{b}\nu\bar{\nu}$ *and (b)* $e^+e^- \to H_2Z^0 \to b\bar{b}\nu\bar{\nu}$.

3.2.2 Introduction to Analysis

The first step was to apply two separate analyses and compare their results. In the first analysis, each event has been split into two hemispheres (two-jet like analysis), while in the second one, each event has been split into quarters (four-jet like analysis). An event is retained if two or four b-tags (respectively) are obtained. Another requirement is that a significant (as will be further defined later) amount of missing energy is present.

In the two-jet like analysis masses of the first and the second H_1 are assumed to be the masses of the first and the second jet[4], respectively. In the four-jet like analysis two light Higgs bosons were reconstructed from the jets that were obtained by minimizing $\Delta m_{H_1} = m_{jj_1} - m_{jj_2}$, where m_{jj_1} and m_{jj_2} were the invariant masses of the two di-jets that corresponded to H_1, $m_{H_1} = m_{jj}$. Figures 3.7 and 3.8 show the mass of the second H_1 vs. the mass of the first H_1 for $m_{H_2} = 105$ GeV, and for $m_{H_1} = 12$ GeV (a), $m_{H_1} = 20$ GeV (b), $m_{H_1} = 30$ GeV (c), $m_{H_1} = 40$ GeV (d) and $m_{H_1} = 50$ GeV (e) for the two-jet and four-jet like analysis, respectively. It can be seen clearly that for the low m_{H_1} the reconstruction of two jets describes the event quite well, but for higher m_{H_1} jet pairing is not done correctly in most of the events in the two-jet like analysis. The schematic view of the event is shown in Figure 3.9 for the low (left) and high (right) m_{H_1}. When two H_1 are light, they are boosted and, consequently, only two jets are often seen in the detector. An attempt to reconstruct four jets then fails and the m_{H_1} acquires a tail at high values (Figure 3.10).

The complete analysis will be described in the next section, and here we will present the overview and results of the two separate analysis. The present analysis was done using Artificial Neural Network[5] (ANN). Some precuts, similar to those used in the search for the SM Higgs boson [47], were applied to reduce background to a manageable level. For both analyses, signal events with $m_{H_1} = 20$ GeV and $m_{H_2} = 100, 105, 110$ GeV were used for the training procedure. The 12 (11) variables, scaled to values between zero and one, were used as inputs to the ANN for the two-jet (four-jet) analysis.

The number of candidate events in the two-jet (four-jet) like analysis is 14(19) with 13.9(19.9) events expected from the SM background. Signal efficiencies for the two- and four-jet like analysis are shown in Figure 3.11 for $m_{H_2} = 105$ GeV. As expected, the two-jet like analysis is slightly better for lower masses of H_1, while the four-jet analysis is better for higher m_{H_1}. To resolve whether the topology of an event is two-jet or four-jet like we used the Durham jet finder two-to-three jet flip value y_{32} [49]. We split the event sample into two subsamples, subsample A, two-jet like events, that contains events which satisfy $y_{32} < 0.05$ ($H_2 \to b\bar{b}$ events and most of the $H_2 \to H_1 H_1 \to b\bar{b}b\bar{b}$ with light H_1), and subsample B, four-jet like events, that contains events which satisfy $y_{32} \geq 0.05$

[4] Only one jet is reconstructed in each hemisphere.
[5] ANN and its application to this analysis is described in Appendix B.

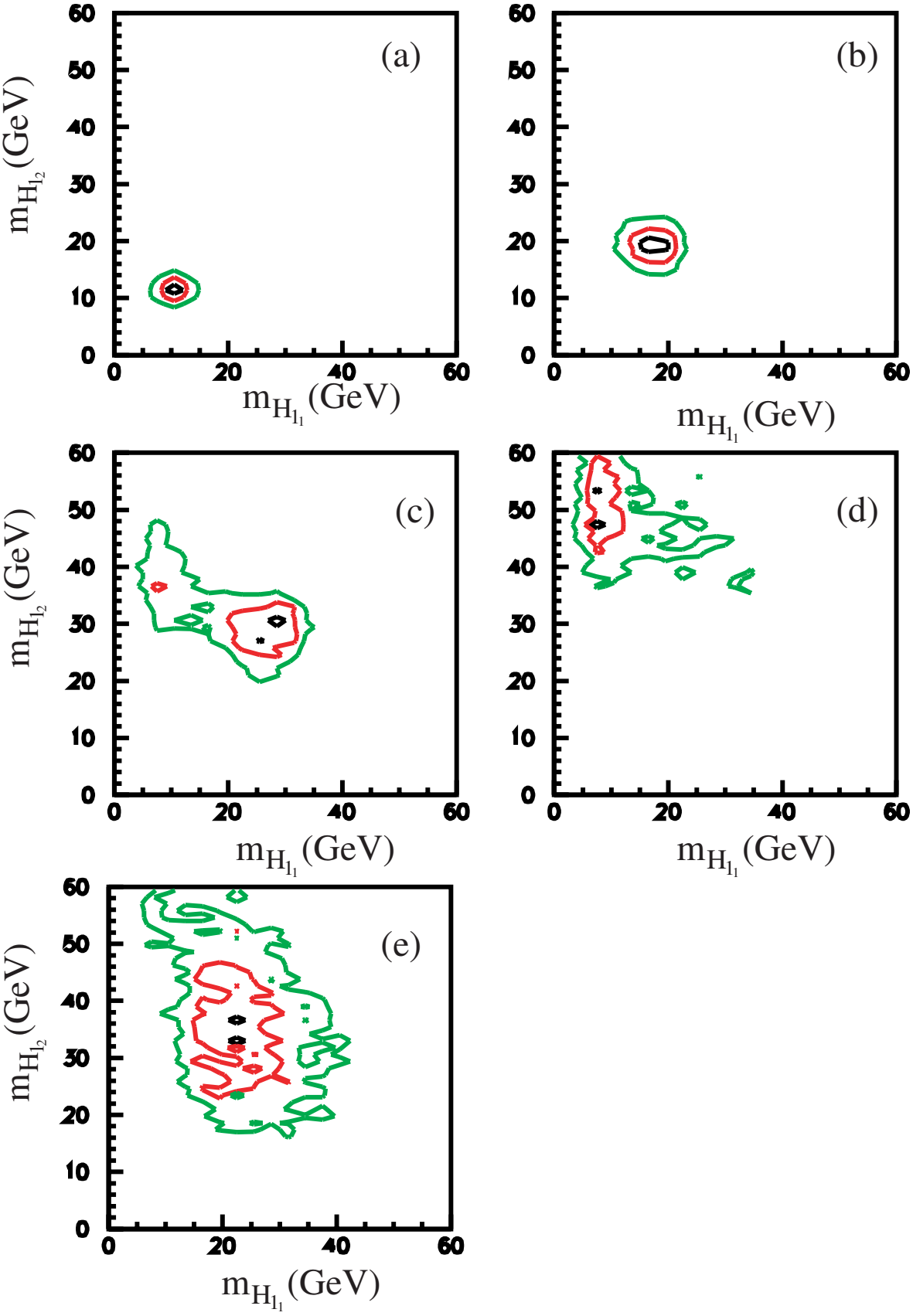

Figure 3.7: *The mass of the second light Higgs vs. the mass of the first light Higgs for the two-jet like analysis for (a)* $m_{H_1} = 12$ *GeV, (b)* $m_{H_1} = 20$ *GeV, (c)* $m_{H_1} = 30$ *GeV, (d)* $m_{H_1} = 40$ *GeV and (e)* $m_{H_1} = 50$ *GeV, and* $m_{H_2} = 105$ *GeV.*

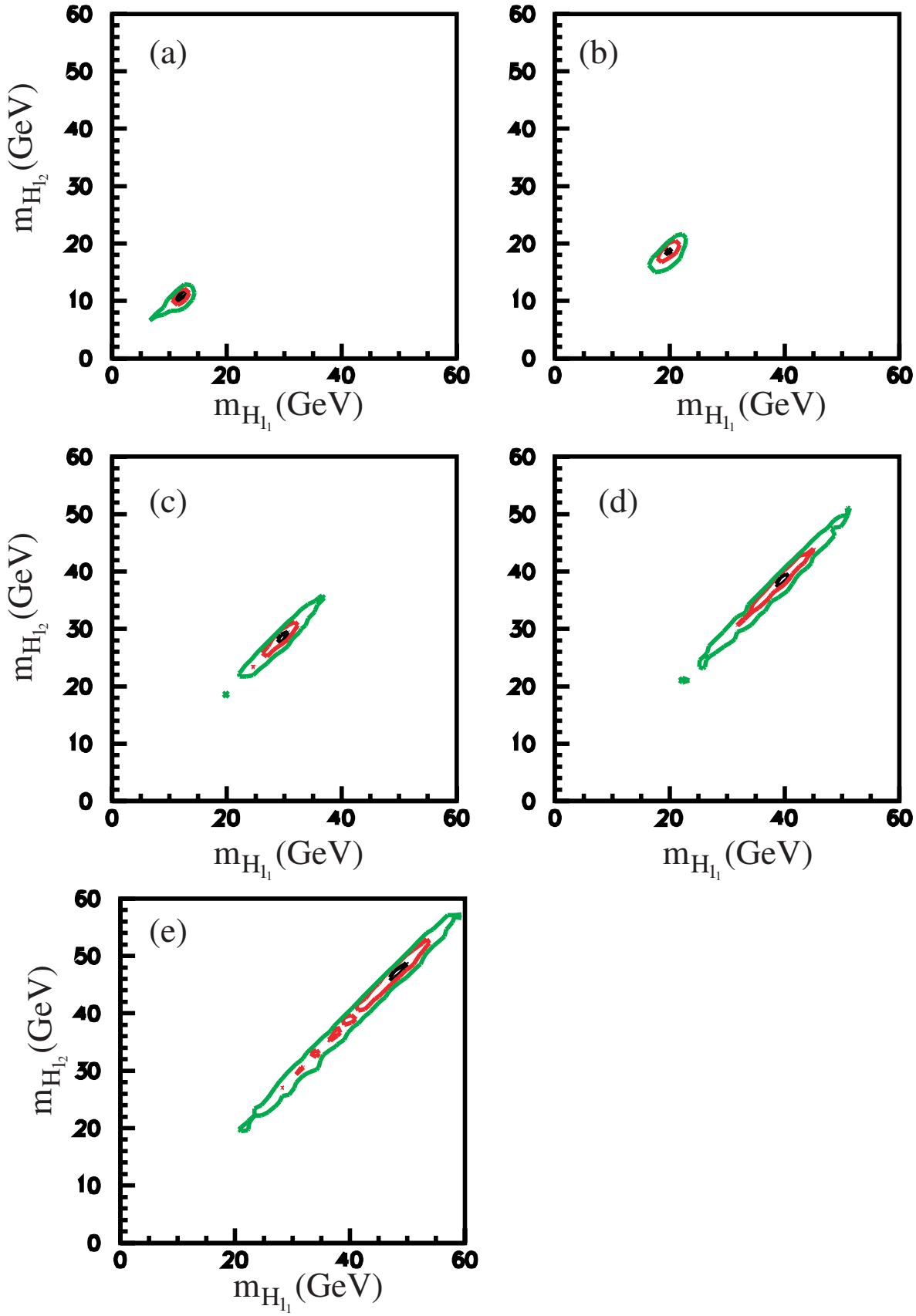

Figure 3.8: *The mass of the second light Higgs vs. the mass of the first light Higgs for the four-jet like analysis for (a)* $m_{H_1} = 12$ *GeV, (b)* $m_{H_1} = 20$ *GeV, (c)* $m_{H_1} = 30$ *GeV, (d)* $m_{H_1} = 40$ *GeV and (e)* $m_{H_1} = 50$ *GeV, and* $m_{H_2} = 105$ *GeV.*

(most of the $H_2 \to H_1 H_1 \to b\bar{b}b\bar{b}$ events with heavy H_1). The separating value of 0.05 has been chosen such that the efficiency of $H_2 \to b\bar{b}$ events in subsample A is basically the same as in the SM search. This is illustrated in Figure 3.12 for the $H_2 \to H_1 H_1 \to b\bar{b}b\bar{b}$ with $m_{H_2} = 105$ GeV and $m_{H_1} = 12 - 50$ GeV (a-e) and for the SM-like $H_2 \to b\bar{b}$ with $m_{H_2} = 105$ GeV (f). The relative fraction of events belonging to subsamples A and B for $H_2 \to H_1 H_1 \to b\bar{b}b\bar{b}$ with $m_{H_2} = 105$ GeV and different m_{H_1} is shown in Table 3.3. Figure 3.13 shows the y_{32} distribution for the data on top of the background.

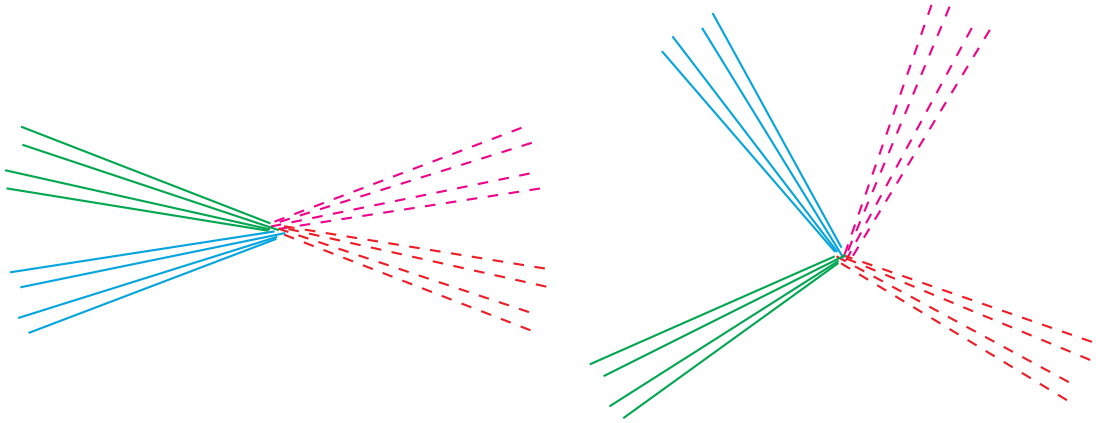

Figure 3.9: *Schematic view of the processes.*

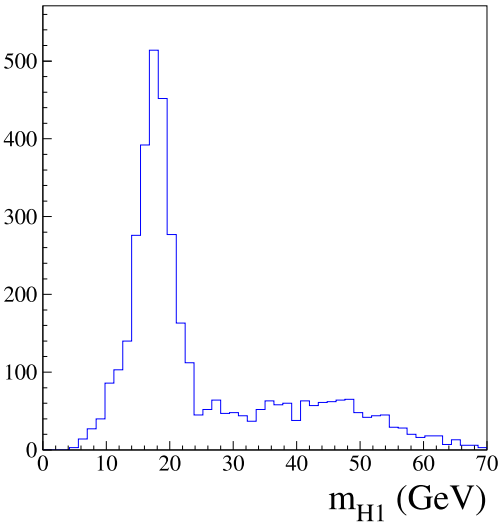

Figure 3.10: *The distribution of the reconstructed m_{H_1} when four-jet analysis is applied to the events with a low mass of the H_1, $m_{H_1}(gen) = 20$ GeV in this case.*

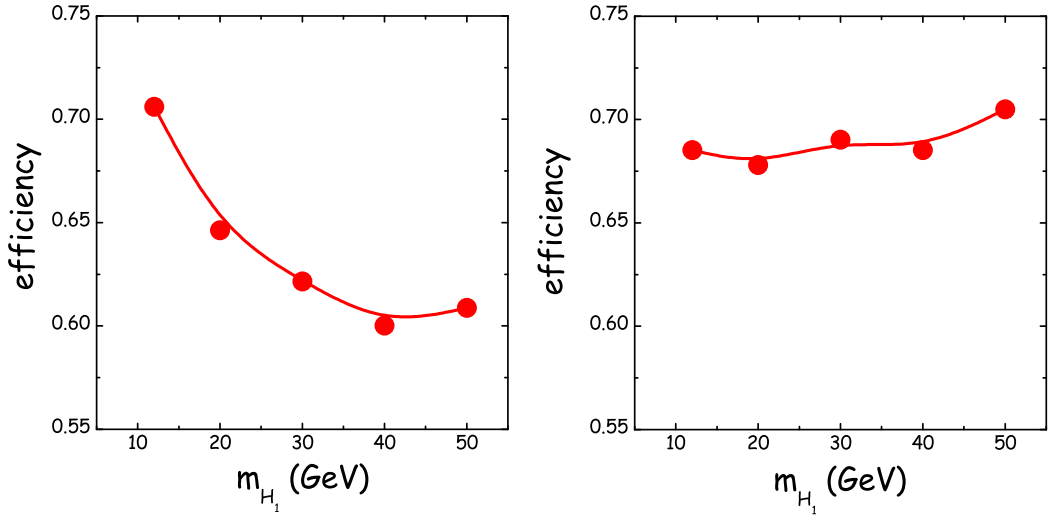

Figure 3.11: *Efficiencies for the two-jet like analysis (left) and for the four-jet like analysis (right) for* $m_{H_2} = 105$ *GeV.*

m_{H_1} (GeV)	$y_{32} < 0.5$	$y_{32} > 0.5$
12	100%	0%
20	99.7%	0.3%
30	62.5%	37.5%
40	21%	79%
50	32%	68%

Table 3.3: *The relative fraction of events belonging to subsamples A and B for* $H_2 \to H_1 H_1 \to b\bar{b}b\bar{b}$ *with* $m_{H_2} = 105$ *GeV and various* m_{H_1}.

3.2.3 Preselection

Based on the analysis that was developed for the search of SM Higgs boson [47], the following basic cuts[6] were applied:

1. Dilepton final states and two-photon processes are reduced by the following requirements:
   - The number of tracks passing the quality requirements[7] must be greater than six and must exceed 20% of the total number of reconstructed tracks.
   - No track momentum and no energy cluster in the electromagnetic calorimeter may exceed $\sqrt{s}/2$.

[6] In addition, all subdetectors described in section 3.1.2 were required to be fully operational.
[7] Quality requirements are given in section 3.1.3.3.

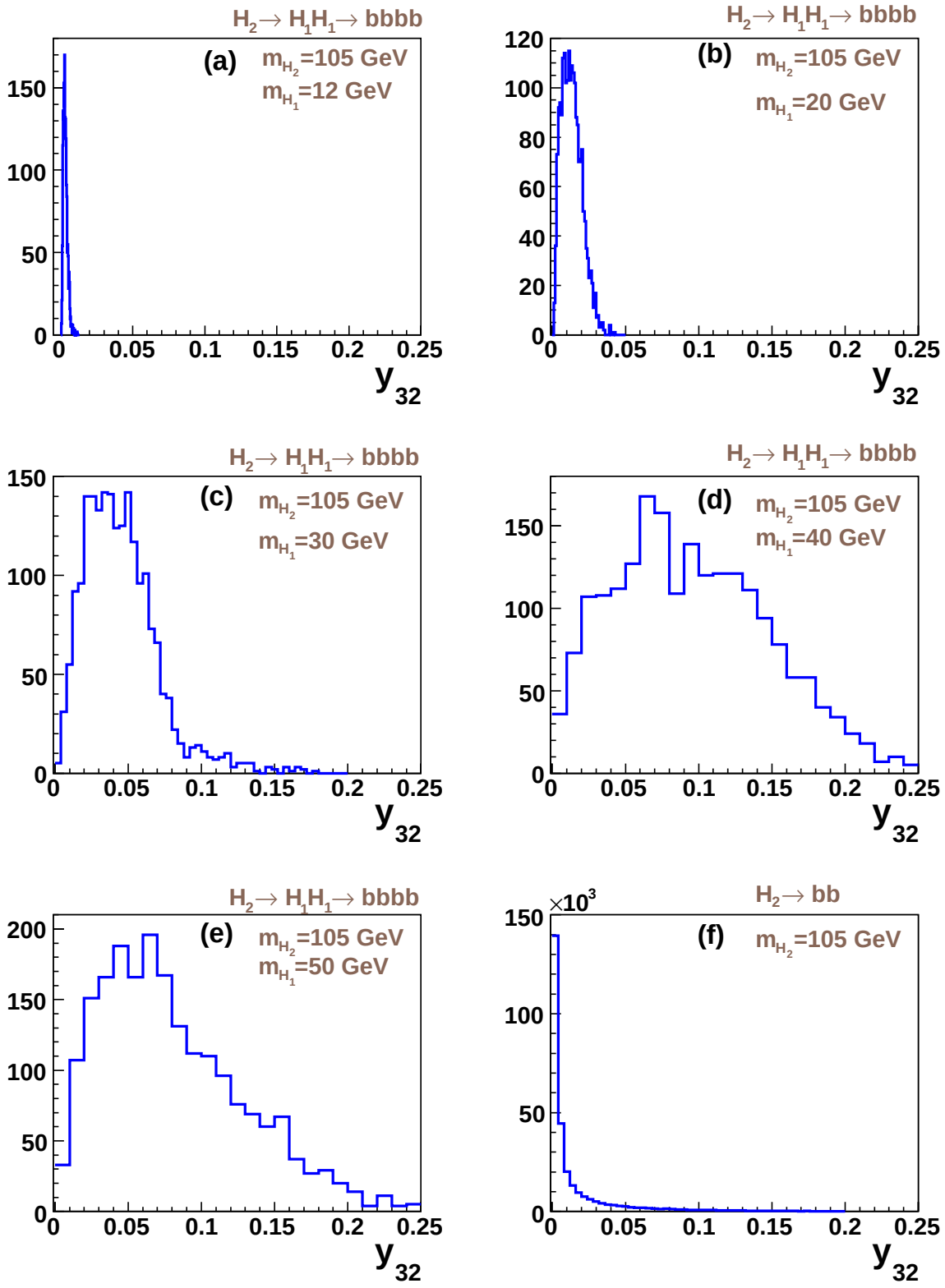

Figure 3.12: *The distribution of the y_{32} for the $H_2 \to H_1 H_1 \to b\bar{b}b\bar{b}$ events with $m_{H_2} = 105$ GeV and $m_{H_1} = 12 - 50$ GeV (a-e), and for the $H_2 \to b\bar{b}$ with $m_{H_2} = 105$ GeV (f).*

– The total visible energy must be smaller than 80% of $\sqrt{s}$.

– The energy deposited in either side of the forward calorimeter must not exceed

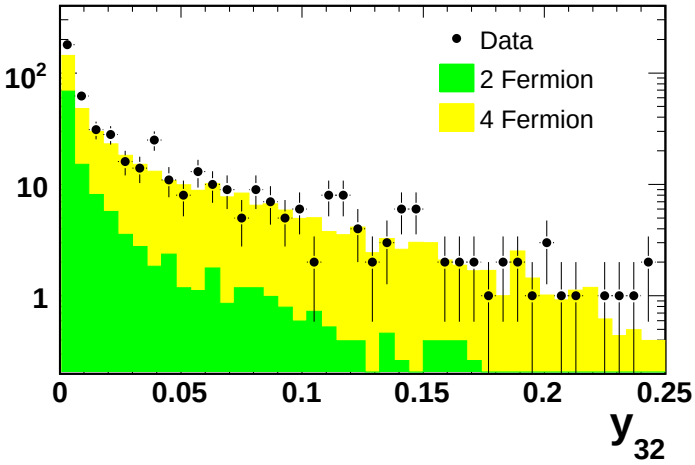

Figure 3.13: *The distribution of y_{32} for background and data events (represented by the points with error bars) after cuts $1-5$ (see text) are applied.*

2 GeV, and the energy deposits in either side of the silicon-tungsten luminometer and the gamma catcher must not exceed 5 GeV.

- The component of the total visible momentum vector transverse to the beam axis must exceed 3 GeV.
- The visible mass must be greater than 4 GeV, to suppress unmodeled two-photon events.
- The thrust value T must exceed 0.6.
- The chi-squared of the one-constraint (1C) HZ fit [55], χ^2_{HZ}, constraining the missing mass to m_Z, is required to be less than 35.

2. The energy[8] deposited in the forward region ($|\cos\theta| > 0.9$) must not exceed 20% of the visible energy (Figure 3.14 (a)).

3. The missing mass must be in the range 50 GeV $< M_{\mathrm{miss}} <$ 130 GeV (Figure 3.14 (b)).

4. The effective center-of-mass energy $\sqrt{s'}$ [56] must exceed 60% of $\sqrt{s}$, to reject events with large amount of initial-state radiation (Figure 3.14 (c)).

5. To reduce background further, in particular $q\bar{q}$ (γ) background, the following cuts are applied:

   - The polar angle of the thrust axis is required to satisfy $|\cos\theta_{\mathrm{thr}}| < 0.95$ to ensure good containment of the event (Figure 3.14 (d)).
   - The projection of the visible momentum along the beam axis, $|P^z_{\mathrm{vis}}|$, must not exceed 25% of $\sqrt{s}$ (Figure 3.14 (e)).

[8] This energy is calculated as a sum of the energies of all charged tracks and ECAL clusters.

- The polar angle of the missing momentum vector must lie within the region $|\cos\theta_{\text{miss}}| < 0.95$ to reject radiative events and also to ensure that the missing momentum is not a result of mismeasurement (Figure 3.14 (f)).
- The jet closest to the beam axis is required to have $|\cos\theta_{\text{jet}}| < 0.95$ to ensure complete reconstruction.

Cuts 1 - 5 correspond to the cuts applied to the SM Higgs search in the missing energy channel.

6. The tracks and clusters in the event are grouped into jets using the Durham algorithm. Depending on y_{32}, the event is either grouped into two jets ($y_{32} < 0.05$) in subsample A, or into four jets ($y_{32} > 0.05$) in subsample B. Each event with $y_{32} > 0.05$ is required to be successfully grouped into 4 jets.

Additional requirements are imposed for the subsample A:

7. The acoplanarity angle (180° minus the angle between the two jets when projected into the xy plane) must be between 3° and 100°, to reject $q\bar{q}$ events, which often have nearly back-to-back jets.

8. The event must not have any identified isolated lepton, to reduce the background from W^+W^- events.

After the preselection, 135 (118) events are observed with 126.3 (112.3) expected from SM background for subsample A (B), as listed in Table 3.4. $\gamma\gamma$ background that represented $\sim$ 18% of the total background after cut 1 came up to less than 1% after complete preselection.

3.2.4 The event selection with ANN

The separate ANN's, ANN_A and ANN_B are trained for events belonging to subsamples A and B, respectively. For subsample A, simulated signal events $H_2 \to H_1 H_1 \to b\bar{b}b\bar{b}$ with $m_{H_1} = 12$ GeV (instead of $m_{H_1} = 20$ GeV) and $m_{H_2} = 105$ GeV are used for the training procedure, while for subsample B the same kind of events with $m_{H_1} = 40$ GeV and $m_{H_2} = 105$ GeV are used as signal events. The 12 (11) variables used as inputs to the ANN for the two-jet (four-jet) analysis are listed below. All variables are scaled to values between zero and one, and some of the variables with peaking distributions are subject to logarithmic transformations to give smoother distributions better suited for use as ANN input variables (see Appendix B). The distributions of the ANN input variables are shown in Figures 3.15 and 3.16 for subsample A, and Figures 3.17 and 3.18 for subsample B. The 9 common variables to both analyses are listed first.

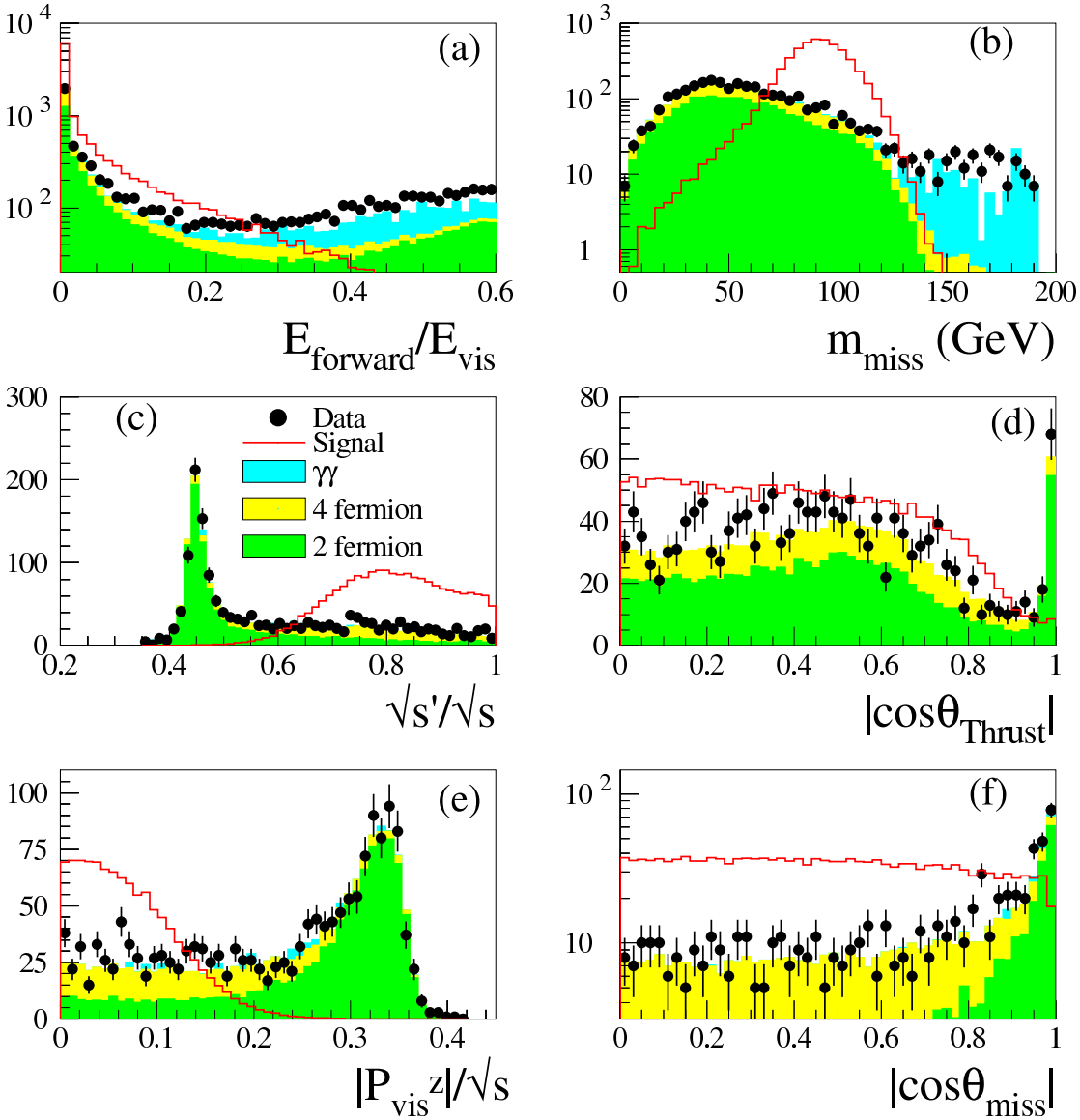

Figure 3.14: *The distribution of the variables used as precuts (see text) for the signal (red line), background and data (points with error bars). The signal is arbitrarily scaled.*

1. The effective center-of-mass energy $\sqrt{s'}$, divided by $\sqrt{s}$ [56];
2. The missing mass M_{miss};
3. The polar angle of the missing momentum vector $|\cos\theta_{\text{miss}}|$;
4. The b-tag likelihood output $\mathcal{B}_1$ [47] of the first (most energetic) jet;
5. The b-tag likelihood output $\mathcal{B}_2$ of the second jet;
6. The angle between the first jet and the missing momentum vector, $\ln(1 - \cos\angle(j_1, p_{\text{miss}}))$;
7. The angle between the second jet and the missing momentum vector, $\cos\angle(j_2, p_{\text{miss}})$;

cut	data	tot. bkg.	qq(γ)	tot 4-f	Eff. $H_2 \to H_1 H_1$ m_{H_2}=105 m_{H_1}=20	Eff. $H_2 \to H_1 H_1$ m_{H_2}=105 m_{H_1}=40	Eff. $H_2 \to b\bar{b}$ m_{H_2}=105
(1)	7856	6598.03	4112.46	1330.30	0.92	0.92	0.73
(2)	4483	4070.02	2851.16	1043.75	0.82	0.84	0.65
(3)	1618	1501.72	1016.11	445.19	0.79	0.82	0.63
(4)	662	572.08	231.82	327.46	0.78	0.79	0.62
(5)	503	424.77	123.94	297.99	0.75	0.74	0.59
2-jet topology subsample A							
(6)	371	308.56	108.66	197.17	0.75	0.16	0.53
(7)	213	201.77	24.70	177.07	0.70	0.15	0.50
(8)	135	126.29	22.85	103.43	0.68	0.14	0.49
ANN	11	10.0	2.63	7.39	0.59	0.11	0.40
4-jet topology subsample B							
(6)	118	112.32	14.42	97.80	0.008	0.57	0.06
ANN	8	7.2	2.83	4.37	0.003	0.55	0.05
Total (2+4 jets)							
ANN	19	17.2 $\pm$ 0.6	5.46	11.8	0.59	0.66	0.45

Table 3.4: *Cut flow table of the missing energy analysis for* $H_2 \to b\bar{b}\nu\bar{\nu}$ *and* $H_2 \to H_1 H_1 \to b\bar{b}b\bar{b}\nu\bar{\nu}$.

8. The logarithm of the χ^2 of the 1C HZ fit, $\ln(\chi^2_{\mathrm{HZ}})$;

9. The scaled missing momentum $p_{miss}/\sqrt{s}$;

The additional three variables for subsample A are:

10. The polar angle of the thrust axis $|\cos\theta_{\mathrm{thr}}|$;

11. The acoplanarity angle of the jets, $\ln(\phi_{\mathrm{acop}})$;

12. The logarithm of the absolute value of the energy difference between the two jets $\ln|E_1 - E_2|$.

The additional two variables for subsample B are:

10. The b-tag likelihood output $\mathcal{B}_3$ of the third jet;

11. The b-tag likelihood output $\mathcal{B}_4$ of the fourth jet.

Candidate events are selected if $\mathrm{ANN_A} > 0.5$ for events in subsample A, or $\mathrm{ANN_B} > 0.5$ for events in subsample B. The efficiency for signal events for both $H_2 \to b\bar{b}$ and $H_2 \to H_1 H_1 \to b\bar{b}b\bar{b}$ is determined for either selection. The expected signal as well as the expected background distributions in the ANN output variables are added from both

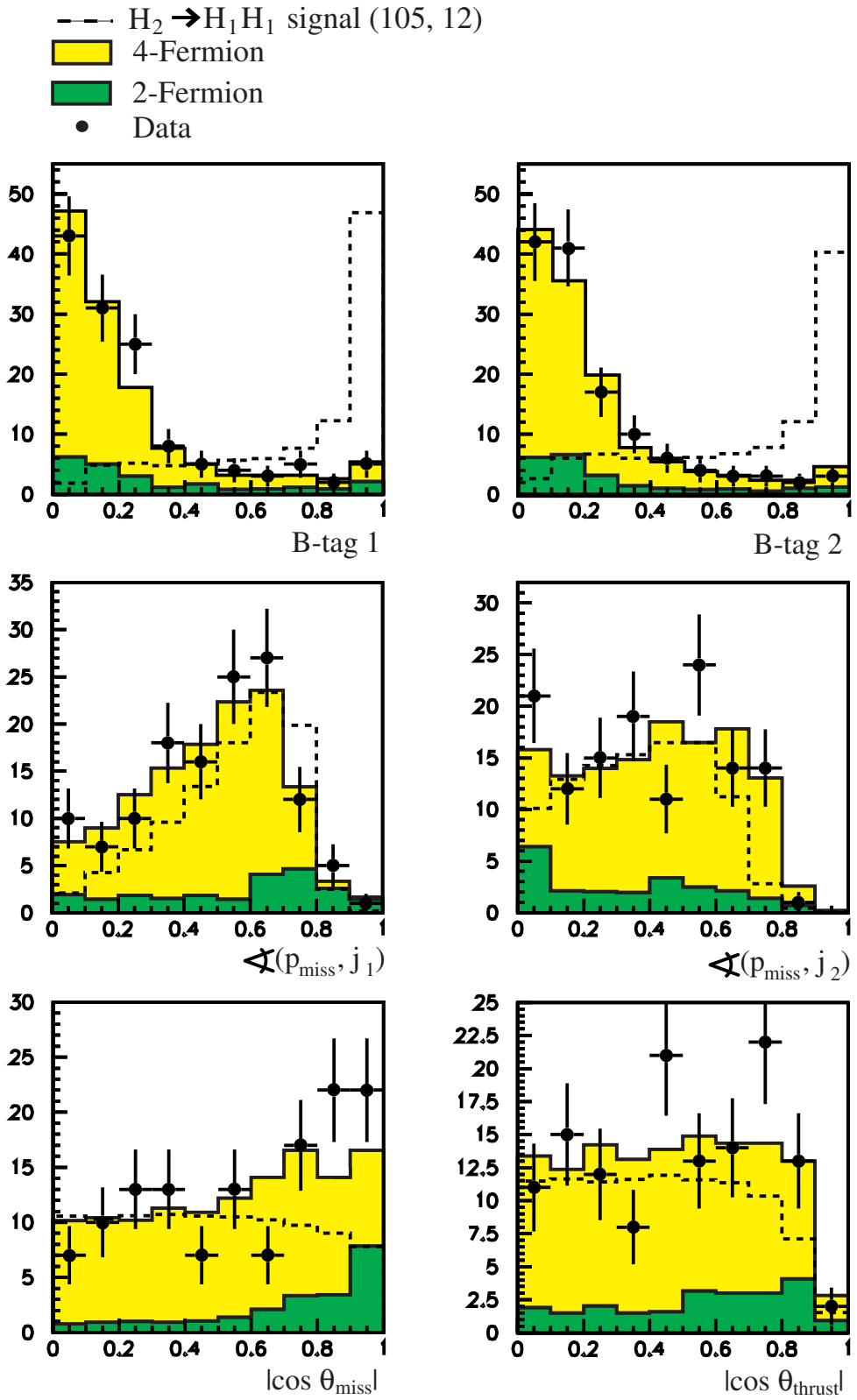

Figure 3.15: *Distributions of the ANN input variables for subsample A assuming 100 GeV* $\leqslant m_{H_2} \leqslant$ *110 GeV. The light shaded (yellow) region is the total background, the dark shaded (green) is the two fermion background. The dotted line shows the arbitrarily scaled signal expectation for* $m_{H_1} = 12$ GeV *and* $m_{H_2} = 105$ GeV*. The points with error bars are the data.*

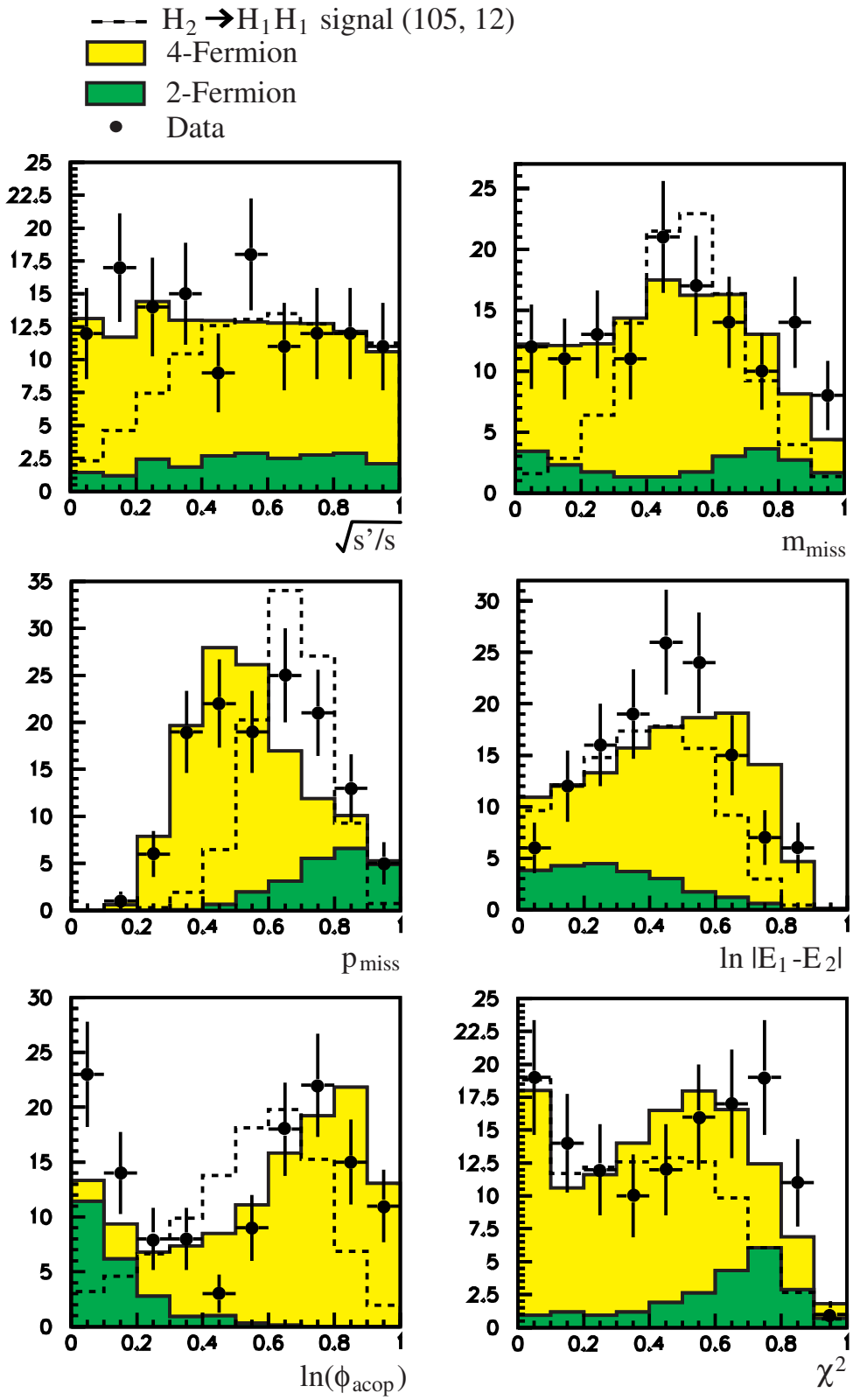

Figure 3.16: *Distributions of the ANN input variables for subsample A assuming 100 GeV* $\leqslant m_{H_2} \leqslant$ *110 GeV. The light shaded (yellow) region is the total background, the dark shaded (green) is the two fermion background. The dotted line shows the arbitrarily scaled signal expectation for* $m_{H_1} = 12$ GeV *and* $m_{H_2} = 105$ GeV*. The points with error bars are the data.*

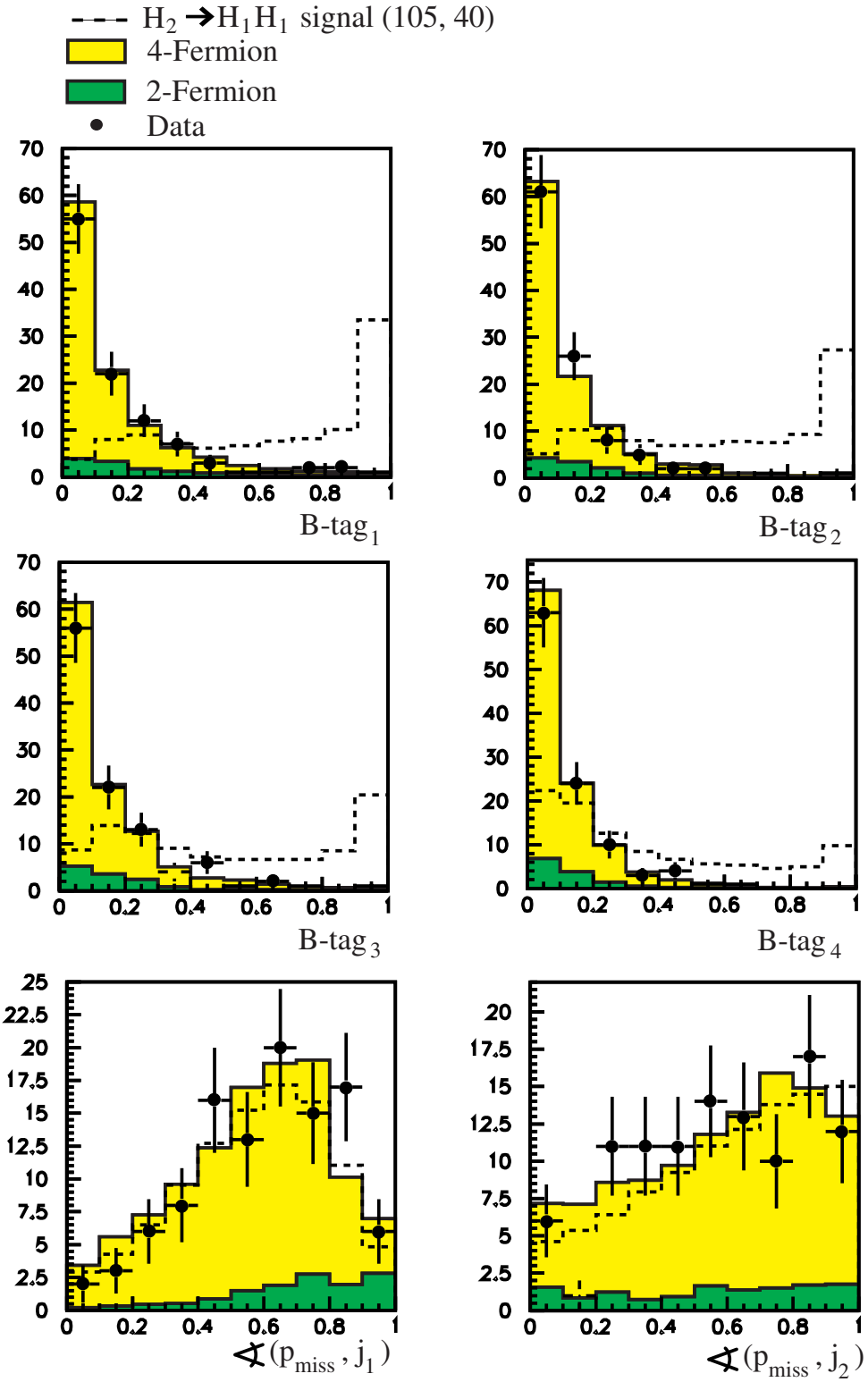

Figure 3.17: *Distributions of the ANN input variables for subsample B assuming 100 GeV* $\leqslant m_{H_2} \leqslant$ *110 GeV. The light shaded (yellow) region is the total background, the dark shaded (green) is the two fermion background. The dotted line shows the arbitrarily scaled signal expectation for* $m_{H_1} = 40$ GeV *and* $m_{H_2} = 105$ GeV*. The points with error bars are the data.*

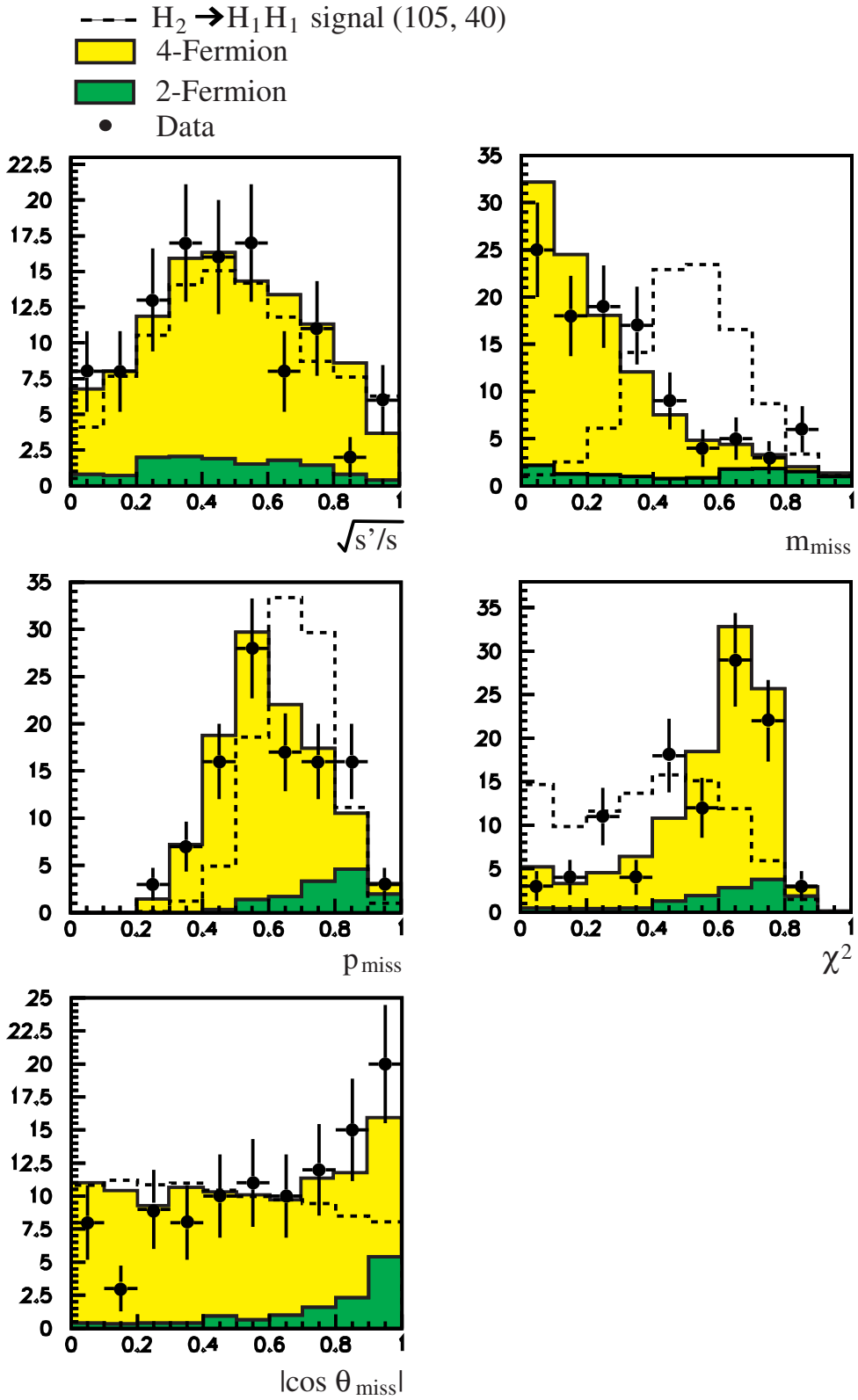

Figure 3.18: *Distributions of the ANN input variables for subsample B assuming 100 GeV* $\leqslant m_{H_2} \leqslant$ *110 GeV. The light shaded (yellow) region is the total background, the dark shaded (green) is the two fermion background. The dotted line shows the arbitrarily scaled signal expectation for* $m_{H_1} = 40$ GeV *and* $m_{H_2} = 105$ GeV*. The points with error bars are the data.*

signal sources according to their expected rates for each scan point. The number of candidate events in subsample A(B) is 11(8) with 10.0 (7.2) events expected from background. The signal efficiencies for subsamples A and B are shown in Figure 3.19 (a,b,c) for the $H_2 \to H_1 H_1 \to b\bar{b}b\bar{b}$ and $m_{H_2} = 100,\ 105,\ 110$ GeV and in 3.19 (d) for $H_2 \to b\bar{b}$. They are also shown in Table 3.5 for various values of (m_{H_2}, m_{H_1}). The distribution of $\mathrm{ANN_A}$ and $\mathrm{ANN_B}$ variables for the background, signal and candidate events are shown in Figure 3.20, and the distributions of the reconstructed mass m_{H_2} in Figure 3.21. The discriminating variable $\mathcal{D}$ which is used for the statistical interpretation is the likelihood calculated from the reconstructed mass and the ANN output.

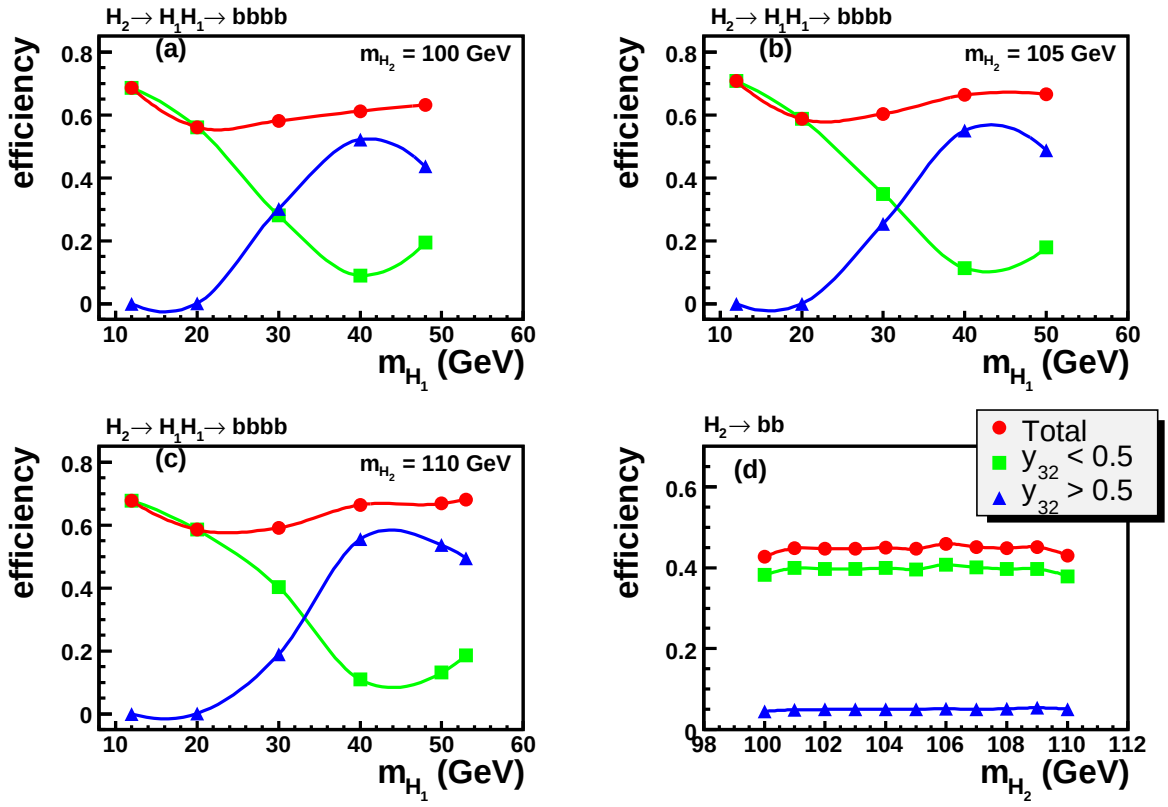

Figure 3.19: *The signal efficiencies for subsamples A and B for* $H_2 \to H_1 H_1 \to b\bar{b}b\bar{b}$ *with* $m_{H_2} = 100,\ 105,\ 110$ *GeV (a-c) and for* $H_2 \to b\bar{b}$ *(d).*

3.2.5 Systematic uncertainties

The different sources of systematic uncertainties which have been considered in the analyses are listed [47].

- **Monte Carlo statistics**: These uncertainties affect the signal and background rates. They are uncorrelated between energies, signal and background.
- **Tracking resolution in $r\phi$**: This uncertainty is evaluated with the Monte Carlo simulation by applying a 5% smearing on the track resolution, i.e. by multiplying the

Efficiency for subsamples A and B for $H_2\nu\bar{\nu} \to b\bar{b}\nu\bar{\nu}$ decays			
m_{H_2} (GeV)	Efficiency of subsample A	Efficiency of subsample B	Total efficiency
100.	0.382	0.045	0.427
101.	0.399	0.049	0.448
102.	0.397	0.050	0.446
103.	0.397	0.050	0.447
104.	0.399	0.050	0.449
105.	0.396	0.050	0.447
106.	0.408	0.051	0.459
107.	0.401	0.050	0.451
108.	0.397	0.052	0.448
109.	0.397	0.054	0.451
110.	0.379	0.051	0.430
	±0.01	±0.01	±0.01

Efficiency for subsamples A and B for $H_2\nu\bar{\nu} \to H_1H_1\nu\bar{\nu} \to b\bar{b}b\bar{b}\nu\bar{\nu}$ decays				
m_{H_2} (GeV)	m_{H_1} (GeV)	Efficiency of subsample A	Efficiency of subsample B	Total efficiency
100.	12.	0.686	0.0	0.69
100.	20.	0.561	0.001	0.56
100.	30.	0.280	0.301	0.58
100.	40.	0.090	0.522	0.61
100.	48.	0.195	0.436	0.63
105.	12.	0.707	0.0	0.71
105.	20.	0.587	0.0	0.59
105.	30.	0.349	0.254	0.60
105.	40.	0.113	0.550	0.66
105.	50.	0.179	0.487	0.67
110.	12.	0.677	0.0	0.68
110.	20.	0.585	0.001	0.59
110.	30.	0.402	0.189	0.59
110.	40.	0.109	0.555	0.66
110.	50.	0.131	0.537	0.67
110.	53.	0.186	0.495	0.68
		±0.01	±0.01	±0.01

Table 3.5: *The efficiencies for subsamples A ($y_{32} < 0.05$) and B ($y_{32} > 0.05$) assuming $100 \leqslant m_{H_2} \leqslant 110$ GeV for $H_2\nu\bar{\nu} \to b\bar{b}\nu\bar{\nu}$ and $H_2\nu\bar{\nu} \to H_1H_1\nu\bar{\nu} \to b\bar{b}b\bar{b}\nu\bar{\nu}$. Only data from 2000 is used. The uncertainty is from MC statistics only. The variations of the uncertainties with different mass combinations are negligible.*

difference between the true and reconstructed values of the track's impact parameter in the $r\phi$ plane, azimuthal angle ϕ and curvature by smearing factors of 1.05 and comparing efficiencies to the simulation without extra smearing.

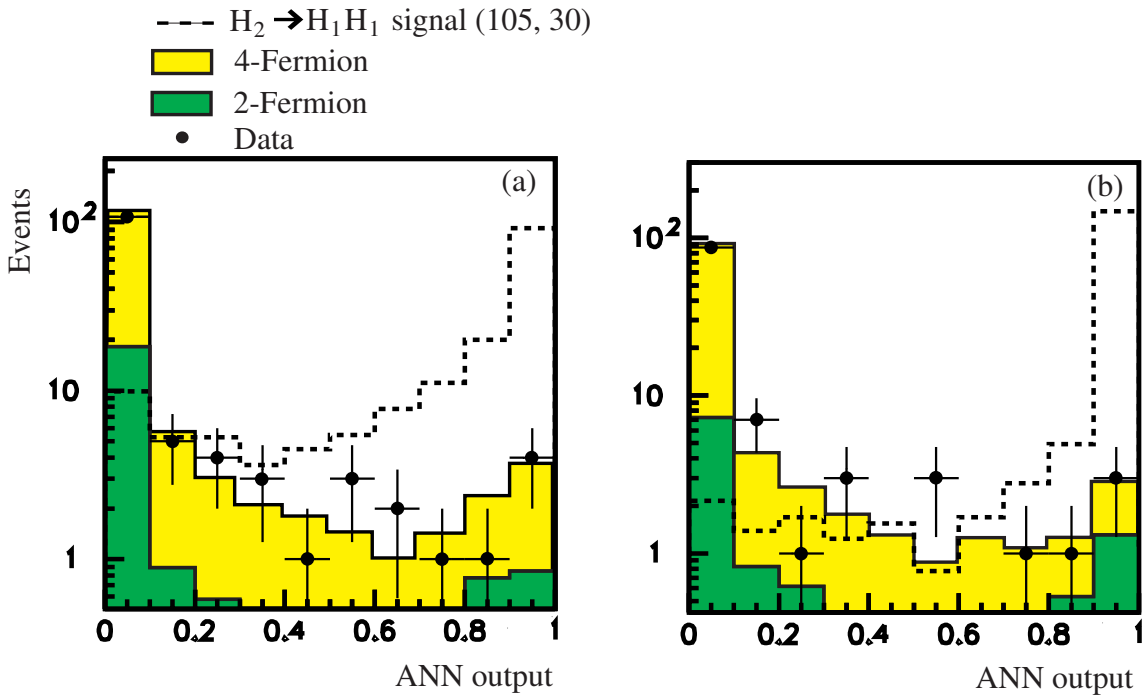

Figure 3.20: *The distributions of the ANN values ANN_{A} (a) and ANN_{B} (b) in the dedicated selection for $e^+e^- \to H_2Z^0 \to b\bar{b}\nu\bar{\nu}$ and $e^+e^- \to H_1H_1Z^0 \to b\bar{b}b\bar{b}\nu\bar{\nu}$ assuming 100 GeV $\leqslant m_{H_2} \leqslant$ 110 GeV. The light shaded (yellow) is the total background, the dark shaded (green) is the two fermion background. The dotted line shows the arbitrarily scaled signal expectation for $m_{H_1} = 30$ GeV and $m_{H_2} = 105$ GeV. The points with error bars are the data.*

- **Tracking resolution in z**: This uncertainty is evaluated by treating the track impact parameter in z and $\tan\lambda = \cot\theta$ in the same way as described above, again using smearing factors of 1.05.

- **Hit-matching efficiency for $r\phi$-hits in the silicon microvertex detector**: One percent of the hits on the $r\phi$ strips of the silicon microvertex detector, which are associated to tracks, are randomly dropped and the tracks are refitted.

- **Hit-matching efficiency for z-hits in the silicon microvertex detector**: This uncertainty is evaluated in the same way as for the $r\phi$ hits, except that 3% of the z-hits are dropped.

- **B hadron charged decay multiplicity**: The average number of charged tracks in B hadron decay is varied within the range recommended by the LEP Electroweak Heavy Flavour Working Group [57], $n_{\mathrm{B}} = 4.955 \pm 0.062$.

- **B hadron fragmentation momentum spectrum**: The b fragmentation function has been varied so that the mean fraction of the beam energy carried by B hadrons, $\langle x_E(\mathrm{b})\rangle$, is varied in the range 0.702 ± 0.008 [57] using a reweighting technique.

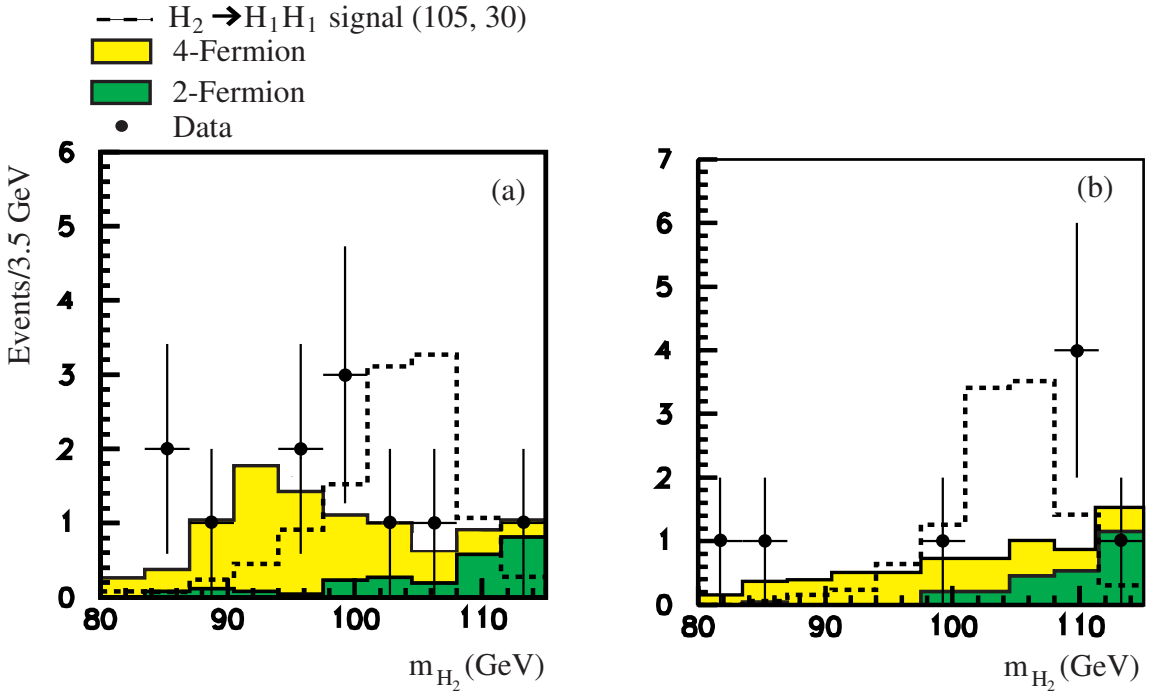

Figure 3.21: *The distribution of the reconstructed mass m_{H_2} in subsamples A and B in the missing energy channel for data taken in 2000 and assuming 100 GeV $\leqslant m_{H_2} \leqslant$ 110 GeV. The light shaded (yellow) is the total background, the dark shaded (green) is the two fermion background. The dotted line shows the arbitrarily scaled signal expectation for $m_{H_1} = 30$ GeV and $m_{H_2} = 105$ GeV. The points with error bars are the data.*

- **Charm hadron fragmentation momentum spectrum**: As for the B hadron momentum spectrum, $\langle x_E(\mathrm{c})\rangle$ has been varied in the range 0.484 ± 0.008 [57].
- **Comparison of different SM background Monte Carlo generators**: Besides the main generators used (see Section 3.1.4.4), the background simulations are cross-checked with alternative generators and fragmentation models in HERWIG [58].
- **Four-Fermion production cross-section**: This is taken to have a 2% relative uncertainty, arising from the uncertainty in the $Z^0 Z^{0(*)}$ and $W^+ W^-$ cross-sections [59].

In addition, a systematic uncertainty of 9% for the background and 1% for the signal has been assigned for the uncertainty of the separation of the events into the subsamples. This has been calculated by shifting the value of y_{32} of each event by the difference of the mean of the background and the data distribution of y_{32}. The systematic uncertainties for this channel are summarized in Table 3.6. The total uncertainty is 2% for the signal and 15% for the background for both subsamples.

Systematic uncertainties at $\sqrt{s}$= 206 GeV				
	subsample A		subsample B	
Source	Signal eff.	Background	Signal eff.	Background
Track Parameter Res. r-phi	0.18%	3.8%	0.32%	1.8%
Track Parameter Res. r-z	0.05%	1.2%	0.37%	2.8%
Si-VTX eff. r-phi	0.27%	1.6%	0.37%	2.7%
Si-VTX eff. r-z	0.14%	2.7%	0.27%	1.2%
Si-VTX dead ladder 25	0.14%	1.0%	0.1%	3.2%
B-had. Multipl.	0.6%	0.84%	0.53%	0.05%
B-had. Fragment.	0.0%	5.1%	0.0%	5.2%
C-had. Fragment.	0.0%	0.23%	0.0%	0.1%
4f-cross-subsection	0.0%	1.5%	0.0%	1.5%
MC-Generators	0.0%	0.5%	0.0%	0.5%
MC statistics	1.6%	9.5%	1.6%	9.5%
Subsample splitting	1.0%	9.0%	1.0%	9.0%
combined	2.0%	15.1%	2.1%	15.2%

Table 3.6: *The systematic uncertainties of the signal efficiency and background at* $\sqrt{s}$ = 206 *GeV for the missing energy search for the process* $e^+e^- \to H_2\nu\bar{\nu} \to b\bar{b}b\bar{b}\nu\bar{\nu}$.

3.2.6 Interpretation of the Search Results within the CPV scenario

In the searches described in the previous section, no evidence of Higgs boson production has been found. Neither has any statistically significant signal been found in the other search channels for Higgs bosons in the MSSM at OPAL [11]. In order to determine if the Higgs boson exists, or, if not, to set exclusion limits, it is necessary to combine several search channels. The search channels are described in [11].

Depending on the values of $\tan\beta$ and masses of the Higgs bosons, different production and decay channels are dominant. The areas of the dominance of different channels are shown in the boxes in Figure 3.22.

The statistical methods for the combination of the search channels and the statistical interpretation of the results are described in Appendix C. In this section the CP violating MSSM benchmark sets under study are introduced and limits on their parameters are presented. Also, the full information from the Higgs boson searches of all four LEP experiments is combined to achieve the maximal sensitivity [12].

3.2.6.1 Limits on Benchmark Scenarios

The presence of neutral Higgs bosons is tested in a constrained MSSM with seven parameters. Two of these parameters are sufficient to describe the Higgs sector at tree level. A convenient choice is $\tan\beta$ (the ratio of the vacuum expectation values of the Higgs fields) and one Higgs mass, m_{H^+} in the CPV scenario under consideration. Additional

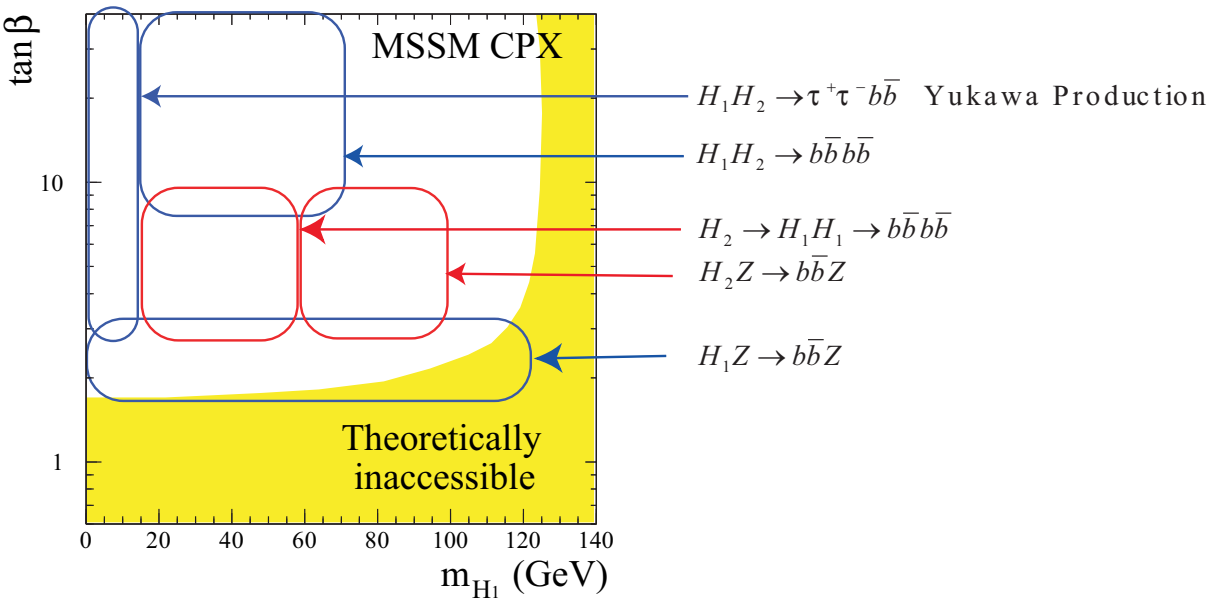

Figure 3.22: *The areas of the dominance of different channels.*

parameters that appear at the level of radiative corrections are: m_{SUSY}, M_2, μ, A, and $m_{\tilde{\mathrm{g}}}$. All soft SUSY-breaking parameters in the sfermion sector are set to m_{SUSY} at the electroweak scale. M_2 is the SU(2) gaugino mass parameter at the electroweak scale and M_1, the U(1) gaugino mass parameter, is derived from M_2 using the GUT relation $M_1 = M_2(5\sin^2\theta_W/3\cos^2\theta_W)$, where θ_W is the weak mixing angle[9]. The supersymmetric Higgs mass parameter is denoted μ. The parameter $A = A_{\mathrm{t}} = A_{\mathrm{b}}$ is the common trilinear Higgs-squark coupling for up-type and down-type squarks. The stop and sbottom mixing parameters are defined as $X_{\mathrm{t}} = A_{\mathrm{t}} - \mu\cot\beta$ and $X_{\mathrm{b}} = A_{\mathrm{b}} - \mu\tan\beta$. The parameter $m_{\tilde{\mathrm{g}}}$ is the gluino mass. The complex phases related to $A_{\mathrm{t,b}}$ and $m_{\tilde{\mathrm{g}}}$ are additional parameters. The phase related to $A_{\mathrm{t,b}}$ enters at one-loop level while the one related to $m_{\tilde{\mathrm{g}}}$ enters as a second-order correction to stop and sbottom loops. Large radiative corrections to the predicted mass m_{H_1} arise from scalar top loops, while the contributions from scalar bottom loops are smaller.

The precise mass of the top quark has a strong impact on m_{H_1}; it is taken to be $m_{\mathrm{top}} = 174.3$ GeV [11]. To account for the current experimental uncertainty, all MSSM interpretations are also done for $m_{\mathrm{top}} = 169$ GeV and $m_{\mathrm{top}} = 179$ GeV.

Rather than varying all of the above MSSM parameters independently, we consider only a certain number of "benchmark sets" where the tree level parameters tanβ and $m_{H^\pm}$ are scanned while all other parameters are fixed. Each scan point within a given benchmark set defines an independent realization of the MSSM (a model), which is tested

[9] M_3, M_2 and M_1 are the mass parameters associated with the SU(3), SU(2) and U(1) subgroups of the Standard Model. M_3 enters only via loop corrections sensitive to the gluino mass.

by comparing its predicted observables (masses, cross-sections and decay branching ratios) with the experimental data. For a given scan point the observables in the Higgs sector are

Parameters varied in the scan	
$\tan\beta$	0.6-40
$m_{H^\pm}$ (GeV)	4-1000
Fixed Parameters	
m_t (GeV)	174.3
$m_{\rm SUSY}$ (GeV)	500
M_2 (GeV)	200
μ (GeV)	2000
$m_{\tilde{\rm g}}$ (GeV)	1000
X_t (GeV)	$A_t - \mu\cot\beta$
$A_{t,b}$ (GeV)	1000
$\arg(A_{t,b})$	90°
$\arg(m_{\tilde{\rm g}})$	90°

Table 3.7: *Parameters of benchmark scenarios considered [34]. Note that the values for* $X_{\rm t}$ *and* $A_{\rm t,b}$ *are given for the* $\overline{\rm MS}$*-renormalization scheme. For a description of the choice of parameters see text.*

calculated using two theoretical approaches. The FEYNHIGGS program [60, 61] is based on a two-loop diagrammatic approach [8, 62] and uses the OS renormalization scheme, while the CPV variant of SUBHPOLE, CPH [34], is based on an one-loop renormalization group improved calculation [63, 64, 65, 66] and uses the $\overline{\rm MS}$ scheme. Both calculations give consistent results although small differences naturally exist. Numerical values for parameters in this thesis are given in the $\overline{\rm MS}$ scheme.

Neither of the two existing calculations is preferred a priori on theoretical grounds. While FEYNHIGGS contains more advanced one-loop corrections, CPH is more precise at the two-loop level. We therefore opted for a solution where, in each scan point, the calculation yielding the more conservative result (less significant exclusion) is retained. For illustration, the results from FEYNHIGGS and CPH are also shown separately for the main CPV scenario CPX (see section 3.2.6.3).

3.2.6.2 CPV benchmark scenarios

As already mentioned in section 2.2.2, the size of the CPV off-diagonal elements of the Higgs boson mass matrix, $\mathcal{M}^2_{ij}$, and hence the size of CPV effect scales qualitatively [34] as

$$\mathcal{M}^2_{ij} \propto \frac{m^4_{\rm top}}{v^2}\frac{{\rm Im}(\mu A_t)}{32\pi^2 m^2_{\rm SUSY}}. \tag{3.9}$$

Large CPV effects, and thus scenarios different from the CP conserving (CPC) case, are therefore obtained if the SUSY breaking scale $m_{\rm SUSY}$ is small and the imaginary

contribution to μA_t are large. Also large values of m_{top} increase the CPV effects.

The basic CPV MSSM benchmark set is CPX [34]. Its parameters are chosen in such a way to approximately fulfill the EDM constraints and to provide features that are the most different from a CPC scenario. The choice of parameters is given in Table 3.7. In the definition of the CPX scenario [34] the relations $\mu = 4m_{\text{SUSY}}$ and $|A_{\text{t,b}}| = |m_{\tilde{\text{g}}}| = 2m_{\text{SUSY}}$ are fixed. Here, $m_{\text{SUSY}} = 500$ GeV is chosen. The parameter M_2 is set to 200 GeV. Additionally the complex phases of $A_{\text{t,b}}$ and $m_{\tilde{g}}$ are fixed at 90° degrees. The scenario with $\arg(A_{\text{t,b}}) = 90°$ has very different features from a CPC case and therefore has good properties for a CPV benchmark scenario.

Variants of the CPX scenario are investigated to check the stability of the CPX results with respect to the choice of its parameters. The phases of $A_{\text{t,b}}$ and $m_{\tilde{g}}$ are varied from 0° to 180°, and μ between 500 and 4000 GeV.

The parameter $\tan\beta$ is scanned from 0.6 to 40, and $m_{H^\pm}$ is scanned from 4 to 1000 GeV. In this region both H_1 and H_2 have a width below 1 GeV, negligible with respect to the experimental resolution of several GeV.

3.2.6.3 Limits on the CP Violating MSSM Models

Exclusion limits from the CPX scenario, and its variations will be given in this section.

- Figure 3.23 shows the combined exclusion result for the CPX scenario with all phases equal to 90°, $m_{\text{SUSY}} = 500$ GeV and $\mu = 2$ TeV.

  Figure 3.23 (a) shows both the expected and observed 95% CL exclusion areas in the plane of m_{H_1} and m_{H_2}. For heavy m_{H_2}, H_1 resembles the SM Higgs boson (almost completely CP-even) with very little effect from CP violation. The limit on the allowed mass of H_1 for large m_{H_2} is found to be $m_{H_1} > 112$ GeV. In the region below $m_{H_2} \approx 130$ GeV CPV effects play a major role.

  Figure 3.23 (b) shows the 95% CL exclusion areas in the parameter space of $\tan\beta$ and m_{H_2}. One can see that $\tan\beta < 2.8$ is excluded. The band at $\tan\beta < 2.8$ is excluded by searches for the SM-like H_1, while the band at $\tan\beta > 10$ and $m_{H_2} < 120$ GeV is excluded by searches for Z^0H_2 and H_1H_2 topologies.

  Figure 3.23 (c) displays the parameter space of $\tan\beta$ and m_{H_1}. Exclusion is obtained for $\tan\beta < 3.2$ and $m_{H_1} < 112$ GeV in the SM-like regime. For $4 < \tan\beta < 10$, Z^0H_2 production is dominant. The large difference between the expected and observed exclusion regions in the area of $4 < \tan\beta < 10$ is mainly due to a less than 2σ excess[10] in the data between $m_{\text{h}} \approx 95$ GeV and

[10] This excess is from the SM searches.

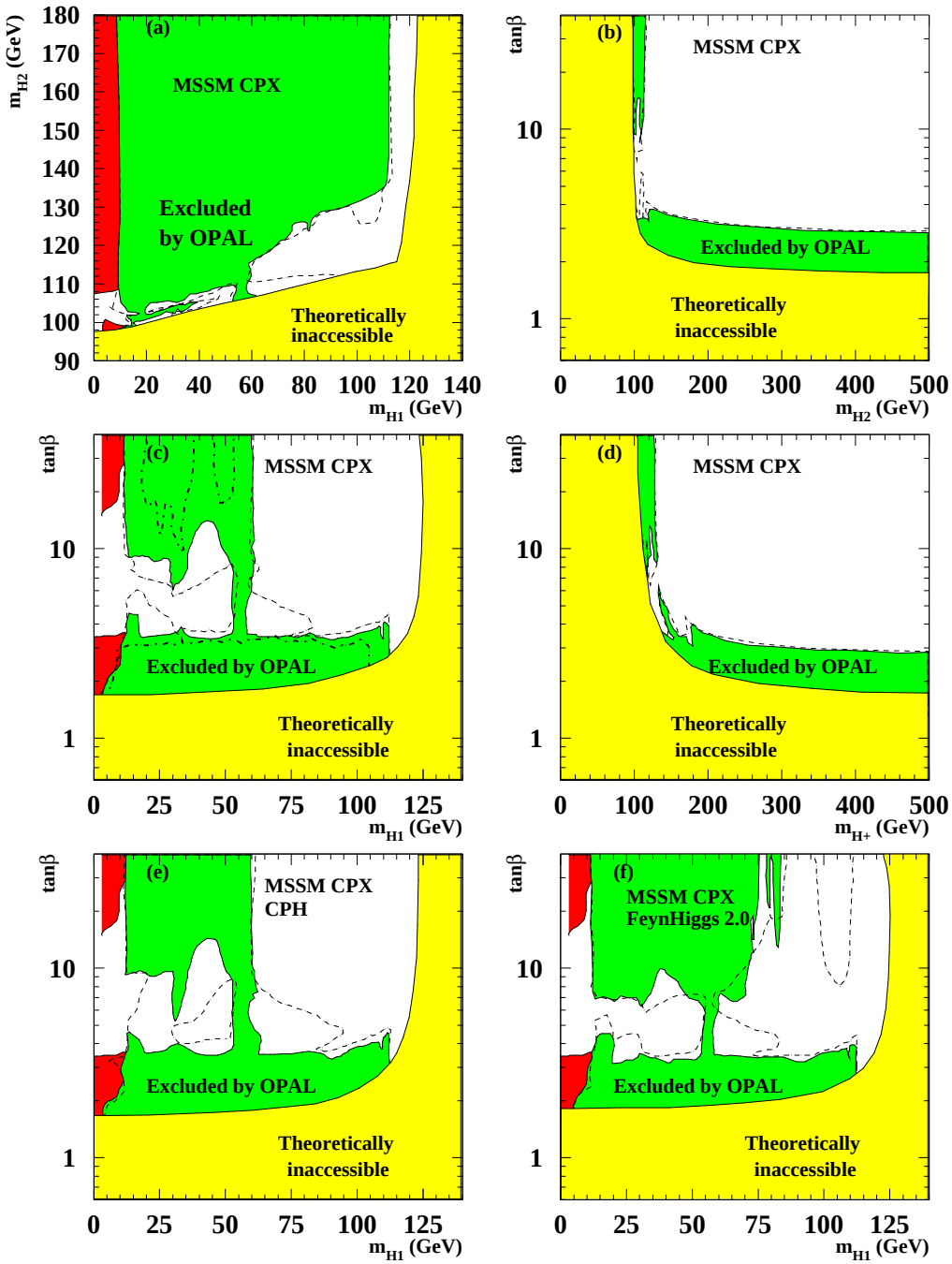

Figure 3.23: *The CPX MSSM* 95 % CL *exclusion areas. The figure shows the excluded regions in darker gray (green) and theoretically inaccessible regions in light gray (yellow) as functions of the MSSM parameters in the following projections: (a) the* (m_{H_1},m_{H_2}) *plane, (b) the* (m_{H_2},tanβ) *plane, (c) the* (m_{H_1},tanβ) *plane, and (d) the* ($m_{H^\pm}$,tanβ) *plane. Figure (e) shows the* (m_{H_1},tanβ) *of the CPH calculation alone, and (f) shows the same projection of the FEYNHIGGS 2.0 calculation. The dashed lines indicate the boundaries of the regions expected to be excluded at the 95% CL if only SM background processes are present. The region excluded by Yukawa searches,* Z^0*-width constraints or decay independent searches is shown in dark gray (red). The dash-dotted line in (c) shows the area excluded on the 99.9% confidence level. In (b) and (d) the area excluded by* Z^0 *width constraints or by decay independent searches is too small to be displayed.*

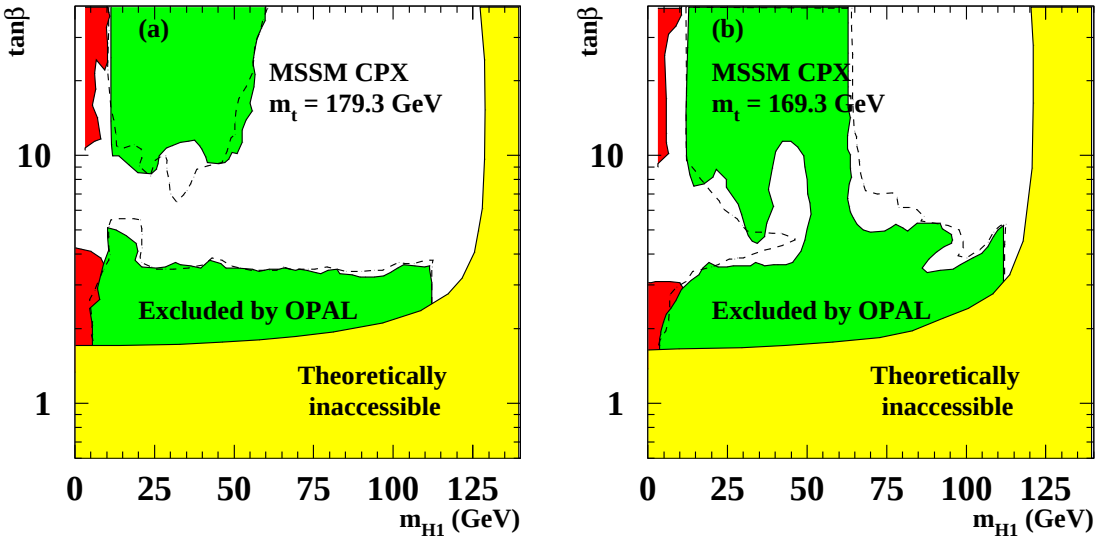

Figure 3.24: *The CPX MSSM* 95 % CL *exclusion areas in the* (m_{H_1},tanβ) *plane, using scans with (a)* $m_t = 179.3$ GeV *and (b)* $m_t = 169.3$ GeV. *Due to the change in the top masses a large difference is observed compared to Figure 3.23 (c). See Figure 3.23 for the notation.*

$m_h \approx 110$ GeV [47], which corresponds to the mass of H_2 in this region. For $m_{H_1} < 50$ GeV there are also unexcluded regions in the expected exclusion, which is due to dominant $Z^0 H_2 \to Z^0 H_1 H_1$ production with relatively large m_{H_1}, yielding broad mass resolutions and therefore reduced sensitivity.

Figure 3.23 (d) shows the exclusion area in the parameter space of the theoretical input parameters tanβ and $m_{H^\pm}$, which are varied during the scan. Since the CPX scenario yields $m_{H_2} \approx m_{H^\pm}$ for most of the scan points, this is very similar to Figure 3.23 (b).

The uncertainty inherent to the two theoretical approaches, CPH and FEYNHIGGS, is illustrated in parts (e) and (f) of Figure 3.23. The largest discrepancy occurs for large values of tanβ, where the FEYNHIGGS calculation (part (f)) predicts a higher cross-section for Higgsstrahlung, and hence a better search sensitivity than the CPH prediction (part (e)).

- The large impact of the value of the top quark mass on the exclusion limits is shown in Figure 3.24.

- The effect of different choices of the CPV phases is illustrated in Figures 3.25 and 3.26. Values of $\arg(A_{t,b}) = \arg(m_{\tilde{g}})$ from 0° to 180° are displayed. Figure 3.25 shows exclusion regions in the parameter space of tanβ and m_{H_1} for $\arg(A_{t,b}) = \arg(m_{\tilde{g}}) = 90°, 60°, 30°$ and 0°. At 30° and at 0° all areas for low m_{H_1} and low

$\tan\beta$ are excluded. The exclusion for the maximally CPV scenario CPX with 90° is very different from the exclusion of a CPC scenario ($\arg(A_{t,b}) = \arg(m_{\tilde{g}}) = 0°$). A variation of the second main parameter governing the size of CPV effects, m_{SUSY}, has similar effects on the exclusion as a variation of $\arg(A_{t,b}) = \arg(m_{\tilde{g}})$.

- Figure 3.26 shows the exclusion regions in the parameter space of $\tan\beta$ and m_{H_1} for phases of (a) 135° and (b) 180°. The scenario in (a) is phenomenologically still similar to the original CPX scenario. The scenario in (b), which is in fact a CPC case, exhibits two allowed regions, of which the lower one from $\tan\beta = 3$ to $\tan\beta = 13$ has a low H_1Z^0 coupling. The unexcluded "hole" in the exclusion region for $90 < m_{H_1} < 100$ GeV is due to an excess of the background in the SM-like channels.

- Since the CPX scenario has a relatively high value of $\mu = 2$ TeV, which influences the mixing of the CP eigenstates into the mass eigenstates (see Eq. (3.9)), μ is varied from $\mu = 500$ GeV to $\mu = 4$ TeV in Figure 3.27. For $\mu = 500$ GeV (Figure 3.27 (a)) and $\mu = 1$ TeV (Figure 3.27 (b)) the CPV effects are small. Therefore no unexcluded regions occur at small m_{H_1}. The scenario with $\mu = 4$ TeV (Figure 3.27 (d)) has strong mixing and a suppression of pair production at large $\tan\beta$, resulting in an exclusion area that is considerably smaller than in the CPX scenario (Figure 3.27 (c)).

- The proposal of the CPX scenario in [34] leaves the choice of m_{SUSY} open, as long as the relations $|A_{t,b}| = 2m_{SUSY}$, $|m_{\tilde{g}}| = 2m_{SUSY}$ and $\mu = 4m_{SUSY}$ are preserved. In order to test the dependence on m_{SUSY}, two scenarios are tested: Figure 3.28 (a) shows the scenario $CPX_{1.0}$, where the ratio between the parameters in the CPX proposal is preserved, while m_{SUSY} is increased from 500 GeV to 1 TeV. Only small differences with respect to the CPX scenario with $m_{SUSY} = 500$ GeV can be seen. Figure 3.28 (b) shows the CPX scenario as given in Table 3.7, but with only m_{SUSY} set to 1 TeV, while the values of $|A_{t,b}|$, $|m_{\tilde{g}}|$ and μ are kept fixed. This results in a decrease of the CPV effects and thus no unexcluded regions at small m_{H_1} are observed.

3.2.6.4 LEP results

The results of the interpretations can be improved significantly, if the full information from all four LEP experiments ALEPH [67], DELPHI [68], L3 [69] and OPAL [11] is used. All searches of the four experiments are combined in the same way as the searches of the OPAL experiment. Over the most part of the parameter space the local excess of the data over the expected background is smaller than two standard deviation, and the strongest excess is $\sim 3\sigma$ at $m_{H_1} = 40$ GeV and $m_{H_2} = 105$ GeV, at the point of the

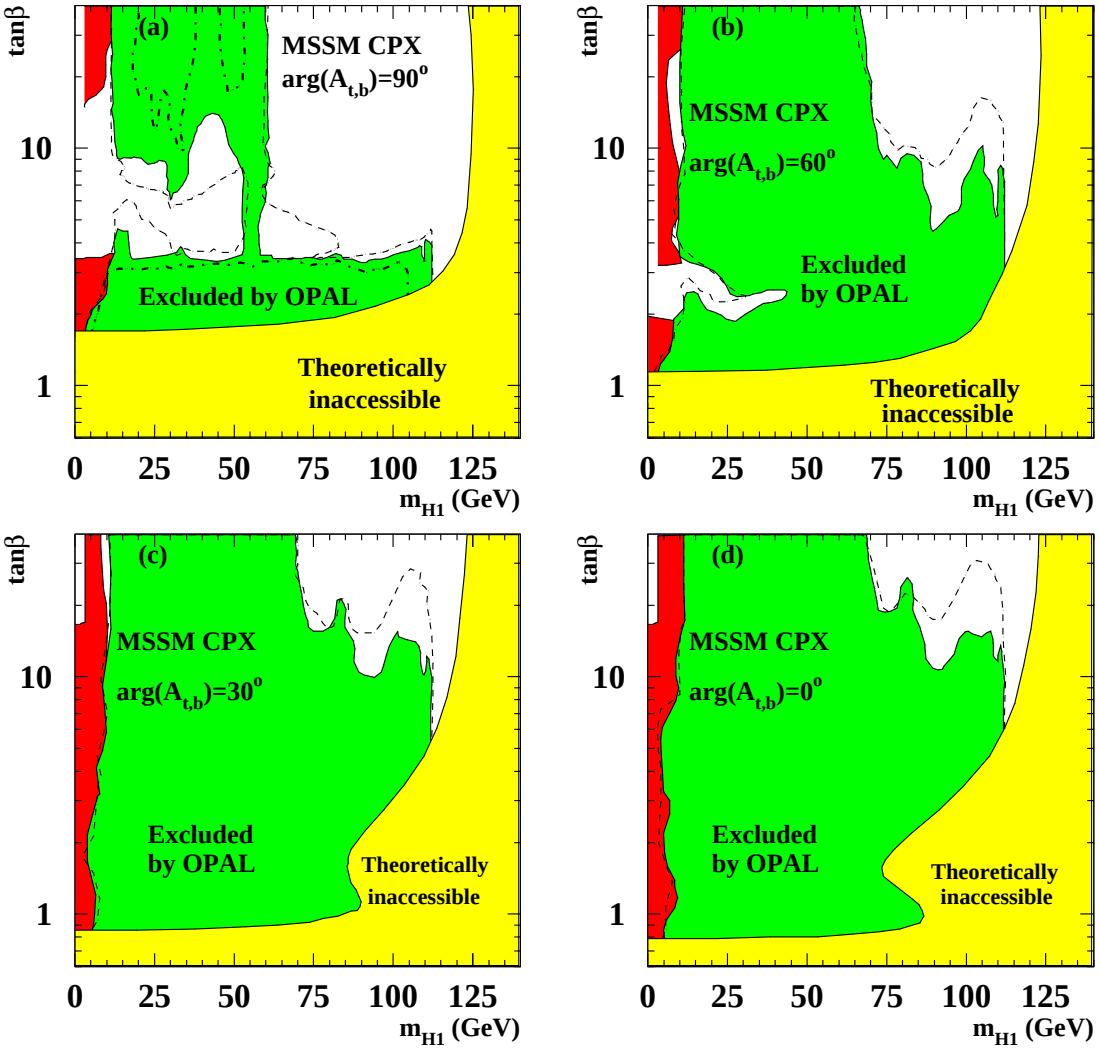

Figure 3.25: *The CPX MSSM* 95 % CL *exclusion areas in the* (m_{H_1},tanβ) *plane, using scans with (a)* $\arg(A_{\mathrm{t,b}}) = \arg(m_{\tilde{\mathrm{g}}}) = 90°$, *(b)* $\arg(A_{\mathrm{t,b}}) = \arg(m_{\tilde{\mathrm{g}}}) = 60°$, *(c)* $\arg(A_{\mathrm{t,b}}) = \arg(m_{\tilde{\mathrm{g}}}) = 30°$ *and (d)* $\arg(A_{\mathrm{t,b}}) = \arg(m_{\tilde{\mathrm{g}}}) = 0°$. *While the CPV phases decrease, effects from CP violation like the strong* $H_2 \to H_1 H_1$ *contribution vanish. See Figure 3.23 for the notation.*

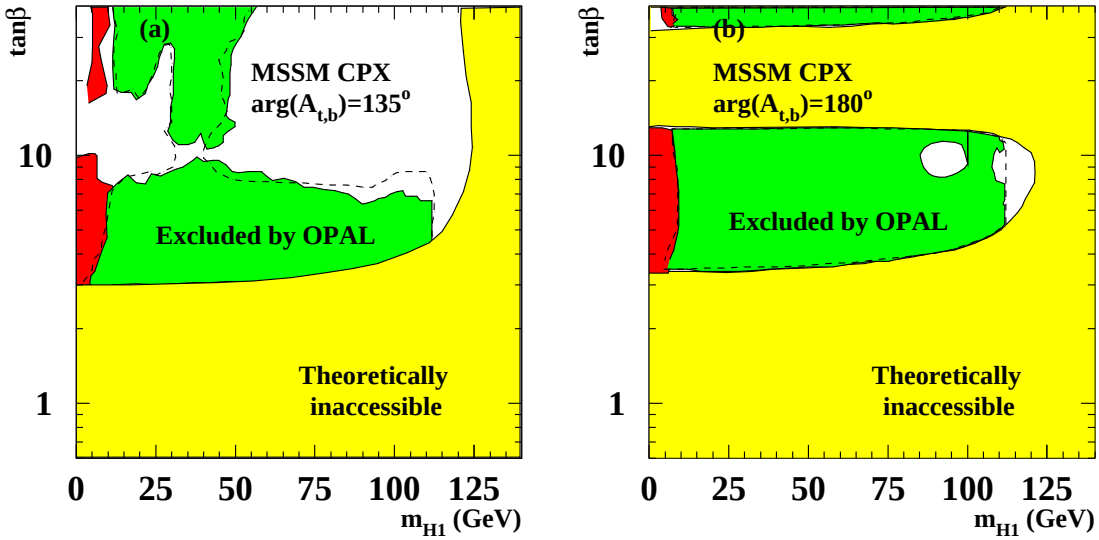

Figure 3.26: *The CPX MSSM* 95 % CL *exclusion areas in the* (m_{H_1},tanβ) *plane, using scans with (a)* $\arg(A_{\mathrm{t,b}}) = \arg(m_{\tilde{\mathrm{g}}}) = 135°$ *and (b)* $\arg(A_{\mathrm{t,b}}) = \arg(m_{\tilde{\mathrm{g}}}) = 180°$. *See Figure 3.23 for the notation.*

strongest excess of the OPAL data over the background. Since no significant excess is found, limits on the MSSM parameters are derived.

The impact of the combination of the four experiments is shown in Figure 3.29. For the default CPX scenario the exclusion from OPAL only is shown in (a), and the exclusion from all four experiments in (b). The preliminary results of other possible CPV scenarios are summarized in [12].

3.2.7 Conclusions

The searches for neutral Higgs bosons in the MSSM with the CP violation described in this thesis are based on the data collected by the OPAL experiment during the year 2000, at energies between 200 and 209 GeV (LEP2 phase). The corresponding integrated luminosity is $\sim 207\,\mathrm{pb}^{-1}$.

The work presented here described the search for the Higgs boson in the channels $e^+e^- \to H_2Z^0 \to H_1H_1Z^0 \to b\bar{b}b\bar{b}\nu\bar{\nu}$ and $e^+e^- \to H_2Z^0 \to b\bar{b}\nu\bar{\nu}$. No significant excess of the data over the expected background is found.

The results from this channel are combined with other searches for the MSSM Higgs bosons in models with CP violation at OPAL. In the case of "CPX" benchmark scenario, designed to maximize the phenomenological differences in the Higgs sector with respect to the CP-conserving scenarios, the region $\tan\beta < 2.8$ is excluded at 95% confidence level, but no universal limit is obtained for either of the Higgs boson masses. However, for $\tan\beta < 3.3$, the limit $m_{H_1} > 112$ GeV can be set for the mass of the lightest neutral Higgs

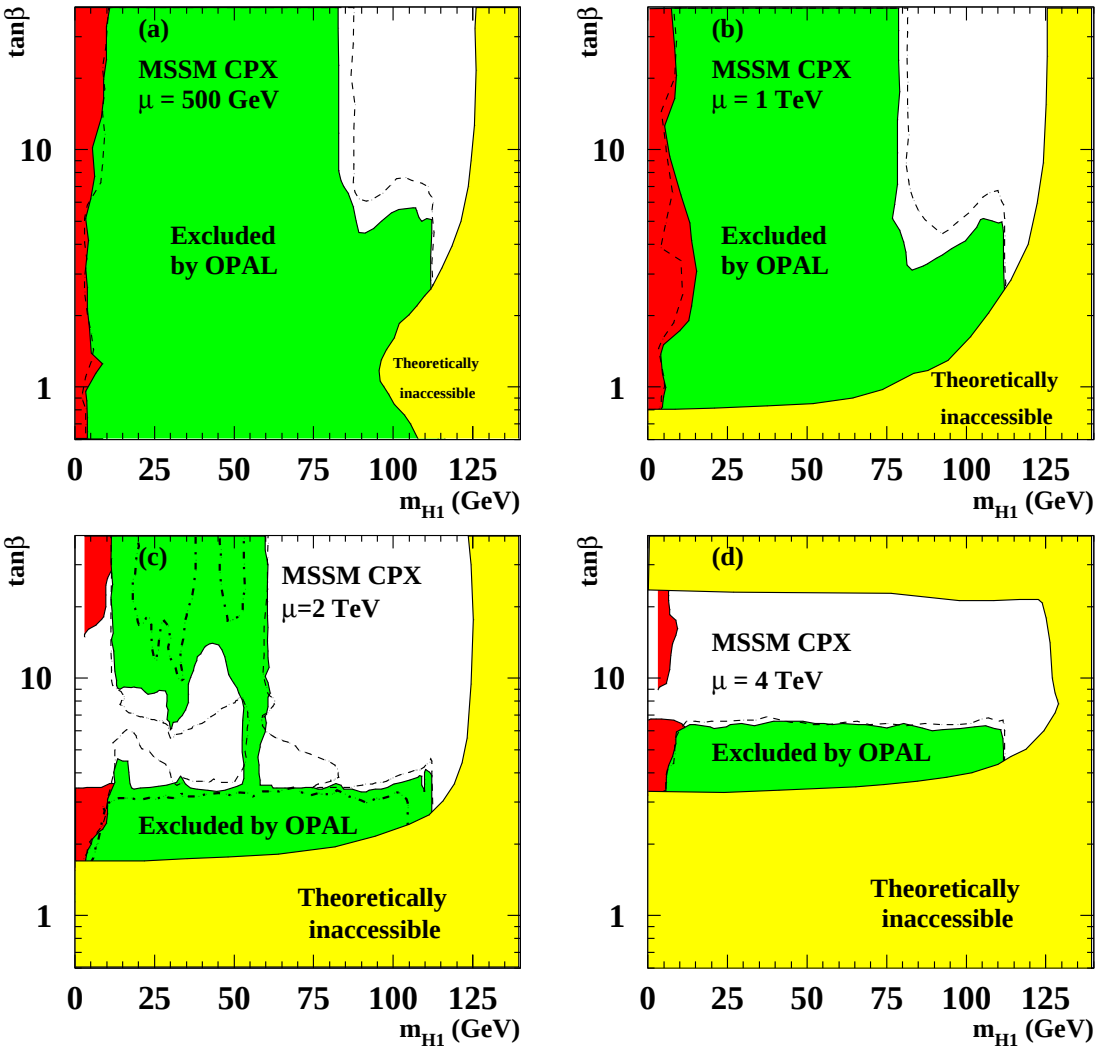

Figure 3.27: *The CPX MSSM* 95 % CL *exclusion areas in the* (m_{H_1},tanβ) *plane, using scans with (a)* $\mu = 500$ *GeV, (b)* $\mu = 1000$ *GeV, (c)* $\mu = 2000$ *GeV (CPX) and (d)* $\mu = 4000$ *GeV. See Figure 3.23 for the notation.*

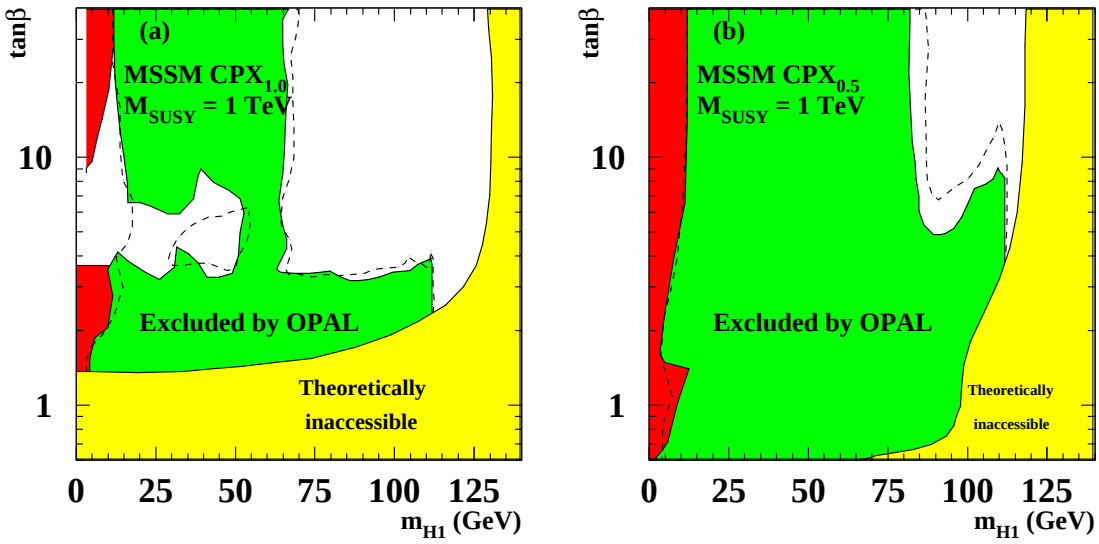

Figure 3.28: *The CPX MSSM* 95 % CL *exclusion areas in the* $(m_{H_1}, \tan\beta)$ *plane, using scans (a) preserving the CPX ratios of* μ, $A_{b,t}$ *and* m_{SUSY}, *using* $m_{SUSY} = 1$ *TeV, and (b)* $m_{SUSY} = 1$ *TeV keeping* μ *and* $A_{b,t}$ *at their CPX values. See Figure 3.23 for the notation.*

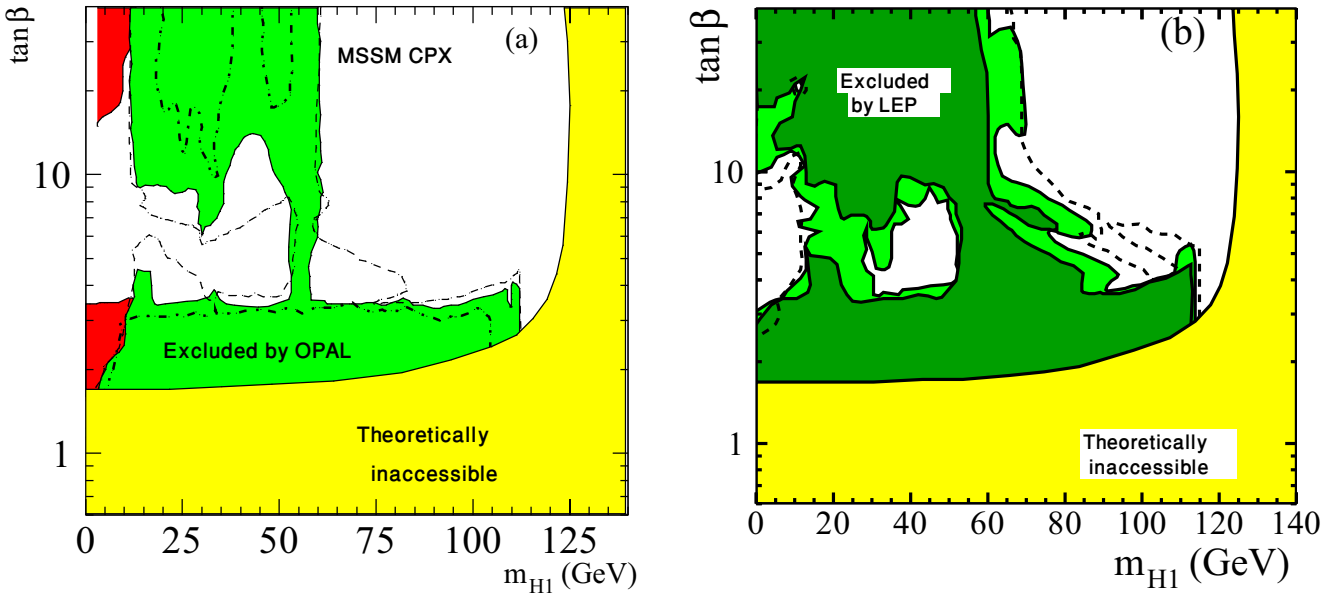

Figure 3.29: *For the default CPX scenario the 95% CL exclusion (light green) from OPAL only is shown in (a), and the exclusion from all four experiments in (b). See Figure 3.23 for the notation. In (b) dark green area is excluded at 99.7% confidence level.*

boson of the model with OPAL experiment only. When the results from all four LEP experiments are combined, $\tan\beta < 2.9$ is excluded.

Chapter 4

ILC and LHC/LC Interplay

4.1 Introduction

Ground-breaking discoveries and measurements are expected from the future experiments: the Large Hadron Collider (LHC) currently under construction, and planned International Linear Collider (ILC). These high-energy particle accelerators will open up a new energy domain that will allow to examine the very fabric of matter, energy, space and time. The experimental results should reveal how particles obtain the property of mass, whether the different forces that we experience in nature are in fact different manifestations of only one fundamental force, whether space and time are embedded into a wider framework of supersymmetric coordinates, and whether dark matter can be produced on Earth.

The way the LHC and ILC will probe the above-mentioned questions will be very different, as a consequence of the distinct experimental conditions of the two machines. The LHC, due to its high collision energy has a large mass reach for direct discoveries. Striking features of the ILC are its clean experimental environment, polarized beams, and known collision energy, enabling precision measurements and therefore detailed studies of directly accessible new particles as well as a high sensitivity to indirect effects of new physics. The results obtained at the LHC and ILC will complement and supplement each other in many ways. Both of them will be necessary in order to reveal the underlying structure of the new physics that lies ahead of us.

The synergy from the interplay of the LHC and ILC can occur in different ways [14]. The combined interpretation of the LHC and ILC data will lead to a much clearer picture of the underlying physics than the results of both colliders taken separately.

An important example is the physics of the Higgs boson, which, if exists, is the key to understanding the mechanism of generating the masses of the elementary particles. The combination of the highly precise measurements possible at the ILC, and the large mass and high-energy coverage of the LHC will be crucial to completely decipher the properties of the Higgs boson (or several Higgs bosons) and thus to reveal the mechanism of mass generation.

We will describe here a scenario where nature is supersymmetric, SUSY is broken in a

way described by MSSM and both LHC and ILC can only observe one light Higgs boson, the h. The others will stay beyond the reach of both machines. In order to understand the Higgs sector a mass determination of the A is mandatory. This mass, M_A, can be derived from the combined data of both colliders [13, 14, 15].

4.2 LHC/ILC Interplay in the MSSM Higgs sector

The prediction of a firm upper bound on the mass of the lightest Higgs boson is one of the most striking predictions of Supersymmetric (SUSY) theories whose couplings stay in the perturbative regime up to a high energy scale [8, 9]. Revealing the structure of the Higgs sector and establishing possible deviations from the Standard Model (SM) predictions will be one of the main goals at the next generation of colliders.

In order to incorporate electroweak symmetry breaking consistently into the Minimal Supersymmetric Standard Model (MSSM), two Higgs doublets are needed[1]. This results in eight degrees of freedom, three of which are absorbed via the Higgs mechanism to give masses to the $W^{\pm}$ and Z bosons. The remaining five physical states are the neutral CP-even Higgs bosons h and H, the neutral CP-odd state A, and the two charged Higgs bosons $H^{\pm}$. At the lowest order, the Higgs sector of the MSSM is described by only two parameters in addition to the gauge couplings, conventionally chosen as M_A and $\tan\beta$, where the latter is the ratio of the vacuum expectation values of the two Higgs doublets.

The Higgs-boson sector of the MSSM is affected, however, by large radiative corrections which arise in particular from the top and scalar top sector and for large values of $\tan\beta$ also from the bottom and scalar bottom sector. Thus, the tree-level upper bound on the mass of the lightest CP-even Higgs boson, $m_h < M_Z$ in the MSSM, arising from the gauge structure of the theory, receives large radiative corrections from the Yukawa sector of the theory [33]. Taking corrections up to two-loop order into account, the mass is shifted by about 50%, establishing an upper bound of $m_h \lesssim 135$ GeV [8, 9].

An e^+e^- International Linear Collider (ILC) will provide precision measurements of the properties of all Higgs bosons that are within its kinematic reach [70]. Provided that a Higgs boson couples to the Z boson, the ILC will observe it independently of its decay characteristics. At the Large Hadron Collider (LHC), Higgs boson detection can occur in various channels (see section 5.1.4). In many cases complementary information from more than one channel will be accessible at LHC. In particular, the LHC has a high potential for detecting heavy Higgs states which might be beyond the kinematic reach of the ILC. Furthermore, experimental information on the parameters entering via large radiative corrections will be crucial for SUSY Higgs phenomenology. This refers in particular to a

[1] This is indeed true for any SUSY model, not just for the MSSM. But in this work we restrict the discussion only to MSSM.

precise knowledge of the top-quark mass, m_t, from the ILC [70, 71, 72] and information about the SUSY spectrum from both LHC and ILC [14].

In the following, an example of a possible interplay between LHC and ILC results in SUSY Higgs physics [14] is investigated. It is based on the benchmark scenario which assumes that nature is described by the SPS 1a benchmark point [73]. In this scenario none of heavy Higgs bosons can be detected at LHC and ILC. The lightest Higgs boson is observable by both, and both machines might see small deviations between the observed properties and the SM predictions. The combined information about the SUSY spectrum from the LHC and ILC, and of Higgs-boson branching ratio measurements at the ILC is used to obtain bounds on the mass of the CP-odd Higgs boson, M_A, in the unconstrained MSSM. Since a realistic analysis requires the inclusion of radiative corrections, the achievable sensitivity on M_A depends on the experimental precision of the additional input parameters and the theoretical uncertainties from unknown higher-order corrections. This means, in particular, that observed deviations in the properties of the light CP-even Higgs boson compared to the SM case cannot be attributed to the single parameter M_A. In the present work, the impact of the experimental and theoretical errors on the precision of the M_A determination is analyzed in detail. This analysis considerably differs from existing studies of Higgs boson branching ratios in the literature [74]. In these previous analyses, all parameters except for the one under investigation (i.e. M_A) have been kept fixed and the effect of an assumed deviation between the MSSM and the SM has solely been attributed to this single free parameter. This would correspond to a situation with a complete knowledge of all SUSY parameters without any experimental or theoretical uncertainty, which obviously leads to an unrealistic enhancement of the sensitivity to the investigated parameter.

This work was done in collaboration with K. Desch *et al.* [13] and below my contribution only is described.

4.2.1 Indirect constraints on M_A from LHC and ILC measurements

In the following, an SPS 1a scenario [73] (see also the Appendix D), where M_A is kept as a free parameter, is analyzed. In particular the situation where the LHC only detects one light Higgs boson is studied. For the present scenario this corresponds to the region $M_A \gtrsim 400$ GeV. The overall discovery potential for Higgs bosons in the "*mhmax*"[2] scenario after collecting 300 fb^{-1} is shown in Figure 4.1 [75]. It is clear that the large area in $(m_A, \tan\beta)$ plane correspond to the considered case.

The precise measurements of Higgs branching ratios at the ILC together with accurate

[2]The scenario in which the lightest Higgs boson has the highest mass.

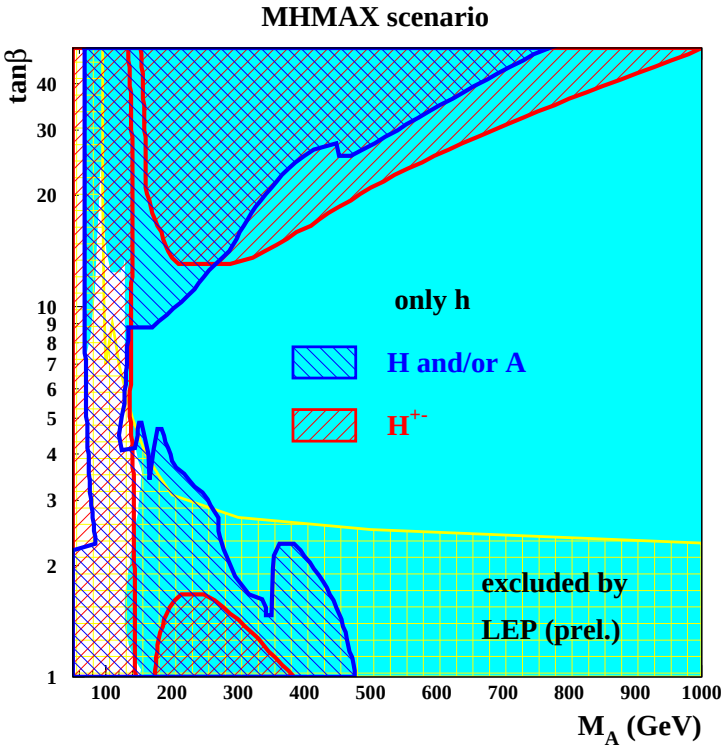

Figure 4.1: *Overall discovery potential for Higgs bosons in the "mhmax" scenario after collecting* 300 fb^{-1}. *The cross hatched (with a yellow line) area is excluded by LEP at 95% CL, and the clear (cyan) area is where only the lightest Higgs boson can be found.*

determinations of (parts of) the SUSY spectrum at the LHC and the ILC (see Ref. [14]) will allow in this case to obtain indirect information on M_A (for a discussion of indirect constraints on M_A from electroweak precision observables, see Ref. [76]). When investigating the sensitivity to M_A it is crucial to take into account realistic experimental errors of the other SUSY parameters that enter the prediction of the Higgs branching ratios. Therefore all the SUSY parameters are varied according to error estimates for the measurements at LHC and ILC in this scenario. The sbottom masses and the gluino mass can be obtained from mass reconstructions at the LHC with ILC input, see Ref. [14]. A precision of $\Delta m_{\tilde{g}} = \pm 8$ GeV and $\Delta m_{\tilde{b}_{1,2}} \approx \pm 7.5$ GeV is assumed. Further assumptions are that the lighter stop (which in the SPS 1a scenario has a mass of about 400 GeV, see Ref. [73]) will be accessible at the ILC, leading to an accuracy of about $\Delta m_{\tilde{t}_1} = \pm 2$ GeV. The impact of the ILC information on the stop mixing angle, $\theta_{\tilde{t}}$, will be discussed below. For $\tan\beta$ an uncertainty of $\Delta \tan\beta = 10\%$ is used (this accuracy can be expected from measurements at the ILC in the gaugino sector for the SPS 1a value of $\tan\beta = 10$ [77]). An error of $\Delta m_t = \pm 0.1$ GeV from the ILC is assumed, so that the parametric uncertainties on the m_h predictions become negligible. Finally, an ILC measurement of m_h is assumed, but a theoretical error from unknown higher-order corrections of ± 0.5 GeV [9]

is included.

In the present analysis we compare the theoretical prediction [60] for the ratio of branching ratios

$$r \equiv \frac{\left[\mathrm{BR}(h \to b\bar{b})/\mathrm{BR}(h \to WW^*)\right]_{\mathrm{MSSM}}}{\left[\mathrm{BR}(h \to b\bar{b})/\mathrm{BR}(h \to WW^*)\right]_{\mathrm{SM}}} \tag{4.1}$$

with its prospective experimental measurement. Even though the experimental error on the ratio of the two BR's is larger than that of the individual ones, the quantity r has a higher sensitivity to M_A than any single branching ratio.

In Figure 4.2 the theoretical prediction for r is shown as a function of M_A, where the scatter points result from the variation of all relevant SUSY parameters within the 3 σ ranges of their experimental errors. The constraint on the SUSY parameter space from the knowledge of m_h is taken into account, where the precision is limited by the theoretical uncertainty from unknown higher-order corrections. The experimental information on m_h gives rise in particular to indirect constraints on the heavier stop mass and the stop mixing angle.[3] Without assuming any further experimental information, two distinct intervals for the heavier stop mass (corresponding also to different intervals for $\theta_{\tilde{t}}$) are allowed. This can be seen from the upper plot of Figure 4.2. The interval with lower values of $m_{\tilde{t}_2}$ corresponds to the SPS 1a scenario, while the interval with higher $m_{\tilde{t}_2}$ values can only be realized in the unconstrained MSSM. In the lower plot the projection onto the M_A–r plane is shown, giving rise to two bands with different slopes. Since the lighter stop mass is accessible at the ILC in this scenario, it can be expected that the stop mixing angle will be determined with sufficient accuracy to distinguish between the two bands. This has an important impact on the indirect determination of M_A.

The central value of r obtained from the band which is realized in the SPS 1a scenario is shown as a function of M_A in Figure 4.3. The plot shows a non-decoupling behavior of r, i.e. r does not go to 1 for $M_A \to \infty$. This is due to the fact that the SUSY masses are kept fixed in the SPS 1a scenario. In order to find complete decoupling, however, both M_A and the mass scale of the SUSY particles have to become large, see e.g. Ref. [78]. It should be noted that the sensitivity of r to M_A is not driven by this non-decoupling effect. In fact, for larger values of the SUSY masses the slope of $r(M_A)$ even increases (one example being the second band depicted in Figure 4.2). Thus, even stronger indirect bounds on M_A could be obtained in this case.

The relation between r and M_A shown in Figure 4.3 corresponds to an idealized situation where the experimental errors of all input parameters in the prediction for r (besides M_A) and the uncertainties from unknown higher-order corrections were negligibly small. The comparison of the theoretical prediction for r (including realistic uncertainties) with

[3] Without the reduction of the intrinsic m_h uncertainty and without a precise determination of m_t the constraint on the SUSY parameter space would be much weaker, which would drastically decrease the sensitivity to M_A.

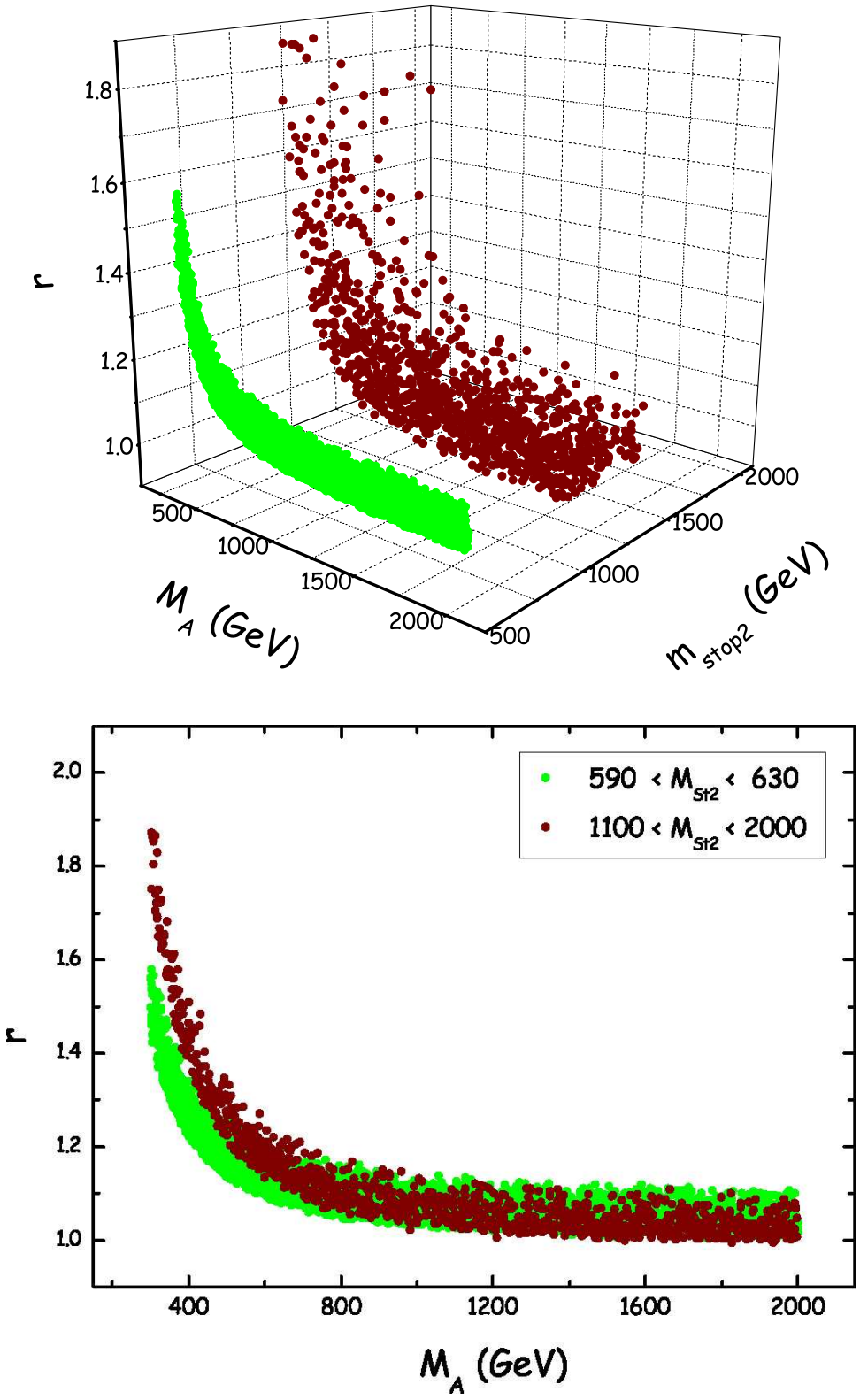

Figure 4.2: *The ratio of branching ratios r, see eq. (4.1), is shown as a function of M_A in the SPS 1a scenario. The other SUSY parameters have been varied within the 3 σ intervals of their experimental errors (see text). The upper plot shows the three-dimensional M_A–$m_{\tilde{t}_2}$–r parameter space, while the lower plot shows the projection onto the M_A–r plane.*

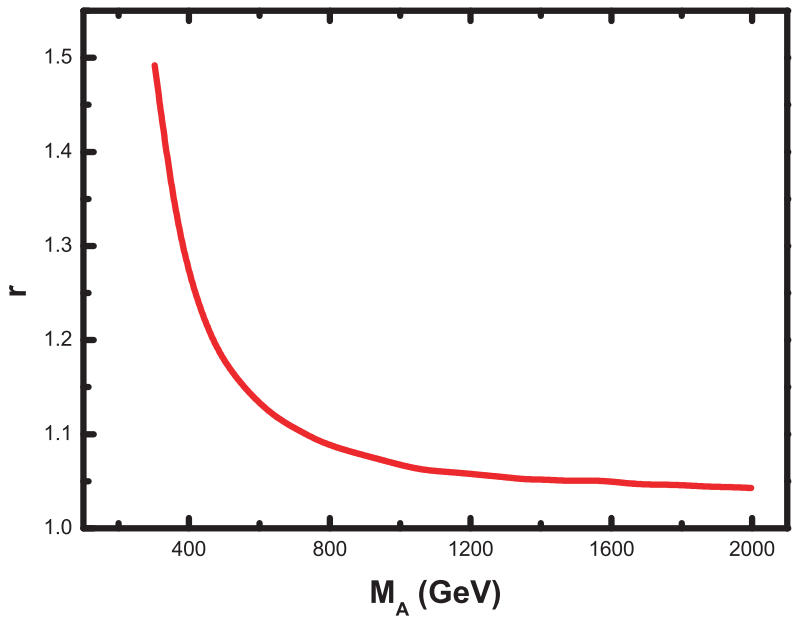

Figure 4.3: *The central value of M_A corresponding to the central value of a prospective r measurement is shown for the SPS 1a scenario. This relation between r and M_A would be obtained if all experimental and theoretical uncertainties were negligible (see text).*

the experimental result at the ILC allows to set indirect bounds on the heavy Higgs-boson mass M_A. Assuming a certain precision of r, Figure 4.3 therefore allows to read off the best possible indirect bounds on M_A as a function of M_A, resulting from neglecting all other sources of uncertainties. This idealized case is compared with a more realistic situation based on the SPS 1a scenario in Figure 4.4.

For the experimental accuracy of r we consider two different values: a 4% accuracy resulting from a first phase of ILC running with $\sqrt{s} \lesssim 500$ GeV [70, 79], and a 1.5% accuracy which can be achieved from ILC running at $\sqrt{s} \approx 1$ TeV [80]. In Figure 4.4 the resulting 1 σ bounds on M_A are shown (the corresponding value of r can be read off from Figure 4.3) for the experimental precisions of r of 4% and 1.5%, respectively, where the estimated experimental errors on the parameters $\tan\beta, m_{\tilde{b}_{1,2}}, m_{\tilde{t}_1}, m_{\tilde{g}}, m_h$, and m_t based on the SPS 1a scenario are taken into account. Also shown is the 1 σ error for $\Delta r/r = 1.5\%$ which would be obtained if all SUSY parameters (except M_A) were precisely known, corresponding to the idealized situation of Figure 4.3.

Figure 4.4 shows that a 4% accuracy on r allows to establish an indirect upper bound on M_A for the values up to $M_A \lesssim 800$ GeV (corresponding to an r measurement of $r \gtrsim 1.1$). With an accuracy of 1.5%, on the other hand, a precision on $\Delta M_A/M_A$ of approximately 20% (30%) can be achieved for $M_A = 600$ (800) GeV. The indirect sensitivity extends to even higher values of M_A. The comparison with the idealized situation where all SUSY parameters (except M_A) were precisely known (as assumed in Ref. [74]) illustrates the importance of taking into account the parametric errors as well as the theory errors

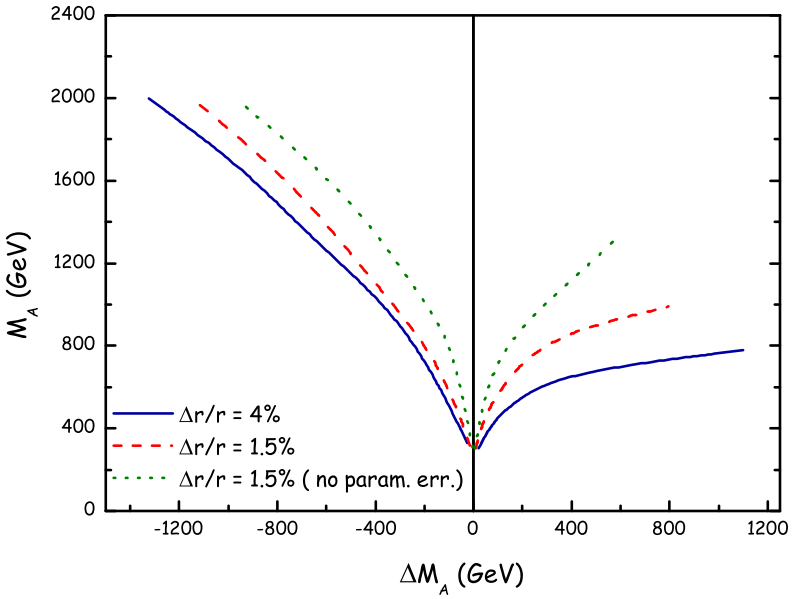

Figure 4.4: *The 1 σ bound on M_A, ΔM_A, versus M_A obtained from a comparison of the precision measurement of r (see text) at the ILC with the MSSM prediction. The results for ΔM_A are shown for a 4% accuracy of r (full line) and a 1.5% accuracy of r (dashed line). The parametric uncertainties in the prediction of r resulting from LHC/ILC measurement errors on $\tan\beta, m_{\tilde{b}_{1,2}}, m_{\tilde{t}_1}, m_{\tilde{g}}, m_h$, and m_t are taken into account. Also shown is the accuracy on M_A which would be obtained if these uncertainties were neglected (dotted line).*

from unknown higher-order corrections. Detailed experimental information on the SUSY spectrum and a precision measurement of m_t are clearly indispensable for exploiting the experimental precision on r.

4.2.2 Conclusions

We have investigated indirect constraints on the MSSM Higgs sector from measurements at LHC and ILC in the SPS 1a benchmark scenario.

In a scenario where LHC and ILC only detect one light Higgs boson (SPS 1a, where M_A is taken as a free parameter), indirect constraints on M_A can be established from combined LHC and ILC data. Taking all experimental and theoretical uncertainties into account, an indirect determination of M_A with an accuracy of about 20% (30%) seems to be feasible for $M_A = 600$ (800) GeV. In order to achieve this, a precise measurement of the branching ratios BR($h \to b\bar{b}$) and BR($h \to WW^*$) at the ILC and information on the parameters of the scalar top and bottom sector from combined LHC / ILC analyses will be crucial.

Chapter 5

LHC and ATLAS

5.1 Introduction to the Experiment

5.1.1 Large Hadron Collider

The Large Hadron Collider (LHC) [81] at CERN is a proton-proton collider currently under construction, and should be completed before 2007. It is built in the LEP tunnel. Two beams of protons will be accelerated in opposite directions in the 27 km long ring up to a beam energy of 7 TeV. Operation with heavy ions is foreseen as well. The beams, each containing 2808 bunches with $1.15 \cdot 10^{11}$ protons per bunch will collide at four interaction points, where the ATLAS, CMS, ALICE and LHCb experiments will be installed (see Figure 5.1). In the first few years of running, the LHC is expected to run under the low-luminosity condition of 10^{33} cm^{-2}s^{-1}, providing a luminosity of approximately 10 fb^{-1} per year. The final luminosity is expected to be 10^{34} cm^{-2}s^{-1}, i.e. 100 fb^{-1} per year.

The LHC is equipped with high-field superconducting dipole magnets. To bend 7 TeV protons around the ring, these dipoles must be able to produce fields of 8.36 T. Since two beams of particles with the same charge must be accelerated in opposite directions, two independent oppositely directed magnetic channels are needed. However, they will be housed in the same yoke and cryostat system.

The protons are obtained from a hydrogen source, and they are pre-accelerated in the LINAC (see Figure 5.1) to energies of 50 MeV. Then they enter the Proton Booster (PB) which increases their energy to 1.4 GeV. Further successive accelerations of the protons take place in the Proton Synchrotron (PS) and the Super Proton Synchrotron (SPS) to energies of 25 GeV and 450 GeV, respectively, before being injected into the LHC.

The main parameters of the LHC are listed in Table 5.1.

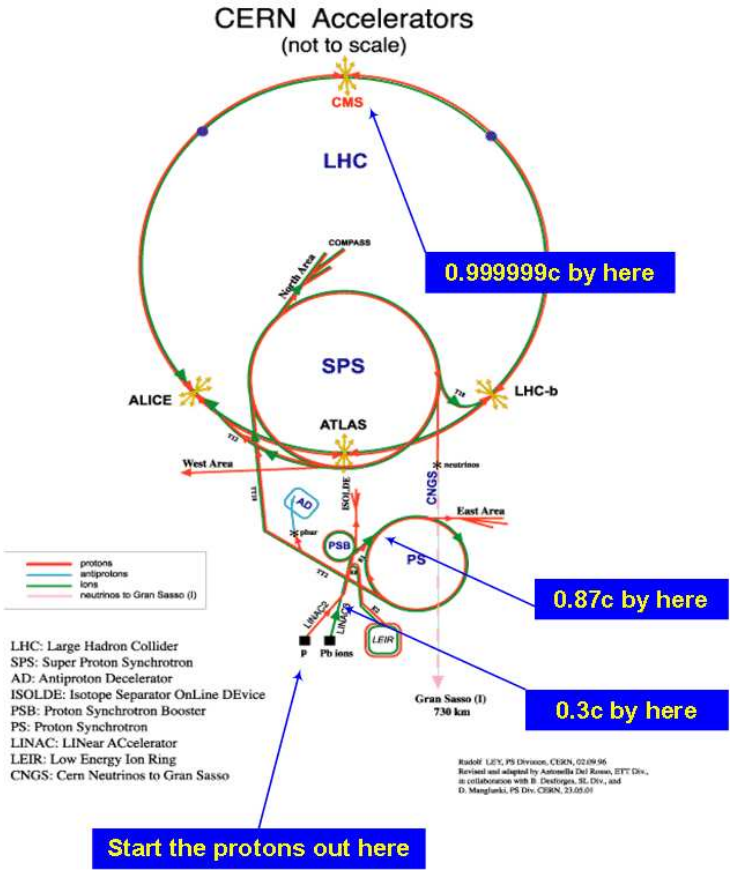

Figure 5.1: *Sketch of the LHC.*

	Value	Unit
Energy at collision	7	TeV
Energy at injection	0.45	TeV
Circumference	26.658	km
Dipole field at 7 TeV	8.36	T
Luminosity	10^{34}	$\mathrm{cm}^{-2}\mathrm{s}^{-1}$
Luminosity lifetime	10	h
Protons per bunch	$1.15 \cdot 10^{11}$	
Bunches per beam	2808	
Bunch spacing	25	ns
Distance between beams (arc)	194	mm
DC beam current	0.56	A
Energy loss per turn	7	keV

Table 5.1: *The main characteristics of the LHC.*

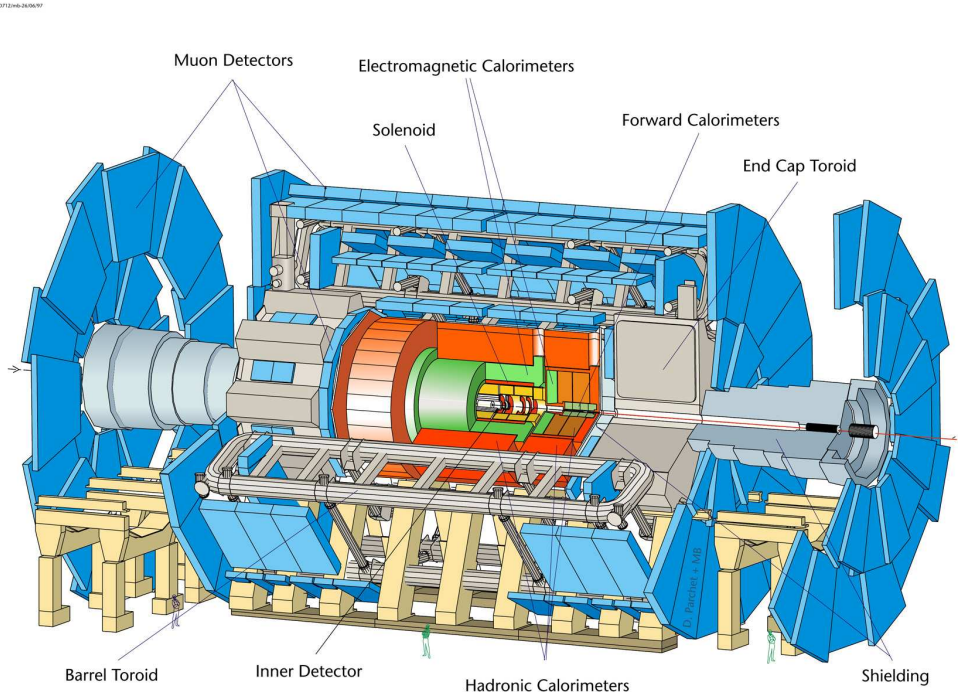

Figure 5.2: *An illustration of the ATLAS detector.*

5.1.2 The ATLAS Detector

The ATLAS[1] detector [82,83] is one of the four detectors at the LHC. It is an omni purpose detector, designed to explore the full physics program of the LHC. Other experiments are CMS [84], also an omni purpose detector, LHCb [85] dedicated to b-physics, and ALICE [86] dedicated to the study of heavy ion collisions.

The overall detector layout is shown in Figure 5.2. It has cylindrical symmetry with a diameter of 22 m and a length of 42 m. The proton beam direction defines the z-axis, while the xy-plane is transverse to the beam direction. The positive x-axis is defined toward the center of the LHC ring, and the positive y-axis is pointing upward. The azimuthal angle ϕ is measured in the transverse plane, and the polar angle θ is the angle from the beam axis. However, it is more common to use the pseudorapidity, defined as $\eta = -\ln\tan(\theta/2)$, than the angle θ. Then, the coordinate system is defined with (p_T, η, ϕ), where $p_T = \sqrt{p_x^2 + p_y^2}$ is the transverse momentum.

Trajectories of the charged particles are described by five helix parameters (the first three are in the xy-plane, and the last two in the Rz-plane) [83]:

- The reciprocal of the transverse momentum with respect to the beam axis, $1/p_T$.
- The azimuthal angle, ϕ.

[1] A Toroidal LHC ApparatuS.

- The transverse impact parameter, d_0, defined as the transverse distance to the beam axis at the point of the closest approach. It is signed according to the reconstructed angular momentum of the track about the axis.
- The cotangent of the polar angle, $\cot\theta$.
- The longitudinal impact parameter, z_0, defined as the z position of the track at the point of the closest approach.

The basic design criteria of the detector include the following:

- A very good electromagnetic calorimetry for the electron and photon identification and measurements, complemented by the full-coverage hadronic calorimetry for the accurate jet and missing transverse energy (E_T^{miss}) measurements.
- High-precision muon momentum measurements, with the capability to guarantee accurate measurements at the highest luminosity using the external muon spectrometer alone.
- An efficient tracking at high luminosity for the high-p_T lepton momentum measurements, electron and photon identification, τ-lepton and heavy-flavour identification, and the full event reconstruction capability at lower luminosity.
- Large acceptance in pseudorapidity (η) with almost full azimuthal angle (ϕ) coverage everywhere.
- Triggering and measurements of the particles at low-p_T thresholds, providing high efficiencies for the most physics processes of interest at LHC.

The detailed description of the detector sub-systems can be found in [82, 87, 88] and the main characteristics are described in the following sections.

5.1.2.1 The Magnet System

The ATLAS superconducting magnet system (Figure 5.3) consists of the central solenoid that provides the Inner Detector with the magnetic field, and the three large toroid systems (one barrel and two endcaps) that generate the magnetic field for the muon spectrometer.

The central solenoid provides a uniform 2 T field in the region $|\eta| < 2.5$. It is placed between the Inner Detector and the Electromagnetic Calorimeter.

The toroid magnet system is divided into one barrel part and two forward systems. Each of them consist of eight air-core superconducting coils. The large barrel toroid, with the peak magnetic field of 3.9 T, provides bending in the region $|\eta| < 1.3$, and the bending power, given by the field integral $\int Bdl$, ranges from 2 to 6 T-m. The endcap

toroid contributes 4 to 8 T-m of bending power in the region $1.6 < |\eta| < 2.7$. In the overlap region, $1.3 < |\eta| < 1.6$, the bending power is lower and strongly dependent on the azimuthal angle.

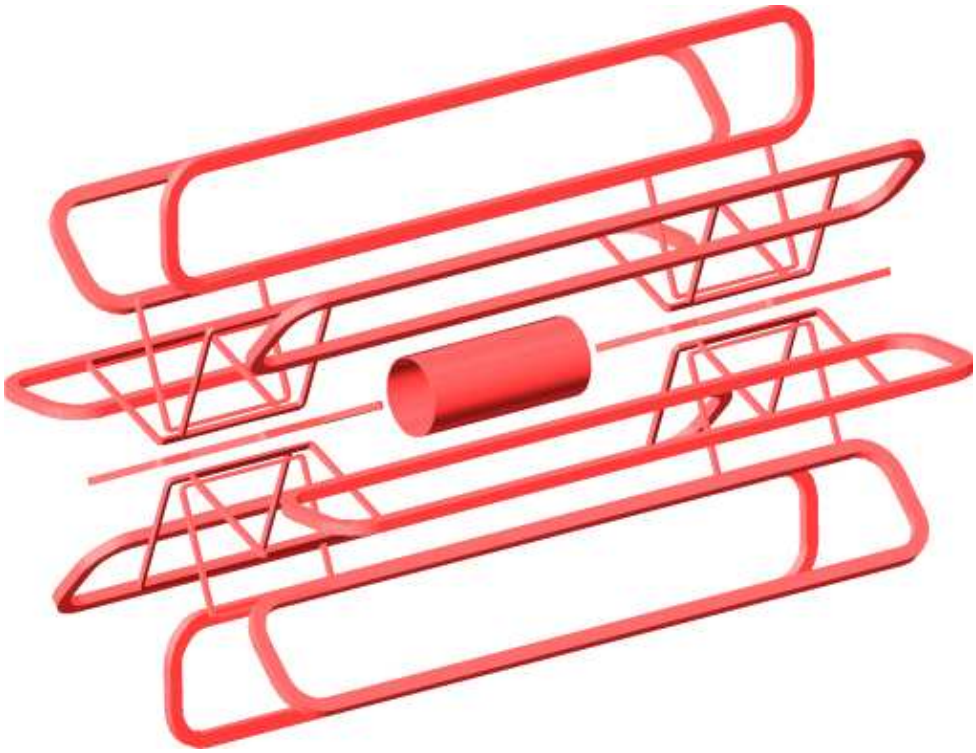

Figure 5.3: *An illustration of the magnet system for the ATLAS detector.*

5.1.2.2 The Inner Detector

The Inner Detector (ID) reconstructs tracks of charged particles and measures their momentum (above 0.5 GeV) from the tracks curvature in the magnetic solenoid field of 2 T. The ID is contained inside a cylinder of 7 m length and a radius of 1.15 m, covering an acceptance of $|\eta| < 2.5$. It is composed of three sub-detectors (Figure 5.4): a high resolution Pixel Detector (PD), a microstrip SemiConductor Tracker (SCT), and a Transition Radiation Tracker (TRT).

The concept was chosen to meet the demands of high-precision measurements of momentum and the reconstruction of vertices in the environment with a high track density. The main characteristics of the ATLAS inner detectors[2] are given in Table 5.2.

Pixel Detector (PD) The pixel detector provides a 3D measurement of tracks as close to the beam pipe as possible. This helps to identify tracks originating from secondary

[2]The parts of the Inner detectors that will be staged are: (1) Pixel Barrel Layer 1 located at a radius of 8.85 cm, (2) Pixel End cap disk located at $z = \pm 58$ cm, and (3) TRT C-Wheels.

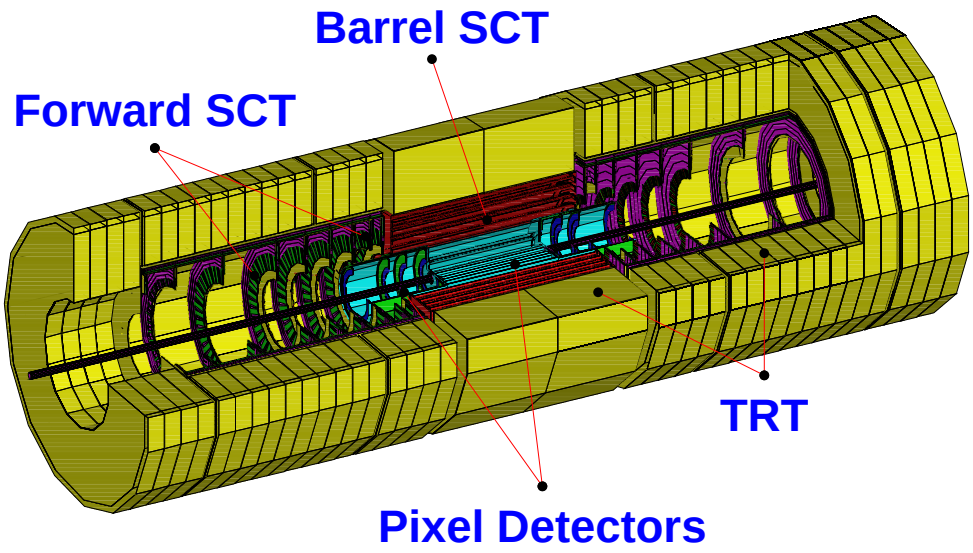

Figure 5.4: *An illustration of the ATLAS Inner Detector.*

vertices, and therefore, to tag jets containing B-hadrons. The detector consists of three barrel-like layers: B-layer located at a radius of 5.05 cm, Layer 1 at 8.85 cm and Layer 2 at 12.25 cm, and three disks on each side of the barrel located at $z = \pm 49.5$ cm, $z = \pm 58$ cm and $z = \pm 65$ cm. The system is designed to be highly modular, containing approximately 1500 barrel's and 700 disk's identical modules with dimensions 62.4×21.4 mm^2. Each pixel is 50μm wide in $R\phi$ and 300μm long. The PD provides a very high granularity set of measurements with 123 milion read-out channels. Due to the hostile environment, the chips must be radiation hardened to withstand over 300 kGy of ionizing radiation and over $5 \cdot 10^{14}$ neutrons per cm^2 over ten years of operation. The innermost pixel layer, B-layer, has been designed to be replaceable in order to maintain the highest possible performance throughout the experiment lifetime. Due to financial constraints barrel layer 1 and the intermediate endcap disks will be missing in the startup of ATLAS and will be installed later.

SemiConductor Tracker (SCT) The SemiConductor Tracker (SCT) is designed to provide four precision measurements per track. The barrel SCT provides precision points in the $R\phi$ and z coordinates with eight layers of silicon microstrip detectors (arranged in four pairs, each with the small stereo angle to obtain the z measurement). The two endcap modules are arranged in nine wheels covering region up to $|\eta| < 2.5$. In total, it consists of 61 m^2 of silicon detectors with 6.2 million readout channels. The spatial resolution is 16 μm in the $R\phi$ and 580 μm in the z direction.

Transition Radiation Tracker (TRT) The Transition Radiation Tracker provides a large number of measurements per track (36 on average). It is based on straw detectors, which can operate at very high rates. Electron identification capability is added by

employing xenon gas to detect transition-radiation photons created in a radiator between the straws. Each channel provides a drift time measurement with a spatial resolution of 170 μm. The barrel contains about 50,000 straws, each of them divided in two at the center[3]. They are arranged in three rings with a total of 73 layers, and grouped in modules with 329 to 793 axial straws, covering radii from 56 to 107 cm. The two endcaps contain 320,000 radial straws which are read at the outer radius. The endcaps consist of 18 wheels each. The wheels are grouped into wheel A (6 disks), wheel B (8 disks), and wheel C (4 disks). Due to financial constraints, wheel 'C' will be installed at later stage.

		Area (m^2)	Resolution $\sigma(\mu m)$	Channels ($\cdot 10^6$)	η coverage
Pixel	B-layer	0.2	$R\phi = 12$, $z = 66$	16	± 2.5
	2 barrel layers	1.4	$R\phi = 12$, $z = 66$	81	± 1.7
	3 endcap disks	0.4	$R\phi = 12$, $z = 77$	26	$\pm$(1.7-2.5)
SCT	4 barrel layers	34.4	$R\phi = 16$, $z = 580$	3.2	± 1.4
	9 endcap wheels	26.7	$R\phi = 16$, $z = 580$	3.0	$\pm$(1.4-2.5)
TRT	Axial barrel straws		170 per straw	0.1	± 0.7
	Radial endcap straws		170 per straw	0.32	$\pm$(0.7-2.5)

Table 5.2: *The main characteristics of the ATLAS Inner detector. B-layer and the 2 barrel layers from the Pixel detector are removable.*

5.1.2.3 The Calorimeters

The calorimeters primarily provide the energy measurement of the electrons, photons and jets, and allow for the calculation of the missing energy. They also provide information concerning the position and the angle, and allow, in certain cases, to identify the impinging particle. The ATLAS calorimeters (Figure 5.5) consist of an electromagnetic calorimeter (EMC) covering the region $|\eta| < 3.2$, a hadronic barrel calorimeter covering the region $|\eta| < 1.7$, hadronic endcap calorimeters (HEC) covering the region $1.5 < |\eta| < 3.2$, and forward calorimeters covering the region $3.1 < |\eta| < 5$. Hermetic calorimetry and a very good energy resolution for electrons and photons are essential for many searches.

Electromagnetic Calorimeter (EMC) The electromagnetic calorimeter (EMC) is a lead-liquid Argon (LAr) sampling calorimeter consisting of a barrel and two endcaps. The barrel consists of two half-barrels, separated by a 6 mm gap at $\eta = 0$. The EMC has an unusual accordion shape, shown in Figure 5.6, with Kapton electrodes and lead absorber plates. The incoming electrons lose energy in the lead absorbers and emit bremsstrahlung

[3]They are read out at each end.

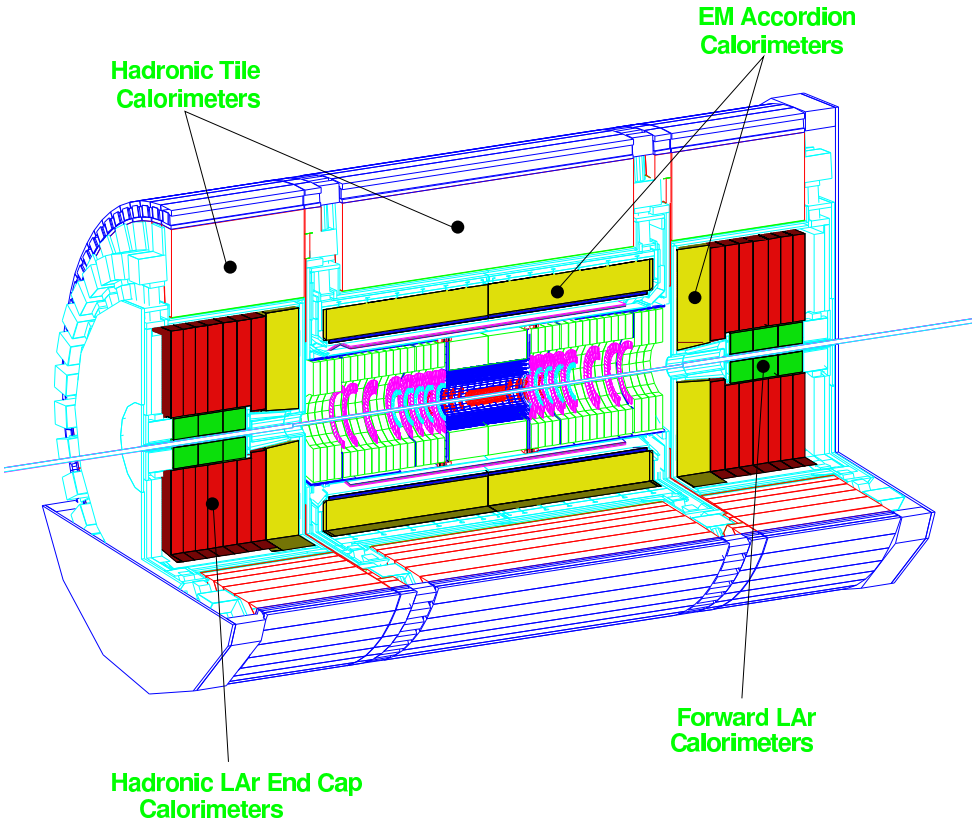

Figure 5.5: *An illustration of the ATLAS calorimeters.*

photons. The photons and electrons interact with the electric field of the lead nuclei and give rise to a dense electromagnetic shower. The secondary particles ionize the liquid argon. Free electrons from the ionization are drawn off to electrodes by a high-voltage field.

The total thickness of the EMC is $\sim$25 radiation lengths (X_0). The region $|\eta| < 2.5$ is segmented into three longitudinal segments. The innermost strip section which has constant thickness of $\sim 6X_0$ is equipped with narrow strips with a pitch of $\sim$ 4 mm in the η direction, leading to the granularity of $\Delta\eta \times \Delta\phi = 0.003 \times 0.1$ in the barrel region (see Table 5.3). This section acts as a preshower detector, enhancing particle identification (γ/π^0, e/π separation, etc.) and providing a precise position measurement in η. The middle section is segmented into square towers of $\Delta\eta \times \Delta\phi = 0.025 \times 0.025$. The total calorimeter thickness up to the end of the second section is $\sim 24X_0$, tapered with increasing rapidity (this includes also the upstream material). The back section has a granularity of 0.05 in η and a thickness varying between 2 and 12 X_0. For $|\eta| > 2.5$, i.e. for the endcap inner wheel, the calorimeter is segmented in two longitudinal sections and has a coarser lateral granularity than for the rest of the acceptance. This is sufficient to satisfy the physics requirements (reconstruction of jets and measurement of E_T^{miss}). The calorimeter cells point toward the interaction region over the complete η-coverage. In total there are nearly 190,000 readout channels.

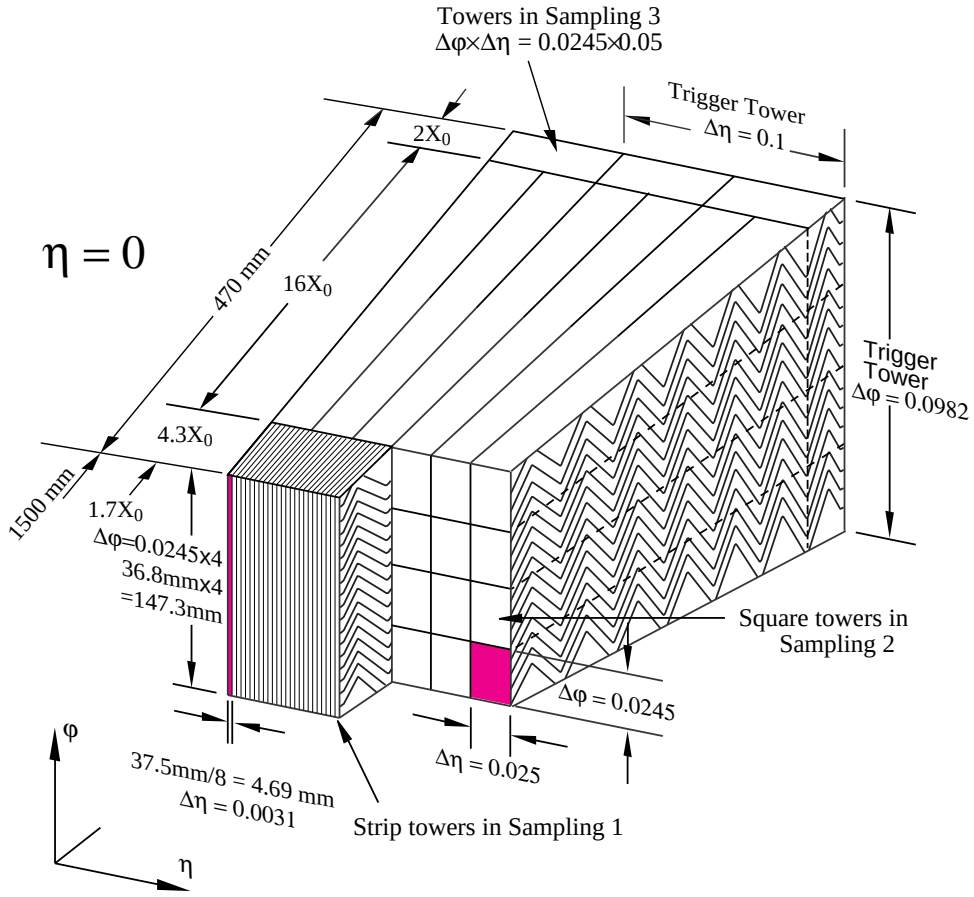

Figure 5.6: *An illustration of the ATLAS LAr electromagnetic calorimeters accordion structure.*

Because of $\sim 2.3X_0$ of material before the front face of the calorimeter, a presampler is used to correct for the up-stream energy loss. The presampler consists of a 1.1 cm and 0.5 cm active LAr layer in the barrel and endcap, respectively. In addition to the presampler, a scintillator slab is inserted in the crack region between the barrel and endcap cryostats ($1.0 < |\eta| < 1.6$). In total there are about 10,000 presampler readout channels.

The coverage, the granularity, and the segmentation of the EM calorimetry and the presampler are summarized in Table 5.3.

The design goal for the energy resolution is:

$$\frac{\sigma_E}{E} = \frac{0.1}{\sqrt{E}} \oplus \frac{0.3}{E} \oplus 0.01 \tag{5.1}$$

Hadronic Calorimeter The hadronic calorimeters are needed to measure the energy of the jets and hadronic particles in cooperation with the electromagnetic calorimeters.

The hadronic barrel calorimeter (Tilecal) is composed of a central barrel part ($|\eta| < 1.0$) and two identical extended barrels ($0.8 < |\eta| < 1.7$). It is based on an alternating

EM Calorimeter	Barrel	endcap	
Coverage	$\|\eta\| < 1.475$	$1.375 < \|\eta\| < 3.2$	
Longitudinal segmentation	3 samplings	3 samplings	$1.5 < \|\eta\| < 2.5$
		2 samplings	$1.375 < \|\eta\| < 1.5$
			$2.5 < \|\eta\| < 3.2$
	Granularity ($\Delta\eta \times \Delta\phi$)		
Sampling 1	0.003×0.1	0.025×0.1	$1.375 < \|\eta\| < 1.5$
		0.003×0.1	$1.5 < \|\eta\| < 1.8$
		0.004×0.1	$1.8 < \|\eta\| < 2.0$
		0.006×0.1	$2.0 < \|\eta\| < 2.5$
		0.1×0.1	$2.5 < \|\eta\| < 3.2$
Sampling 2	0.025×0.025	$0.025 \times 0.0.25$	$1.375 < \|\eta\| < 2.5$
		0.1×0.1	$2.5 < \|\eta\| < 3.2$
Sampling 3	0.05×0.025	0.05×0.025	$1.5 < \|\eta\| < 2.5$
Presampler	Barrel	endcap	
Coverage	$\|\eta\| < 1.52$	$1.5 < \|\eta\| < 1.8$	
Longitudinal segmentation	1 sampling	1 sampling	
Granularity ($\Delta\eta \times \Delta\phi$)	0.025×0.1	0.025×0.1	

Table 5.3: *The main characteristics of the ATLAS EM calorimeters.*

structure of a plastic scintillator plates (tiles) and an iron absorbers. Traversing particles initiate showers in the absorbers. The secondary particles excite the atoms in the scintillator which then emit light. The light is transmitted inside wavelength shifting fibers to photomultipliers which convert the light into an electronic signal.

The hadronic endcap calorimeter (HEC) is a copper-LAr detector with parallel-plate geometry covering the region up to $\eta = 3.2$.

The forward calorimeters (FCAL) ($3.1 < |\eta < 4.6$) also use a LAr, but with a high density design due to the high level of radiation they will experience. They consist of three sections. The first is made of copper and the last two are made of tungsten. The metal has longitudinal channels which house rods, which are at high positive voltage, and tubes which are grounded. The gaps are filled with LAr which serves as an active material. The presence of the forward calorimeters allows for detecting jets at large η, which is important, for instance, for the Higgs searches in the vector boson fusion channels, and for the measurement of the missing energy.

The characteristics of the hadronic and forward calorimeters are specified in Table 5.4. The design goal for the energy resolution is:

$$\frac{\sigma_E}{E} = \frac{0.5}{\sqrt{E}} \oplus 0.03 \tag{5.2}$$

Hadronic Tile	Barrel	Extended barrel	
Coverage	$\|\eta\| < 1.0$	$0.8 < \|\eta\| < 1.7$	
Longitudinal segmentation	3 samplings	3 samplings	
	Granularity ($\Delta\eta \times \Delta\phi$)		
Samplings 1 and 2 Sampling 3	0.1×0.1 0.2×0.1	0.1×0.1 0.2×0.1	
Hadronic LAr		endcap	
Coverage Longitudinal segmentation Granularity ($\Delta\eta \times \Delta\phi$)		$1.5 < \|\eta\| < 3.2$ 4 samplings 0.1×0.1 0.2×0.2	 $1.5 < \|\eta\| < 2.5$ $2.5 < \|\eta\| < 3.2$
Forward calorimeter		Forward	
Coverage Longitudinal segmentation Granularity ($\Delta\eta \times \Delta\phi$)		$3.1 < \|\eta\| < 4.9$ 3 samplings $\sim 0.2 \times 0.2$	

Table 5.4: *The main characteristics of the ATLAS hadronic calorimeters.*

5.1.2.4 The Muon System

The ATLAS Muon system provides both a precision muon spectrometer and a stand-alone trigger subsystem. The precision measurements, provided by the Monitored Drift Tubes (MDTs) and the Cathode Strip Chambers (CSCs), are made in a direction parallel to the bending direction: the z coordinate in the barrel and the R coordinate in the endcap. The trigger system covers the range $|\eta| < 2.4$ and consist of the Resistive Plate Chambers (RPCs) and the Thin Gap Chambers (TGCs). The trigger chambers must have a time resolution better than the LHC bunch spacing of 25 ns, and should provide triggering with well-defined p_T thresholds. In the endcap, where the bending power depends on ϕ, they should also provide measurement of the second coordinate in a direction orthogonal to the one measured by the precision chambers, with a typical resolution of 5-10 mm.

An illustration of the ATLAS muon system is shown in Figure 5.7, and the side view of one quadrant in Figure 5.8.

Muon precision system The precision measurement of the muon trajectories is realized by two types of chambers, Monitored Drift Tubes (MDT) and Cathode Strip Chambers (CSC). The MDTs are used in the barrel and are positioned at three cylindric layers in the barrel, located at radii of about 5, 7.5, and 10 m. MDTs (in the outer ring) and CSCs (in the inner ring) are used in the endcap region covering the range of $1 < |\eta| < 2.7$. They are located at distances of 7, 10, 14, and 21-23 m from the interaction point.

MDTs cover most of the η range. The chambers consist of aluminum tubes with a diameter of 3 cm. They are filled with a mixture consisting of 93% Argon and 7% CO_2

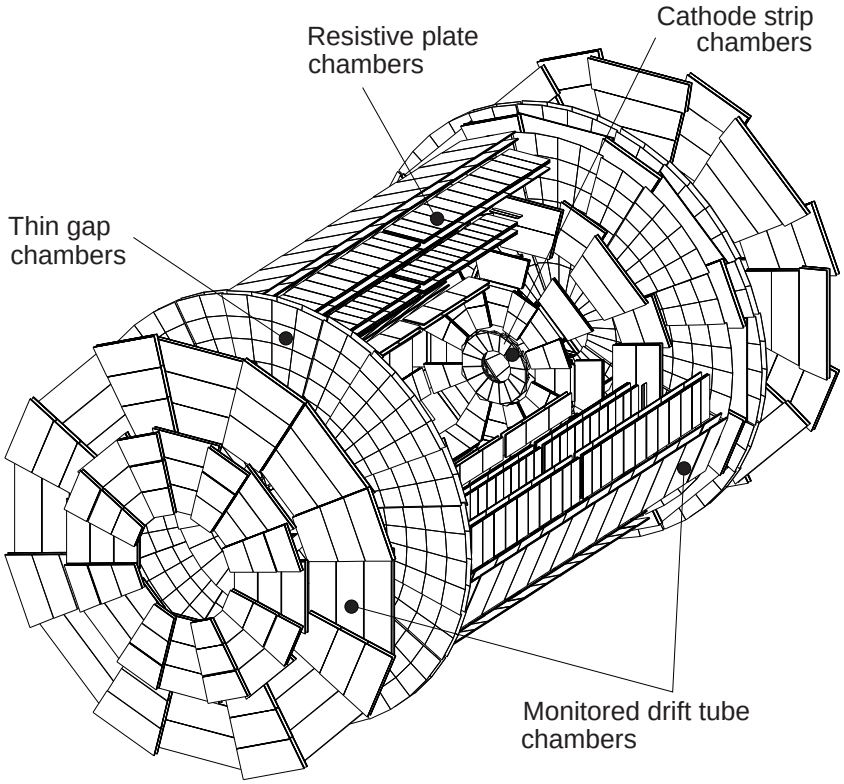

Figure 5.7: *An illustration of the ATLAS muon system.*

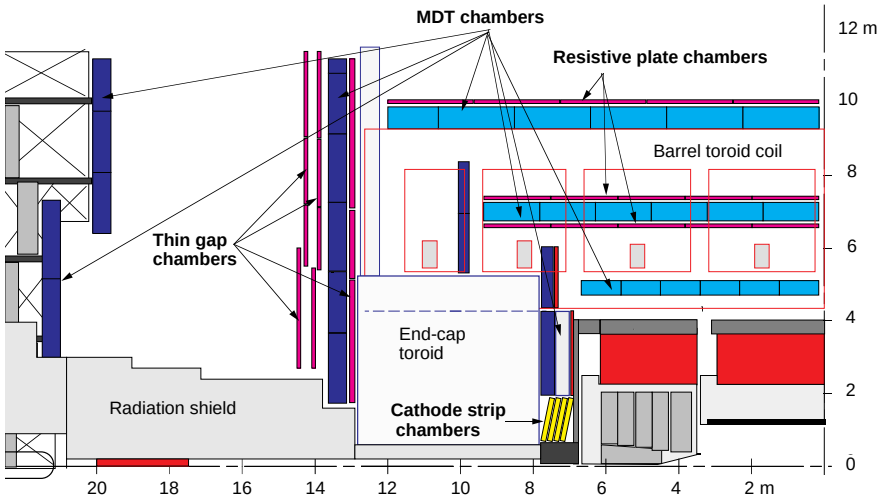

Figure 5.8: *Side view of one quadrant of the muon spectrometer.*

at a pressure of 3 bar. The 50 μm sense wire in the middle is made of tungsten-rhenium and provides a single wire resolution of ~ 80 μm. The total tubes volume is 800 m^3.

CSCs with a higher granularity are used in the innermost plane and cover $2 < |\eta| < 2.7$,

where large rates and backgrounds put high demands on the system. They are multi-wire proportional chambers with anode wires made of tungsten-rhenium. The segmented cathode strips and charge interpolation between neighboring strips provide good spatial resolution of 60 μm. The total of 1.1 m^3 gas volume is filled with 30% Ar, 50% CO_2, and 20% CF_4.

Muon trigger system Three layers of the Resistive Plate Chambers (RPC) provide trigger functionality in the barrel region. They are situated on both sides of the middle MDT layer, and inside the outer MDT layer. The Thin Gap Chambers (TGC) are used for triggering and the second coordinate determination in the endcaps. They are arranged in the three layers near the middle MDT layer.

The RPCs consist of two parallel resistive plates, separated by insulating spacers. The volume between plates is filled with a gas mixture based on $C_2H_2F_4$ with some small admixture of SF_6. An electric field of 4.5 kV/mm multiplies electrons originating from the ionization of the gas by traversing muons, via the avalanche effect. Quick response of the cells is requested for the trigger purpose, and the typical space-time resolution is 1 cm $\times$ 1 ns.

Most of the TGCs are produced at the Weizmann Institute of Science. Since part of this thesis is related to them, they will be described in section 5.2.

5.1.2.5 Trigger and Data Acquisition

The ATLAS trigger and data-acquisition (DAQ) system is based on the three levels of online event selection (Figure 5.9). Starting from an initial bunch-crossing rate of 40 MHz, the rate of selected events must be reduced to ~100 Hz for permanent storage.

The hardware based Level-1 trigger (LVL1) performs the initial event selection and reduces the rate to less than 75 kHz. It makes several initial selections, one of which is based on high-p_T muons in the RPCs and TGCs. Some of others are based on the reduced-granularity calorimeter signatures from all the ATLAS calorimeters (electromagnetic and hadronic; barrel, endcap and forward). The calorimeter trigger searches for various objects: high p_T electrons and photons, jets, and taus decaying into hadrons, as well as large missing and total transverse energy. In the case of the electron/photon and hadron/tau triggers, also isolation can be required.

The LVL1 identifies regions in the detector in which interesting activity may occur, so-called Regions of Interest (RoIs). Informations from all RoIs are combined and passed to the Level-2 trigger (LVL2), which applies a series of optimized selection algorithms to the event. The LVL2 trigger will reduce LVL1 rate from 75 kHz to ~1 kHz.

The Event Filter (EF) processes the output from LVL2 with more sophisticated reconstruction and trigger algorithms using tools similar to the offline software. The EF then takes the final decision if the event is discarded or written out. Level-2 trigger and

Event Filter form the High Level Trigger (HLT). The output rate from the HLT is of the order of 100 Hz, and selected events have an average size of ∼1.5 Mbyte.

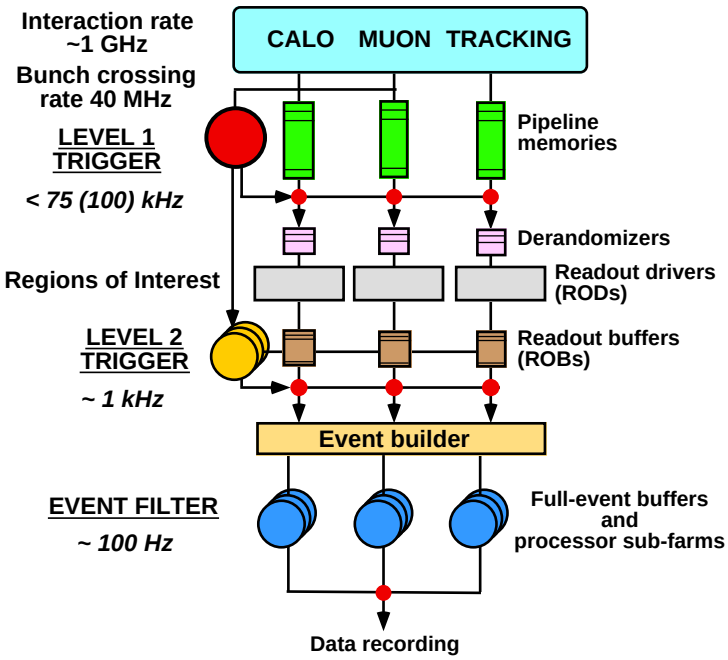

Figure 5.9: *A schematic view of the ATLAS trigger.*

5.1.3 Simulation of the ATLAS Detector

The complexity of the physics events to be analyzed at the LHC and the diversity of the detectors to be integrated into ATLAS make it an absolute necessity to provide an accurate detector simulation program, with which the detector and physics performance can be evaluated in detail. ATLAS has adopted an object-oriented approach to software, based primarily on the C++ programming language, but with some components implemented using FORTRAN and Java [89].

The Athena framework is an enhanced version of the Gaudi framework [90] that was originally developed by the LHCb experiment, but is now a common ATLAS-LHCb project. Major design principles are the clear separation of the data and the algorithms, and of the transient (in-memory) and the persistent (in-file) data. All levels of the processing ATLAS data, from the high-level trigger to the event simulation, reconstruction and analysis, take place within the Athena framework. In this way it is easier for code developers and users to test and run algorithmic code, with the assurance that all geometry and conditions data will be the same for all types of applications (simulation, reconstruction, analysis, visualization).

Figure 5.10 shows a simplified view of the processing stages in the simulation flow. Input for the simulation comes from event generators after a particle filtering stage. Data objects representing Monte Carlo truth information from the generators are read by the

simulation and processed. Hits produced by the simulation can be directly processed by the digitization algorithm and transformed into Raw Data Objects (RDOs). Alternatively they can be sent first to the pile-up algorithm and then passed to the digitization stage. RDOs produced by the simulation data-flow pipeline are used directly by the reconstruction processing pipeline.

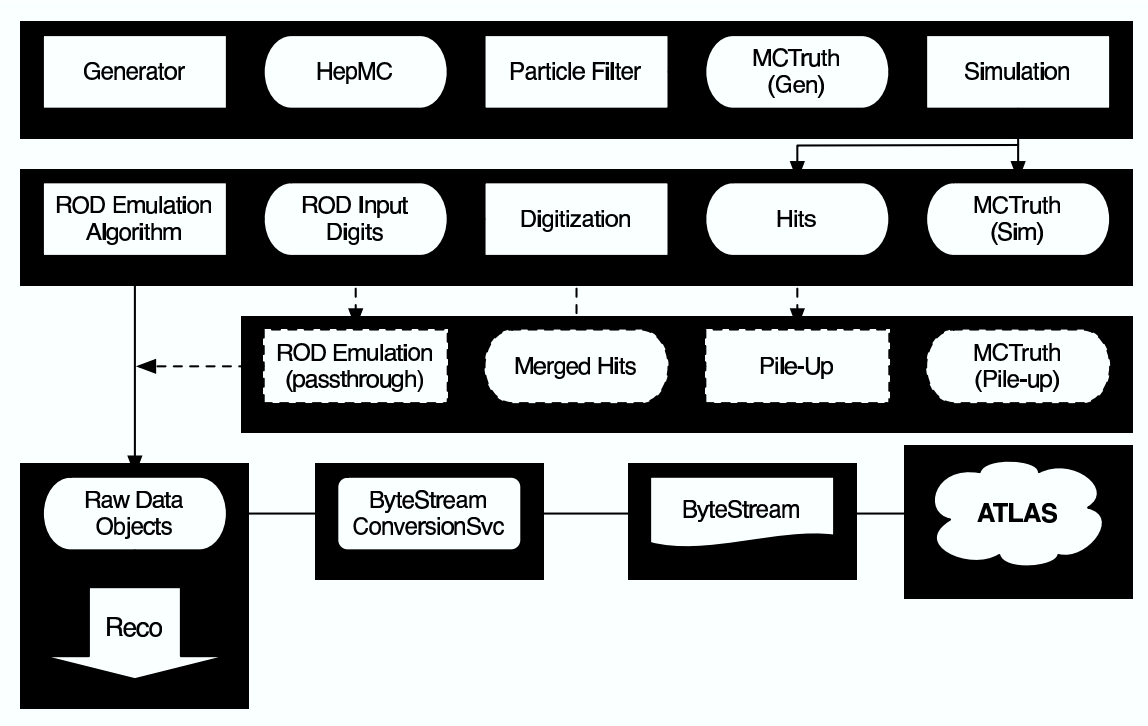

Figure 5.10: *A schematic view of the processing stages in the simulation data flow.*

5.1.3.1 Generators

Event generators are indispensable as tools for modelling of the complex physics processes that lead to the production of hundreds of particles per collision at LHC energies. They model the physics of hard processes, initial- and final-state radiation, multiple interactions, disintegration of beam remnants, hadronization of quarks and gluons, and decays of unstable hadrons. The current list of supported generators includes Herwig [58], PYTHIA [45], Isajet [91], Hijing [92], AcerMC [93], CompHep [94], AlpGen [95], Tauola [96], Photos [96], Phojet [52] and ParticleGenerator [97]. Some utility classes to enable filtering[4] of events and facilitate handling of Monte Carlo truth are also provided.

[4]Filtering is introduced in order to remove unwanted events already at the tree-level.

5.1.3.2 Full Simulation

The ATLAS detector simulation programs are heavily based on the GEANT3[5] and GEANT4 simulation packages and infrastructure [98]. The GEANT toolkit provides both a framework and the necessary functionality for running the detector simulation in the particle physics. The provided functionalities include optimized solutions for geometry description and navigation through a given geometry, the propagation of particles through detectors and modelling of their response, the modelling of physics processes in matter (e.g. a huge effort has been invested in recent years into the development and improvement of hadronic-physics models), visualization, and many more. A basic concept is that of Sensitive Detectors, which allows for the definition of an active detector elements, performs corresponding actions within them, and writes out hits (which may carry information like position, energy deposition, active element identification, etc.).

5.1.3.3 Digitization

The hits produced by GEANT need to be translated into the output that is actually produced by the ATLAS detectors. The propagation of charges (as in the tracking detectors and the liquid argon calorimeter) or light (as in the case of the tile calorimeter) into the active media has to be considered as well as the response of the readout electronics. Unlike the previous steps in the simulation chain, this is detector-specific task. The final outputs of the digitization step are Raw Data Objects (RDOs) that should resemble the real detector data. Digitization operates locally at the level of each sub-detector (e.g. a pixel module or a calorimeter cell), and the same code can be used in the context of the full ATLAS simulation, or a test beam.

5.1.3.4 Reconstruction

The role of reconstruction is to derive from the stored raw data the relatively few particle parameters and auxiliary information necessary for physics analysis: photons, electrons, muons, τ-leptons, K^0s, jets, missing transverse energy, primary and secondary vertices locations. Information from all detectors is combined such that the four-momentum reconstruction is optimal for the full momentum range, full rapidity range and any luminosity. The particles are identified with the least background, and with the understanding that the optimum between efficiency and background rejection can be analysis dependent.

As a part of this thesis an extensive effort in validating of the different reconstruction algorithms has been done. All Figures in the following paragraphs are done using $t\bar{t}H \rightarrow t\bar{t}\tau^+\tau^-$ events with a Higgs mass of 120 GeV (that will be discussed in section 5.4).

[5] Until the summer 2003.

Generation and simulation were done with the 9.0.4 Athena version, while version 10.0.1 was used for digitization and reconstruction[6].

Reconstruction consists of the following algorithms:

Tracking System Reconstruction A desirable feature for the tracking algorithm is the integration of all the tracking devices available at ATLAS under a single computer code, e.g. the tracking software should use the information provided by the muon chambers and drift tubes, the inner-detector transition radiation tubes and silicon detectors. The final output objects of the algorithm are the *Primary Vertex* and the *Track Particle*.

Calorimeter Reconstruction The two types of the calorimeters have different data formats at the raw data level. However, for the reconstruction purposes, one common calibrated input object is used, CaloCell. Neighboring CaloCells are used to produce calorimeter "towers". These towers (as well as cells) are then used to construct "clusters", i.e. collections of calorimeter elements. Electromagnetic clusters can be reconstructed using different algorithms: the *Sliding Window* [99] and the *Topological Clustering* [100].

Combined Reconstruction At this stage the information from different detectors is combined in an optimal way. The output is designed to support a wealth of tagging variables from different algorithms.

- **Photon/Electron Identification**

  Electron reconstruction is performed in two ways [101]. Candidates for high-p_T electrons are obtained by associating tracks to EM calorimeter clusters, and computing shower-shape variables, track-to-cluster association variables, and TRT hits variables. The characteristic variables for the electron identification are shown in Figures 5.11 and 5.12. In addition a *Likelihood* (Figure 5.13 (a)) and an *Artificial Neural Network*, ANN, (Figure 5.13 (b)) methods are applied. High-p_T photons are identified in a similar way, with the main difference being that the TRT is abscent, the track association is not there also and instead a track veto is imposed except for the reconstructed conversions.

  Soft-electron reconstruction proceeds by extrapolating a charged track to the calorimeter, and building a cluster around the charged-track impact point. This procedure has a better efficiency for electrons with p_T less than 10 GeV, and for electrons inside jets, which is pertinent for b-tagging.

  The p_T resolution for MC isolated[7] electrons is shown in Figure 5.14.

[6] This is so-called Rome production.

[7] Electron candidates are labeled as MC-isolated if they contain a true (tree-level) electron within a cone of 0.2, and if this true electron is isolated from other tree-level particles.

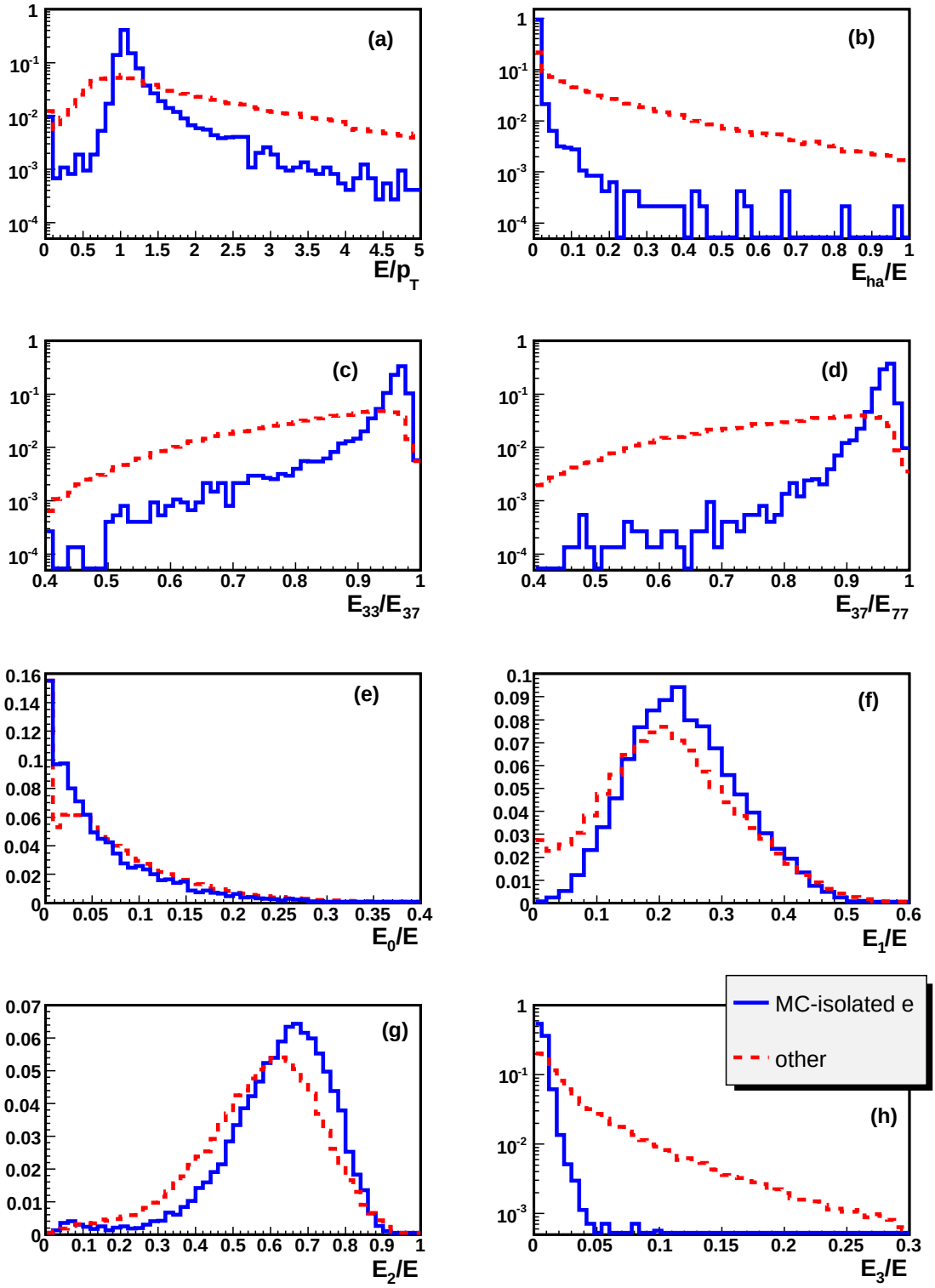

Figure 5.11: *Characteristic variables used for electron identification calculated from calorimetric quantities: (a) the ratio of the transverse energy measured in the calorimeter and the momentum measured by the inner detector (from tracking), E/p_T, (b) relative (to the total energy) energy leakage into the first sampling of hadronic calorimeter, E_{ha}/E, (c) the ratio of the uncorrected energies in 3×3 and 3×7 cells in the second sampling of the EM calorimeter, E_{33}/E_{37}, (d) the ratio of the uncorrected energies in 3×7 and 7×7 cells in the second sampling of the EM calorimeter, E_{37}/E_{77}, (e) the fraction of the total energy measured in the presampler, E_0/E, (f) the fraction of the total energy measured in the first sampling of the EM calorimeter, E_1/E, (g) the fraction of the total energy measured in the second sampling of the EM calorimeter, E_2/E, and (h) the fraction of the total energy measured in the third sampling of the EM calorimeter, E_3/E.*

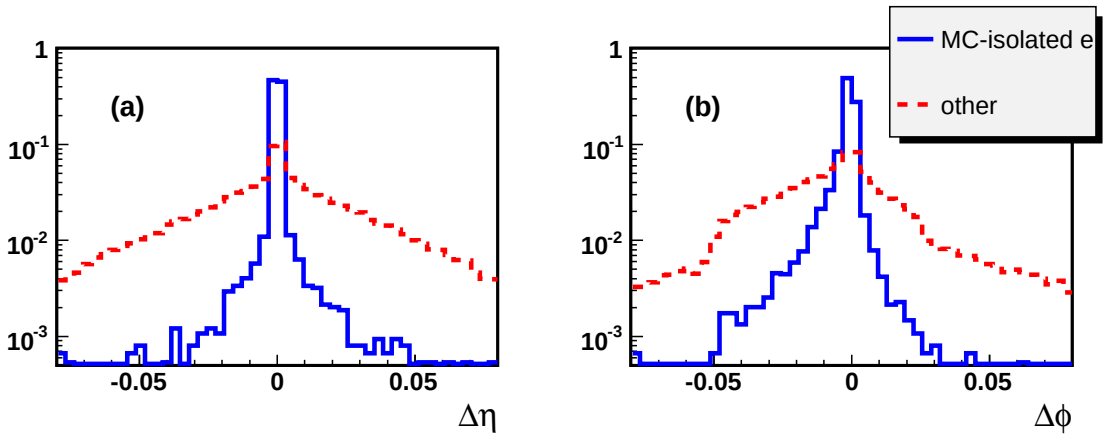

Figure 5.12: *Characteristic variables used for electron identification calculated from calorimetric and track quantities: (a) $|\Delta\eta| = |\eta_{strips} - \eta_{ID}|$, where η_{strips} is the position in the first sampling of the EM calorimeter, i.e. strips, and η_{ID} is the position in the inner detector, (b) $|\Delta\phi| = |\phi_2 - \phi_{ID}|$, where ϕ_2 is the position in the second sampling of the EM calorimeter, and ϕ_{ID} is the position in the inner detector.*

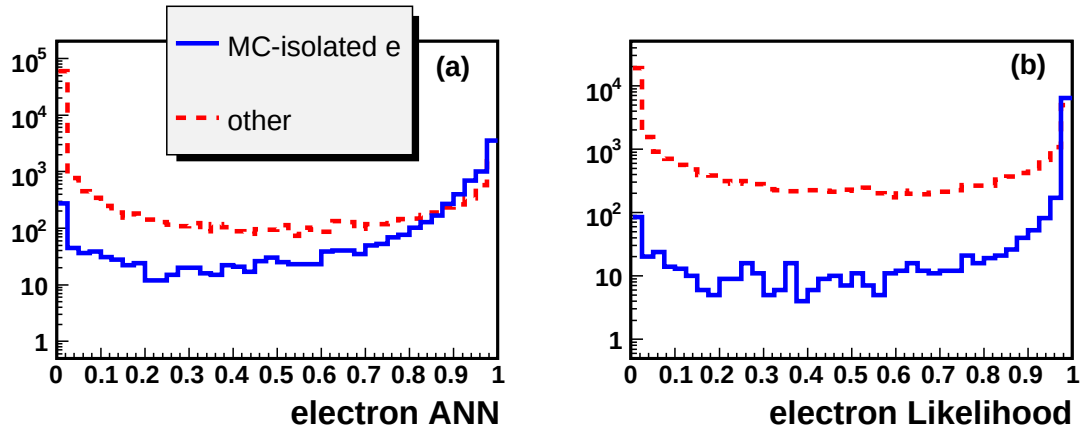

Figure 5.13: *The ANN (a) and likelihood (b) output used for the electron identification.*

- **Muon Identification**

  High-p_T muons (> 100 GeV) are measured by extrapolating the muon spectrometer track parameters inward to the interaction point through the calorimeters and the inner tracker. The extrapolation of the muon trajectory to the inner detector track allows for computing the energy loss through the intervening material. This can be applied to correct the muon momenta and recompute it at the interaction point. Furthermore, the direct measurement of catastrophic energy loss[8] (important at high p_T) can be used to correct the muon momentum.

  For muons in the 6-100 GeV p_T range, momentum determination is performed by

[8]Muons traveling through the matter lose energy due to the ionization. At sufficiently high energies, the radiative processes become more important than the ionization. Beyond the critical energy (a few hundred GeV in iron), where radiative mechanisms dominate, the probability that a muon suffers severe or catastrophic energy loss increases.

both systems, the muon spectrometer and the inner detector. The muon spectrometer provides a flag that uniquely identifies the muon. For momenta below 30 GeV, the measurement resolution derives mostly from the inner tracker as the muon-spectrometer resolution is dominated by multiple Coulomb scattering.

For p_T between 3 and 6 GeV, muons lose a large fraction or most of their energy in the calorimeters, and do not cross the full muon spectrometer and therefore cannot be reconstructed there. In this case, muon tracks are found in the inner detector and extrapolated to hit segments in the spectrometer [102].

The efficiency of the muon identification[9] as a function of p_T and η is shown in Figure 5.15. Except for the low p_T muons, the efficiency is $\gtrsim 80\%$ and it is flat as a function of the p_T. The efficiency as a function of η has a dip[10] around $|\eta| = 1.3$, and drops[11] for the $|\eta| > 2.$.

The p_T resolution for identified muons is shown in Figure 5.16.

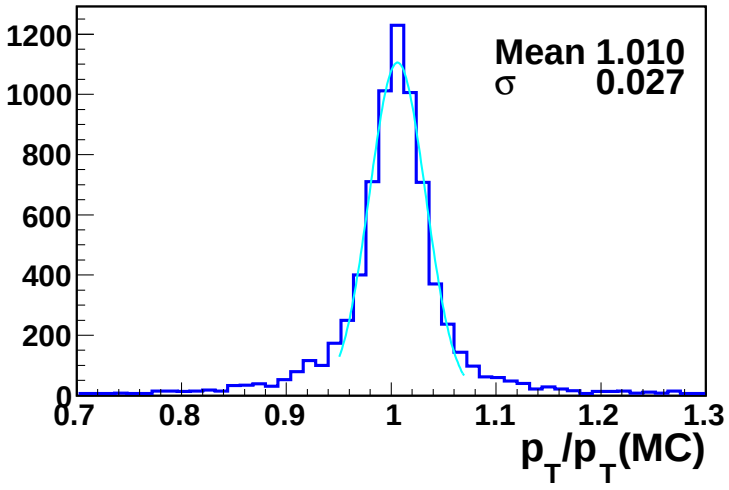

Figure 5.14: *The p_T resolution for MC isolated electrons with $p_T > 5$ GeV.*

- **Jet Reconstruction**

  Jets can be reconstructed from the detector signals, and, for the Monte Carlo information about the generated particles[12]. The available algorithms are the seeded and the seedless Cone, and the k_t algorithms [103, 104].

  Calorimeter jets can be calibrated in various ways. The standard calibration, i.e. H1-style, for jets is based on a cell-signal weighting scheme, where weights are

[9] We use combined muon identification for the high p_T (> 6 GeV) muons.
[10] This dip is due to the removed middle section in the endcap of muon spectrometer, i.e. EE chambers.
[11] These drops are due to the removed one (out of two) layer in the CSC in the endcap of muon spectrometer.
[12] These jets are called Truth jets.

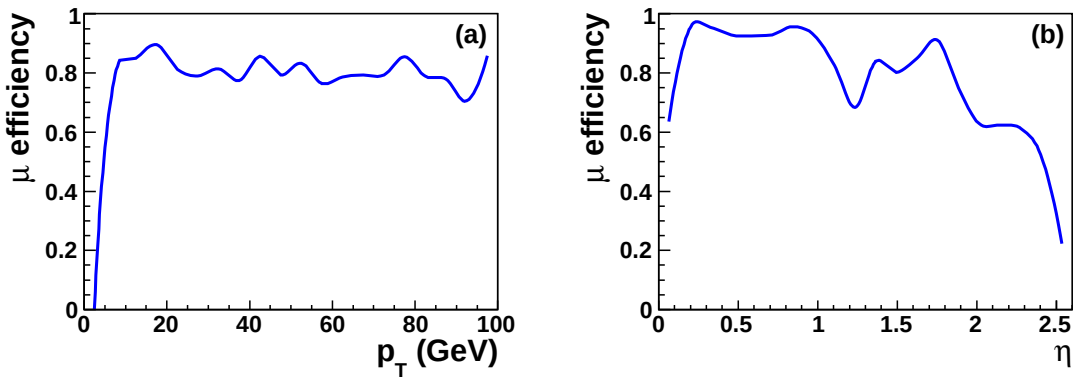

Figure 5.15: *The efficiency of muon identification as a function of p_T (a) and η (b).*

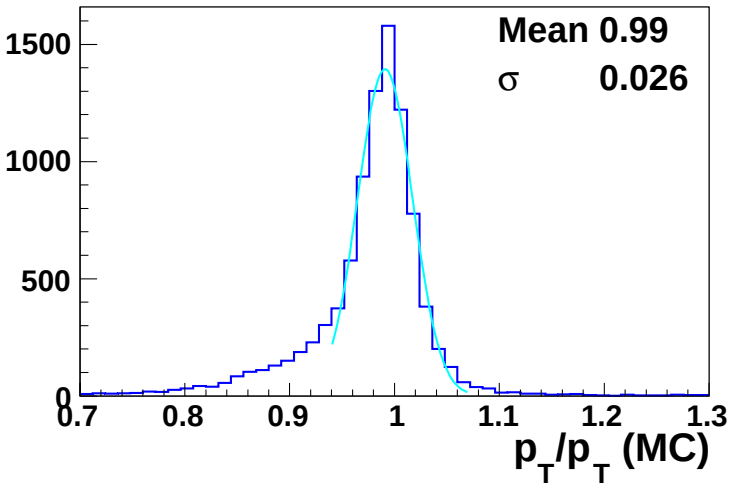

Figure 5.16: *The p_T resolution for identified muons with $p_T > 5$ GeV. The tail toward lower values is mostly due to the low p_T muons.*

applied to the signal contribution from each cell [105]. These weights have been computed such that the response to jets is flat over a large energy range, and using the constraint of an optimized energy resolution. p_T resolution for Cone jets with $\Delta R = 0.4$ and k_t jets is given in Figure 5.17.

Identification of the jets containing decay products from hadrons containing b-quarks, or b-tagging, requires jets with tracks. This implies that the calorimeter jets cannot be used directly. A new jet-object has to be constructed using track objects as well as calorimetric information. The relatively long lifetimes of B-hadrons can give rise to displaced vertices. The "secondary" vertices can be tagged by examining the impact parameters of the tracks in the jet. b-jets have a characteristic long, positive tail in the distribution of impact parameters; for the "light" jets (from the light quarks) one expects a symmetrical distribution. Another method is to explicitly reconstruct the secondary vertex using vertex-finding algorithms. If there are two or more tracks in the jet with a significant impact parameter, a secondary vertex

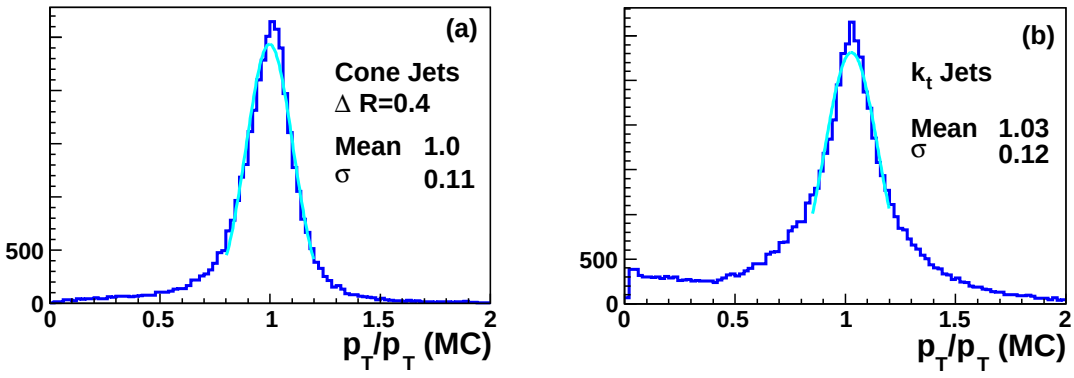

Figure 5.17: *The p_T resolution for reconstructed jets with the Cone (a) and k_t (b) algorithms. The tail toward lower values seen in (b) is due to the noise.*

can be searched. Properties of the secondary vertex, for example, the fraction of the jet energy and the reconstructed vertex mass, can be used to improve the discrimination of b-jets from "light" jets. In addition, "soft" leptons (from semi-leptonic decays of B-hadrons) can provide a limited but valuable complement to the spatial tagging. The results of all methods can be combined into one single discriminating variable in different ways, using different test-statistics and combination methods.

- **Tau Reconstruction**

  Hadronic τ-jet appears as a very narrow jet in the calorimeter with a small number of charged tracks. The τ reconstruction can be seeded by different types of calorimeter clusters, jets or by a charged track. τ identification is based on calorimeter quantities such as the radius of the electromagnetic shower, the isolation of the τ-jet in the calorimeters, the width in the strip section of EM calorimeter, and on quantities given by the tracker such as the number of associated tracks, the total charge and the impact parameters. Likelihood and multi-variate analysis techniques are used to discriminate τ-jets from normal QCD jets. The characteristic variables for the τ-identification are given in Figure 5.18 for labeled[13] and non labeled τ-objects. τ-jets are calibrated using the same cell-weighting scheme as jets.

  Throughout this thesis we are using Cone jets with $\Delta R = 0.4$ as seeds for τ-objects. However, we have checked if the performance of the τ-tagging would have been changed for different seeds. Eventhough the p_T spectrum differs (Figure 5.19), as well as the characteristic variables (shown for the Likelihood in Figure 5.20), the

[13] A jet is labeled as a τ jet if there is a τ Monte Carlo (MC) hadronic jet with transverse momentum $p_T > 10$ GeV and pseudorapidity $|\eta| < 2.5$ within $\Delta R < 0.3$ from the jet axis. A τ MC hadronic jet is a pseudo particle defined by the sum of all hadronic τ decay products. These definitions hold for both the fast and full Monte Carlo.

overall performance is similar. This is shown in Figure 5.21 for τ-tag efficiency (a), rejection againest other jets (b), and purity and contamination (c).

- **Missing Energy Reconstruction**
  The LHC is colliding protons that are composite particles. Only a fraction of the total energy of the proton is carried by the particle involved in the primary interaction. Thus, in order to compute the missing energy, only the conservation of momentum in the transverse (xy) plane can be used. The components of the missing momentum are defined as:

$$p_{x(y)}^{miss} = -\sum p_{x(y)}^{i}, \tag{5.3}$$

  where $p_{x(y)}^{i}$ is the $x(y)$ component of the visible object (calorimetric cell, cluster, or finite object[14]) momentum. The missing p_T is then:

$$p_T^{miss} = \sqrt{(p_x^{miss})^2 + (p_y^{miss})^2}. \tag{5.4}$$

  The missing energy is reconstructed from the energy deposed in all calorimeter cells and from the reconstructed muons momenta. A correction is applied for the energy loss in the cryostat between the electromagnetic and hadronic calorimeters.

  The calorimeter cell energy is weighted using the H1-style weights [105], depending on the cell energy density (E/V) and on the calorimeter region. For muons, only the reconstructed momentum from the chambers is used, to avoid double energy-counting in the calorimeters. The correction for the energy loss in the cryostat is calculated from the energy deposited in the cryostat by jets. To suppress the effect of noise in the calorimeters, a cell energy threshold in terms of the number of noise sigmas is applied.

  The missing energy can alternatively be reconstructed from the energy measured in the topologically clustered calorimeter cells. In this case the noise suppression is given by the thresholds applied in the topological clustering reconstruction.

  The obtained resolution is shown in Figure 5.22 for the missing energy calculated from the calorimetric cells (a) and from TopoClusters (b).

5.1.3.5 Fast Simulation

Since ATLAS is a huge and complicated detector, full simulations are very CPU intensive, in particular for events with high particle multiplicities[15]. Studies of the physics channels of interest and their associated background processes usually require the generation and

[14] Electrons, photons, muons, jets...
[15] For the channel $t\bar{t}H \to t\bar{t}\tau^+\tau^-$, studied in this thesis, $\sim$ 20 min is needed to simulate one event.

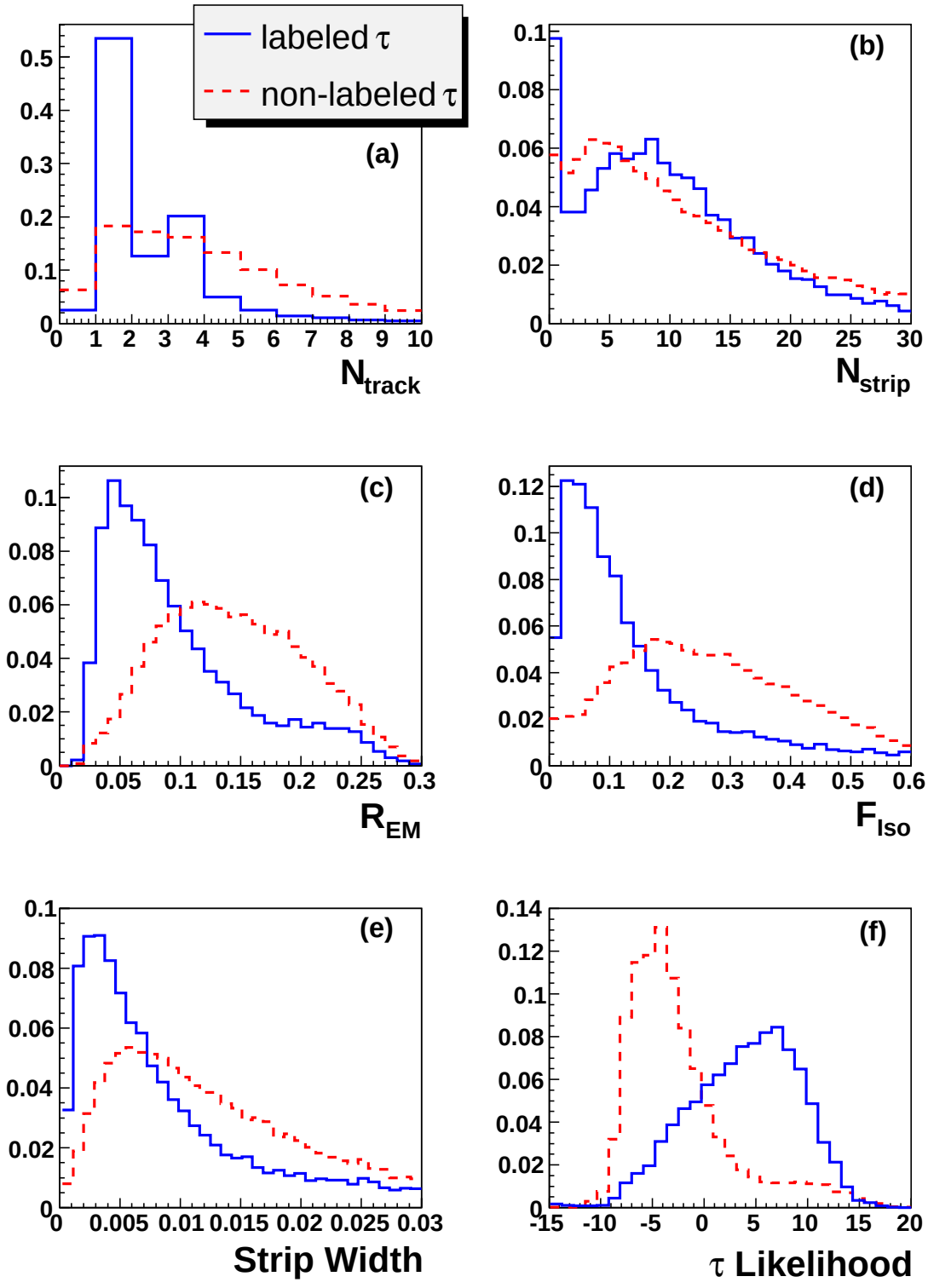

Figure 5.18: *Characteristic variables for the τ identification: (a) number of charged tracks, N_{track}, (b) number of hit strip cells, N_{strip}, (c) electromagnetic radius, R_{EM}, (d) isolation fraction, F_{Iso}, (e) strip width, and (f) τ likelihood.*

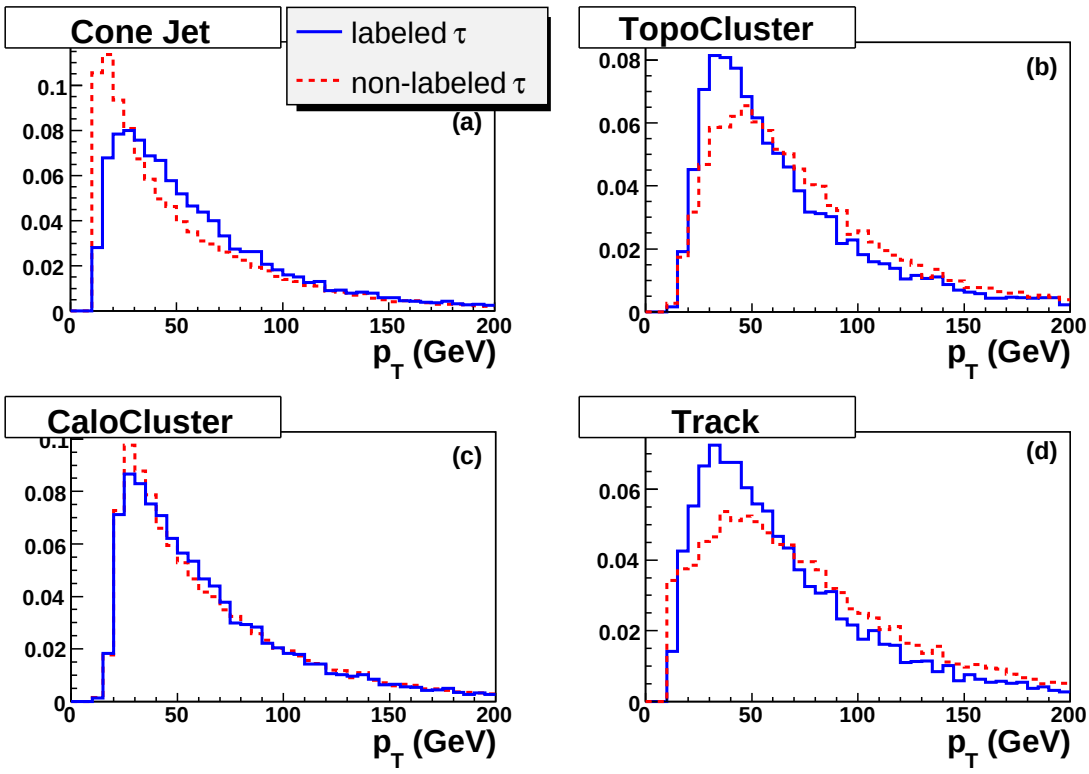

Figure 5.19: *Transverse momentum for labeled (blue solid line) and non labeled (red dashed line) τ candidate jets for different objects used as seeds: (a) Cone jets, (b) topological clusters, (c) calorimetric clusters and (d) isolated track.*

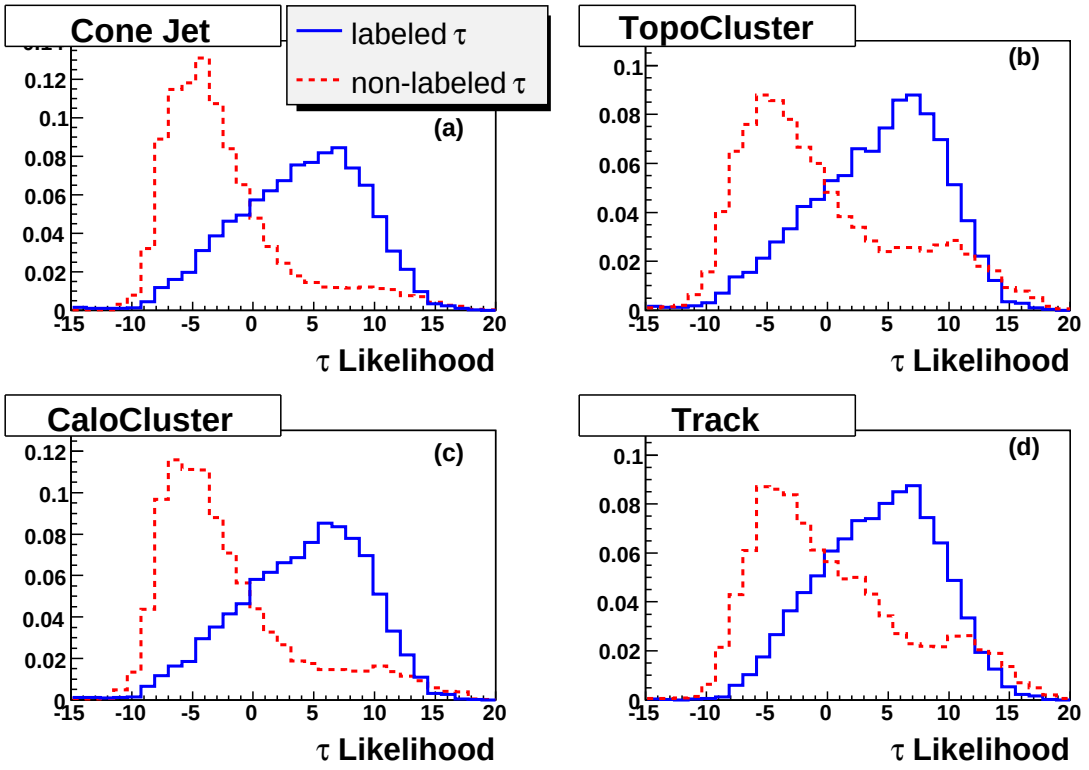

Figure 5.20: *Likelihood output for labeled (blue solid line) and non labeled (red dashed line) τ candidate jets for different objects used as seeds: (a) Cone jets, (b) topological clusters, (c) calorimetric clusters and (d) isolated track.*

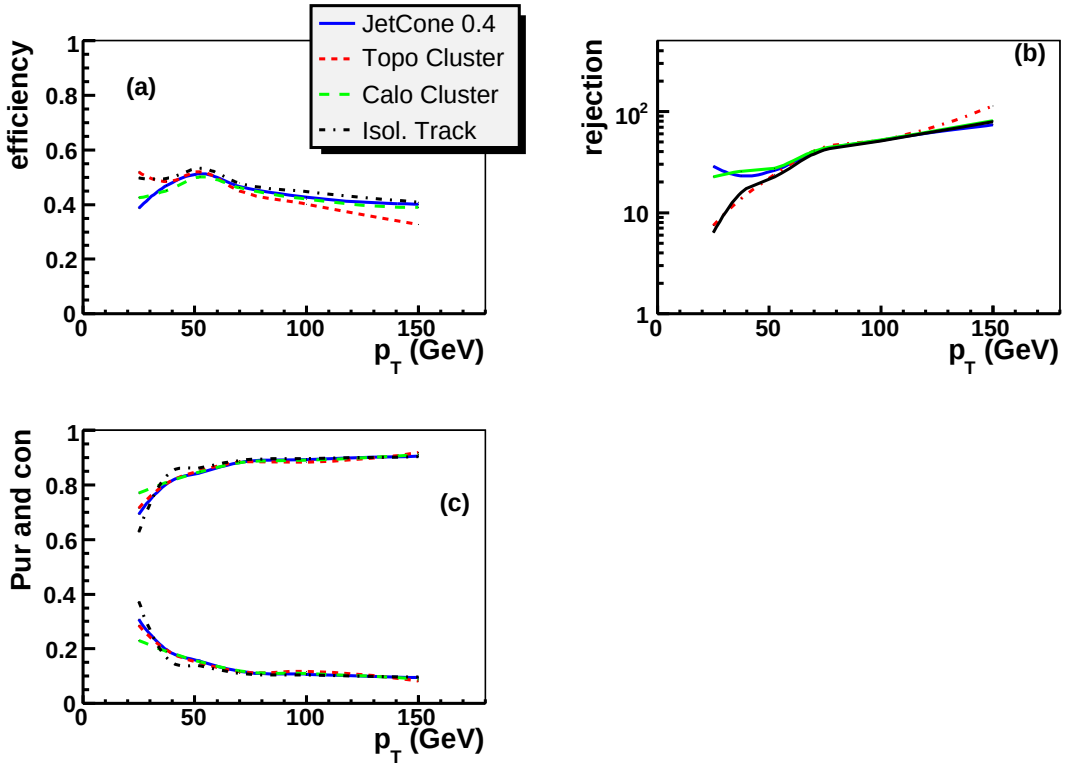

Figure 5.21: *The efficiency (a), rejection (b), and purity and contamination (c) for the τ identification for different objects used as seeds: Cone jets (blue solid line), topological clusters (red short-dashed line), calorimetric clusters (green long-dashed line) and isolated track (black dash-dotted line).*

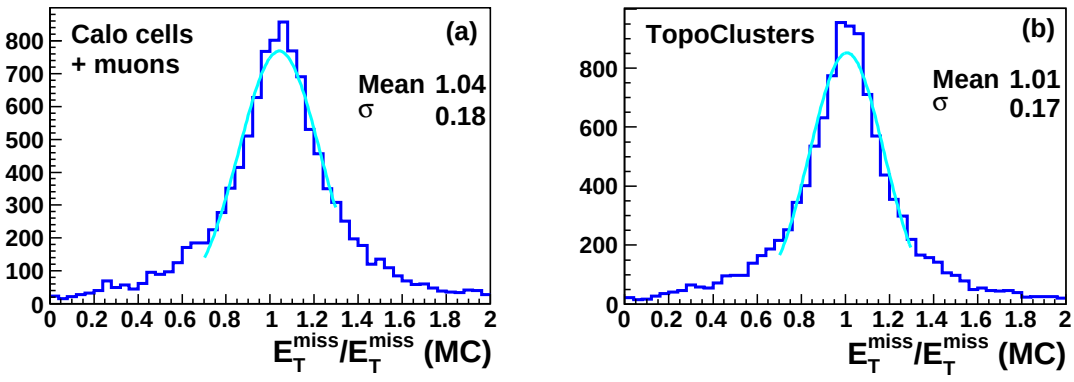

Figure 5.22: *The resolution of the missing energy reconstructed from the calorimetric cells (a) and topological clusters (b).*

simulation of millions of events. This is not feasible with the full simulation of ATLAS detector. Therefore, a fast simulation, ATLFAST [106], was developed in which the detector response is parametrized as a function of p_T and η. Four-vectors corresponding to electrons, photons and muons are passed to the appropriate smearing function, and the resulting four-vectors are output for use by downstream physics analysis. The calorimeter response to the event is calculated by summing the transverse energy deposits by all the interacting particles.

Smearing is applied to the energy which has been deposited in the calorimeter cells. Then, several jet finding algorithms are applied and the resulting jet objects are output for further physics analysis. The jet momenta are recalibrated by a calibration factor $K_{jet} = p_T^{parton}/p_T^{jet}$, where p_T^{parton} is the transverse momentum of the parton that initiated jet, and p_T^{jet} the transverse momentum of non-calibrated jets. Calibration factors K_{jet} are obtained from full simulation studies of the invariant masses m_{jj} in the $WH \to Wu\bar{u}, gg, b\bar{b}$ events.

Flavour tagging, i.e. b- and τ-tagging, has been done via parameterization from the full simulation studies. However, as we will show in section 5.3, using the parametrization for the τ-tagging might not provide good description to all the processes which are included in the analysis. For that reason, we have developed an algorithm for the τ-tagging within the ATLFAST (section 5.3) [16].

Other quantities calculated by ATLFAST are track helix parameters and global event quantities such as total E_T and missing momentum.

Recently, the FastShower [107] has been included in the ATLFAST. The FastShower library simulates the energy deposition in the towers of the ATLAS calorimeters, where the modelling of the deposition process includes two compartments in depth (electromagnetic and hadronic), and transverse shower spread. The correlation of energy deposition among neighboring towers is included.

5.1.4 Physics processes

The high energy and luminosity of the LHC offer a large range of physics opportunities, from the precise measurement of the properties of known objects to the exploration of the high energy frontier. The desire to probe the origin of the electroweak scale leads to a major focus on the Higgs boson. Other important goals are searches for other phenomena possibly related to the symmetry breaking, such as particles predicted by supersymmetry [32] or Technicolor theories [108], as well as new gauge bosons and evidence for composite quarks and leptons [109]. The investigation of CP violation in B decays [110] and the precision measurements of W and top-quark masses, and triple gauge boson couplings will also be important components of the ATLAS physics programme. This thesis deals with the Higgs physics which is briefly introduced below. Physics processes that can serve as background are also described.

5.1.4.1 Higgs Physics

In this section we will present the performance of the ATLAS detector in the searches for a Standard Model Higgs boson.

The Standard Model Higgs Boson The main production processes for the SM Higgs boson are [111]:

- **Gluon gluon fusion** (Figure 5.23 (a))
  This production process has the highest cross-section at LHC over total accessible mass range. The Higgs boson is produced in the fusion of the two gluons via the heavy quark loop. The loop is dominated by the top quark. QCD corrections can increase the cross-section of this process by more than 50%.

- **Vector boson fusion (VBF)** (Figure 5.23 (b))
  VBF is the second largest production mechanism of the Higgs boson at LHC. The Higgs boson is produced in the fusion of the weak bosons, $W^{\pm}$ and Z, which are radiated from the incident quarks. Eventhough the cross-section of the VBF become comparable with the gluon fusion for the Higgs masses beyond $\sim$ 700 GeV, this production process is important over total accessible mass range. The NLO corrections can increase the production cross section by about 10% and are thus small and under theoretical control.

- **Associated production with the weak bosons**, $W^{\pm}H$ and ZH, (Figure 5.23 (c))
  These production processes are significant for $m_H < 2m_Z$. Their cross-sections fall rapidly with the increase of m_H. QCD corrections increase the production cross sections by about 30-40%.

- **Associated production with the top quark**, $t\bar{t}H$, (Figure 5.23 (d))
  This production process (which is the subject of this theses) has a cross-section about five times smaller than the associated production $W^{\pm}H$ for $m_H < 200$ GeV. However, it is important because it provides the means for measuring the top-Yukawa coupling. QCD corrections increase the production cross sections by about 20-40%.

The cross-sections of these processes are given in Figure 5.24.

The Standard Model Higgs boson can be discovered at the LHC throughout the whole mass range starting at the experimental limit set by LEP, $m_H > 114.4$ GeV, and extending all the way to the theoretical upper bound ($\sim$ 1 TeV). On the other hand, the existence of the Higgs boson can be excluded after less than a year of the nominal planned luminosity. Expected significances for the Higgs boson discovery with the ATLAS experiment [83,112] are shown in Figure 5.25.

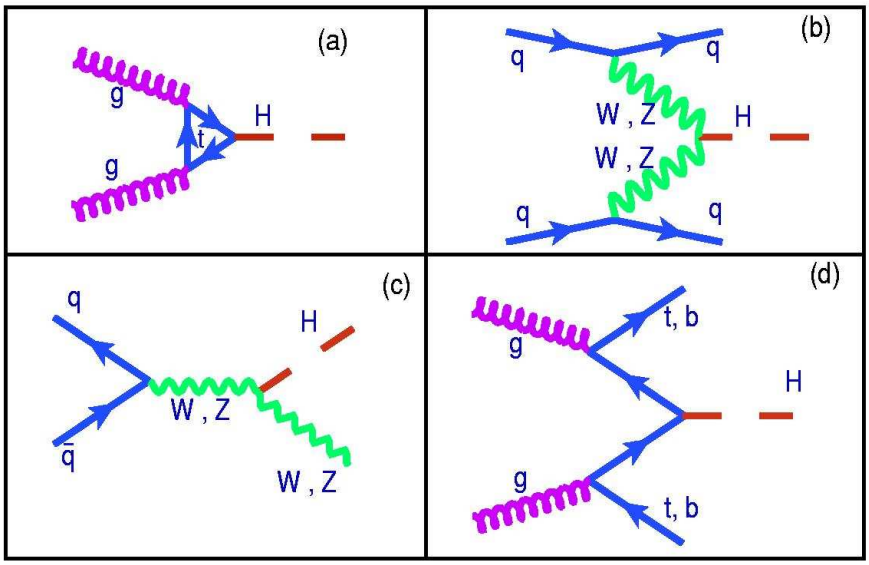

Figure 5.23: *Higgs boson production mechanisms at the LHC: (a) gluon gluon fusion, (b) vector boson fusion, (c) associated production with the weak bosons, and (d) associated production with the top quark.*

Precision measurements of the properties of Standard Model Higgs boson allow a deeper understanding of the electroweak symmetry-breaking mechanism [17,113,114,115]. In the majority of channels the Higgs boson appears as a resonant peak above the background, thus the background can be subtracted using the control regions outside the resonance. In these channels the mass can be measured directly. The Higgs boson mass can be measured with a precision of 0.1% up to masses of about 400 GeV. For higher masses, the precision deteriorates because the Higgs boson width becomes large and the statistical error increases. However, even for masses as large as 700 GeV, the Higgs boson mass can be measured with an accuracy of 1%. To achieve this precision, the absolute energy scale must be known to 0.1% for photons and leptons, and 1% for each jet. However, the ATLAS goal is to determine the absolute energy scale for photons and leptons with a precision of 0.02%.

Measurements of other properties, like coupling constants, branching ratios and the total width will be also possible at ATLAS. With an integrated luminosity of 300 fb^{-1}, the width of the Higgs boson can be measured with an error of $10\% - 20\%$, the production rates with $10\% - 20\%$, the relative branching ratios with $15\% - 45\%$, and the relative coupling ratios with $10\% - 20\%$.

The Standard Model Higgs boson is a CP even, spin 0 particle. For $m_H > 2m_{W^\pm}$ this can be tested by studying angular distributions and correlations among the decay leptons

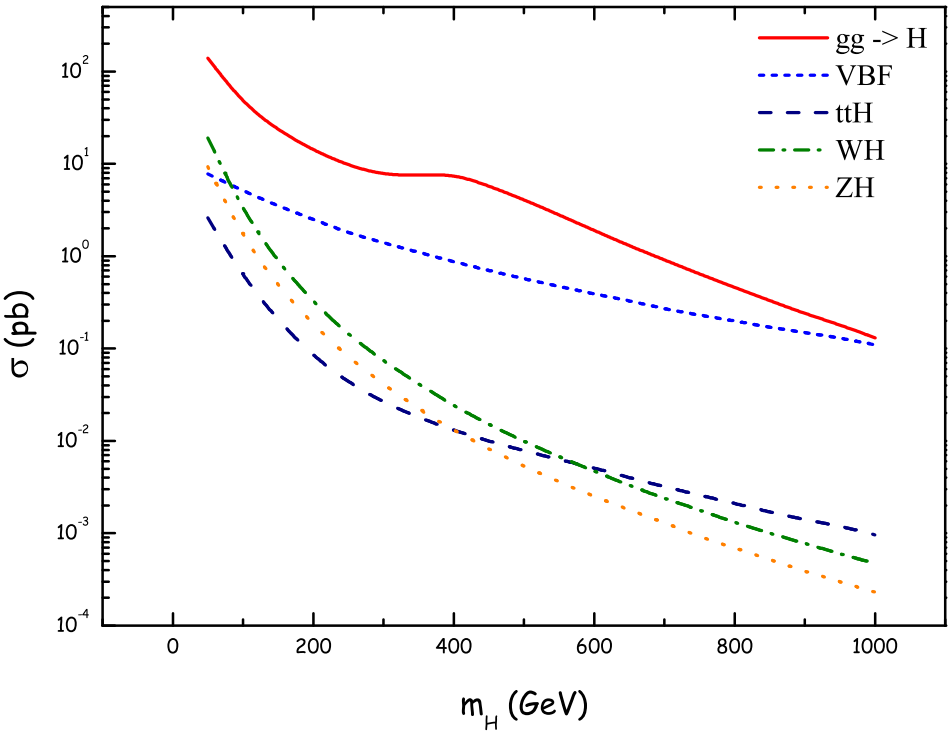

Figure 5.24: *The cross-sections of the Higgs boson production processes at the LHC [111].*

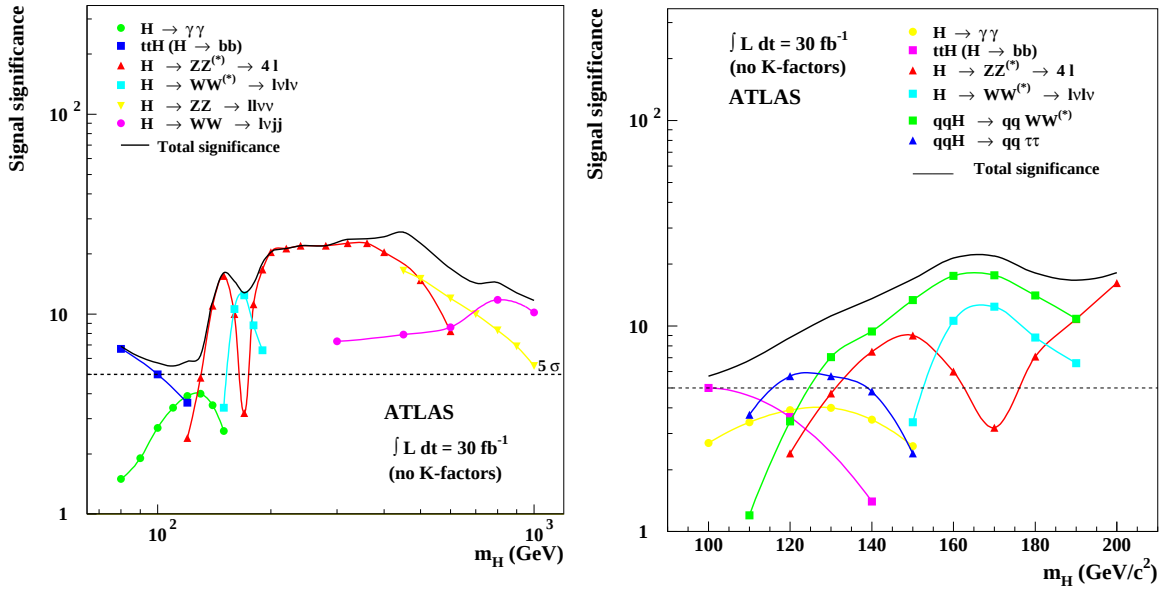

Figure 5.25: *ATLAS sensitivity for the discovery of the Standard Model Higgs boson for the* 30 fb^{-1} *for the whole mass range (left) [83], and for the Higgs masses* $\lesssim$ 200 *GeV with VBF channels included (right) [112].*

in the $H \to ZZ \to 4l$ channel [116]. For $m_H > 200$ (230) GeV a spin 0 CP-odd and a spin 1 (CP-even and CP-odd) Higgs boson can be ruled out at 2σ (5σ) level with an integrated luminosity of 100 fb^{-1}.

In the following, we will briefly present the search channels and strategies which are somewhat relevant to this thesis.

The $t\bar{t}H \to t\bar{t}b\bar{b}$ channel: In spite the fact that $BR(H \to b\bar{b})$ is the highest one for $m_H < 135$ GeV, searches with this decay mode are possible only with the associated production. In the gluon fusion process it is impossible to extract signal from the huge QCD background. In order to trigger the event, the presence of (at least) one isolated lepton is required, so one of the top quarks has to decay semi-leptonically. A crucial detector requirement is an excellent b-tagging. A significance ~ 3 [117] can be obtained after three years of run with low luminosity. This channel is expected to provide precision measurements of the Higgs mass, and top and bottom Yukawa couplings.

The $t\bar{t}H$ channel followed by $H \to \tau^+\tau^-$: $t\bar{t}H \to t\bar{t}\tau^+\tau^-$ channel will be very difficult to observe at the LHC. However, it could improve the measurement of the top-Yukawa coupling if the mass of the Higgs boson is close to the LEP limit. Being the subject of this thesis, it will be described in greater details in the following sections.

5.1.4.2 Background processes

In order to reduce the dependence of the analysis on theoretical uncertainties it is necessary to estimate the normalization of the most influential backgrounds from the measured data. That requires an excellent understanding of the involved SM processes.

- QCD processes represent a major part of the background to other Standard Model processes and to the signals of new physics at the LHC. Precise measurements and knowledge of these processes are therefore crucial.

- Gauge bosons and gauge-boson pairs will be abundantly produced at the LHC. The measurements related to the inclusive gauge boson production, gauge-boson pair production and gauge boson plus jet(s) production will, therefore, be important to understand. Also Z+jets production will be one of the main tools for the in situ calibration of the jet energy scale.

- The $t\bar{t}$ processes is among the most important backgrounds.

5.2 Thin Gap Chambers

The Thin Gap Chambers (TGC) [88] provide two functions in the end-cap of the ATLAS Muon Spectrometer:

- low and high transverse momentum muon trigger;
- the measurement of the second (azimuthal) coordinate which allows for the determination of the bending power of the magnetic field, and, therefore, is essential for the evaluation of the correct momentum measurement of the MDT.

The TGC chambers are being mounted on three wheels in each endcap. One wheel, with three detector layers (triplet), will be placed before the middle MDT station and two wheels, with two detector layers (doublet) each, behind it (see Figure 5.8). Additional two detector layers will be attached to the inner MDT station in the forward region. These two layers will provide the second coordinate measurement for the MDTs, and will not be used for the trigger.

The TGC wheels are segmented into sectors and rings. All component detectors have trapezoid shape with an average surface ~ 2 m^2. A cross section of the two types of TGC units (a doublet and a triplet) is shown in Figure 5.26.

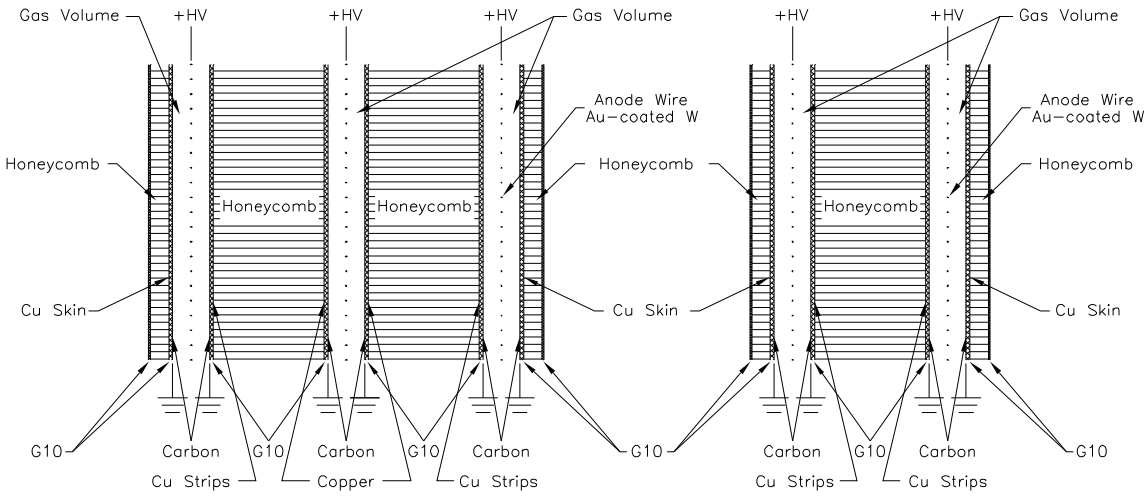

Figure 5.26: *A cross-section drawing of a TGC triplet (left) and doublet (right).*

As trigger chambers, the TGCs are required to have good time resolution in order to provide bunch-crossing identification. Good time resolution means assigning more than 99% of the triggered muons to the correct bunch-crossing. TGCs are also required to have fine granularity to provide a sharp cutoff in the momentum of the triggered muon. Fine granularity is needed since the trigger chambers can have only a relatively short lever arm of approximately 1 m. To match the geometric granularity to the needed momentum resolution, the number of wires in a wire-group varies, as a function of η, from 4 to 20

wires, i.e. from 7.2 to 36 mm in length in such a way that they cover regions with constant pseudorapidity. The alignment of the wire-groups in two (three) consecutive layers is staggered by half (third) of the group width. This achieves good position resolution with a smaller number of electronics channels. The required azimuthal granularity of 2-3 mrad is obtained by staggering the radial strips. The design described here satisfies the time, momentum, and azimuthal coordinate resolution requirements.

The TGCs are similar in design to multiwire proportional chambers, with the difference that the anode wire pitch is larger than the cathode-anode distance. First used on a large scale in the OPAL experiment (Sections 3.1.2.3 and 3.1.2.4), they are operated with a highly quenching gas mixture of 55% CO_2 and 45% n-pentane ($n - C_5H_{12}$).

Inside a 2.8 mm wide chambers, 50 μm thick gold-plated tungsten wires at distances of 1.8 mm are serving as anodes. They are parallel to trapezoid basis of the chamber. The detector walls, which serve as a cathode, are made of copper-plated G10 boards (the copper is outside the gas volume), coated (inside the gas volume) with a layer of high resistivity graphite that is electrically grounded. The copper on inner side of the detector wall is divided into strips (except for the middle detector of the triplet which is without strips) to provide ϕ-coordinate measurement. Distance between anode wires and cathode planes is 1.4 mm (see Figure 5.26). The operating voltage of $\sim$3 kV generates a strong field in the gas filled chamber. Charged particles passing trough the detector ionize gas molecules, then the free electrons drift to the anode wires generating an avalanche near the wire.

This type of cell geometry permits operation in semisaturated mode, with a number of advantages:

- small sensitivity to mechanical deformations, which is important to minimize the cost of large-area chambers;
- small dependence of the pulse height on the incident angle, up to angles of 40°;
- nearly Gaussian pulse height distribution with small Landau tails, and no streamer formation.

Two or three detectors are put together into a so-called units. In a unit, the detectors are separated using a 20 mm thick honeycomb paper layer, and they are protected by a 5 mm layer of paper honeycomb covered by 0.5 mm of G10 from outside. These layers, held by fiber-glass frames, provide the rigid mechanical structure for the detectors.

The TGC signals will be immediately processed by the on-board detector electronics. The coincidence matrices identify tracks in hit patterns and calculate the momentum from the curvature. If the requested trigger threshold momentum is exceeded, a signal is sent to the global level one trigger. If a bunch-crossing is accepted by the first level trigger, the TGC data will be read out.

Approximately 3600 TGC chambers will be installed in ATLAS. About 60% of these chambers have been produced in Israel - manufactured at the Weizmann Institute of Science and tested with cosmic radiation at the Technion or at Tel Aviv University. Other production facilities were at KEK in Japan (30%) and Shandong University in China (10%).

5.2.1 A Test Pulse System for the TGC Production

In this section the hardware part with which I was involved as a part of this thesis is described.

The thin gap of the gas in the detectors and the resulting strong electric fields inside set high requirements on the quality of the production process of the TGCs. The smallest deformation, material inhomogeneity or pieces of dust that were left inside can distort the signal and cause malfunctioning.

After testing the geometrical accuracy and the gas tightness of the chambers, the wires are put under high voltage for several days. If no leakage is discovered and no sparks are observed, the readout adapters are mounted on the chambers edges. In order to decouple the readout electronics from high voltage, capacitors are inserted on the wire channels.

The test pulse system has been built to verify the integrity of all electrical connections of the TGC units in the last step of production [118]. The system sends test pulses into the high voltage of the chambers and reads the capacitor charge discharge response signals through readout connectors. Typical errors like short circuits or missing capacitors can be detected. The test pulse system consists of a pulse generator, a signal multiplexer to cope with nearly 200 independent TGC channels, a computer oscilloscope to read and store the response signals, and a PC-based program to analyze and record the signals, and to control the device (outline is shown in Figure 5.27). A pulse generator produces rectangular signals with an amplitude of 15 V and a duration of 2.5 ms. Pulses are then transmitted to the detectors consecutively in order to avoid cross-talk. Groups of wires are connected to the high voltage input via a resistor of 10 Ω, and, on the readout end, they have capacitors of 235 pF.

Up to 16 channels, either wires or strips[16], are combined into an ASD[17] readout group, two for 32 strips and two to eight for the wires. The signals are transmitted through shielded multiwire cables to a multiplexer, which selects one strip and one wire signal at the time, amplifies and passes them to computer oscilloscope. The two-channel oscilloscope board, produced by Gage Applied INC. [119], has 128 kB memory and is plugged into the ISA bus of a regular PC. It is triggered, read out and controlled by a software that was designed for this purpose. The same software triggers the pulse generator and

[16]It is recommended that all the strips are measured in the same measurement.
[17]Amplifier Shaper Discriminator.

addresses the multiplexer (both are in the same external box) through standard I/O[18] board. The whole system is shown in the photo in Figure 5.28.

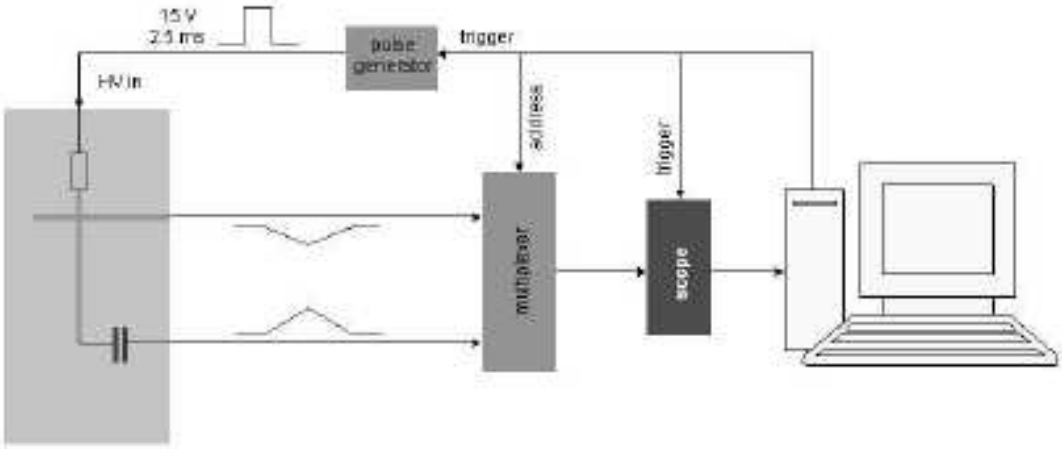

Figure 5.27: *Outline of the pulse test system for the TGC mass production.*

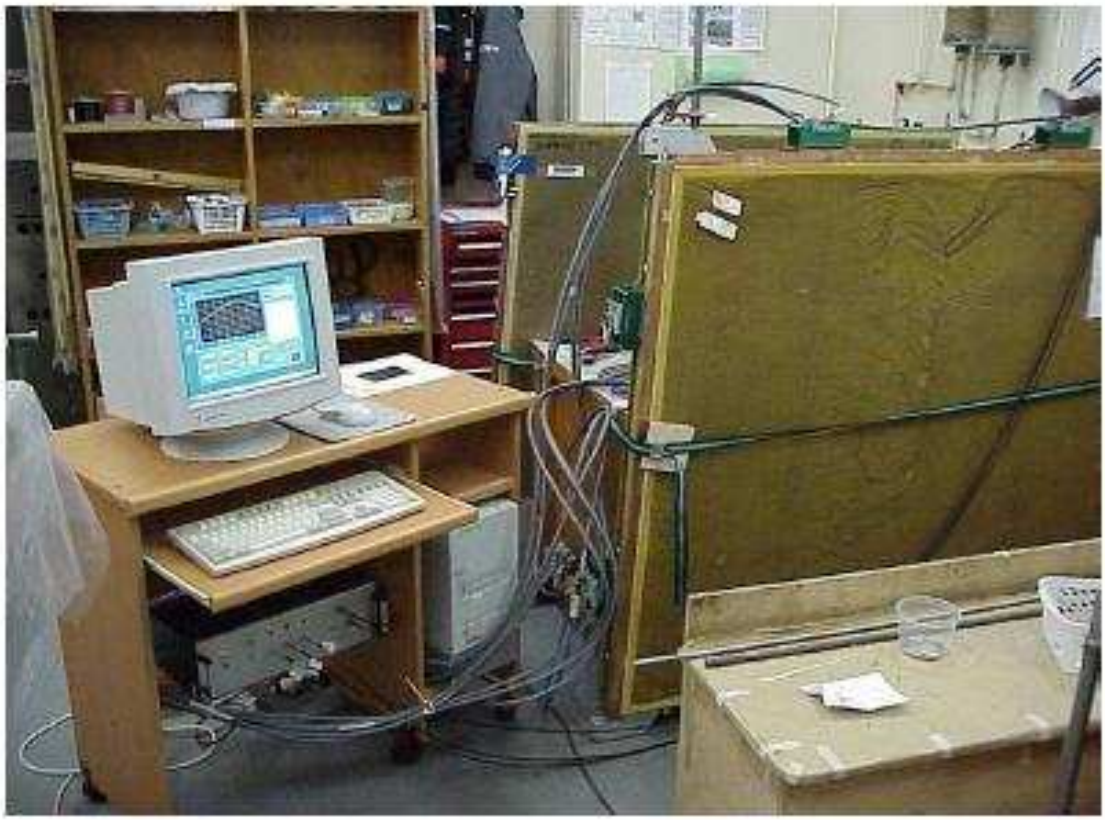

Figure 5.28: *A TGC triplet connected to one of the two pulse test systems that have been built for the quality control during the final assembly of electronic components.*

[18] Input/Output.

The TGC units are tested via a user interface (screenshot of the graphic interface is shown in Figure 5.29). Every unit has unique barcode that is read by the program, and, accordingly, corresponding configuration (the number of ASD readout groups, number of channels, calibration values) is read.

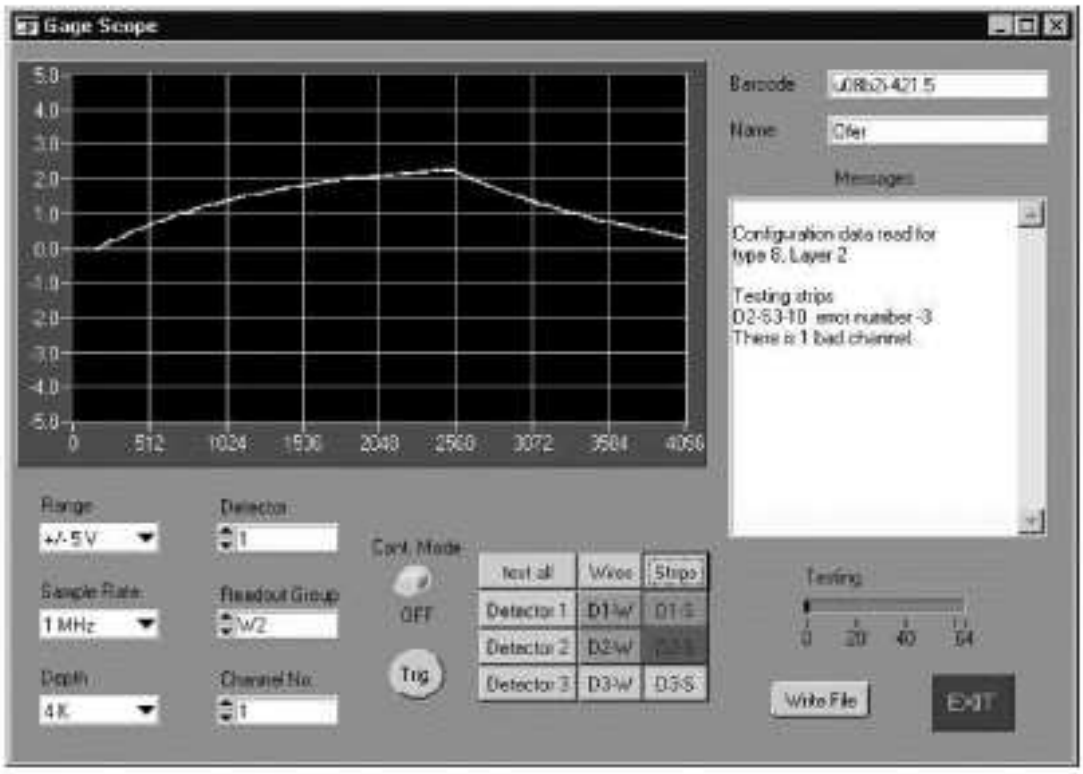

Figure 5.29: *The user interface for the test pulse station, showing the response of a wire channel to a square stimulus test pulse. The characteristic charge/discharge curve of the capacitor (which decouples the chamber wire) is shown on the display.*

The oscilloscope display (Figure 5.29) shows the amplified response of the signal of a wire group. The characteristic rise during the charge time is followed by the capacitor discharge curve. The capacitance in the circuit is inversely proportional to the voltage that the response reaches at the end of pulse stimulus. The peak height is used to detect shorted capacitors. As the capacity of a wire channel increases with the number of wires that it contains, the board groups of chambers in the outer rings yield smaller signals than the narrow groups closer to the center of TGC wheel. On the other hand, all strips have equal width within a detector, except the first and the last one that can be smaller. They carry the induced response signal of the perpendicular wire groups of the detector. Differences among the peak heights of the strips are not expected within one TGC unit.

It was found out that the essential information can be obtained by comparing the peak voltage of the signal with the default value. Due to the geometrical complexity of the chambers it is almost impossible to calculate the expected signal peak strength. Thus, an

average value of the peak strength taken over sufficiently big sample of tested units of the same type is taken to be the default value. Mean values are calculated separately for each wire channel, since the wire groups are not uniform in the number of wires throughout the detector. Wire signals are allowed to vary within ±10% around the default value. In addition, the voltage before the pulse is also measured.

Besides the strips on the edges, strip signals are equal within one detector. However, one detector may have strip signals twice as high as another detector. These differences originate from variations in the graphite resistivity, but they do not influence the performance of the chambers under operating conditions. Therefore, it is required that signal heights are equal (within ±20%) for all strips within one detector.

Several malfunctions of the system can be discovered using the test pulse system. If the voltage before the pulse differs from zero significantly (DC offset), those channels have an abnormal ground connection on the far side of the readout connectors. Shorted or missing capacitors increase the signal height, while ground leaks or unclean conductors can decrease it. No signal is observed in case of a severed conductor or a short to the chamber ground.

A test is completed if all channels have been successfully checked. An example of the signal peaks is shown in Figure 5.30. It shows an output of a good detector (a) and of a bad one (b). Different tints represent different units, while the maximum and minimum allowed value[19] are plotted with the dotted line. One can clearly see that all the good units are similar (as they should be), while every bad is bad in its own way.

[19] ±10% of the average value.

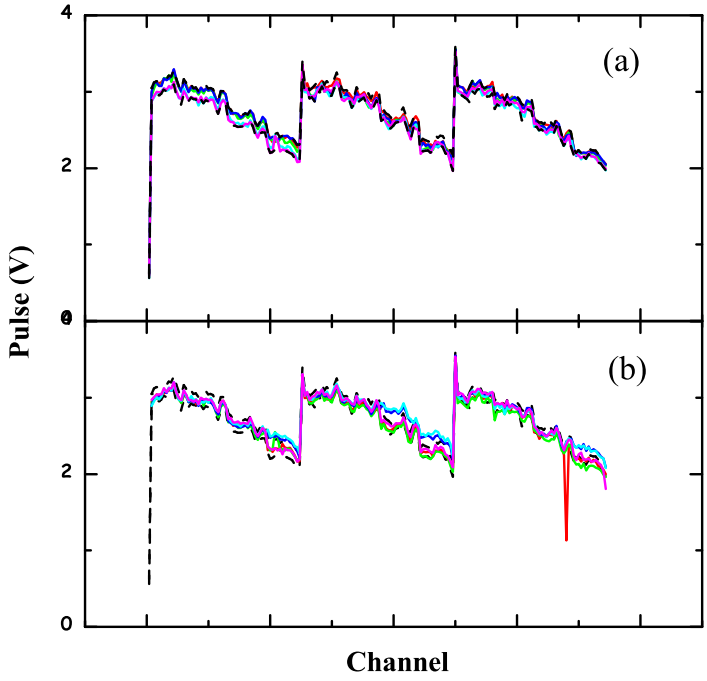

Figure 5.30: *High voltage test pulse output for the good (a) and bad (b) units. Different tints correspond to different units, while minimum and maximum allowed value is plotted with dotted line.*

5.3 An Alternative Algorithm for the Fast Tau Tagging

This section contains a description of one of the main subjects of this thesis.

5.3.1 Introduction

The need for an identification of τ-jets, i.e. jets originating in hadronic decays of τ-leptons, within the framework of fast simulation is apparent. With background processes like $t\bar{t}$ or QCD production which have huge cross sections, it becomes impossible to use full simulation in order to generate enough events to estimate the correct background rejection. One way to identify τ-jets within the fast simulation of the ATLAS detector is by parameterization [120, 121]. Parameterization by its nature is determined by the environment under which it was developed. The parameterization at the time of writing this thesis is taking into account the kinematics of the τ-jet (the dependence on transverse momentum and pseudorapidity), while the environment effects are currently under study (it should eventually lead to different parameterization for different processes) [121]. Consequently, using the parameterization might not be fully consistent with all processes involved in a given analysis. For that reason a different approach for the fast identification of the τ-jets is introduced in this work [16]. Instead of parameterization, a simple algorithmic based τ-jet identification is proposed.

After a detailed description of the simulations used to develop the algorithm in section 5.3.2, τ labelling is introduced in section 5.3.3. The proposed algorithm is motivated in section 5.3.4. Fast shower and its limitations are discussed in section 5.3.5. The identification algorithm is presented in section 5.3.6 and its performance and comparison with the parameterization based τ identification is discussed in section 5.3.7. Conclusions are drawn in section 5.3.8.

5.3.2 The Monte Carlo Programs

Originally the τ-ID algorithm was developed for the analysis of the $t\bar{t}H \rightarrow t\bar{t}\tau^+\tau^-$ and its most severe background, namely $t\bar{t}$ events. The signal process involves τ-leptons which decay into hadrons, i.e. τ-jets, as well as other jets coming from the decay products of top quarks. It, therefore, makes an excellent substance to study τ identification including impurities. After developing the algorithm, it was applied to the cleaner Vector Boson Fusion (VBF) $H \rightarrow \tau^+\tau^-$ channel [112] and its corresponding $t\bar{t}$, QCD and Z+jets backgrounds. Since the VBF signal hardly contains non-τ jets in the central region, its adjusting was done against $t\bar{t}$ background (as a source for non-τ jets). The above processes allowed to study the algorithm dependence on the jets environment and type (quark vs. gluon jets).

For both fast and full simulation studies, the Athena framework was used. Events were generated with Pythia 6.2 [45] except Z+jets, where MadCUP [122] was used for the event generation, and Pythia for hadronization. For the fast simulation studies a modified[20] Atlfast [106] version with fast shower [107] was used. For the full simulation, we used Geant3 and ATLAS reconstruction, version 7.0.2. Statistics was not a limiting factor since thousands of events were generated for each study.

5.3.3 Labelling Tau Jets

In real data analysis, there is no way to know if a tagged τ is originating from a true τ or not. However, in Monte Carlo events one can use the truth tree and see if there is a τ particle in the neighborhood of the candidate τ jet. That way the concept of labelling was developed. A jet is labeled as a τ jet if there is a τ Monte Carlo (MC) hadronic jet with transverse momentum $p_T > 10$ GeV and pseudorapidity $|\eta| < 2.5$ within $\Delta R < 0.3$ from the jet axis[21]. A τ MC hadronic jet is a pseudo particle defined by the sum of all hadronic τ decay products[22]. These definitions hold for both the fast and full Monte Carlo. Once a jet is tagged as a τ jet, it is considered real if it is labeled and fake if it is not labeled. That way, the definitions of efficiency and purity naturally emerge (section 5.3.7).

5.3.4 Motivation

τ identification in the fast simulation should reproduce the efficiency and purity attainable with full simulation with the highest possible fidelity without introducing a bias to the kinematic distributions of the τ-jets. Hadronic τ-identification is done in full simulation via various cut or likelihood methods [120], [123]. Our first τ-identification algorithm was based on the simple TDR cut method. A jet is tagged as a τ-jet if it has:

- 1 or 3 charged tracks with $p_T(track) > 5\ GeV$ within a cone of $\Delta R < 0.07$ around the jet axis;
- $p_T(\tau_j) > 20\ GeV$ (before calibrating the jet energy);
- The isolation fraction F_{Iso} defined as the fraction of transverse momentum within an annulus of $0.2 < \Delta R < 0.4$, i.e. $F_{Iso} = (p_T(0.4) - p_T(0.2))/p_T(0.2)$, is less than 0.03;
- The number of calorimetric cells with $E > 0$ and within a cone $\Delta R < 0.4$ around the jet axis is less than 6;

[20] Class that calculate calorimetric variables for τ-ID was added.
[21] $\Delta R = \sqrt{\Delta\eta^2 + \Delta\phi^2}$.
[22] In that sense, a τ MC hadronic jet is a reconstruction of the τ lepton (hadronic) decay products excluding the neutrino.

Later we will show that the last variable (number of calorimetric cells) is fully correlated with the Electromagnetic Radius R_{EM}. R_{EM} is the E_T-weighted jet radius computed from the transverse electromagnetic energy, E_{Ti}, of the cells ($i = 1, ...$) within $\Delta R_i < 0.4$ around the jet axis. It is defined by the following formula:

$$R_{EM} = \frac{\Sigma_{i=1}^{n} E_{Ti} \Delta R_i}{\Sigma_{i=1}^{n} E_{Ti}}, \tag{5.5}$$

Note also that at this point calorimeter showering was not yet implemented in the fast simulation. It was taken into account at a later stage.

We have applied this τ-identification algorithm to the $t\bar{t}H \rightarrow t\bar{t}\tau^+\tau^-$ process. We then compared the η distributions of the real and fake τ-jets with those obtained with the parameterization based τ- identification (based on [120])[23], and with the distributions obtained from the full simulation. The distributions are shown in Figure 5.31. It can be seen that for fake τ-jets there is an incompatibility between the distributions and there is a bias towards the end-cap region in the parameterization based τ-tag. This bias is not seen in the algorithmic based τ-tag. The bias introduced by the parameterization motivated a further development of the algorithmic fast τ-jet identification.

5.3.5 Understanding the Tau Identification Quantities

The above mentioned fast algorithmic τ ID suffers from two drawbacks. One essential variable, the number of cells, has no parallel in the detector full simulation and the lateral shower development in electromagnetic calorimeter is not taken into account[24].

To overcome the latter problem, we have implemented a new version of the fast simulation in which the lateral shower development was taken into account [107]. The impact of this improvement on the τ ID variables was dramatic. For example let us have a look at the isolation fraction (F_{Iso}) and the electromagnetic radius (R_{EM}). Figures 5.32 shows R_{EM} (top) and F_{Iso} (bottom) calculated with the Atlfast without (left) and with (right) the fast lateral shower development implementation.

The natural calorimeter spatial resolution is $\Delta\eta \times \Delta\phi = 0.025 \times 0.025$. Yet, the parametrization is done assuming a resolution of $\Delta\eta \times \Delta\phi = 0.1 \times 0.1$[25]. This is sufficient for trigger studies but might not be realistic for some physics studies, and in particular for τ studies that require high granularity.

Fig 5.33 (a) shows the number of electromagnetic cells (with $p_T(cell) > 1$ GeV) that are contained in a τ jet for labeled (blue solid line) and non-labeled (red dashed line) candidates. Figure 5.34 shows the number of calorimetric cells within the fast τ-ID.

[23] This parameterization is still the official one at the time of writing this thesis, a new one is in preparation.

[24] The reason was, that at the time, the fast shower was not implemented in the ATLAS fast simulation.

[25] This is the granularity of the trigger towers.

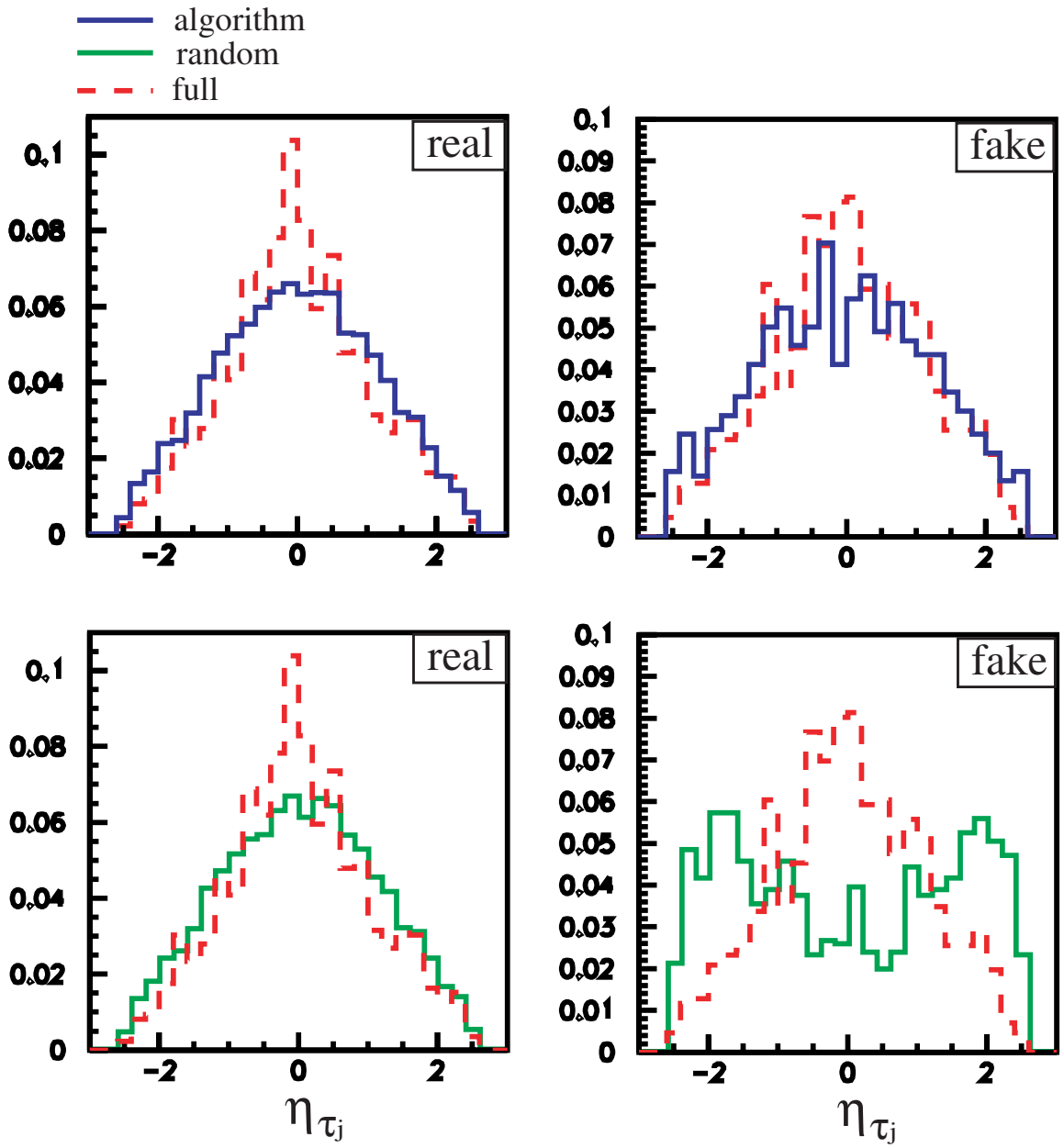

Figure 5.31: *Comparison of the η distributions of the real (left) and fake (right) τ-jets obtained with a full simulation (red dashed line) and the fast algorithmic (top, solid blue line) and the old parameterization (bottom, solid green line).*

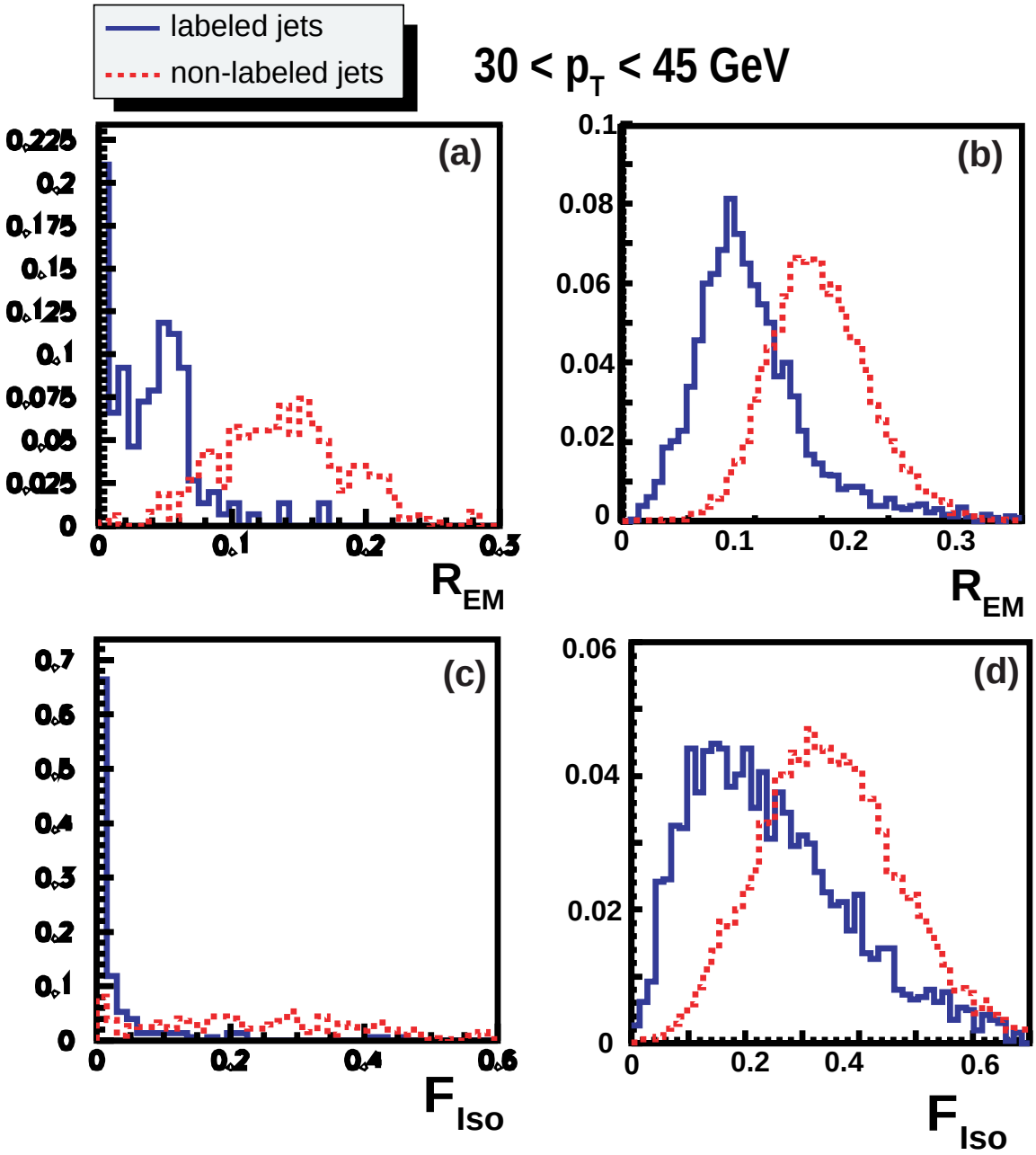

Figure 5.32: *The electromagnetic radius R_{EM} (top) and isolation fraction F_{Iso} (bottom) calculated within Atlfast without (left) and with (right) the fast shower implementation. Distributions are shown for the τ-labeled (blue solid line) and non-labeled (red dashed line) jets.*

The difference between the two quantities is easily notable. However, when the (fully simulated) electromagnetic cells were grouped into towers which were then projected into 2-D cells with the requested granularity (Figure 5.33 (b)), the fast simulation quantity (Figure 5.34) acquires a physical meaning and can be used in τ-ID. Moreover, there is a clear correlation between the electromagnetic radius and the number of cells as can be seen in Figure 5.35 (based on full simulation). This means that both variables play similar roles in the τ-ID and one can use either of the two.

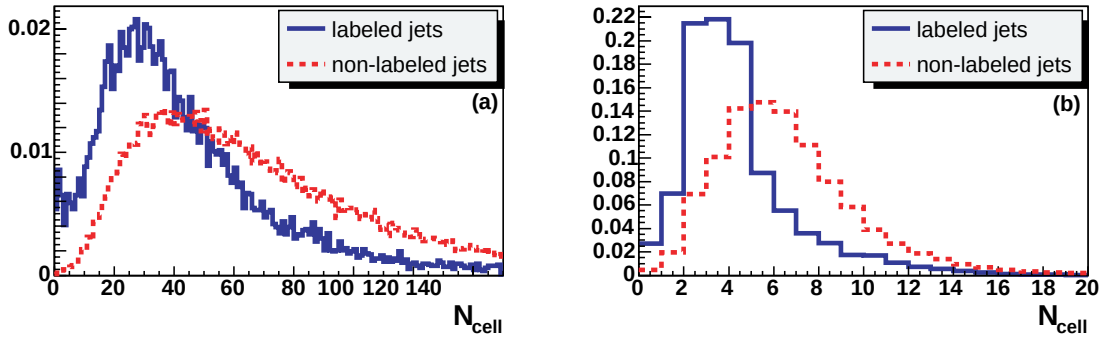

Figure 5.33: *The number of electromagnetic cells in τ-labeled (blue solid line) and non-labeled (red dashed line) jets in full simulation before (a) and after (b) grouping and projection.*

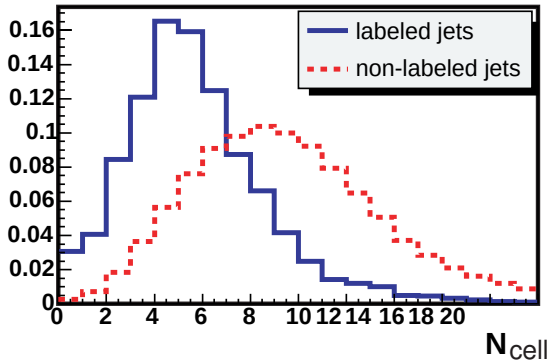

Figure 5.34: *The number of electromagnetic cells in τ-labeled (blue solid line) and non-labeled (red dashed line) jets in the fast simulation.*

After understanding the definition of electromagnetic cells we have studied the effect of granulation. Figure 5.36 (a) shows the electromagnetic radius of τ-jets (from $t\bar{t}H$) in the momenta range $30 < p_T < 45$ GeV (black solid, built in default granularity) vs that obtained from grouping cells with a granularity of 0.1×0.1 (red dashed)[26]. One can clearly see a disagreement between the two histograms. However, when cells are defined with a finer granularity of 0.025×0.025 there is a reasonable agreement between

[26]Note that both quantities were derived from the full simulation.

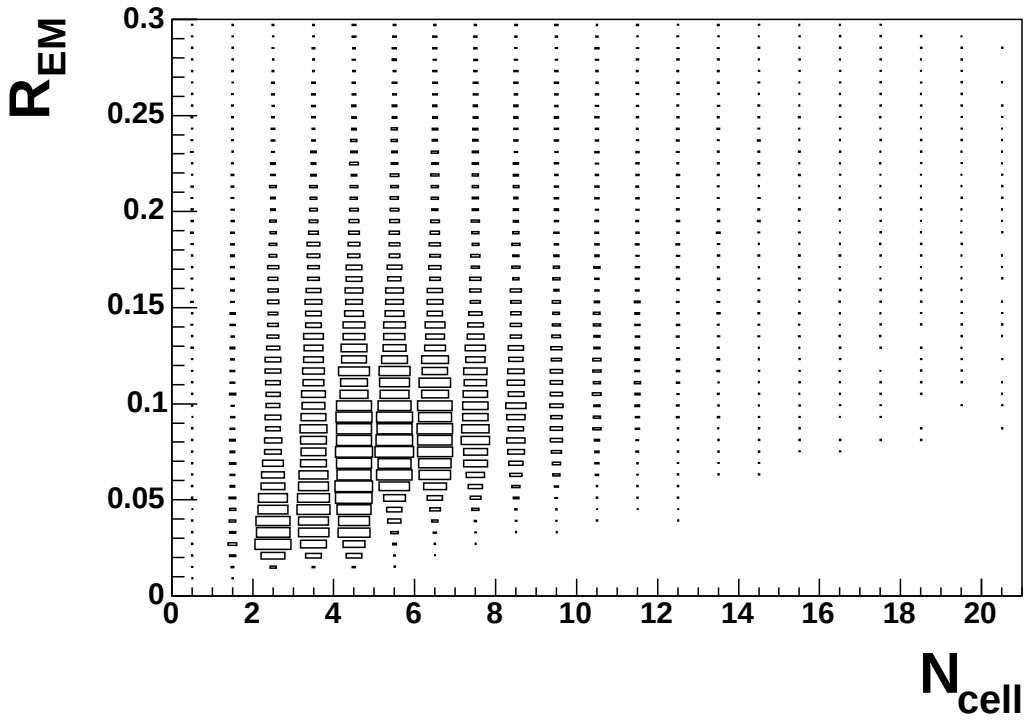

Figure 5.35: *The correlation between the electromagnetic radius R_{EM} and the number of electromagnetic cells in a jet (both labeled and non-labeled) in the full simulation after grouping and projection.*

the histograms (5.36 (b)). Since it is technically impossible to simulate fine granularity cells in the fast Monte Carlo, one should not attempt to achieve an agreement between calorimetric related quantities in fast and full simulation, but rather develop an algorithm that take the differences into account as described in the next section.

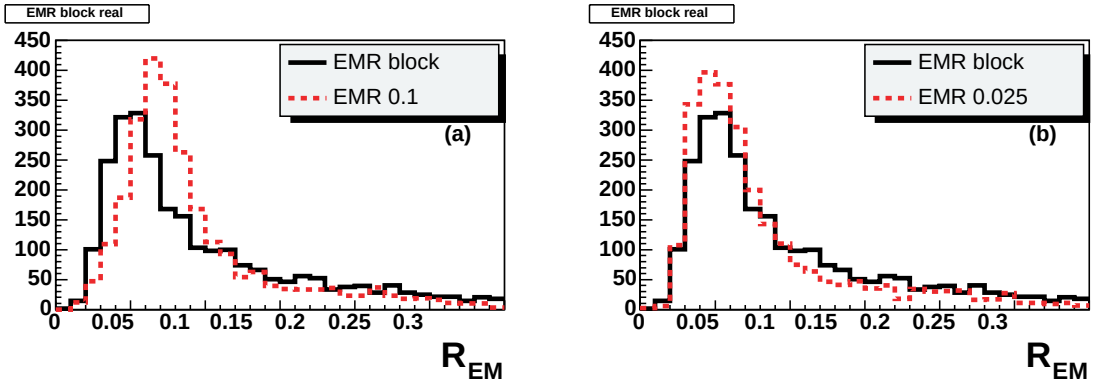

Figure 5.36: *Electromagnetic radius of the τ-labeled jets from the full simulation obtained with the default granularity (black solid line) is compared with the one calculated when cells are grouped into towers of 0.1×0.1 (a), and 0.025×0.025 (b), and then projected (red dashed line).*

5.3.6 The Fast τ- Identification Algorithm

The variables we use for τ- tag are similar to those described in section 5.3.4. The fast lateral development shower description allows to refine their definition. A jet is considered as a tagged τ-jet if:

- It has 1 or 3 charged tracks (Figure 5.37) with $p_T(track) > p_{Tmin}$ within a cone of $\Delta R < \Delta R_0$ around jet axis, where p_{Tmin} and ΔR_0 are optimized according to the specific signal environment. For a clean environment like VBF (Vector Boson Fusion) we recommend $p_{Tmin} = 2\ GeV$ and $\Delta R_0 = 0.2$ while for a more busy environment like $t\bar{t}H$ we recommend tightening the selection, e.g. $p_{Tmin} = 5\ GeV$ and $\Delta R_0 = 0.15$.

- The isolation fraction which is now redefined

$$F_{Iso} = \frac{p_T(0.2) - p_T(0.1)}{p_T(0.4)} \tag{5.6}$$

  should satisfy $F_{Iso} < F^0_{Iso}(p_T)$ where $F^0_{Iso}(p_T)$ is determined using the following procedure: The signal F_{Iso} is plotted in slices of p_T for labeled (blue solid) and non labeled (red dashed) jets (Figure 5.38). The crossing point of the labeled and non-labeled F_{Iso} for a given p_T slice is $F^0_{Iso}(p_T)$.

- The number of electromagnetic cells, with $p_T(cell) > 1\ GeV$ within a cone $\Delta R < 0.4$ around jet axis should be less than $N^0_{cell}(p_T)$. $N^0_{cell}(p_T)$ is determined using the following procedure: The signal N_{cell} is plotted in slices of p_T for labeled (blue solid) and non labeled (red dashed) jets (Figure 5.39). The crossing point of the labeled and non-labeled N_{cell} for a given p_T slice is $N^0_{cell}(p_T)$. Alternatively, as mentioned above, one may use Electromagnetic radius (Figure 5.40) instead of number of cells.

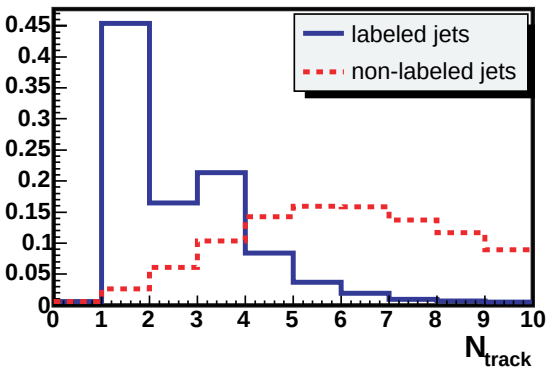

Figure 5.37: *The number of charged tracks in τ-labeled (blue solid line) and non-labeled (red dashed line) jet.*

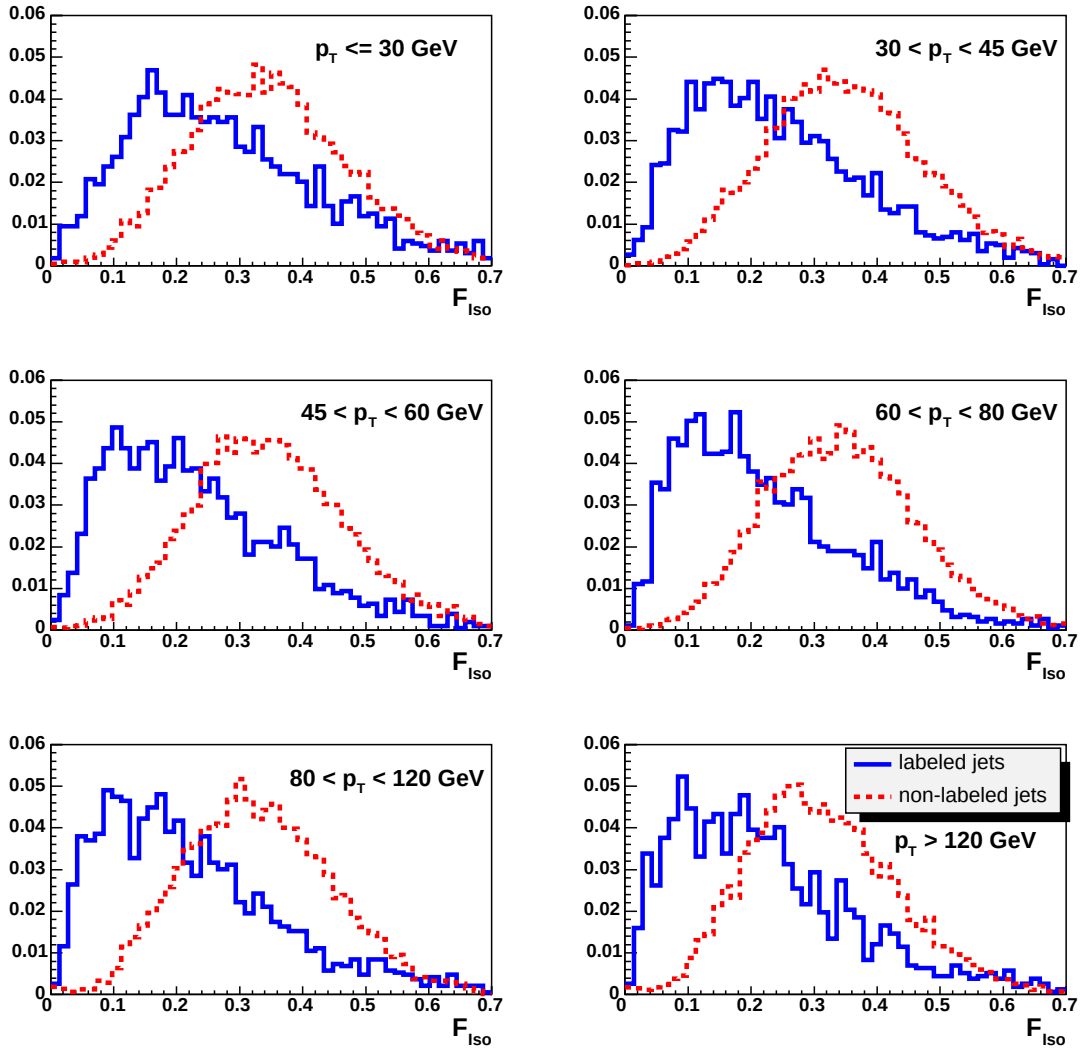

Figure 5.38: *Isolation fraction, F_{Iso}, for τ-labeled (blue solid) and non-labeled (red dashed) jets for different transverse momenta of the jet. The cutoff value $F^0_{Iso}(p_T)$ is determined by the crossing of the two histograms in each of the plots.*

5.3.7 Results

The better the τ identification is, the higher the efficiency and the lower is the contamination, i.e. better acceptance for τ jets and higher rejection for non τ- jets. The definitions of efficiencies and rejections follow naturally from the labelling and the tagging prescription (section 5.3.3). Following Figure 5.41 we define

$$Eff = \frac{N_{labeled\&tagged}}{N_{labeled}} \tag{5.7}$$

$$Rej = \frac{N_{non-labeled}}{N_{non-labeled\&tagged}} \tag{5.8}$$

$$Pur = \frac{N_{labeled\&tagged}}{N_{tagged}} \tag{5.9}$$

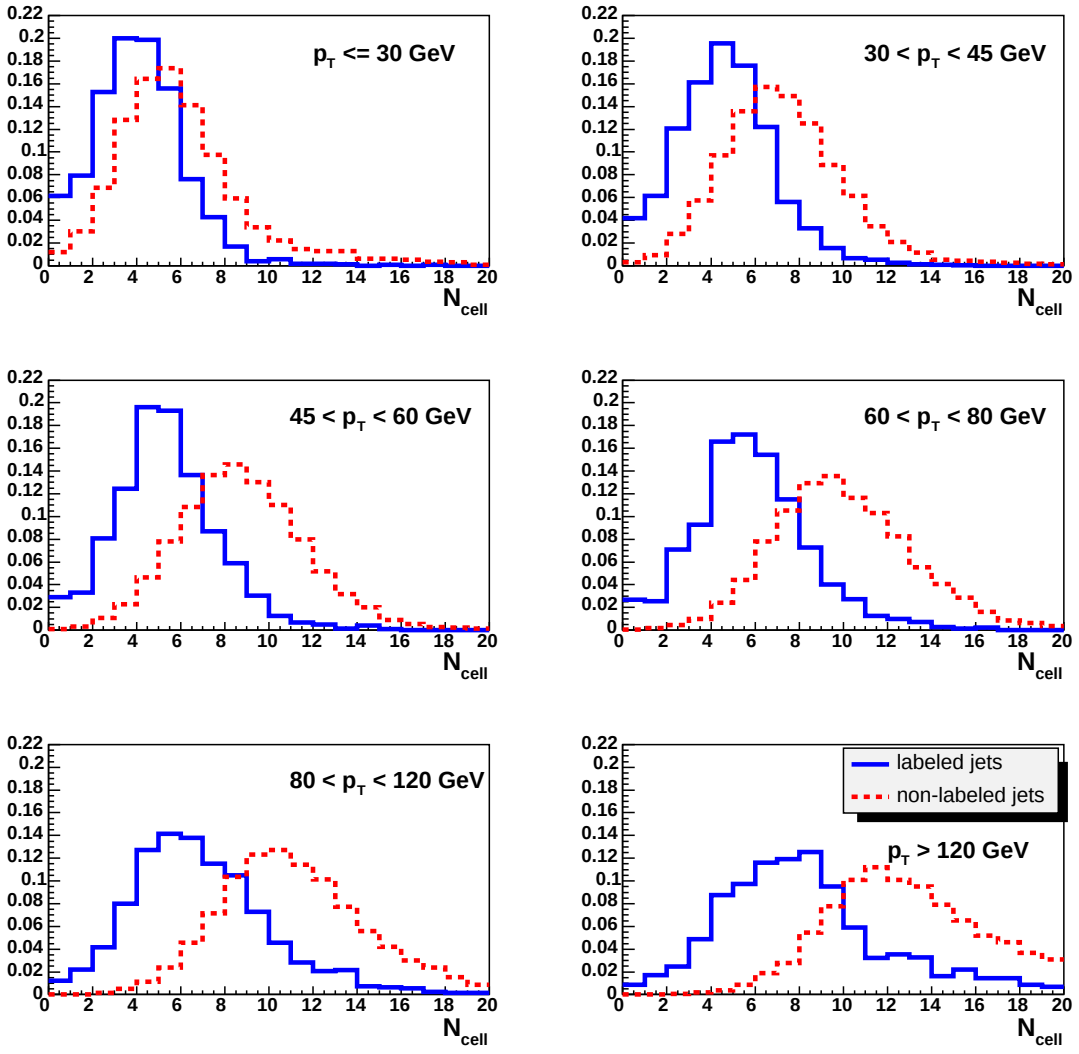

Figure 5.39: *The number of electromagnetic cells for τ-labeled (blue solid line) and non-labeled (red dashed line) jets for different transverse momenta of the jet. The cutoff value $N^0_{cell}(p_T)$ is determined by the crossing of the two histograms in each of the plots.*

$$Con = \frac{N_{non-labeled\&tagged}}{N_{tagged}} \tag{5.10}$$

The algorithm described above was applied to the $t\bar{t}H \to t\bar{t}\tau^+\tau^-$ and VBF with $H \to \tau^+\tau^-$ channels in the fast simulation. It was compared with the full (cuts-based [120]) simulation and, also, with the most recent parameterization existing at the time of writing this thesis [121][27]. The efficiencies (a) and rejections (b) for the $t\bar{t}H \to t\bar{t}\tau^+\tau^-$ are shown as a function of p_T in Figure 5.42, and as a function of η in Figure 5.43. The purity and contamination of the signal are shown in Figures 5.42 (c) and 5.43 (c). The rejections for the corresponding backgrounds, $t\bar{t}$ - (d) and QCD - (e), are also presented in Figures 5.42

[27]Note that the parameterization was derived based on a Likelihood method while our comparison is done with a cuts-based τ tag and therefore some disagreement is bound to appear; moreover, the parameterized rejection was given for QCD jets only.

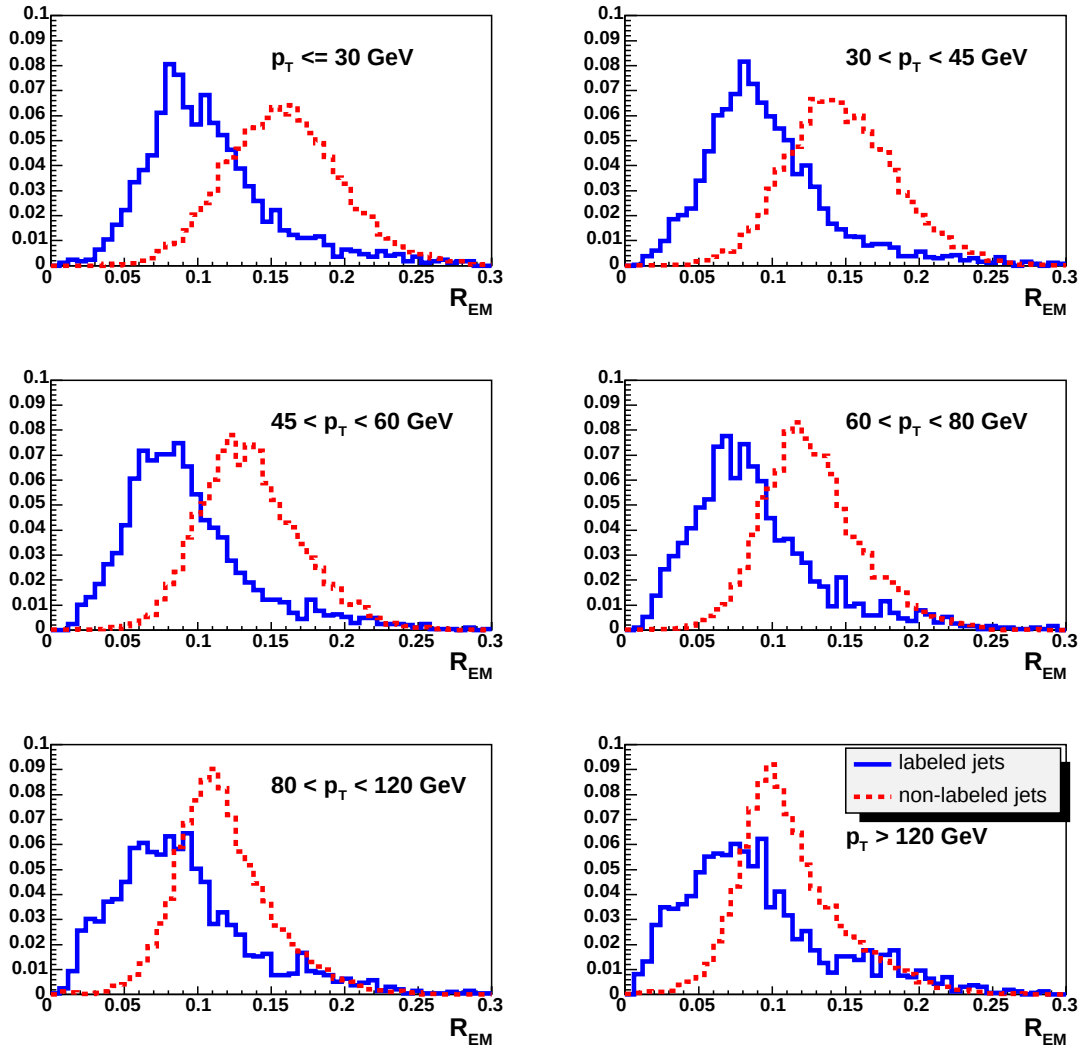

Figure 5.40: *The electromagnetic radius for τ-labeled (blue solid line) and non-labeled (red dashed line) jets for different transverse momenta of the jet. The cutoff value $R^0_{EM}(p_T)$ is determined by the crossing of the two histograms in each of the plots.*

and 5.43.

Similarly, results obtained from the VBF channel are shown in Figures 5.44 and 5.45.

There is a nice agreement between the performance obtained by the fast algorithm and the one obtained with the full simulation. Note that the rejection power, as predicted by fast simulation and the parametrization τ-ID method is about two orders of magnitude better than the results based on the full simulation. Since the parameterization was done using likelihood method in the full simulation, we have also tested the efficiencies and rejections with the full simulation likelihood based τ-ID [121]. The results (for the $t\bar{t}H \rightarrow t\bar{t}\tau^+\tau^-$ process) are shown in Figure 5.46. There is not an apparent difference between the rejection in cuts based vs likelihood based full simulation.

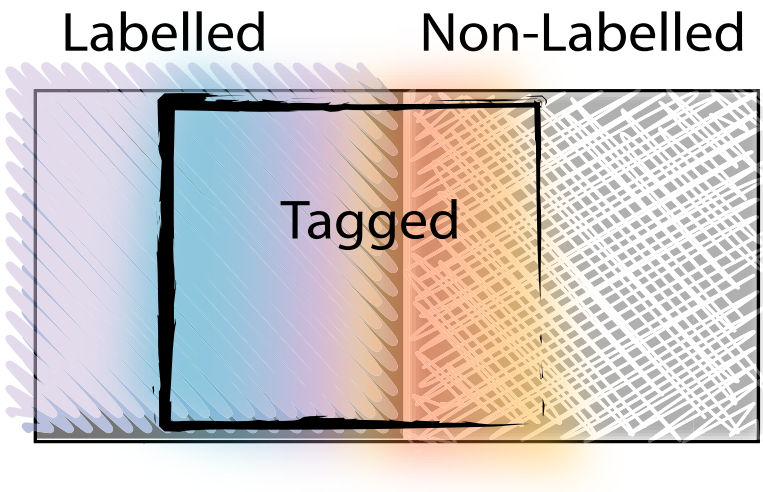

Figure 5.41: *The definition of efficiency and rejection (see text).*

5.3.8 Conclusions

In this section we introduced a new algorithmic method for τ identification within the framework of the fast simulation of the ATLAS detector. We found out that this method is reproducing the results obtained using the full detector simulation τ ID in both efficiency and rejection power.

The new algorithmic approach is in a good agreement with the full simulation. This agreement is better than the agreement between the full simulation and the parameterization method which fails to reproduce the rejection power correctly. Even though there is no substitute for full simulation - it is often unusable for practical reasons, and a prescription for fast simulation τ tag, as the one given here is providing a reliable and accurate fast alternative.

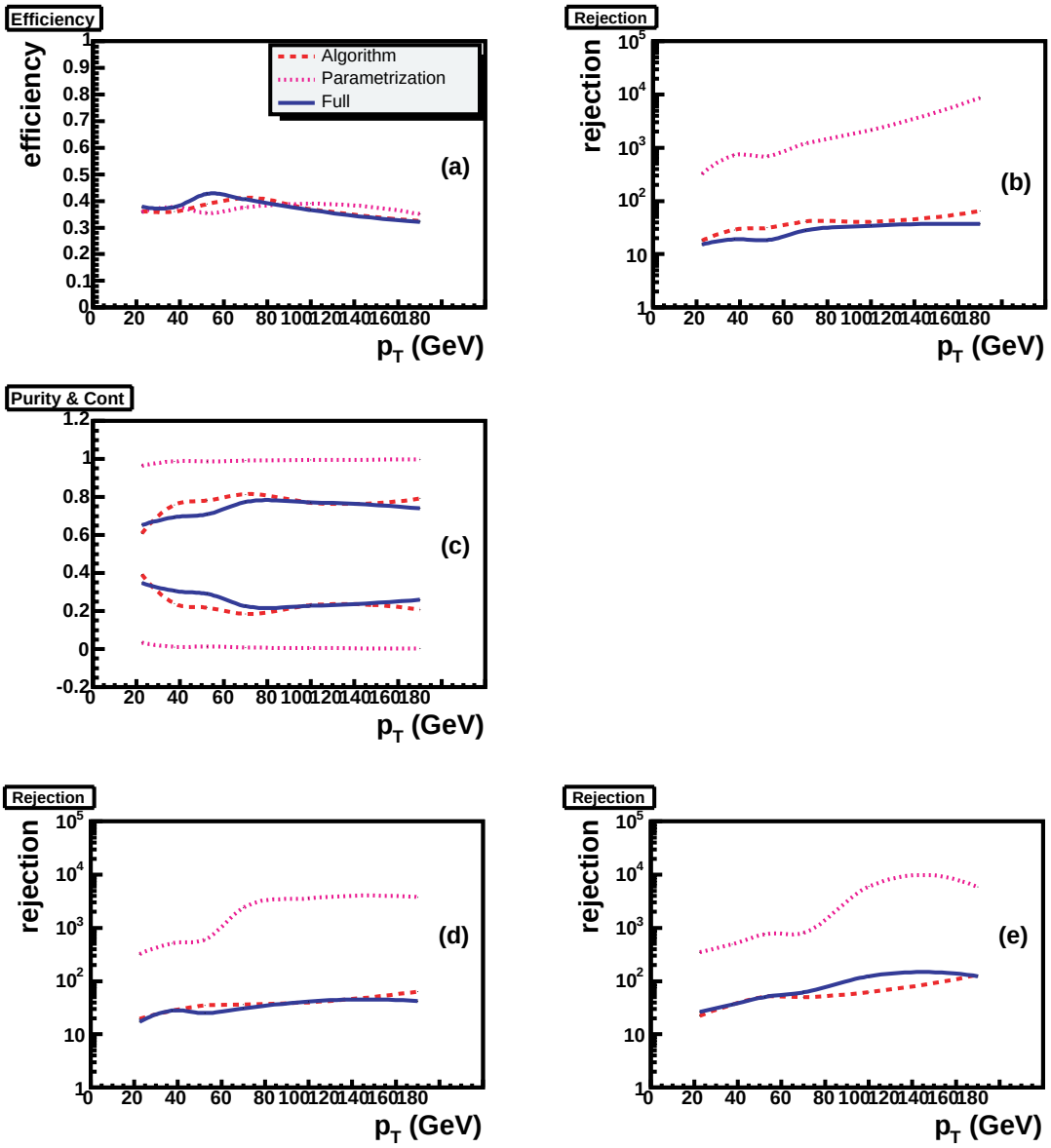

Figure 5.42: *Dependence of the τ-id efficiency (a) on the p_T of the jet for the $t\bar{t}H \to t\bar{t}\tau^+\tau^-$, rejection (b) in the signal sample, purity and contamination (c) of the signal sample, rejection of the jets from $t\bar{t}$ background (d) and rejection from QCD (e). Results from full simulation are shown in blue-solid, from the fast simulation algorithm in red-dashed, and from the fast simulation parameterization in magenta-dotted.*

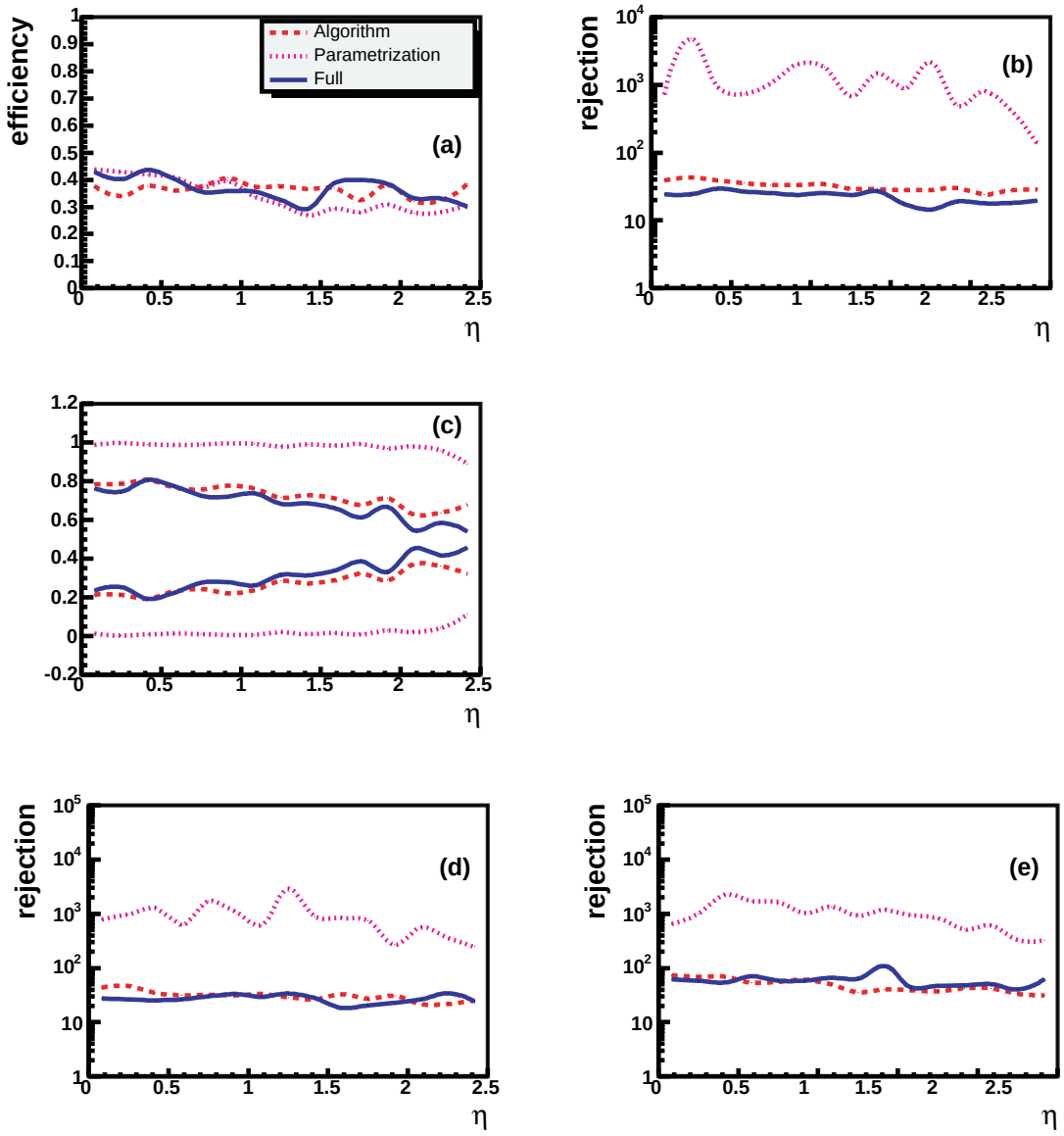

Figure 5.43: *Dependence of the τ-id efficiency (a) on the η of the jet for the $t\bar{t}H \rightarrow t\bar{t}\tau^{+}\tau^{-}$, rejection (b) in the signal sample, purity and contamination (c) of the signal sample, rejection of the jets from $t\bar{t}$ (d) and rejection from QCD (e). Results from full simulation are shown in blue-solid, from the fast simulation algorithm in red-dashed, and from the fast simulation parameterization in magenta-dotted.*

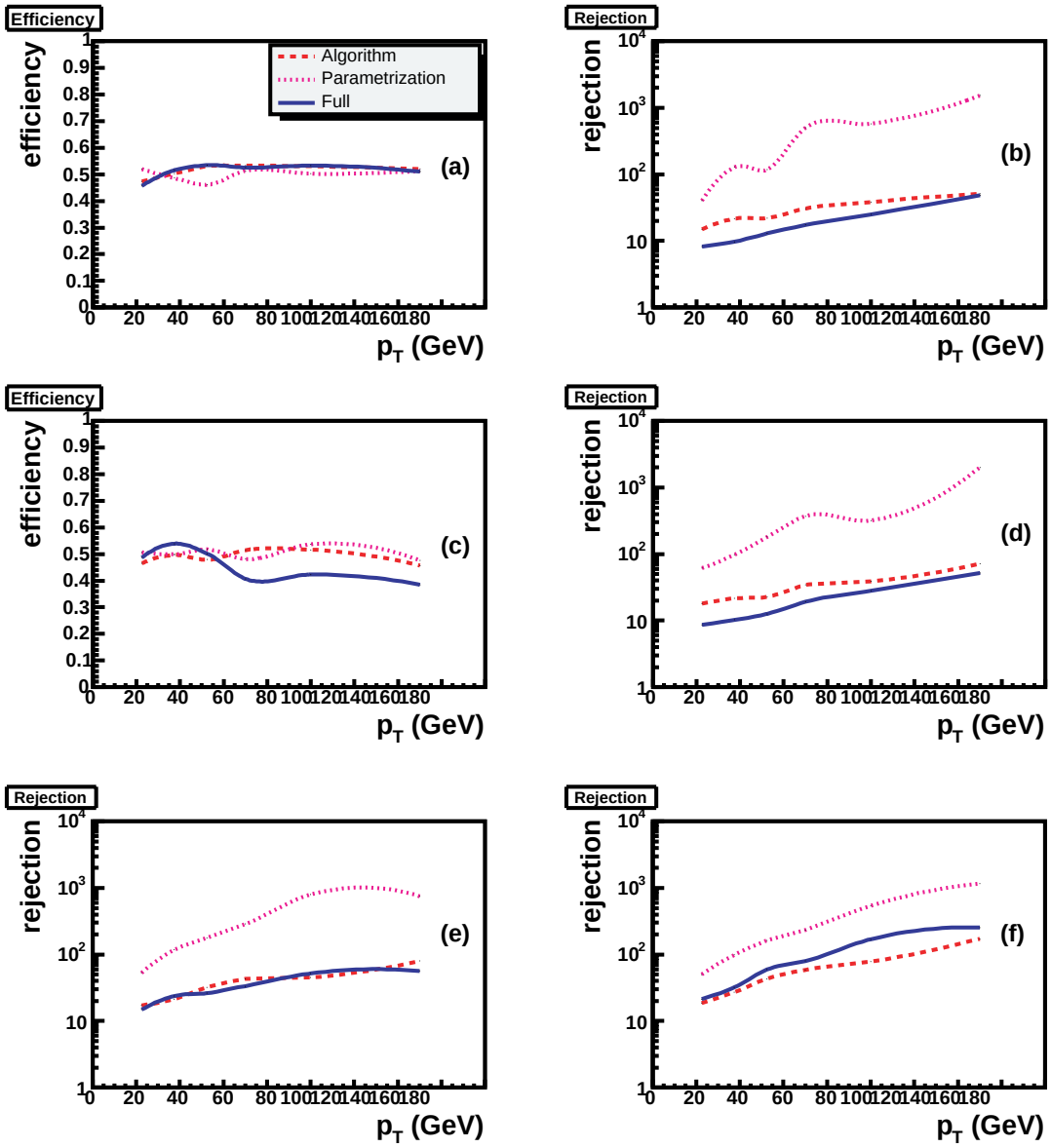

Figure 5.44: *Dependence of the τ-id efficiency (a) on the p_T of the jet for the VBF with $H \to \tau^+\tau^-$, rejection (b) in the signal sample, efficiency (c) and rejection (d) for the corresponding Z+jets background, rejection of the jets from $t\bar{t}$ (e) and rejection from QCD (f). Results from full simulation are shown in blue-solid, from the fast simulation algorithm in red-dashed, and from the fast simulation parameterization in magenta-dotted.*

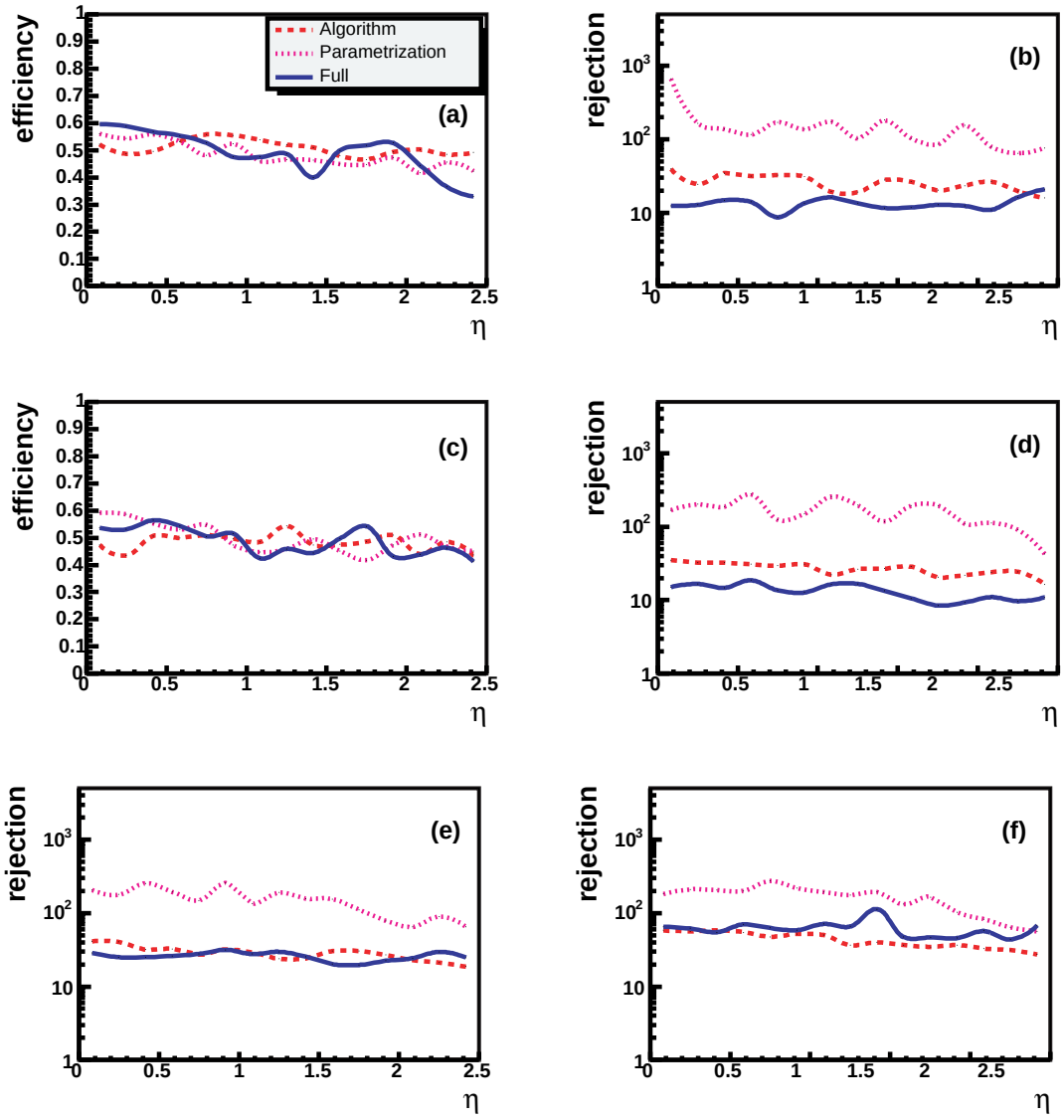

Figure 5.45: *Dependence of the τ-id efficiency (a) on the η of the jet for the VBF with $H \to \tau^+\tau^-$, rejection (b) in the signal sample, efficiency (c) and rejection (d) for the corresponding Z+jets background, rejection of the jets from $t\bar{t}$ (e) and rejection from QCD (f). Results from full simulation are shown in blue-solid, from the fast simulation algorithm in red-dashed, and from the fast simulation parameterization in magenta-dotted.*

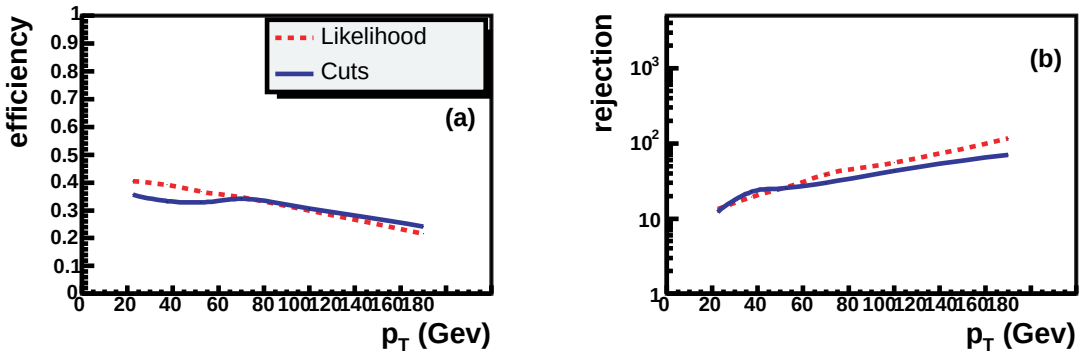

Figure 5.46: *Comparison of the τ-id efficiency (a) and rejection (b) for the Likelihood (red-dashed) and Cut (blue solid) methods within the full simulation.*

5.4 $t\bar{t}H \rightarrow t\bar{t}\tau^+\tau^-$ - Toward the Measurement of the top-Yukawa Coupling

5.4.1 Motivation

One of the most challenging measurements of the Higgs boson properties is the determination of the Yukawa coupling to the top quark. Theory predicts that fermion masses are generated via the interaction with the Higgs scalar. The fermion masses are therefore given by $m_f = g_{f\bar{f}H} \cdot v/\sqrt{2}$, where $g_{f\bar{f}H}$ is the Yukawa coupling of the Higgs boson to the fermion and v is the vacuum expectation value (VEV). The puzzle of the top mass being a few orders of magnitude bigger than the masses of other fermions can be formulated in terms of the relation of the top Yukawa coupling to the couplings to other fermions. Therefore the measurement of the top Yukawa coupling is of extreme importance and will enable us to further investigate the mass generation mechanism[28].

Even if the Higgs boson mass is above the $t\bar{t}$ threshold the branching ratio $BR(H \rightarrow t\bar{t})$ would be low due to the open decay channels to the W and the Z boson pairs (see Figure 2.3). Moreover, top quark decay modes contain neutrinos[29] and make the full reconstruction of the Higgs boson difficult. Precision fits of the Standard Model indicate that the Standard Model Higgs boson mass[30] is below $\sim$200 GeV [6], while in the MSSM a light Higgs boson mass is theoretically bounded to be below $\sim$135 GeV [8, 9, 33]. The experimental lower bounds on the Standard Model and light MSSM Higgs boson are 114.4 GeV [5] and $\sim$90 GeV [12], respectively. The most favorable Higgs boson scenario is a Standard Model like light Higgs boson with a mass around or below 130 GeV. Such a Higgs boson will not have an open decay channel to a top quark pair. So the only way to directly measure the Higgs boson coupling to the top quark is via its direct coupling to the top quark in the associated (with a top quarks pair) production process (see Figure 5.47). The motivation to detect and measure the $pp \rightarrow t\bar{t}H$ process is therefore clear.

For a 120 GeV Higgs boson the most significant final state of the $t\bar{t}H$ channel is the one with the Higgs boson decaying to a b-quarks pair. Here one can tag four b-jets, as well as fully reconstruct the signal. The feasibility of this channel was studied with ATLAS fast simulation [117] and gave promising results for the ATLAS low luminosity benchmark of 30 fb^{-1}. The validity of these results is subject to the confirmation with a full detector simulation study. To complement the $t\bar{t}H \rightarrow t\bar{t}b\bar{b}$ channel, we introduce in this work a feasibility study of the $t\bar{t}H$ channel with the Higgs boson decaying to a pair of τ leptons. The cross section times branching ratio is about an order of magnitude below that of

[28] Most extensions of the SM, in particular the MSSM, contain a SM like light Higgs boson that couples in a similar fashion to fermions. Thus, the importance of the precision measurement of the top Yukawa coupling remains valid.

[29] Except for the fully hadronic decays, which would be very difficult to trigger.

[30] The upper limit strongly depends on m_{top}.

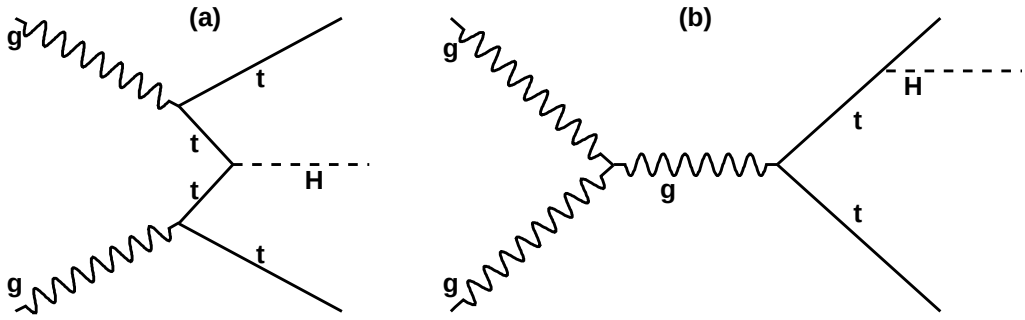

Figure 5.47: *Feynman diagrams of the $t\bar{t}H$ production processes.*

the $t\bar{t}H \to t\bar{t}b\bar{b}$ channel, and the τ tag efficiency is lower than the b-tag efficiency, yet, preliminary studies indicated that combining several final state topologies, there might be a significant contribution from this channel. However, a significant amount of work was invested in improving the τ tagging in the fast simulation and make it as realistic as possible (see section 5.3 and [16]). In this part of the thesis we describe in details the results of the $t\bar{t}H \to t\bar{t}\tau^+\tau^-$ analysis. The cross section and the various topologies are described in section 5.4.2. The Monte Carlo simulations are presented in section 5.4.3. The analysis objects, i.e. electron and muon identification, and the b, τ and light jet reconstruction are described in section 5.4.4. We then describe the signal's selection criteria in section 5.4.5. Fast simulation high luminosity results are given in section 5.4.6. Systematic uncertainties are discussed in section 5.4.7 and the background normalization from the data is described in section 5.4.8. The results are summarized in section 5.4.9.

5.4.2 Cross Section and Topologies

Recent calculations were used for the $t\bar{t}H$ cross section [124] and the branching ratios of $H \to \tau^+\tau^-$ [23]. The cross section times the branching ratio of $t\bar{t}H \to t\bar{t}\tau^+\tau^-$ is shown in Table 5.5 and Figure 5.48. One can clearly see that the cross section drops as the Higgs boson mass increases.

A priory, since each top quark can decay to a b quark accompanied either by two jets (bjj) or by a lepton and a neutrino ($bl\nu$), and each τ can decay hadronically ($\tau_j\nu$) or leptonically ($l\nu\nu$), nine channels are possible. For obvious reasons only muonic or electronic decays of the top are considered, and therefore $l = e, \mu$. Table 5.6 shows the nine a priory considered channels, their relative fraction, and the number of expected events (for 30 fb^{-1} and $m_H = 120$ GeV). Since we consider here only the low luminosity benchmark (30 fb^{-1}) it is clear that only channels 1, 2, 4, 5 and 6 have enough signal events to proceed with the analysis. However, channel 1, $t\bar{t}H \to t\bar{t}\tau^+\tau^- \to bjj\bar{b}jj\tau_j\bar{\nu}_\tau\tau_j\nu_\tau$, is purely hadronic with a small amount of missing energy and suffers from huge $t\bar{t}$ and QCD backgrounds. Likewise, channel 6, $t\bar{t}H \to t\bar{t}\tau^+\tau^- \to b\ell\bar{\nu}_\ell\bar{b}jj\ell\nu_\ell\bar{\nu}_\tau\ell\bar{\nu}_\ell\nu_\tau$, suffers from

a huge irreducible $Zt\bar{t} \to \ell^+\ell^- t\bar{t}$ background[31]. We therefore consider in this analysis only channels 2, 4 and 5.

m_H (GeV)	σ (fb)	$BR(H \to \tau^+\tau^-)$	$\sigma \times BR$ (fb)
110	894	0.07636	68.26584
120	692	0.06838	47.31896
130	541	0.05383	29.12203

Table 5.5: *Cross sections [124] for the $t\bar{t}H$ production, Branching Ratios [23] for $H \to \tau^+\tau^-$, and $\sigma \times BR(H \to \tau^+\tau^-)$.*

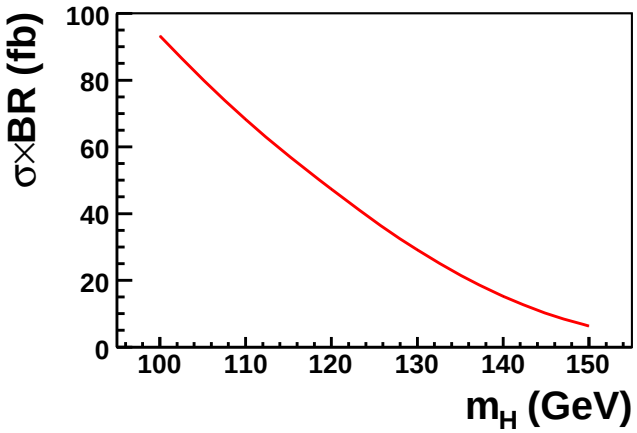

Figure 5.48: *Cross section times Branching ratio, $\sigma \times BR$, for the $t\bar{t}H \to t\bar{t}\tau^+\tau^-$ process as a function of the m_H (see Table 5.5).*

5.4.3 Monte Carlo

The complexity of the physics events to be analyzed at the LHC and the diversity of the detectors to be integrated into ATLAS make it an absolute necessity to provide an accurate detector simulation program, with which the detector response to various processes can be evaluated in detail. The complete simulation is performed in several stages. The input for the simulation comes from the event generators after a particle filtering stage. Data objects representing the Monte Carlo truth information from the generators are read by the simulation and processed. Hits produced by the simulation can be directly processed by the digitization algorithm and transformed into Raw Data Objects (RDOs). Alternatively they can be sent first to the pile-up algorithm and then

[31] We applied the Z-mass veto, i.e. we cut-off events with $75 < m_Z < 105$ GeV, but $Zt\bar{t} \to \ell^+\ell^- t\bar{t}$ background was still prevailing.

	Channel	$t\bar{t}H^0 \to t+t+\tau+\tau$	BR	No of events	No of triggered events
				(30 fb^{-1}, $m_H = 120$ GeV)	
Group 1	1	$bjj + bjj + \tau_j\nu + \tau_j\nu$	19%	270.2	9.54
	2	$bjj + bjj + \tau_j\nu + \ell\nu\nu$	**20%**	**284.4**	**30.91**
	3	$bjj + bjj + \ell\nu\nu + \ell\nu\nu$	6%	85.3	3.25
Group 2	**4**	$bjj + b\ell\nu + \tau_j\nu + \tau_j\nu$	**12%**	**170.6**	**8.82**
	5	$bjj + b\ell\nu + \tau_j\nu + \ell\nu\nu$	**13%**	**184.9**	**13.94**
	6	$bjj + b\ell\nu + \ell\nu\nu + \ell\nu\nu$	3%	42.7	7.15
Group 3	7	$b\ell\nu + b\ell\nu + \tau_j\nu + \tau_j\nu$	2%	28.4	0.73
	8	$b\ell\nu + b\ell\nu + \tau_j\nu + \ell\nu\nu$	2%	28.4	1.8
	9	$b\ell\nu + b\ell\nu + \ell\nu\nu + \ell\nu\nu$	1%	14.2	1.4

Table 5.6: *Final states and Branching Ratios for the $t\bar{t}H^0 \to t\bar{t}\tau^+\tau^-$. The number of events and number of triggered events for 30* fb^{-1} *and $m_H = 120$ GeV are also given. We consider only channels 2, 4 and 5 in the following sections.*

passed to the digitization stage. RDOs produced by the simulation data-flow pipeline are used directly by the reconstruction processing pipeline [89].

Since ATLAS is a huge and complicated detector, and we are intrested in the high energy processes, full simulations are heavily CPU time consuming, in particular for events with high particle multiplicities[32]. Studies of physics channels of interest and the associated backgrounds usually require the generation and simulation of millions of events. This is not feasible with the full simulation of the ATLAS detector. Therefore, a fast simulation program, ATLFAST [106], was developed in which the detector response was parametrized as a function of p_T and η.

5.4.3.1 Signal generation

Signal events were generated using PYTHIA 6.2 [45] with Tauola[33] [96] turned on. Events were accepted if they passed the 1-lepton filter, where a lepton was required to have a $p_T > 20$ GeV and $|\eta| < 2.5$. The efficiency of the filter was $\sim$60% for the signal. For the full simulation analysis, events that have passed the filter were simulated with GEANT4 (Athena version 9.0.4), then digitized and reconstructed using Athena 10.0.1. For the fast simulation we used ATLFAST implementing the Fast Shower [107] and including the Tau-algorithm [16]. We have produced 10^5 events for $m_H = 110,\ 120$, and 130 GeV each, and for different topologies as shown in Table 5.6. $2 \cdot 10^4$ events with $m_H = 120$ GeV were generated with the full simulation.

[32] For the channel $t\bar{t}H \to t\bar{t}\tau^+\tau^-$, studied in this thesis, $\sim$ 20 minutes are required to fully simulate one event.

[33] The TAUOLA package was developed for the accurate simulation of τ-lepton decays.

The τ's and the t-quarks were left to decay freely, except for Group 3 where t-quarks were forced to decay simultaneously to $b\ell\nu$ (Table 5.6).

5.4.3.2 Background generation

The most relevant background processes with the corresponding cross-sections are listed in Table 5.7. $t\bar{t}$ events were generated with PYTHIA[34], while for the $Zt\bar{t}$ processes, AcerMC [93] was used for the generation, and PYTHIA for the hadronization. Events were required to satisfy the 1-lepton filter mentioned above. The 1-lepton filter efficiencies are shown in the last column of Table 5.7.

Process	Decay	Generator	$\sigma \times BR$	Generated No of events	Filter efficiency
$t\bar{t}$	$t\bar{t} \to bjj\bar{b}jj$	PYTHIA	224 pb	$2.5 \cdot 10^7$	12%
$t\bar{t}$	$t\bar{t} \to b\ell\bar{\nu}_\ell\bar{b}jj$	PYTHIA	215 pb	$2.4 \cdot 10^7$	60%
$t\bar{t}$	$t\bar{t} \to b\ell\bar{\nu}_\ell\bar{b}\ell\nu_\ell$	PYTHIA	52 pb	$1.2 \cdot 10^7$	80%
$gg \to Zt\bar{t}$	$Z \to \tau^+\tau^-, \ell^+\ell^-$	AcerMC	7.5 fb	$5 \cdot 10^4$ (each)	88% $Z \to \tau\tau$
$qq \to Zt\bar{t}$	$t\bar{t} \to b\ell\bar{\nu}_\ell\bar{b}jj$		3.8 fb	$5 \cdot 10^4$ (each)	98% $Z \to \ell^+\ell^-$
$gg \to Zt\bar{t}$	$Z \to \tau^+\tau^-, \ell^+\ell^-$	AcerMC	3.7 fb	$5 \cdot 10^4$ (each)	45% $Z \to \tau\tau$
$qq \to Zt\bar{t}$	$t\bar{t} \to b\tau\bar{\nu}_\tau bjj$		1.9 fb	$5 \cdot 10^4$ (each)	94% $Z \to \ell^+\ell^-$
$gg \to Zt\bar{t}$	$Z \to \tau^+\tau^-, \ell^+\ell^-$	AcerMC	12.25 fb	10^5 (each)	37% $Z \to \tau\tau$
$qq \to Zt\bar{t}$	$t\bar{t} \to bjj\bar{b}jj$		6.2 fb	10^5 (each)	94% $Z \to \ell^+\ell^-$

Table 5.7: *The number of generated events (column 5) and $\sigma \times BR$ for various background processes. The last two processes were used as background sources for channel 2 only.*

5.4.4 Event Reconstruction

The $t\bar{t}H \to t\bar{t}\tau^+\tau^-$ channel contains most of the particles that can be reconstructed with the ATLAS detector. It could serve as an excellent tool to fully understand the reconstruction. In this section we will describe the reconstruction within the full and the fast simulation of all ingredients of the relevant channel.

5.4.4.1 Lepton Reconstruction

We consider here electrons and muons as leptons. Our goal is to identify those that originate in t-quark or τ-lepton.

[34] Recently, NLO@MC [125] generator became the standard tool for $t\bar{t}$ production. However, from a point of view of this analysis we did not find much differences.

Electron Identification In the full simulation, electron candidates are reconstructed from the calorimeter and tracking system information. A likelihood function calculated from several quantities (see Appendix E) [126], based on single electron and single pion samples, and defined as

$$L_e = \frac{weight_{EM}}{(weight_{EM} + weight_{\pi})} \tag{5.11}$$

is used to identify electrons[35]. In addition, calorimeter and track isolation is applied. In order to determine the efficiency of the identification, electron candidates are labeled as MC-isolated if they contain a true electron within a cone of 0.2, and if this true electron is isolated from other MC-particles[36]. They are labeled as non-MC-isolated if they contain a true electron within a cone of 0.2, but this true electron is not isolated from other MC-particles. Further on, they are labeled as MC-τ if they contain a τ_{had}[37] within a cone of 0.2. Finally, if they contain a pion within a cone of 0.2, they are labeled as MC-π.

Figure 5.49 shows the distribution of the electron identification likelihood L_e for MC-isolated electrons (blue solid line), non-MC-isolated electrons (green dash-dotted line), MC-τ (red dotted line), and MC-π (black dashed line). We tag a particle as an electron if the $L_e > 0.92$.

In order to determine if the electron is isolated we apply two criteria - calorimeter and track isolation. Figure 5.50 (a) shows the sum of the transverse momenta of charged tracks in the Inner Detector in a cone of 0.2 around an electron candidate track. We required that this sum is less than 5 GeV. Figure 5.50 (b) shows the additional calorimeter energy in a cone of 0.2 around the electron candidate. We required that this additional calorimeter energy is less than 5 GeV.

The obtained electron selection efficiency is $\sim 82\%$ with a purity of more than 95%. Rejection ratios are given in Table 5.8.

Following these results, electron identification efficiency for the fast simulation is set to 85%[38].

Muon Identification In the full simulation, the muon identification is done using the combined muon reconstruction (see section 5.1.3.4 and [89]). Additionally, it is required that the muon track is isolated. To determine the efficiency of the muon identification, all MC muons originating in a t-quark or a τ-lepton are labeled as MC-isolated, while those coming from other sources are considered as non-MC-isolated.

Figure 5.51 shows the sum of the transverse momenta of charged tracks in the Inner

[35] In order to reject photons, the likelihood is set to zero if there is no associated track.
[36] MC refers to the truth information.
[37] τ_{had} is defined as the sum of the hadronic products of the τ-lepton.
[38] The total number of tagged electrons includes also fake electrons (that do not originate in MC-isolated electrons). In order to have the same total number of tagged electrons we set the efficiency to 85% rather than 82%.

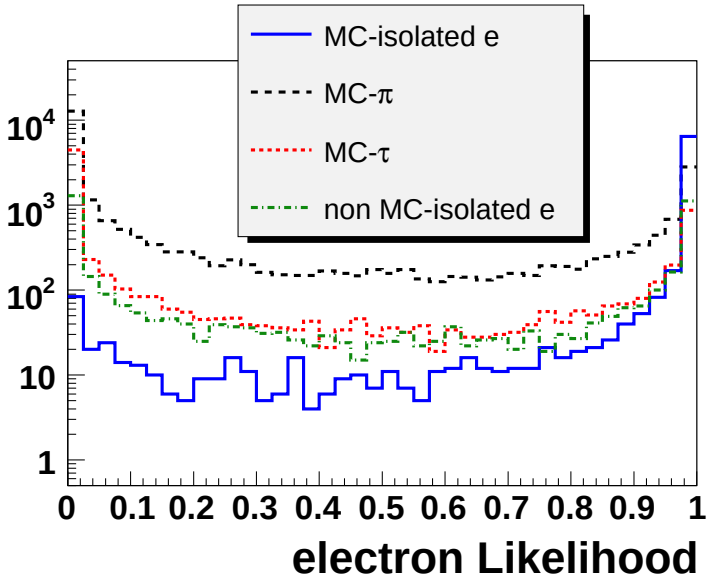

Figure 5.49: *The likelihood [126] used for the electron identification for MC-isolated electrons (blue solid line), non-MC-isolated electrons (green dash-dotted line), MC-τ (red dotted line), and MC-π (black dashed line).*

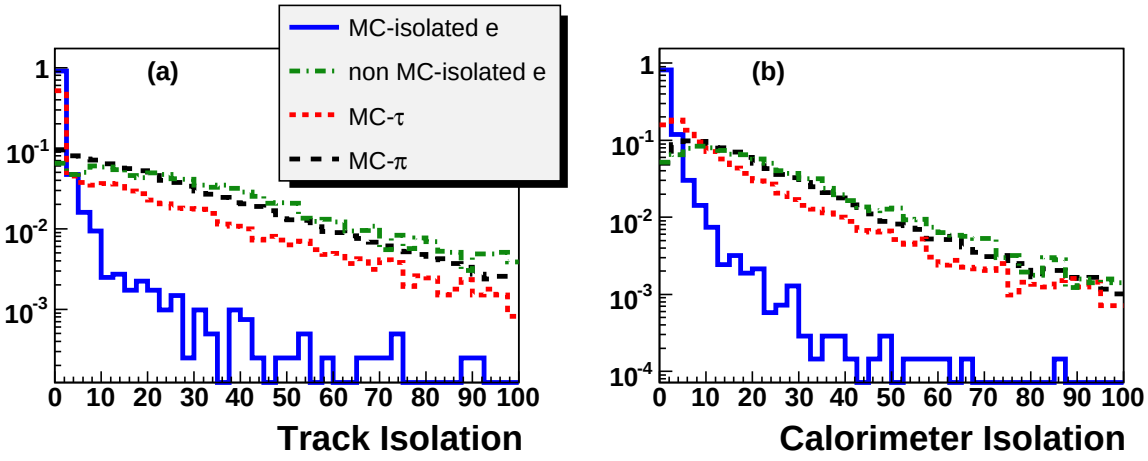

Figure 5.50: *Track (a) and calorimeter (b) isolation for MC-isolated electrons (blue solid line), non-MC-isolated electrons (green dash-dotted line), MC-τ (red dotted line), and MC-π (black dashed line).*

sample	rejection
total	180
π	1340
τ	270
non-MC-isolated e	37

Table 5.8: *Rejection of the non-electrons.*

Detector in a cone of 0.2 around a muon candidate track for a MC-isolated (blue solid line) and a non MC-isolated (red dashed line) muon. We required that this sum is less

than 10 GeV.

The obtained efficiency is $\sim 85\%$. Accordingly, this efficiency is applied in the fast simulation for isolated muons.

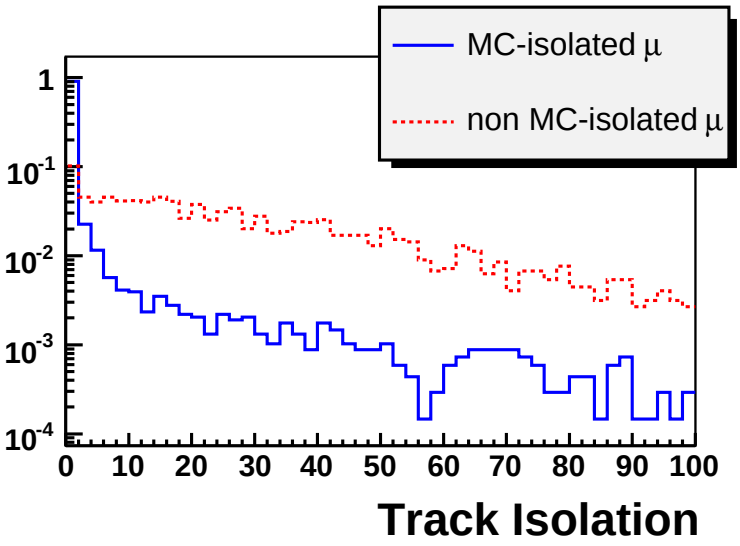

Figure 5.51: *Track isolation for MC-isolated muons (blue solid line) and non-MC-isolated muons (red dashed line).*

5.4.4.2 Jet Reconstruction

We use a Cone algorithm, with $\Delta R = 0.4$, for jet reconstruction in the full and fast simulation[39]. We also add to the jet a non-isolated muon if found within a cone of $\Delta R = 0.4$ around the jet axis[40].

Light Jet Reconstruction In the present analysis, light jets are important for the W-boson reconstruction. Therefore, it is necessary that they are well reconstructed and calibrated. We consider a jet as a light one if it is not tagged as a b-jet or as a τ-jet, both in the full and the fast simulation.

b Jet Reconstruction The b-tagging is one of the most important aims of the reconstruction software. In the full simulation of the ATLAS detector, it is done using several space and secondary vertex algorithms [127]. We use the "3D + secondary vertex", so-called $SV2$ algorithm. The resulting likelihood function is shown in Figure 5.52, where labeled[41] b-jets are represented with the blue solid line, labeled c-jets with the brown dashed line and light jets with the red dotted line. We tagged a jet as a b-jet if $W_{SV2} > 3$.

[39] This is the default option in the fast simulation.
[40] This is a novel feature of our analysis.
[41] We label jets if they contain a corresponding (b or c) parton within a cone of $\Delta R = 0.4$ around the jet axis.

The obtained average efficiency is 60%, with a rejection of 57 against light jets, and 7 against c-jets. The average purity is 89%.

In the fast simulation, b-jet tagging is done via a parametrization[42]. We set our efficiency to 60%. The corresponding default rejections are 35 against light jets and 7 against c-jets, with an average purity of 84%.

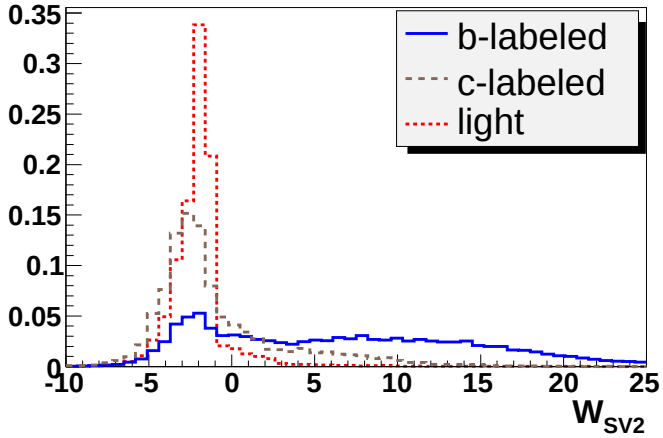

Figure 5.52: *The resulting likelihood function for the SV2 algorithm for labeled b-jets (blue solid line), labeled c-jets (brown dashed line) and light jets (red dotted line).*

τ Jet Reconstruction Excellent τ-tagging is crucial for this analysis. For the τ-tagging in the full simulation[43], we use a likelihood calculated from several calorimetric and track quantities (see Appendix F and [128]). Figure 5.53 shows the τ-Likelihood for different p_T ranges of the labeled (blue solid line) and non labeled (red dashed line) τ-candidates[44]. The values where we cut on the likelihood depend on the p_T of the jet (see Table 5.9). Additionally, we ask that the ratio of the hadronic energy and the sum of the p_T of all tracks is bigger than 0.1[45]. In the fast simulation, we used our own algorithm described in section 5.3 [16]. The cut values are given in a Table 5.10. Figure 5.54 shows the efficiency (a), the rejection (b), and the purity and contamination (c) for the fully simulated events (blue full line), for those with our fast τ-algorithm applied (red dotted line), and for those with the parametrization (magenta dashed line).

[42] Currently, the b-tag performance in the full simulation is found to be better than in the fast one.

[43] In the full simulation τ-candidates might be obtained using several different input objects - Calorimetric clusters, Topological clusters, different type of jets... We use Cone jets (we have not observed any significant difference when using different input objects (see 5.1.3.4)), with $\Delta R = 0.4$.

[44] A jet is labeled as a τ jet if there is a τ Monte Carlo (MC) hadronic jet with transverse momentum $p_T > 10$ GeV and pseudorapidity $|\eta| < 2.5$ within $\Delta R < 0.3$ from the jet axis. A τ MC hadronic jet is a pseudo particle defined by the sum of all hadronic τ decay products. These definitions hold for both the fast and full Monte Carlo.

[45] This cut removes non identified electrons.

p_T range (GeV)	cut value
< 30	3
(30, 45)	3
(45, 60)	2
(60, 80)	2
(80, 120)	2
> 120	0

Table 5.9: *Cut values on the τ-Likelihood as a function of the p_T of the jet in the fully simulated events.*

p_T range (GeV)	R_{EM}	F_{Iso}
< 30	0.14	0.3
(30, 45)	0.13	0.27
(45, 60)	0.12	0.26
(60, 80)	0.1	0.26
(80, 120)	0.095	0.24
> 120	0.09	0.23

Table 5.10: *Cut values on the τ variables, R_{EM} and F_{Iso}, as a function of the p_T of the jet in the fast simulation.*

5.4.4.3 Missing Energy Reconstruction

In the full simulation there are several ways to calculate the missing energy [89]. The most common one is to sum up the energies from all calorimeter cells. Instead of calorimetric cells, reconstructed objects can be used as well. Finally, the energy of the muons calculated from the muon spectrometer is added. We use Topological clusters as input objects.

5.4.4.4 W Reconstruction

For the W reconstruction we used several approaches. In the first one we used a constrained fit [55] to reconstruct the W-boson from the two light jets. In addition we developed a multivariate technique to reconstruct the whole $t\bar{t}$ system. This approach is described in the next paragraph.

5.4.4.5 Top Reconstruction

In the first approach we reconstruct the hadronic t-quark as a sum of the reconstructed W[46] and b-jet. The combination that gives the invariant mass m_{bW} closer to m_{top} is chosen. We also tried to reconstruct the t-quark that decayed semileptonically[47]. The

[46] We use a constrained fit for the W reconstruction.
[47] We tried this for the channels from the second group - 4 and 5.

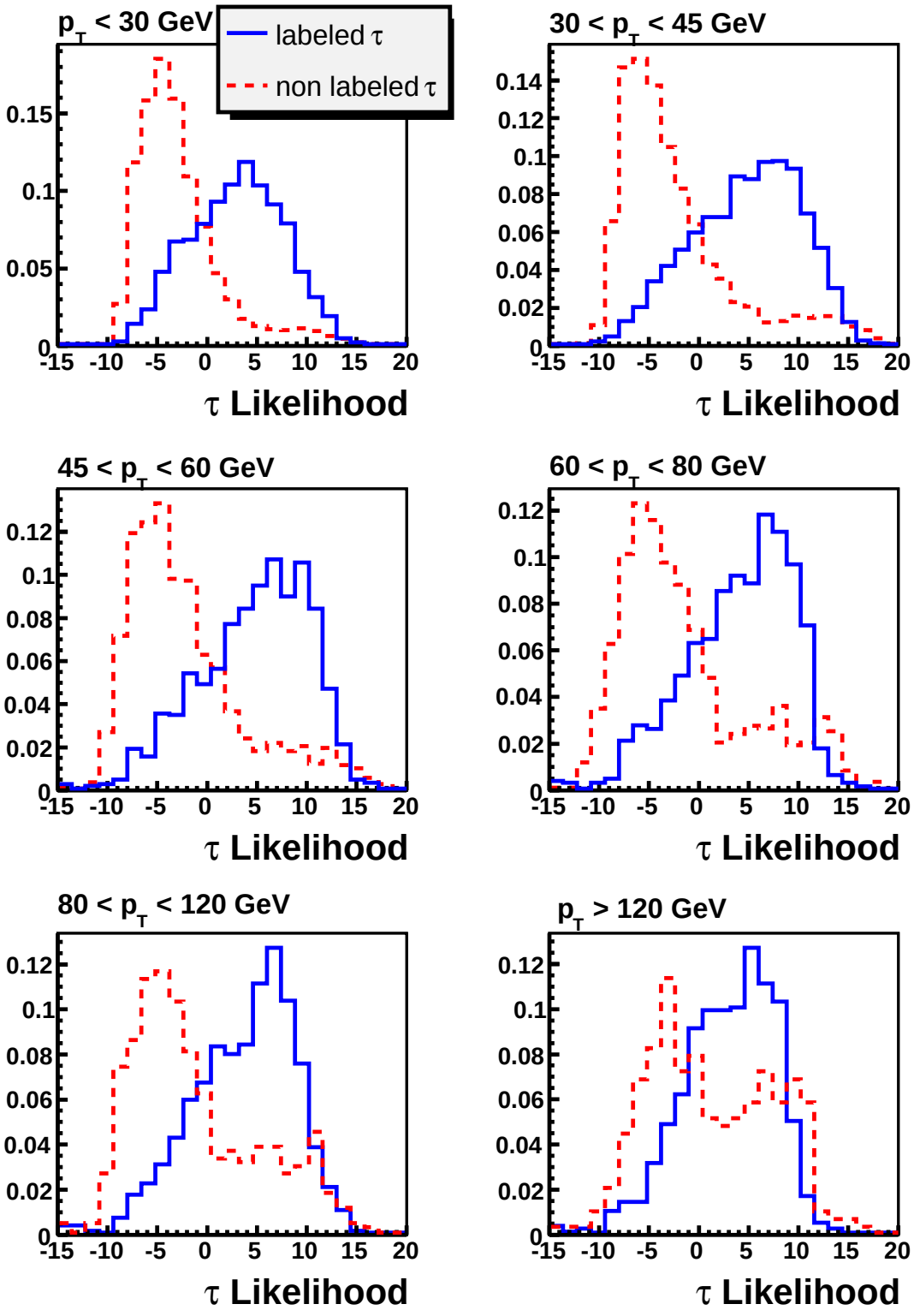

Figure 5.53: *The value of the likelihood function for τ-labeled (blue solid line) and non-labeled (red dashed line) jets for different transverse momenta of the jet.*

reconstruction failed in 30% of the events when we assumed that the ν_ℓ carried the total missing momentum. The reconstruction failed in 20% of the events when we assumed that m_H was already measured, such that we reconstructed the total momentum of the

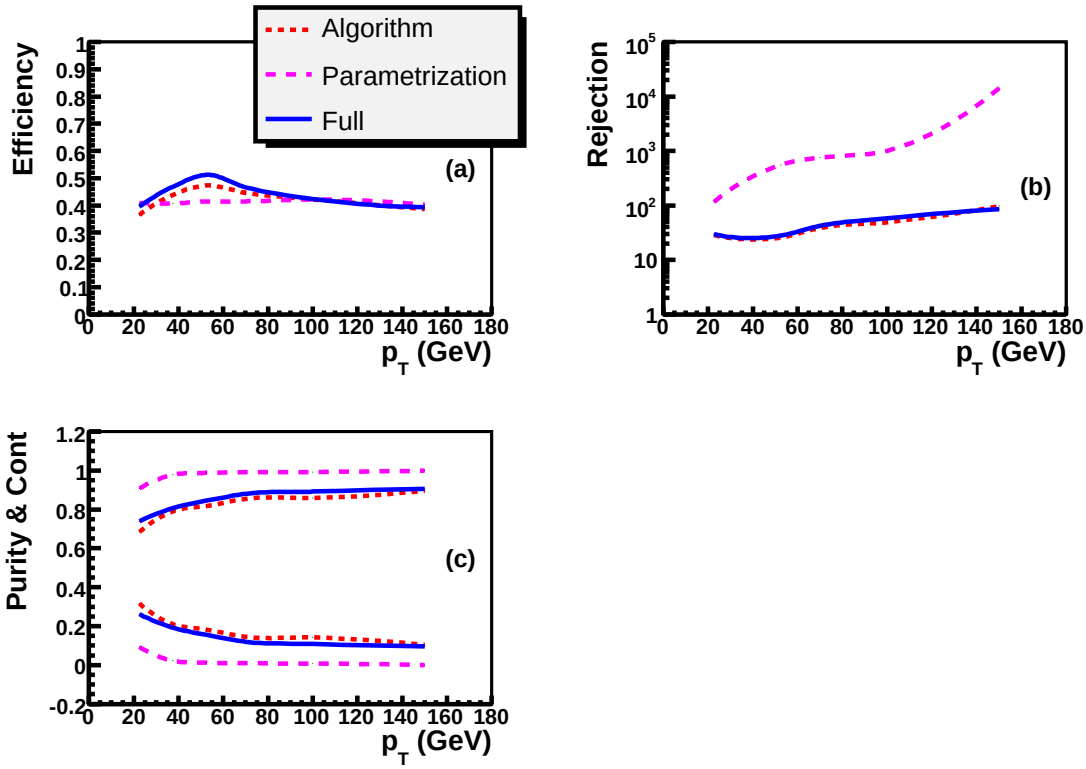

Figure 5.54: *Dependence of the (a) τ-id efficiency, (b) rejection, and purity and contamination (c) on the p_T of the jet of the signal sample. Results are shown for the full simulation (blue solid line), for our fast simulation algorithm (red dashed line), and for the parameterization (magenta dotted line).*

τ-neutrinos and subtracted it from the total missing momentum in order to reconstruct the ν_ℓ. When we combined these two methods, the reconstruction failed in 13% of the events. Eventually, we dropped the reconstruction of the semi-leptonic top quark because it could not give us any distinguishable signal.

In the second method for the reconstruction of the $t\bar{t}$ system[48] we use a multivariate technique based on the distributions of the correct and incorrect combinations of the $t\bar{t}$ system ingredients. For the discriminant variable we use $\ln(L_W)$, where L_W is defined as:

$$L_W = \frac{\prod pdf(V_{true})}{\prod pdf(V_{fake})} \tag{5.12}$$

where *true* denotes the reconstructed $t\bar{t}$ system that matches the MC $t\bar{t}$ system[49], i.e. the correct one, and *fake* denotes the $t\bar{t}$ system that does not match the MC $t\bar{t}$ system, i.e.

[48] $t\bar{t}$ system is $bjjbjj$ for channel 2 and $bjjb\ell\bar{\nu}_\ell$ for channels 4 and 5.

[49] For channels 4 and 5 the matching of the reconstructed $t\bar{t}$ system and the MC one requires that b-jet originating in hadronic(leptonic) decay of the t-quark has the corresponding b-parton within a cone of $\Delta R < 0.3$, that the reconstructed lepton is within $\Delta R < 0.2$ from the MC lepton from the semileptonically decaying t-quark, and that both jets are within $\Delta R < 0.3$ from the partons originating in the W-boson. Similarly, for channel two we asked that all MC partons can be matched to the corresponding reconstructed object.

the incorrect one, V stands for the variable and *pdf* for the probability density function[50]. We use the mass(es)[51] of the W-boson(s) and the t-quark(s), and distances between the reconstructed particles for the calculation of the likelihood. The combination with the maximal likelihood is chosen[52]. Figure 5.55 shows the distribution of the input variables[53] - (a) the mass of the W-boson from hadronically decayed t-quark, (b) the distance ΔR between jets from the W-boson from hadronically decayed t-quark, (c) the mass of the hadronically decayed t-quark, (d) the distance ΔR between the b-jet and the W-boson from hadronically decayed t-quark, and (e) the distance ΔR between the b-jet and the lepton from semileptonically decayed t-quark for the matched combinations (blue solid line), non matched ones (red dashed line) and those that give maximal likelihood (brown dash-dotted line) for $t\bar{t}H^0 \to b\ell\bar{\nu}_\ell\bar{b}jj\tau^+\tau^-$. The $\ln(L_W)$ is shown in Figure 5.55 (f).

5.4.4.6 Final Reconstruction

As an example we describe here the final reconstruction of channel 5, $t\bar{t}H \to t\bar{t}\tau^+\tau^-$ $\to b\ell\bar{\nu}_\ell\bar{b}jj\tau_j\bar{\nu}_\tau\ell\bar{\nu}_\ell\nu_\tau$. A comparison of the full and the fast simulation is presented. The detailed analyses of all channels, including channel 5, are given in sections 5.4.5.1, 5.4.5.2 and 5.4.5.3

Events are preselected if they fulfill the topology requirement: 2 b-tagged jets, one τ-tagged jet, two light jets and two leptons. Every event is required to satisfy at least one High Level Trigger (HLT) condition. These conditions are shown in Table 5.11 for low and high luminosity. We also require that the hadronic W-boson and t-quark are successfully reconstructed[54]. We compare several properties of the reconstructed objects in the full and fast simulation. This is shown in Figure 5.56 for p_T of the first lepton (a), p_T of the τ_j (b), p_T of the first b-jet (c), and p_T of the first jet from W (d). The comparisons of the masses of the reconstructed W-boson and t-quark are shown in Figure 5.56 (e) and (f). Finally, Figure 5.57 shows the invariant mass of the τ-jet and lower-energy lepton (that is the lepton originating from τ in 70% of the cases). One can see a fair agreement between the various reconstructions in the full (blue solid line) and the fast (red dashed line) simulation.

This agreement exists also quantitatively. To demonstrate it, we performed a simple cuts based analysis on channel 5 using $t\bar{t} \to b\ell\bar{\nu}_\ell\bar{b}jj$ as the dominant background. The cut flow is given in Table 5.12 where a good agreement is seen at each stage.

[50] We fit histograms.
[51] In the case of channels 4, 5 we use the mass of the hadronic W boson and top quark. For channel 2 we use the masses of both W-bosons and t-quarks.
[52] Also for events with no matching at all.
[53] For channels 4 and 5.
[54] We use a constrained fit method for the W reconstruction, and minimization of the $|m_{top} - m_{bW}|$ for the top reconstruction at this point.

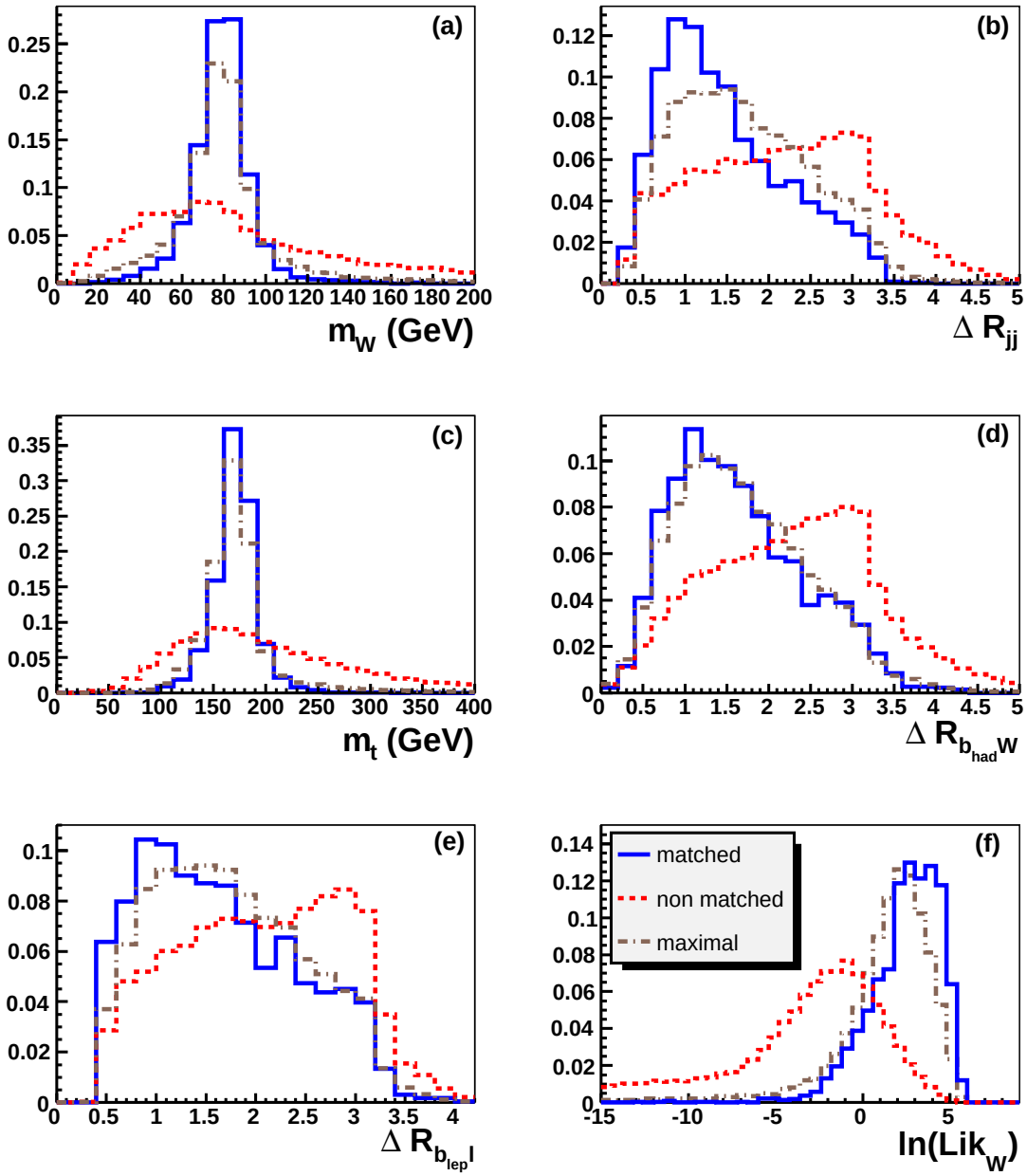

Figure 5.55: *The input variables for the L_W: (a) the mass of the W-boson from hadronically decayed t-quark, (b) the distance ΔR between jets from the W-boson from hadronically decayed t-quark, (c) the mass of the hadronically decayed t-quark, (d) the distance ΔR between the b-jet and the W-boson from hadronically decayed t-quark, and (e) the distance ΔR between the b-jet and the lepton from semileptonically decayed t-quark. Final likelihood $\ln(L_W)$ is given in (f). The matched combination is shown with a blue solid line, the non-matched with a red dashed, and the combination that gives the maximal likelihood L_W with a brown dash-dotted line.*

5.4.5 Analysis

In this section channels 2, 4, and 5 are described in great detail. Every event is required to pass corresponding topology and trigger conditions. We further require that the $t\bar{t}$ system

Selection	Low Luminosity	High Luminosity
Electron (1) or (2)	$p_T(e_1) > 25$ GeV, $p_T(e_2) > 15$ GeV	$p_T(e_1) > 30$ GeV $p_T(e_2) > 20$ GeV
Muon (1) or (2)	$p_T(\mu_1) > 20$ GeV, $p_T(\mu_2) > 10$ GeV	$p_T(\mu_1) > 20$ GeV, $p_T(\mu_2) > 10$ GeV
Electron + Muon	$p_T(e_1) > 15$ GeV and $p_T(\mu_1) > 10$ GeV	$p_T(e_1) > 15$ GeV and $p_T(\mu_1) > 10$ GeV
Jets (1) or (3) or (4)	$p_T(j_1) > 400$ GeV, $p_T(j_3) > 165$ GeV, $p_T(j_4) > 110$ GeV	$p_T(j_1) > 590$ GeV, $p_T(j_3) > 260$ GeV, $p_T(j_4) > 150$ GeV
Jet + $\not{p}_T$	$p_T(j_1) > 70$ GeV and $\not{p}_T > 70$ GeV	$p_T(j_1) > 100$ GeV and $\not{p}_T > 100$ GeV
τ_j + $\not{p}_T$	$p_T(\tau_j) > 35$ GeV and $\not{p}_T > 45$ GeV	$p_T(j_1) > 60$ GeV and $\not{p}_T > 60$ GeV

Table 5.11: *The High Level Trigger (HLT) menu for the low and high luminosity conditions. "Electron (1) or (2)" (for instance) means that the trigger condition is either one electron with the $p_T > 25$ GeV (for low luminosity), or two electrons both having $p_T > 15$ GeV. "Electron + muon" means that the trigger condition is one electron with the $p_T > 15$ GeV and one muon with the $p_T > 10$ GeV (low luminosity).*

Cut flow	Signal fast	Signal full	Background ($t\bar{t} \to b\ell\bar{\nu}_\ell\bar{b}jj$)
Reconstruction	14.1	17.3	341
Trigger	13.9	17.1	330
W reconstruction	11.3	10.4	270
top reconstruction	7.0	6.7	134
$\Sigma p_T(t\bar{t}) > 300$ GeV	6.3	6.0	88
$p_T(lep) > 18$ GeV	3.6	3.6	6
$q_{lep} \cdot q_\tau < 0$	2.8	2.7	3.1
$q_{lep} \cdot q_{lep} > 0$	1.4	1.2	1.5
$m_H > 40$ GeV	1.3	1.1	0.7

Table 5.12: *The number of expected events for 30* fb^{-1} *after simple cuts for $t\bar{t}H \to t\bar{t}\tau^+\tau^- \to b\ell\bar{\nu}_\ell\bar{b}jj\tau_j\bar{\nu}_\tau\ell\bar{\nu}_\ell\nu_\tau$ ($m_H = 120$ GeV) simulated with the full and the fast simulation, and for the $t\bar{t} \to b\ell\bar{\nu}_\ell\bar{b}jj$ simulated with the fast simulation. Reconstruction in the second row means that the event is fully reconstructed.*

is successfully reconstructed[55] and that some preselection requirements are fulfilled.

For the analysis we use a multivariate technique. For all events that pass the topology, trigger and some preselection requirements, we use a discriminant $\ln(L_H)$, where L_H is

[55] We use a multivariate technique in this part (see 5.4.4.5).

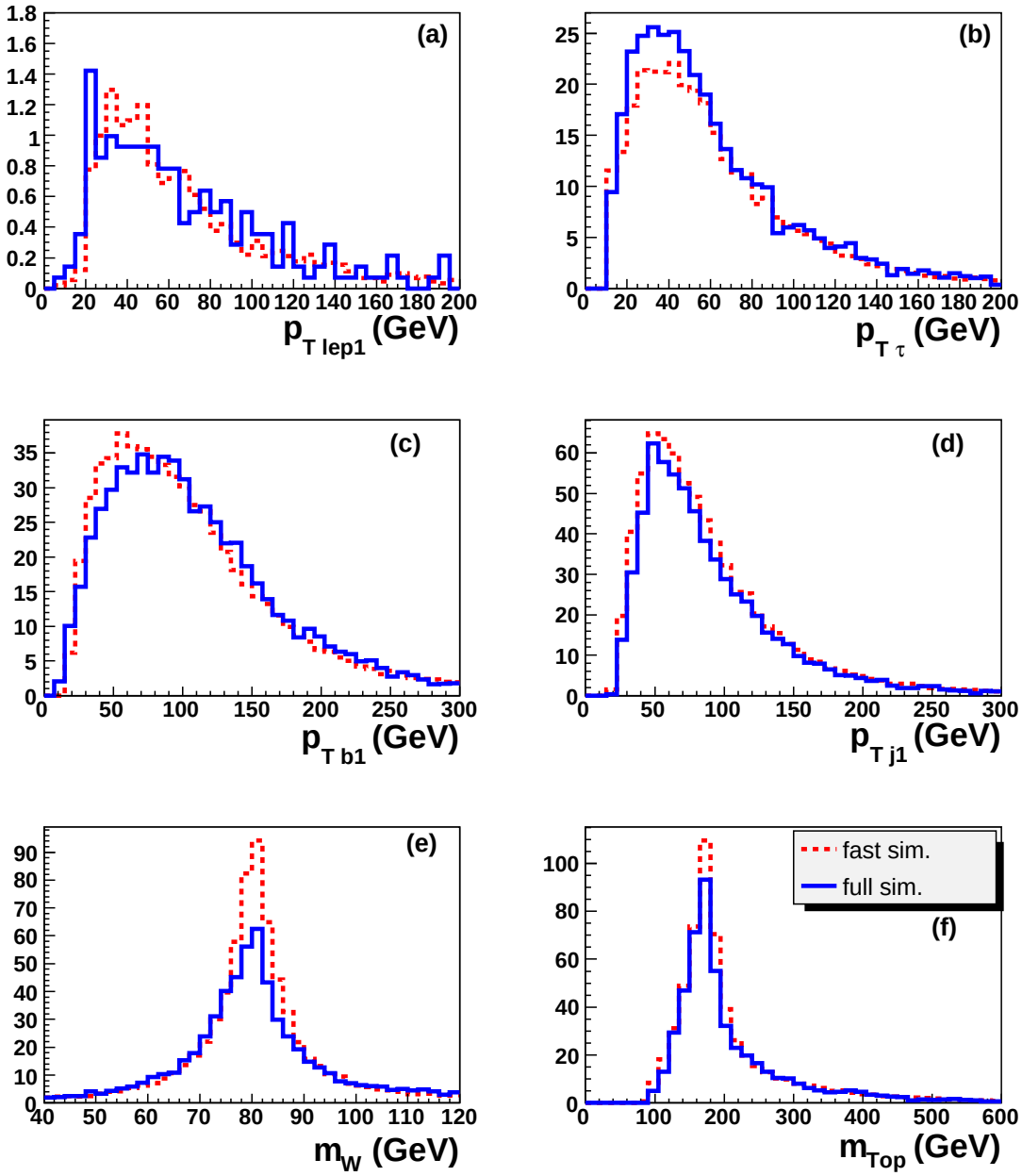

Figure 5.56: *The distributions of the: (a) transverse momentum of the higher energy lepton, (b) transverse momentum of the τ-jet, (c) transverse momentum of the higher energy b-jet, (d) transverse momentum of the higher energy jet from W-boson, (e) mass of the W-boson from hadronically decayed t-quark, and (f) mass of the hadronically decayed t-quark, for events simulated with the fast simulation (red dashed line) and the full simulation (blue solid line) in the $t\bar{t}H \to t\bar{t}\tau^+\tau^- \to b\ell\bar{\nu}_\ell\bar{b}jj\tau_j\bar{\nu}_\tau\ell\bar{\nu}_\ell\nu_\tau$ channel.*

defined as:

$$L_H = \frac{\prod pdf(V_{Sig})}{\prod pdf(V_{Bkg})} \tag{5.13}$$

where $V_{Sig(Bkg)}$ stands for the Signal (Background) Variable. For the background we use the dominant $t\bar{t}$ source.

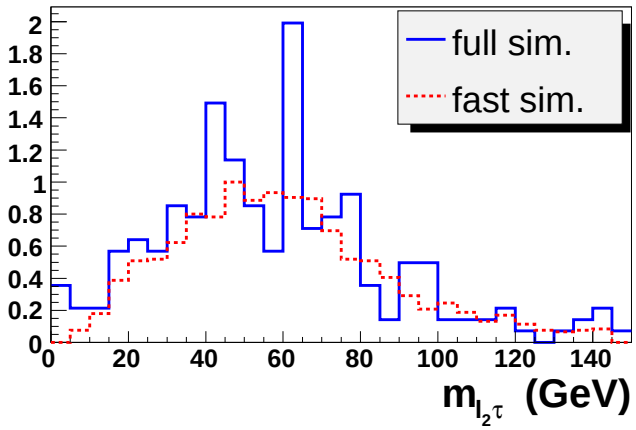

Figure 5.57: *The distribution of the invariant mass of the τ-jet and the lower energy lepton in the fast (red dashed line) and the full simulation (blue solid line) in the $t\bar{t}H \to t\bar{t}\tau^+\tau^- \to b\ell\bar{\nu}_\ell\bar{b}jj\tau_j\bar{\nu}_\tau\ell\bar{\nu}_\ell\nu_\tau$ channel.*

5.4.5.1 Channel 2

Channel 2, $t\bar{t}H \to t\bar{t}\tau^+\tau^- \to bjj\bar{b}jj\tau_j\bar{\nu}_\tau\ell\bar{\nu}_\ell\nu_\tau$, contains one τ-jet, two b-jets, four light jets, one energetic lepton and missing energy. The fact that both t-quarks in the signal decay hadronically has two important consequences:

1. Both t-quarks can be fully reconstructed.
2. The total physical[56] missing energy originates in the Higgs boson. That enables to reconstruct the real mass of the Higgs boson using a collinear approximation (see Appendix G).

The dominant backgrounds are $t\bar{t}$ with both t-quarks decaying hadronically, $t\bar{t} \to bjj\bar{b}jj$, or one decays semileptonically and the other hadronically, $t\bar{t} \to b\ell\bar{\nu}_\ell\bar{b}jj$. To suppres background, we applied the following preselection cuts:

- The reconstructed Higgs mass[57] is in a window between 0 and 250 GeV. This variable is also an input variable to the Likelihood and it is shown in Figure 5.60 (b).
- The charges of the τ-jet and the lepton must be opposite.
- The transverse momentum of the lepton is bigger than 10 GeV (Figure 5.58 (a)).
- The transverse momentum of the τ-jet is bigger than 35 GeV (Figure 5.58 (b)).
- The missing p_T is bigger than 20 GeV (Figure 5.58 (c)).
- $\ln(L_W) > 0.75$ (defined in 5.4.4.5)(Figure 5.58 (d)).

[56] The physical missing energy originates in neutrinos. The non-physical can be detector related.
[57] Where we use a collinear approximation to reconstruct the Higgs mass.

- The mass of the first reconstructed W-boson[58] is between 60 and 110 GeV (Figure 5.59 (a)).
- The mass of the second reconstructed W-boson[59] is between 40 and 110 GeV (Figure 5.59 (c)).
- The masses of both t-quarks are between 140 and 210 GeV (Figure 5.59 (b) and (d)).

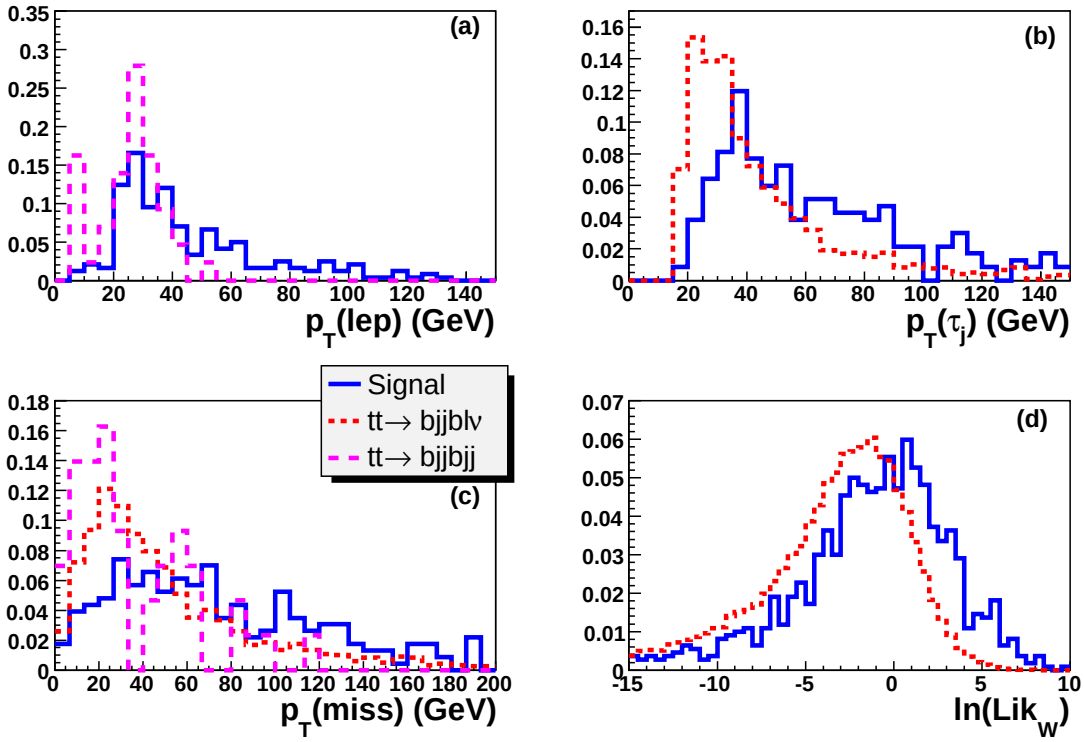

Figure 5.58: *The transverse momenta of the lepton (a) and τ_j (b), the missing momentum (c), and the* $\ln(L_W)$ *(d) for the signal events (blue solid line), and for the $t\bar{t} \to b\ell\bar{\nu}_\ell\bar{b}jj$ (red dotted line) and the $t\bar{t} \to bjj\bar{b}jj$ (magenta dashed line) background processes. Only the backgrounds affected with the cut are shown in the corresponding part of the Figures.*

For the determination of the likelihood the $t\bar{t} \to b\ell\bar{\nu}_\ell\bar{b}jj$ events serve as a background. The input variables for the discriminant likelihood are:

- The transverse mass of the lepton[60] and missing p_T, defined as

$$m_T(l\not{p}_T) \equiv \sqrt{(|p_T(l)| + |\not{p}_T|)^2 - |\overrightarrow{p_l} + \overrightarrow{\not{p}_T}|^2}. \tag{5.14}$$

[58]The first reconstructed t-quark is the one with the more energetic b-jet. The corresponding W-boson is called the first.

[59]The second reconstructed t-quark is the one with the less energetic b-jet. The corresponding W-boson is called the second.

[60]The mass of the lepton is neglected.

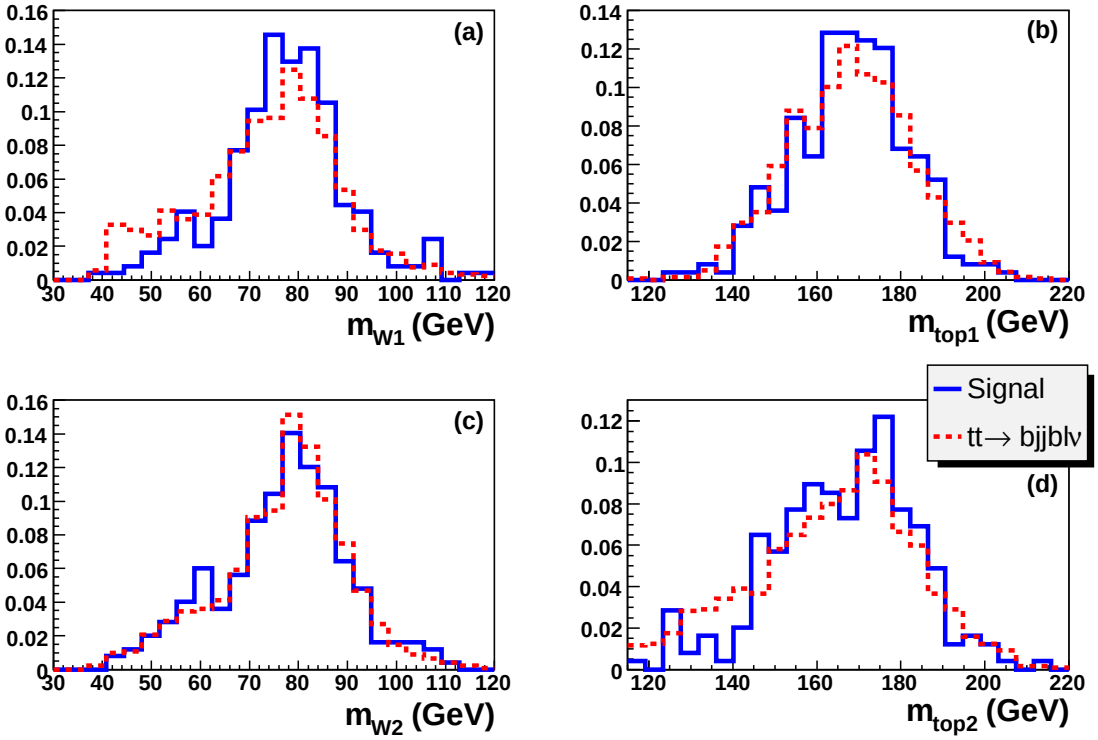

Figure 5.59: *The reconstructed masses of the first W-boson (a), the first t-quark (b), the second W-boson (c), and the second t-quark (d) for the signal events (blue solid line), and the $t\bar{t} \to b\ell\bar{\nu}_\ell\bar{b}jj$ (red dotted line) background process.*

In the $t\bar{t} \to b\ell\bar{\nu}_\ell\bar{b}jj$ events, most of the missing energy originates in $W \to \ell\bar{\nu}_\ell$ decay, while in the signal events the biggest part of the missing energy originates in τ_l decays. It is expected that $m_T(l\not{p}_T)$ would have an edge at m_W for the $t\bar{t} \to b\ell\bar{\nu}_\ell\bar{b}jj$ events, and would peak toward zero for the signal events. This is shown in Figure 5.60 (a).

- The reconstructed Higgs mass shown in Figure 5.60 (b) (see Appendix G). In order to further suppress backgrounds, especially the irreducible $Zt\bar{t} \to \tau^+\tau^- t\bar{t}$, the likelihood is set to zero if the reconstructed Higgs mass is smaller[61] than 100 GeV or bigger than 170 GeV.

- x_l, i.e the fraction of the energy of the leptonically decayed τ_l carried by neutrinos from that decay shown in Figure 5.60 (c) (see Appendix G). The likelihood is set to zero if either x_l or x_h, i.e. the fraction of the energy of the hadronically decayed τ_l carried by ν_τ, are bigger than 1.

- The following distances:

[61] For a Higgs mass of 110 GeV, the lower limit was set to 92 GeV, and for a Higgs mass of 130 GeV to 105 GeV.

  - $\Delta R_{\tau_j l}$ between the τ-jet and the lepton. This distance is smaller in the signal than in the $t\bar{t}$ events (Figure 5.60 (d)).
  - ΔR_{jj2} between the light jets from the W-boson. This distance is smaller in the signal than in the $t\bar{t}$ events. We use the distance between the jets that correspond to the second W-boson.
  - ΔR_{bW1} between the b-jet and the reconstructed W-boson. This distance is smaller in the signal than in the $t\bar{t}$ events. We use the distance between the b-jet and the W that correspond to the first t-quark.

- The following angular distances in the transverse plane:
  - The minimal and maximal $\Delta\Phi$ between τ_j or lepton, and the missing momentum (the maximal one is shown in Figure 5.60 (e))
  - $\Delta\Phi$ betwen the visible Higgs boson ($l\tau_j$)[62] and the missing momentum. In the signal events complete missing energy originates in the Higgs boson. Thus, it is expected that the $\vec{\not{p}}_T$ and visible Higgs boson are closer in the signal than in the background (Figure 5.60 (f)).
  - $\Delta\Phi$ between the reconstructed $t\bar{t}$ system and the missing momentum. There is no missing energy originating in the $t\bar{t}$ system in the signal events. Thus, the reconstructed $t\bar{t}$ system and $\vec{\not{p}}_T$ are more back-to-back in the signal events.

The resulting discriminant for $m_h = 120$ GeV is shown in Figure 5.61. For both $m_h = 110$ GeV and $m_h = 130$ GeV, the likelihood was slightly changed[63]. The events are accepted if $\ln(L_H) > 2.5$ for $m_h = 110$ GeV and $m_h = 120$ GeV, and if $\ln(L_H) > 2.1$ for $m_h = 130$ GeV. Results for 30 fb^{-1} are shown in Table 5.13. The $t\bar{t}$ background contributes more than 80% to the total background (Table 5.14).

m_H (GeV)	Signal	Background	S/B	$S/\sqrt{B}$
110	0.77	0.72	1.07	0.91
120	0.93	0.82	1.13	1.03
130	0.45	0.77	0.58	0.51

Table 5.13: *The number of expected events for the signal and the total background for* 30 fb^{-1} *for channel 2,* $t\bar{t}H \to t\bar{t}\tau^+\tau^- \to bjj\bar{b}jj\tau_j\bar{\nu}_\tau\ell\bar{\nu}_\ell\nu_\tau$. S/B *and* $S/\sqrt{B}$ *are also given.*

[62] Sum of the τ-jet and lepton.
[63] The reconstructed mass of the Higgs boson is changed.

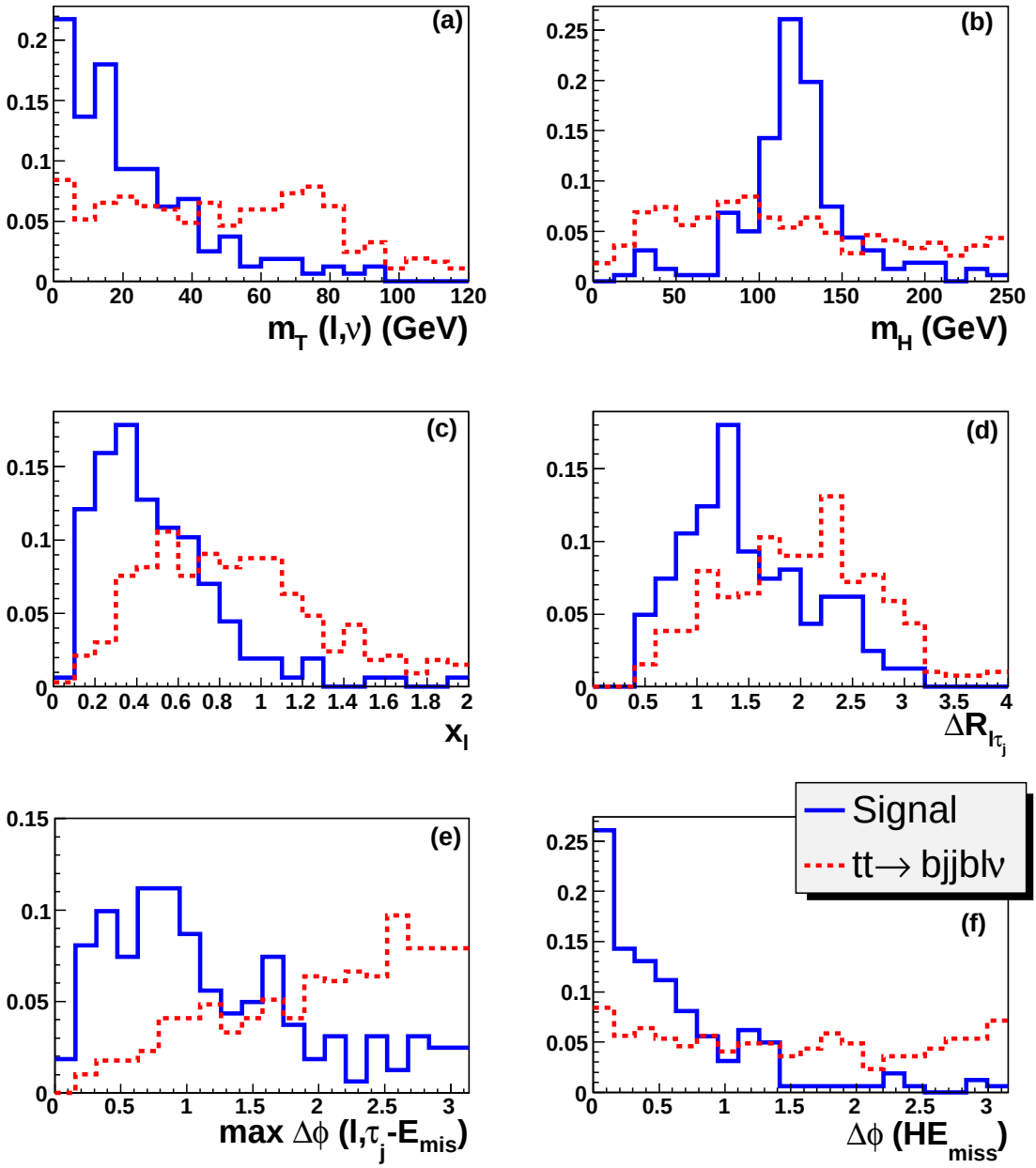

Figure 5.60: *The input variables for the L_H: (a) the transverse mass of the lepton and neutrino, (b) the reconstructed Higgs mass, (c) x_l, (d) the distance between lepton and τ_j, (e) maximal $\Delta\phi$ between lepton or τ_j, and missing p_T, and (f) $\Delta\phi$ between reconstructed Higgs boson and missing p_T. The distributions are shown for the signal events (blue solid line), and the $t\bar{t} \to b\ell\bar{\nu}_\ell\bar{b}jj$ (red dotted line) background process.*

m_H (GeV)	$t\bar{t}(\%)$	$Zt\bar{t}(\%)$ $Z \to \tau^+\tau^-$ $t\bar{t} \to b\ell\bar{\nu}_\ell\bar{b}jj$	$Zt\bar{t}(\%)$ $Z \to \tau^+\tau^-$ $t\bar{t} \to bjj\bar{b}jj$
110	79	3	18
120	84	3	13
130	89	3	8

Table 5.14: *The dominant background sources for channel 2,* $t\bar{t}H \to t\bar{t}\tau^+\tau^- \to bjj\bar{b}jj\tau_j\bar{\nu}_\tau\ell\bar{\nu}_\ell\nu_\tau$*, (in %).*

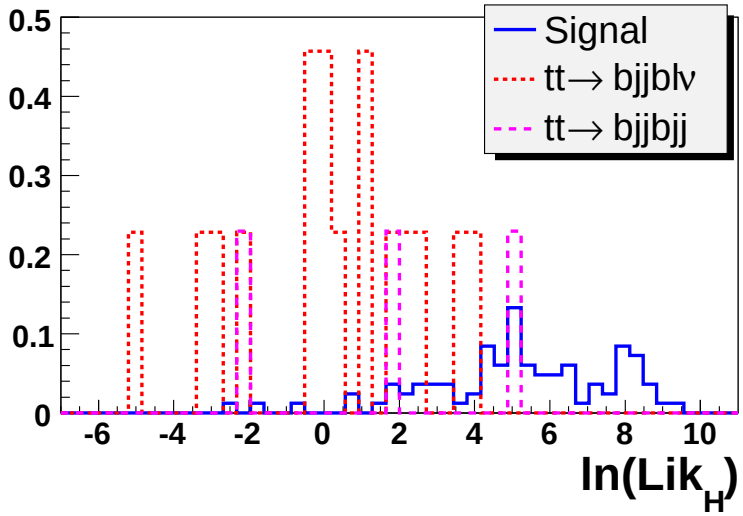

Figure 5.61: *The resulting likelihood* L_H *for the the signal with* $m_H = 120$ *GeV (blue solid line), and the* $t\bar{t} \to b\ell\bar{\nu}_\ell\bar{b}jj$ *(red dotted line) and the* $t\bar{t} \to bjj\bar{b}jj$ *(magenta dashed line) background processes.*

5.4.5.2 Channel 4

Channel 4, $t\bar{t}H \rightarrow t\bar{t}\tau^+\tau^- \rightarrow b\ell\bar{\nu}_\ell\bar{b}jj\tau_j\bar{\nu}_\tau\tau_j\nu_\tau$, contains two τ-jets, two b-jets, two light jets, one energetic lepton and missing energy. The dominant background is $t\bar{t} \rightarrow b\ell\bar{\nu}_\ell\bar{b}jj$. In order to suppress the background we applied the following preselection cuts:

- The charges of the two τ-jets must be opposite to remove fake τ-jets.
- The transverse momenta of the τ-jets should fulfill $p_T(\tau_{j_1}) > 50$ GeV and $p_T(\tau_{j_2}) > 30$ GeV (Figures 5.62 (a) and (b)).
- The transverse momentum of the lepton is bigger than 10 GeV (Figure 5.62 (c)).
- The missing p_T must be bigger than 30 GeV (Figure 5.62 (d)).
- $\ln(L_W) > 0$ (Figure 5.63 (a)).
- The invariant mass of the lepton and b-jet from the semileptonic t-quark decay $m_{t_l} > 30$ GeV(Figure 5.63 (b)).
- The mass of the reconstructed W-boson from the hadronically decayed t-quark is between 40 and 110 GeV (Figure 5.63 (c)).
- The mass of the reconstructed hadronically decayed t-quark is between 135 and 210 GeV (Figure 5.63 (d)).

The input variables for the discriminant likelihood are:

- The transverse mass of the lepton and missing energy (Eq. (5.14)). In the $t\bar{t} \rightarrow b\ell\bar{\nu}_\ell\bar{b}jj$ events most of the missing energy is coming from $W \rightarrow \ell\bar{\nu}_\ell$ decay, while in the signal events the significant part of the missing energy originates in $\tau_l \rightarrow \tau_j\nu_\tau$. This is shown in Figure 5.64 (a).
- The transverse momentum of the hadronically decayed t-quark (Figure 5.64 (b)).
- The following distances:
  - $\Delta R_{\tau_j\tau_j}$ between the two τ-jets. This distance is smaller in the signal than in the $t\bar{t}$ events (Figure 5.64 (c)).
  - ΔR_{bW} between the b-jet and the reconstructed W-boson from hadronically decayed t-quark. This distance is smaller in the signal than in the $t\bar{t}$ events (Figure 5.64 (d)).
- The following angular distances in transverse plane:

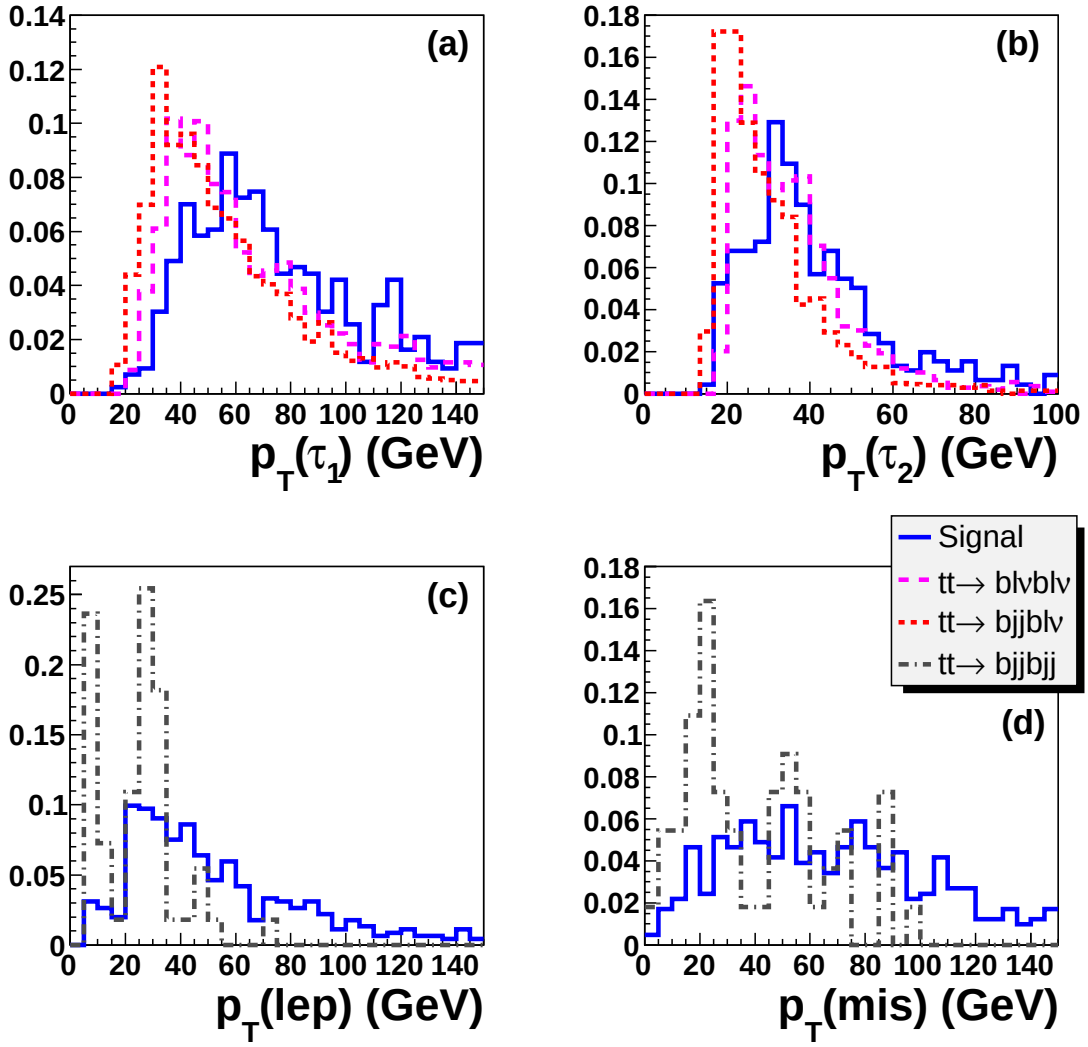

Figure 5.62: *The transverse momenta of the first τ-jet (a), the second τ-jet (b), the lepton (c), and the missing transverse momentum (d) for the signal events (blue solid line), and for the $t\bar{t} \to b\ell\bar{\nu}_\ell\bar{b}jj$ (red dotted line), the $t\bar{t} \to b\ell\bar{\nu}_\ell\bar{b}\ell\nu_\ell$ (magenta dashed line) and the $t\bar{t} \to bjj\bar{b}jj$ (black dash-dotted line) background processes.*

– The minimal $\Delta\Phi$ between the τ_j and the missing momentum (Figure 5.65 (a))[64].

– $\Delta\Phi$ between the lepton and the missing momentum (Figure 5.65 (b)).

– $\Delta\Phi$ between the reconstructed visible Higgs boson[65] and the missing momentum (Figure 5.65 (c)).

– $\Delta\Phi$ between the reconstructed visible Higgs boson and the b-jet from the hadronically decayed t-quark[66] (Figure 5.65 (d)).

– $\Delta\Phi$ between the reconstructed hadronically decayed t-quark and the missing

[64]There are two τ_j in events, so we chose the smaller $\Delta\Phi$.
[65]The sum of the two τ-jets.
[66]In the $t\bar{t} \to b\ell\bar{\nu}_\ell\bar{b}jj$ events both jets from W-boson are often tagged as τ-jets.

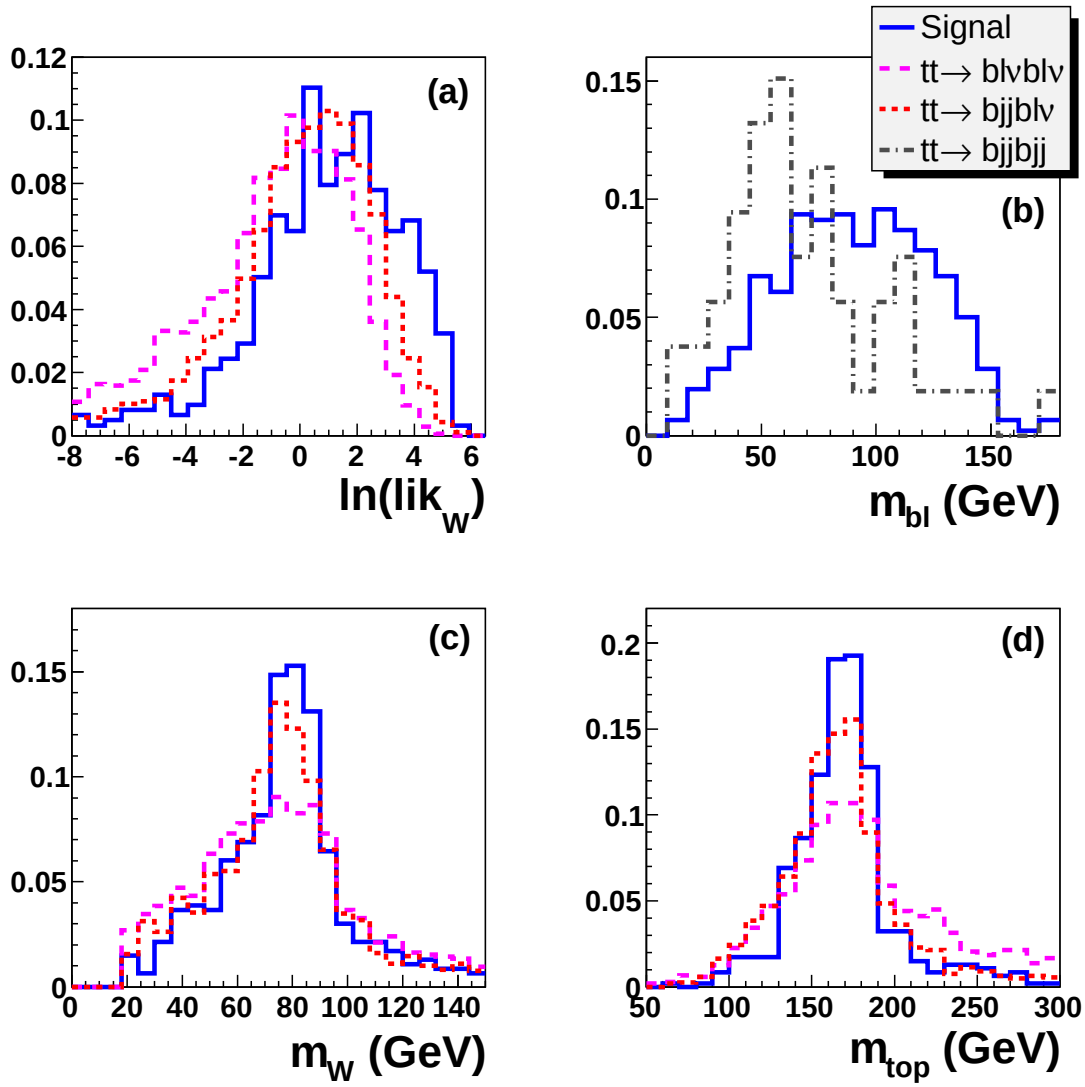

Figure 5.63: *The* $\ln(L_W)$ *(a), the invariant mass of the lepton and b-jet from semileptonically decayed t-quark (b), the mass of the reconstructed W-boson from hadronically decayed t-quark (c), and the mass of the reconstructed hadronically decayed t-quark (d) for the signal events (blue solid line), and for the* $t\bar{t} \to b\ell\bar{\nu}_\ell\bar{b}jj$ *(red dotted line), the* $t\bar{t} \to b\ell\bar{\nu}_\ell\bar{b}\ell\nu_\ell$ *(magenta dashed line) and the* $t\bar{t} \to bjj\bar{b}jj$ *(black dash-dotted line) background processes.*

momentum (Figure 5.65 (e)).

- Finally, we have used the maximal $\Delta\eta$ between the visible Higgs boson and the reconstructed t-quark[67] (Figure 5.65 (f)).

The resulting discriminant is shown in Figure 5.66. For all masses we accepted events if $\ln(L_H) > 1.3$. For the $m_H = 110$ GeV and $m_H = 120$ GeV we required that the invariant mass of the two τ_j, i.e. the visible Higgs mass, is between 50 and 140 GeV, while for $m_H = 130$ GeV we set the mass window to (55, 140) GeV. The distribution of

[67] We consider the fully reconstructed hadronically decayed t-quark, while for the semileptonically decayed t-quark, we encountered just its visible part, i.e. $t_l = b + l$.

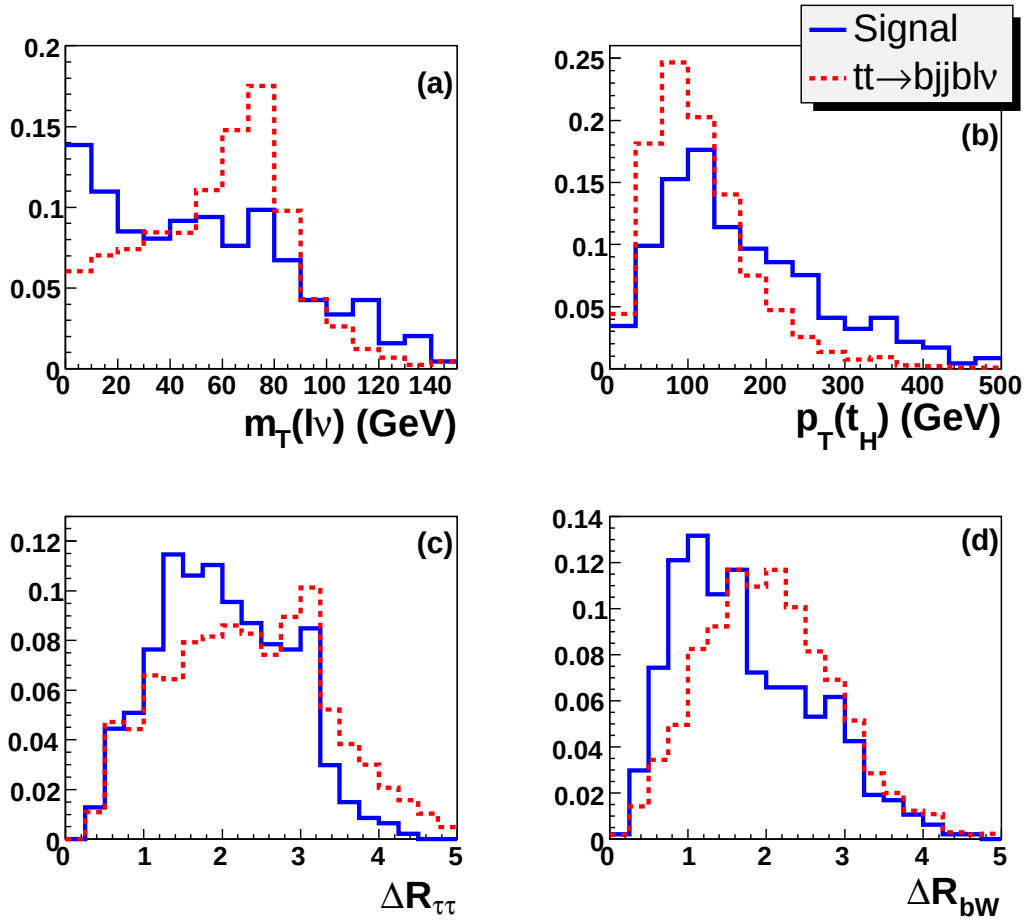

Figure 5.64: *The input variables for the L_H: (a) the transverse mass of the lepton and neutrino, (b) the transverse momentum of the reconstructed hadronically decayed t-quark, $p_T(t_H)$, (c) the ΔR between two τ-jets, and (d) the ΔR between the b-jet and the W-boson from the hadronically decayed t-quark, for the signal events (blue solid line), and for the $t\bar{t} \to b\ell\bar{\nu}_\ell\bar{b}jj$ (red dotted line) background process.*

the visible Higgs mass for $m_H = 120$ GeV is shown in Figure 5.67 before (a) and after (b) the aforementioned cut on the likelihood. It can be seen clearly that $t\bar{t}$ events, where both jets from the W-boson decay are tagged as τ-jets, have smaller values of the likelihood, and, therefore, are cut off.

The final results for this channel for 30 fb^{-1} are shown in Table 5.15. About 50% of the total background originates from $t\bar{t}$ events, and $\sim 40\%$ is from the irreducible $Zt\bar{t} \to \tau^+\tau^- t\bar{t}$ (Table 5.16).

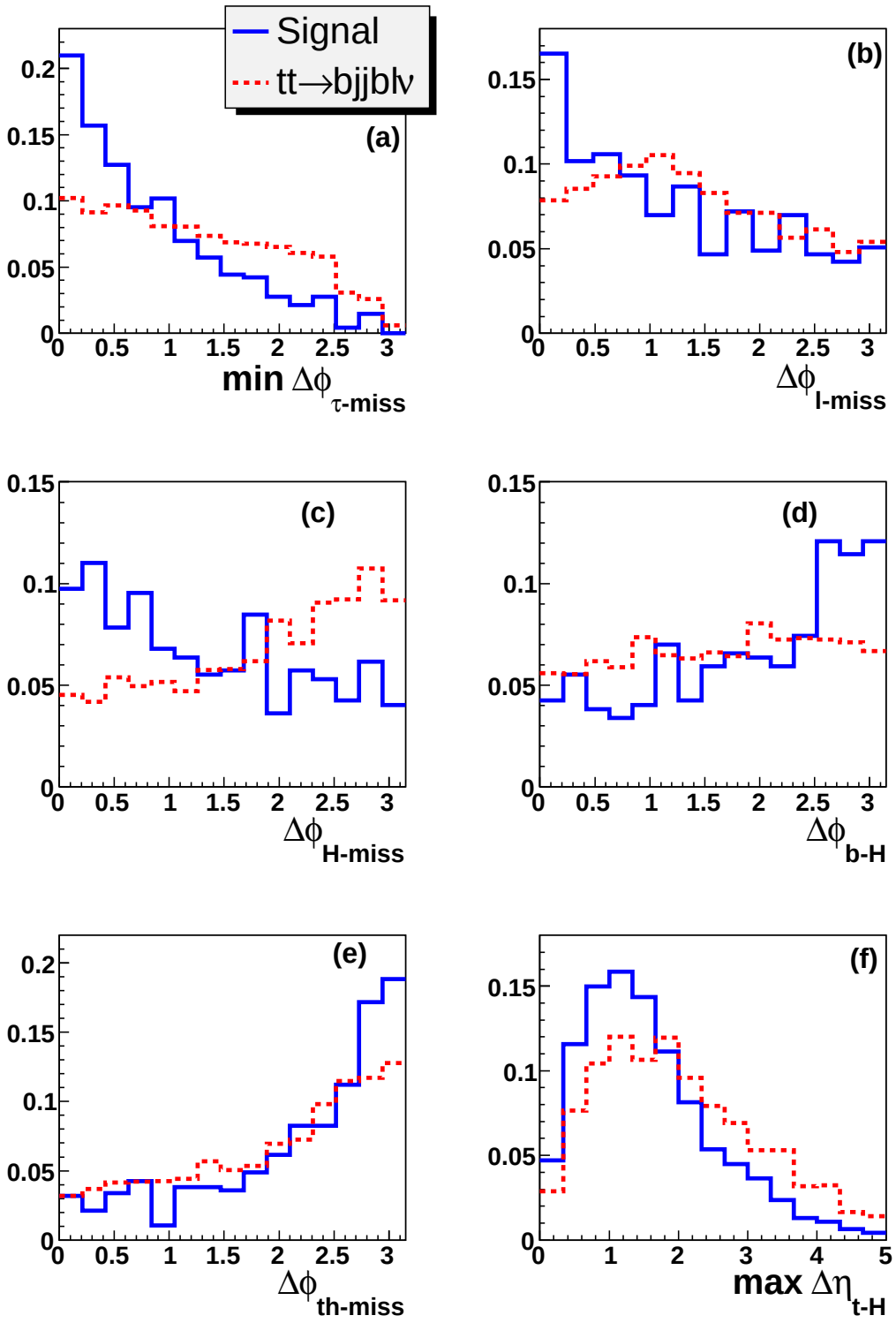

Figure 5.65: *The input variables for the L_H: (a) the minimal $\Delta\phi$ between the τ-jet and the missing momentum, (b) $\Delta\phi$ between the lepton and the missing momentum, (c) $\Delta\phi$ between the visible Higgs boson and the missing momentum, (d) $\Delta\phi$ between the visible Higgs boson and the b-jet from the hadronically decayed t-quark, (e) $\Delta\phi$ between the hadronically decayed t-quark and the missing momentum, and (f) the maximal $\Delta\eta$ between the reconstructed visible Higgs boson and the t-quark. The distributions are shown for the signal events (blue solid line), and for the $t\bar{t} \to b\ell\bar{\nu}_\ell\bar{b}jj$ (red dotted line) background process.*

m_H (GeV)	Signal	Background	S/B	$S/\sqrt{B}$
110	0.56	0.7	0.8	0.67
120	0.71	0.7	1.01	0.85
130	0.35	0.65	0.54	0.43

Table 5.15: *The number of expected events for the signal and the total background for* 30 fb^{-1} *for channel 4,* $t\bar{t}H \to t\bar{t}\tau^+\tau^- \to b\ell\bar{\nu}_\ell\bar{b}jj\tau_j\bar{\nu}_\tau\tau_j\nu_\tau$. *$S/B$ and $S/\sqrt{B}$ are also given.*

m_H (GeV)	$t\bar{t}$(%)	$Zt\bar{t}$(%) $Z \to \tau^+\tau^-$ $t\bar{t} \to b\ell\bar{\nu}_\ell\bar{b}jj$	$Zt\bar{t}$(%) $Z \to \tau^+\tau^-$ $t\bar{t} \to b\tau\bar{\nu}_\tau\bar{b}jj$
110	49	41	10
120	49	41	10
130	52	37	11

Table 5.16: *The dominant background sources for channel 4,* $t\bar{t}H \to t\bar{t}\tau^+\tau^- \to b\ell\bar{\nu}_\ell\bar{b}jj\tau_j\bar{\nu}_\tau\tau_j\nu_\tau$ *(in %).*

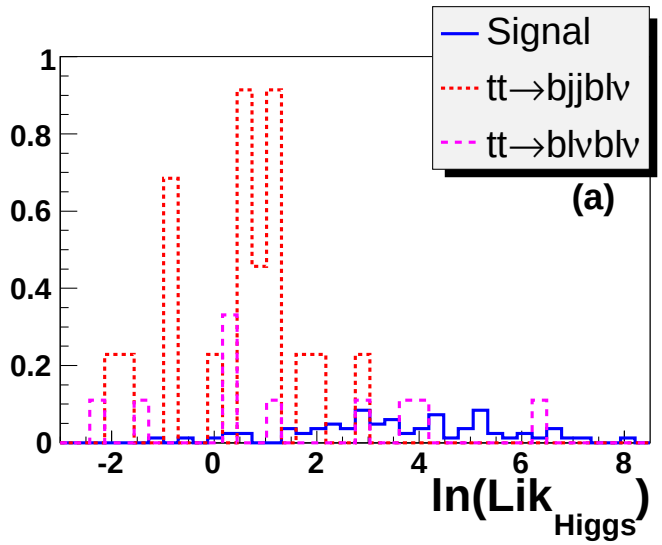

Figure 5.66: *The resulting likelihood L_H for the the signal with $m_H = 120$ GeV (blue solid line), and for the $t\bar{t} \to b\ell\bar{\nu}_\ell\bar{b}jj$ (red dotted line) and the $t\bar{t} \to b\ell\bar{\nu}_\ell\bar{b}\ell\nu_\ell$ (magenta dashed line) background processes.*

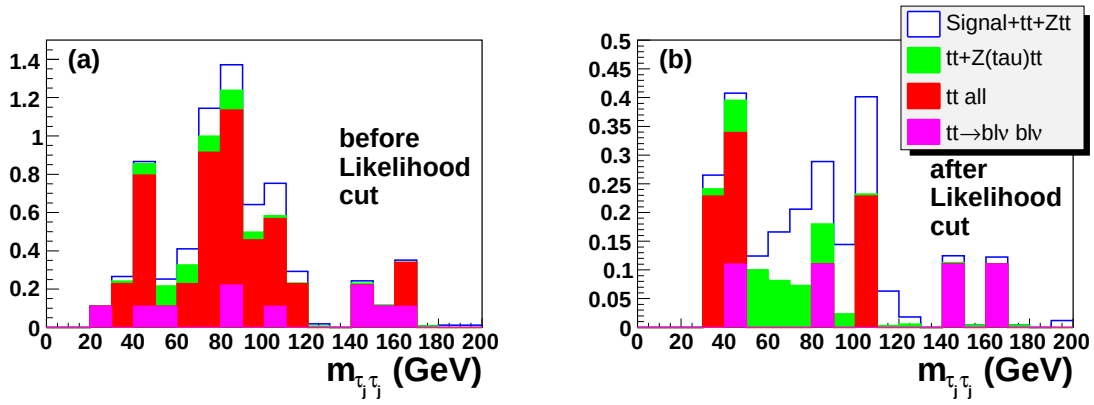

Figure 5.67: *The invariant mass of the two τ-jets (visible Higgs boson) before (a) and after (b) cut on the likelihood (see text) for $m_H = 120$ GeV, shown for the signal on top of the backgrounds.*

5.4.5.3 Channel 5

Channel 5, $t\bar{t}H \to t\bar{t}\tau^+\tau^- \to b\ell\bar{\nu}_\ell\bar{b}jj\tau_j\bar{\nu}_\tau\ell\bar{\nu}_\ell\nu_\tau$, contains one τ-jet, two b-jets, two light jets, two energetic leptons and missing energy. The dominant backgrounds are $t\bar{t}$ with both top-quarks decay semi-leptonically, or one decays semi-leptonically and the other hadronically, $t\bar{t} \to b\ell\bar{\nu}_\ell\bar{b}\ell\nu_\ell$ and $t\bar{t} \to b\ell\bar{\nu}_\ell\bar{b}jj$, respectively. In order to reduce the background, we applied the following preselection cuts:

- The charges of the τ-jet and the lepton[68] coming from the other τ must be opposite.
- $\ln(L_W) > 0.5$ (Figure 5.68 (a)).
- The missing p_T is bigger than 30 GeV (Figure 5.68 (b)).
- The transverse momenta of each of the leptons is bigger than 15 GeV (Figure 5.68 (c) and (d)).
- The mass of the reconstructed W-boson from the hadronically decayed t-quark is between 40 and 110 GeV (Figure 5.68 (e)).
- The mass of the reconstructed hadronically decayed t-quark is between 130 and 210 GeV (Figure 5.68 (f)).

For the determination of the likelihood the $t\bar{t} \to b\ell\bar{\nu}_\ell\bar{b}\ell\nu_\ell$ events serve as a background. The input variables for the discriminant likelihood are:

- The transverse momentum of the τ-jet. This is shown in Figure 5.69 (a).
- The scalar sum of the transverse momenta of the visible particles from the $t\bar{t}$ system and the missing momentum (Figure 5.69 (b)):

$$p_T(t\bar{t} + \not{p}_T) \equiv p_T(l_1) + p_T(b_1) + p_T(b_2) + p_T(j_1) + p_T(j_2) + \not{p}_T \tag{5.15}$$

- The distance, ΔR, between the light jets that originate in the W-boson (Figure 5.69 (c)). The light jets are closer in the signal than in the $t\bar{t}$ events.
- The following angular distances in the transverse plane:
  - $\Delta\Phi$ between the Higgs boson[69] and the missing momentum (Figure 5.69 (d)).
  - $\Delta\Phi$ between the reconstructed hadronically decayed t-quark and the missing momentum.

[68] Since we reconstruct the complete $t\bar{t}$ system, the lepton that is not associated with the semileptonically decayed top quark, is assumed to originate in the τ (see section 5.4.4.5).

[69] Here, the Higgs boson is the pseudo particle defined by the sum of the τ-jet and lepton originating from the other τ.

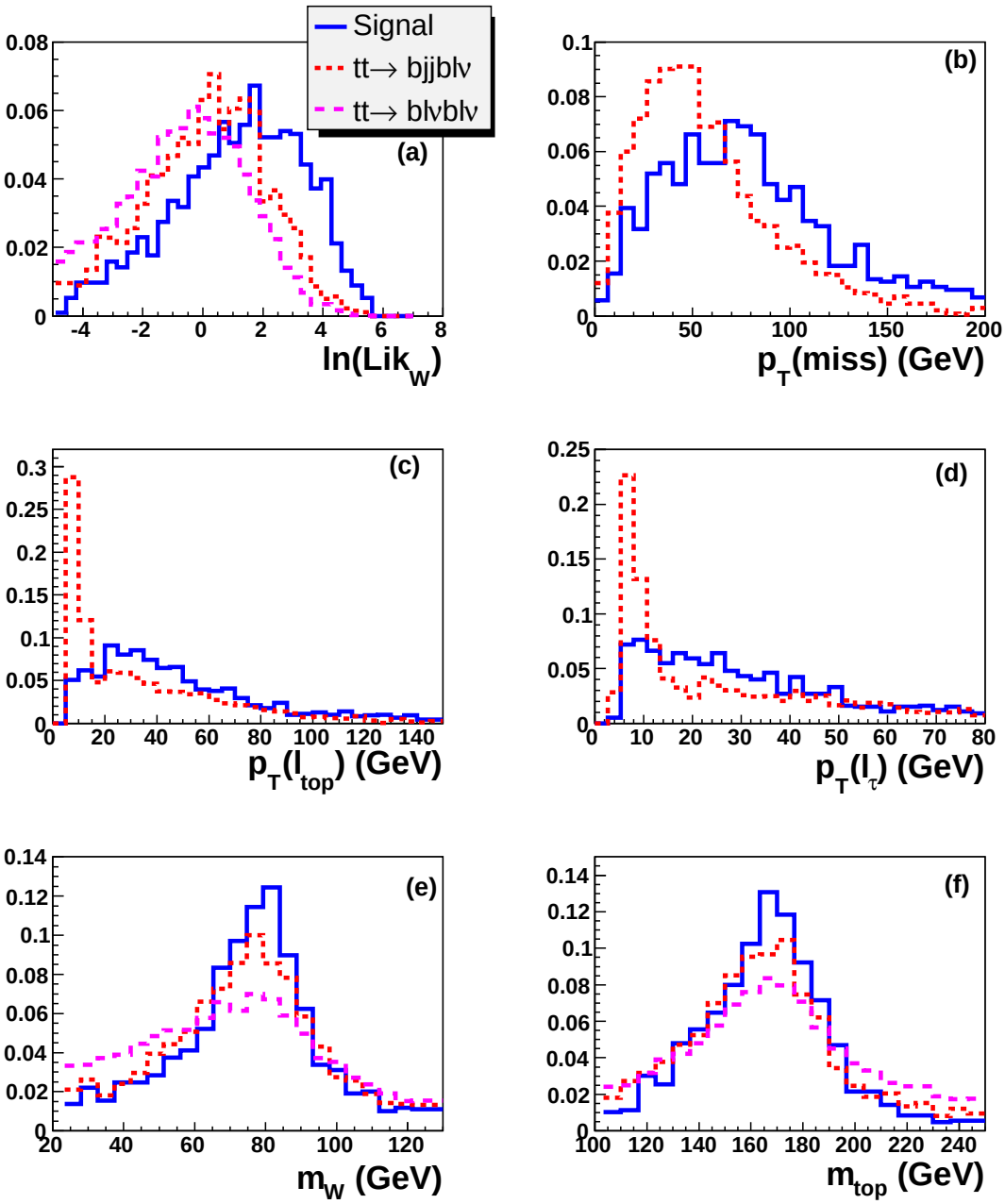

Figure 5.68: *The distributions of the: (a)* $\ln(L_W)$*, (b) missing transverse momentum, (c) transverse momentum of the lepton from semileptonically decayed t-quark, (d) transverse momentum of the lepton from* τ*, (e) mass of the W-boson from hadronically decayed t-quark, and (f) mass of the hadronically decayed t-quark, for the signal events (blue solid line), and for the* $t\bar{t} \to b\ell\bar{\nu}_\ell\bar{b}jj$ *(red dotted line) and the* $t\bar{t} \to b\ell\bar{\nu}_\ell\bar{b}\ell\nu_\ell$ *(magenta dashed line) background processes.*

- Finally, we use $\Delta\eta$ between the following reconstructed objects:
  - The τ-jet and the lepton coming from the other τ (Figure 5.69 (e)).
  - The b-jet and the reconstructed W coming from the hadronically decayed t-quark (Figure 5.69 (f)).

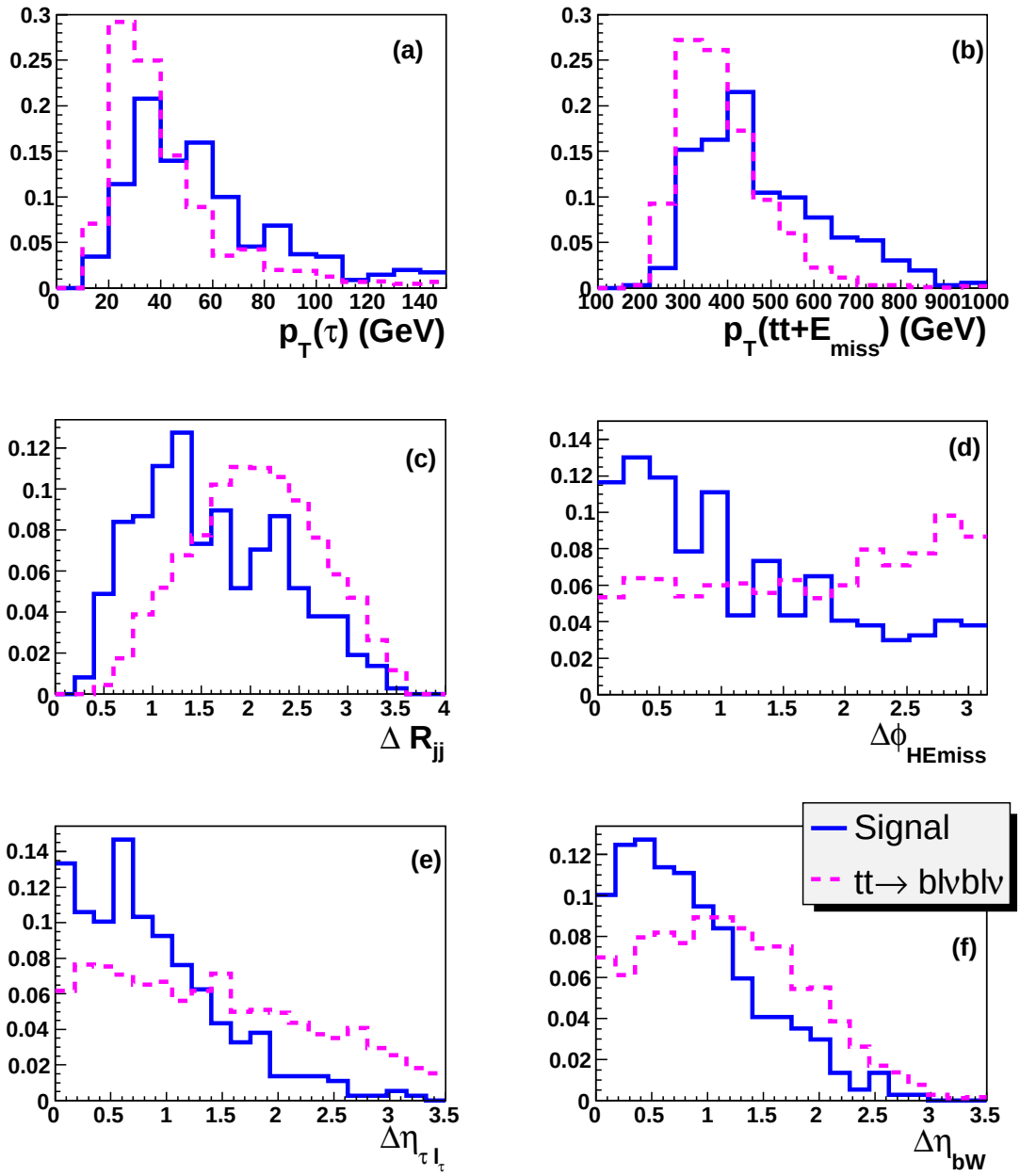

Figure 5.69: *The distribution of the input variables of the likelihood: (a) the transverse momentum of the τ-jet, (b) the sum of the transverse momenta of the tt-system and missing momentum (see text), (c) the distance ΔR between jets from the W-boson, (d) the transverse distance $\Delta\phi$ between missing momentum and visible part of the Higgs boson, (e) the $\Delta\eta$ between τ-jet and lepton coming from the other τ, and (f) the $\Delta\eta$ between the b-jet and the W-boson from hadronically decayed t-quark. The distributions are shown for the signal events (blue solid line), and for the $t\bar{t} \to b\ell\bar{\nu}_\ell\bar{b}\ell\nu_\ell$ (magenta dashed line) background process.*

The resulting discriminant is shown in Figure 5.70 (a). Note that the distributions are normalized to 1. When normalized to the corresponding cross-sections (Figure 5.70 (b)), it appears that $t\bar{t} \to b\ell\bar{\nu}_\ell\bar{b}\ell\nu_\ell$ (magenta dashed line) is by two orders of magnitude bigger than the signal (blue solid line) and $t\bar{t} \to b\ell\bar{\nu}_\ell\bar{b}jj$ (red dotted line). To suppress this

background, and also $Z + X \to \ell^+\ell^- + X$, we require that both leptons have the same charge (Figure 5.70 (c)). The efficiency of this cut for the signal, and the $t\bar{t} \to b\ell\bar{\nu}_\ell\bar{b}jj$ and $t\bar{t} \to b\ell\bar{\nu}_\ell\bar{b}\ell\nu_\ell$ backgrounds is given in Table 5.17. The final discriminant after this cut is shown in Figure 5.70 (d). We require that $\ln(L_H) > 2.6$. Figure 5.71 shows the "Higgs mass", i.e. invariant mass of the τ-jet and lepton coming from τ. We count events if the Higgs mass is between 40 and 120 GeV. Results for three Higgs masses are shown in a Table 5.18. About 40% of the total background is irreducible $Zt\bar{t} \to \tau^+\tau^- t\bar{t}$, and $\sim 26\%$ originates in $t\bar{t}$ events (Table 5.19).

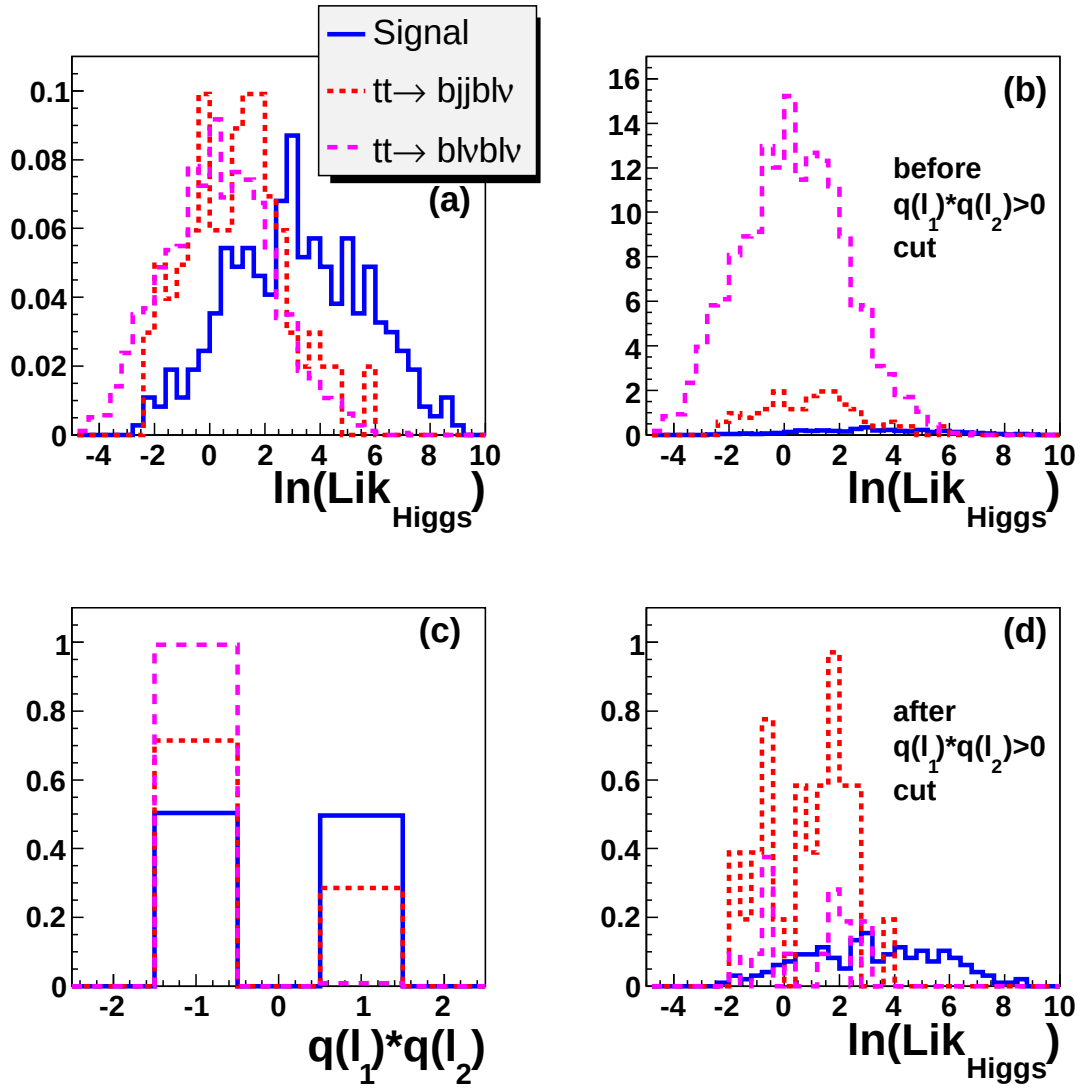

Figure 5.70: *The distribution of the final likelihood* $\ln(L_H)$ *normalized to unity (a), normalized to corresponding cross-sections before the same lepton charge cut (see the text for the explanation) (b) and after the same lepton charge cut (d), and the product of the charges of the two leptons, for the signal (blue solid line), and for the* $t\bar{t} \to b\ell\bar{\nu}_\ell\bar{b}jj$ *(red dotted line) and the* $t\bar{t} \to b\ell\bar{\nu}_\ell\bar{b}\ell\nu_\ell$ *(magenta dashed) background processes.*

	Signal	$t\bar{t} \to b\ell\bar{\nu}_\ell\bar{b}jj$	$t\bar{t} \to b\ell\bar{\nu}_\ell\bar{b}\ell\nu_\ell$
Before same lepton charge cut	3.7	19.8	164
After same lepton charge cut	1.9	6	1.4
Efficiency (%)	50	30	1

Table 5.17: *The number of expected events (for 30 fb^{-1}) for the signal $t\bar{t}H \to t\bar{t}\tau^+\tau^- \to b\ell\bar{\nu}_\ell\bar{b}jj\tau_j\bar{\nu}_\tau\ell\bar{\nu}_\ell\nu_\tau$, and the backgrounds $t\bar{t} \to b\ell\bar{\nu}_\ell\bar{b}jj$ and $t\bar{t} \to b\ell\bar{\nu}_\ell\bar{b}\ell\nu_\ell$, before and after the "same lepton charge" cut.*

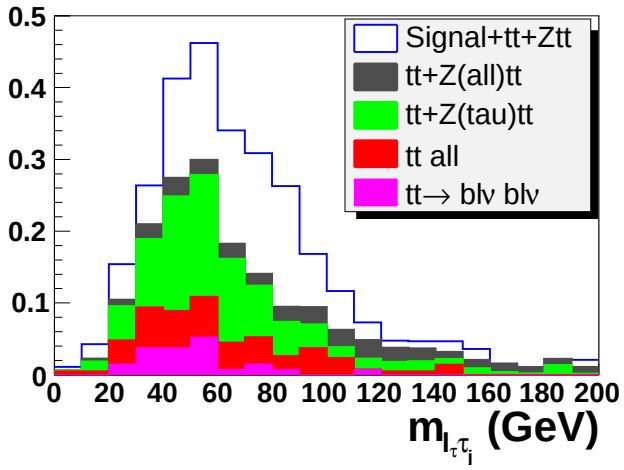

Figure 5.71: *The invariant mass $m_{\ell_\tau\tau_j}$ of the signal on top of the backgrounds for 30* fb^{-1} *and $m_H = 120$* GeV.

m_H (GeV)	Signal	Background	S/B	$S/\sqrt{B}$
110	1.0	1.07	0.93	0.97
120	1.01	1.07	0.94	0.98
130	0.45	0.94	0.48	0.46

Table 5.18: *The number of expected events for the signal and the total background for* 30 fb^{-1} *for channel 5, $t\bar{t}H \to t\bar{t}\tau^+\tau^- \to b\ell\bar{\nu}_\ell\bar{b}jj\tau_j\bar{\nu}_\tau\ell\bar{\nu}_\ell\nu_\tau$. S/B and $S/\sqrt{B}$ are also given.*

m_H (GeV)	$t\bar{t}$(%)	$Zt\bar{t}$(%) $Z \to \tau^+\tau^-$ $t\bar{t} \to b\ell\bar{\nu}_\ell\bar{b}jj$	$Zt\bar{t}$(%) $Z \to e^+e^-, \mu\mu$ $t\bar{t} \to b\ell\bar{\nu}_\ell\bar{b}jj$	$Zt\bar{t}$(%) $Z \to \tau^+\tau^-$ $t\bar{t} \to b\tau\bar{\nu}_\tau\bar{b}jj$	$Zt\bar{t}$(%) $Z \to e^+e^-, \mu\mu$ $t\bar{t} \to b\tau\bar{\nu}_\tau\bar{b}jj$
110	26	40	10	15	9
120	26	40	10	15	9
130	30	35	13	13	9

Table 5.19: *The dominant background sources for channel 5 $t\bar{t}H \to t\bar{t}\tau^+\tau^- \to b\ell\bar{\nu}_\ell\bar{b}jj\tau_j\bar{\nu}_\tau\ell\bar{\nu}_\ell\nu_\tau$ (in %).*

5.4.5.4 Combined results for the low luminosity (30 fb^{-1})

The combined results for all three channels under consideration are given in Table 5.20.

m_H (GeV)	Signal	Background	S/B	$S/\sqrt{B}$
110	2.33	2.42	0.96	1.50
120	2.61	2.61	1.0	1.62
130	1.23	2.53	0.46	0.77

Table 5.20: *The number of expected events for the signal and the total background for* 30 fb^{-1} *for the combined three channels under consideration.* S/B *and* $S/\sqrt{B}$ *are also given.*

5.4.6 High Luminosity

Even though this thesis is a feasibility study for the low luminosity benchmark case (30 fb^{-1}), a preliminary fast simulation study of the high luminosity is performed. Though, one is tempted to believe that increasing the luminosity by a factor x would result in an increase of a $S/\sqrt{B}$ by a factor of $\sqrt{x}$, this is not the case. When the luminosity is increased the pile up becomes a major issue. At the design luminosity of 10^{34} cm^{-2}s^{-1}, an average 23 minimum bias events are expected per bunch-crossing. The minimum bias events with small transverse momenta arise from long-range p-p interactions. They can be viewed as a bath of energy superposed on the hard scattering of interest, a phenomenon known as *pile-up*.

It is found that the performance of the tau-algorithm worsened. Figure 5.72 shows the characteristic variables for the fast τ-tagging. It can be seen that the electromagnetic radius shown in 5.72 (a) and (b) becomes smaller when the high luminosity condition is applied. The effect is more dramatic for non-labeled jets. Also, the p_T spectrum of non-labeled jets is harder (Figure 5.72 (c)). One can either keep the same efficiency of the τ-tagging, or the same rejection against light jets (Figure 5.73). Analysis is performed in both cases and it is found that keeping the same rejection gives slightly better overall results (Table 5.21).

Moreover, the trigger conditions are tighter (see Table 5.11). The performance of channel 4, $t\bar{t}H \to t\bar{t}\tau^+\tau^- \to b\ell\bar{\nu}_\ell\bar{b}jj\tau_j\bar{\nu}_\tau\tau_j\nu_\tau$ worsened too much and we dropped it from the calculation of the final result.

5.4.6.1 Channel 2, $t\bar{t}H \to t\bar{t}\tau^+\tau^- \to bjj\bar{b}jj\tau_j\bar{\nu}_\tau\ell\bar{\nu}_\ell\nu_\tau$

We optimized the analysis for the high luminosity conditions. The following preselection cuts were changed:

- The cut on the transverse momentum of the τ-jet was raised to 50 GeV.

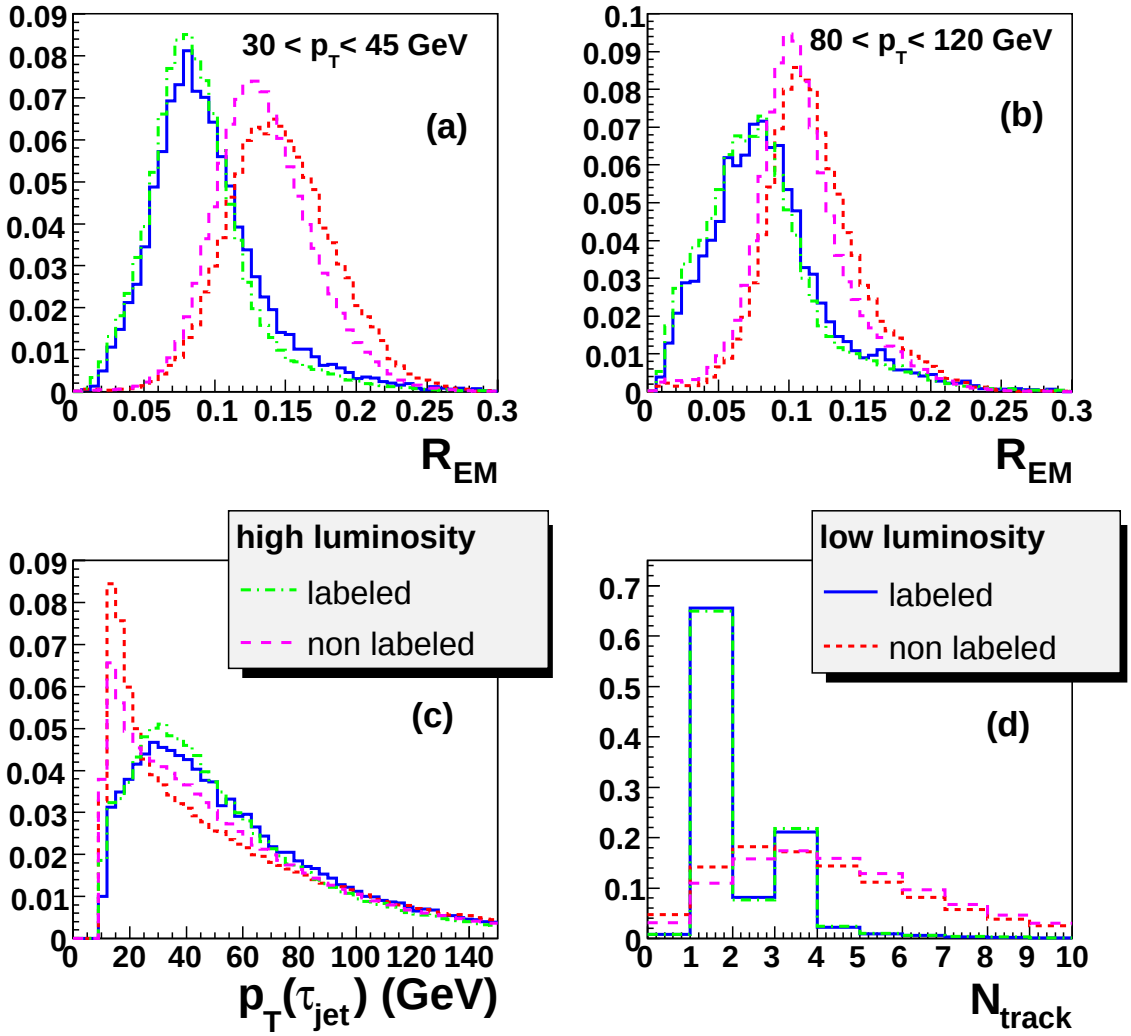

Figure 5.72: *The characteristic variables for the fast τ-tagging: (a) the electromagnetic radius R_{EM} for $30 < p_T < 45$ GeV, (b) the electromagnetic radius for $80 < p_T < 120$ GeV, (c) the transverse momentum, p_T, of the candidate τ-jet, and (d) the number of charged tracks, shown for the low luminosity labeled (blue solid line) and non-labeled (red dotted line) jets, and the high luminosity labeled (green dash-dotted line) and non-labeled (magenta dashed line) jets.*

- The cut on the missing p_T was raised to 35 GeV.
- The cut on the $\ln(L_W)$ was raised to 1.5.
- The mass of both reconstructed W-boson was required to be between 40 and 110 GeV.

An additional variable used as an input for the L_H was the total scalar sum of the transverse momenta of the $t\bar{t}$-system ingredients:

$$p_T(t\bar{t}) \equiv p_T(b_1) + p_T(b_2) + p_T(j_1^{W_1}) + p_T(j_2^{W_1}) + p_T(j_1^{W_2}) + p_T(j_2^{W_2}) \tag{5.16}$$

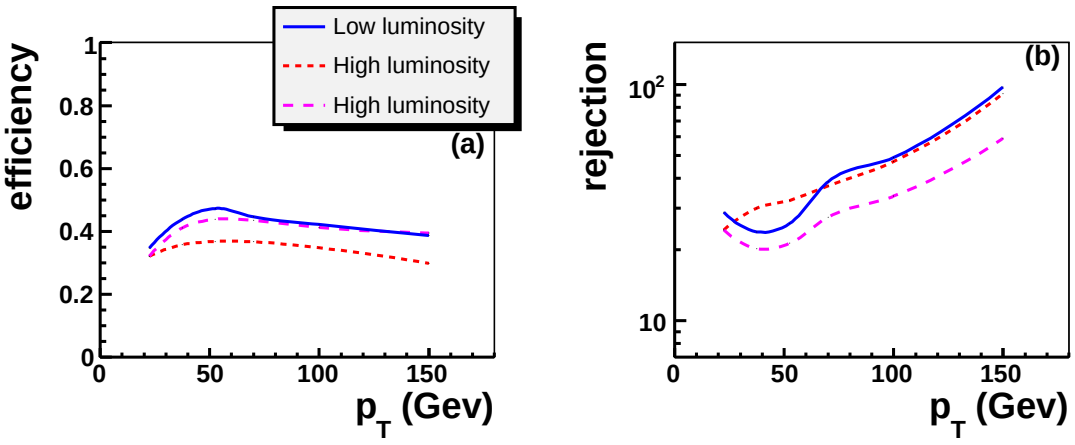

Figure 5.73: *The efficiency and rejection of the tau-algorithm for the low luminosity (blue solid line), and for the high luminosity when cuts for the tagging of the τ-jet are not changed (magenta dashed line), and when they are changed in order to preserve the rejection (red dotted line).*

	high (300 fb^{-1})				low (30 fb^{-1})	
	same τ efficiency		same rejection			
Signal	events	%	events	%	events	%
N^0	$1.422 \cdot 10^4$	100	$1.422 \cdot 10^4$	100	$1.422 \cdot 10^3$	100
1 τ-jet	3192.99	22.45	2783.96	19.58	351.12	24.69
rec pass	124.51	3.9	109.07	3.9	19.58	5.6
Final	4.03	3.2	3.66	3.4	1.01	5.1
$t\bar{t} \to b\ell\bar{\nu}_\ell bjj$						
N^0	$6.45 \cdot 10^7$	100	$6.45 \cdot 10^7$	100	$6.45 \cdot 10^6$	100
1 τ-jet	$4.648 \cdot 10^6$	7.21	$3.745 \cdot 10^6$	5.81	$4.937 \cdot 10^5$	7.5
rec pass	8127	0.18	6192	0.17	1115.85	0.22
Final	1.86	$2.3 \cdot 10^{-2}$	1.24	$2 \cdot 10^{-2}$	0.19	$1.7 \cdot 10^{-2}$
$t\bar{t} \to b\ell\bar{\nu}_\ell b\ell\nu_\ell$						
N^0	$1.56 \cdot 10^7$	100	$1.56 \cdot 10^7$	100	$1.56 \cdot 10^6$	100
1 τ-jet	$1.381 \cdot 10^6$	8.85	$1.208 \cdot 10^6$	7.75	$1.456 \cdot 10^5$	9.33
rec pass	$1.853 \cdot 10^4$	1.4	$1.538 \cdot 10^4$	1.3	2349.36	1.6
Final	1.35	$1.7 \cdot 10^{-3}$	0.9	$6 \cdot 10^{-3}$	0.09	$4 \cdot 10^{-3}$
Overall results						
S/B	0.56		0.65		0.94	
$S/\sqrt{B}$	1.5		1.54		0.98	

Table 5.21: *The expected number of events at several stages of the analysis, for the low and high luminosity when two different criteria for the τ-tagging are adopted. "rec pass" means that topology requirement, i.e. 2 b-jets, 1 τ-jet, 1 lepton and 2 light jets, is fulfilled. In columns 3, 5 and 7 percentage is given with respect to the previous row.*

The final likelihood for the $m_H = 120$ GeV is shown in Figure 5.74. We count events if $\ln(L_H) > 6.6$ for the Higgs masses of 110 and 120 GeV and if $\ln(L_H) > 6.7$ for the Higgs mass of 130 GeV. The final result is given in Table 5.22

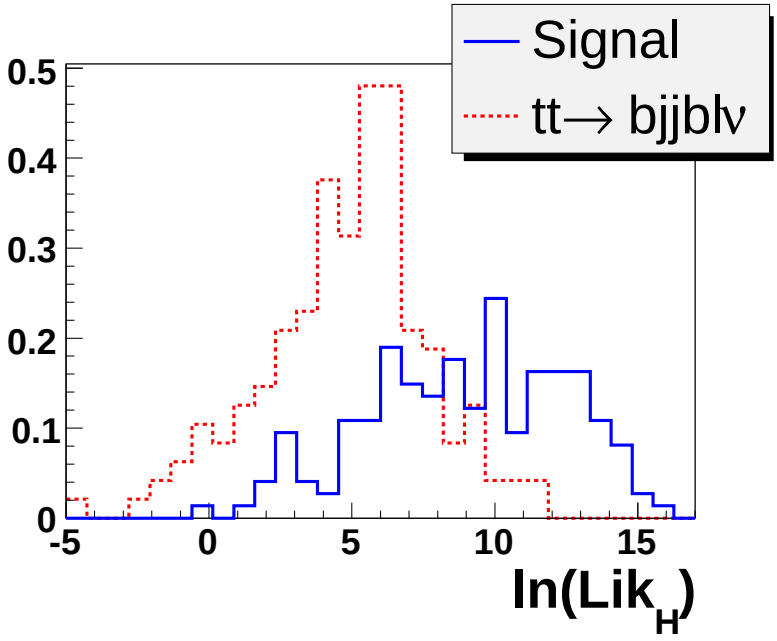

Figure 5.74: *The resulting likelihood L_H for the the signal with $m_H = 120$ GeV (blue solid line), and the $t\bar{t} \to b\ell\bar{\nu}_\ell\bar{b}jj$ (red dashed line) background process for high luminosity, i.e.* 300 fb^{-1}.

m_H (GeV)	Signal	Background	S/B	$S/\sqrt{B}$
110	1.92	1.73	1.11	1.46
120	1.60	1.54	1.05	1.30
130	0.71	1.22	0.58	0.64

Table 5.22: *The number of expected events for the signal and the background for* 300 fb^{-1} *for channel 2, $t\bar{t}H \to t\bar{t}\tau^+\tau^- \to bjj\bar{b}jj\tau_j\bar{\nu}_\tau\ell\bar{\nu}_\ell\nu_\tau$. S/B and $S/\sqrt{B}$ are also given.*

5.4.6.2 Channel 5, $t\bar{t}H \to t\bar{t}\tau^+\tau^- \to b\ell\bar{\nu}_\ell\bar{b}jj\tau_j\bar{\nu}_\tau\ell\bar{\nu}_\ell\nu_\tau$

For channel 5 the following preselection cuts were changed:

- The cut on the $\ln(L_W)$ was raised to 1.
- We cut on the distance between the τ-jet and the lepton from the other τ, $\Delta R_{\tau_j l} < 2.5$.

The resulting discriminant is shown in Figure 5.75. We require that $\ln(L_H) > 0.6$. Figure 5.76 shows the "Higgs mass", i.e. invariant mass of the τ-jet and the lepton coming from τ. We count events if the Higgs mass is between 45 and 120 GeV. The results for the three Higgs masses are shown in a Table 5.23.

Combined results for the high luminosity Combined results for the two channels under consideration are given in Table 5.24.

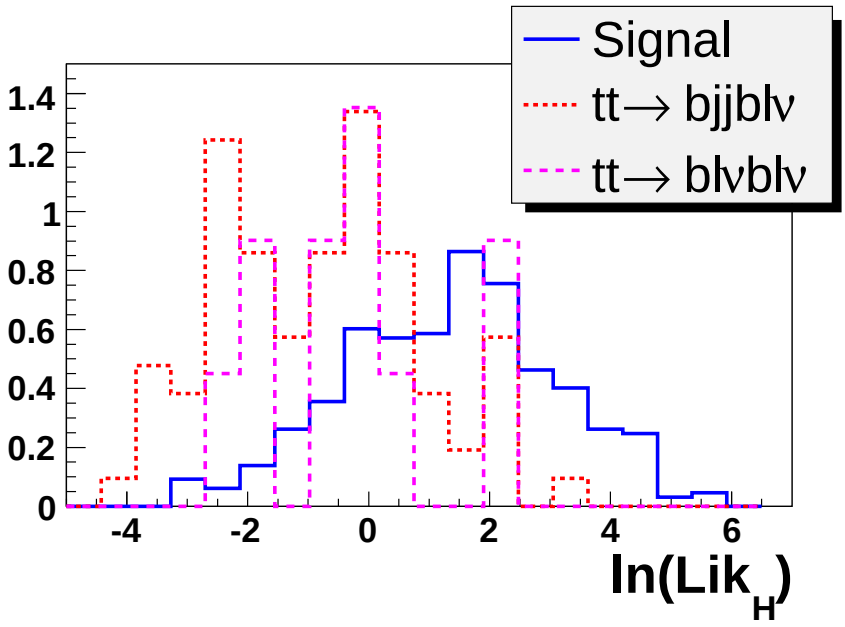

Figure 5.75: *The resulting likelihood L_H for the the signal with $m_H = 120$ GeV (blue solid line), and for the $t\bar{t} \to b\ell\bar{\nu}_\ell\bar{b}jj$ (red dotted line) and the $t\bar{t} \to b\ell\bar{\nu}_\ell\bar{b}\ell\nu_\ell$ (magenta dashed line) background processes for high luminosity, i.e.* 300 fb^{-1}.

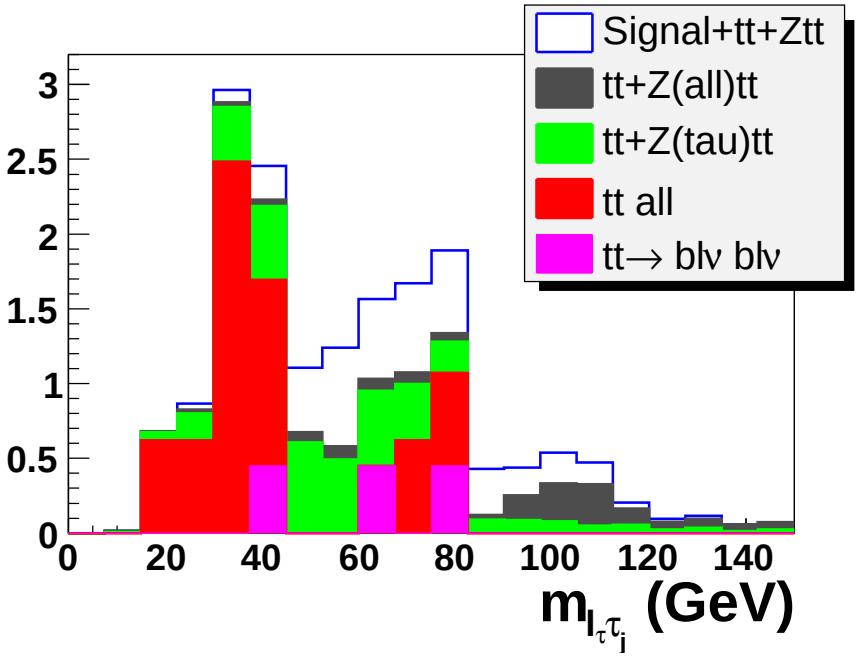

Figure 5.76: *The invariant mass $m_{\ell_\tau\tau_j}$ of the signal on top of the backgrounds for 300* fb^{-1} *and $m_H = 120$* GeV.

5.4.7 Systematic uncertainties

We consider the following sources of the systematic uncertainties:

- **Background uncertainties.**
  We compared $t\bar{t}$ events generated with two generators, PYTHIA and HERWIG 6.5 [58]. We obtained an uncertainty of $\sim 7\%$ for the events passing topology and

m_H (GeV)	Signal	Background	S/B	$S/\sqrt{B}$
110	4.29	5.67	0.76	1.80
120	3.66	5.67	0.65	1.54
130	2.23	5.67	0.39	0.92

Table 5.23: *The number of expected events for the signal and the background for* 300 fb^{-1} *for channel 5,* $t\bar{t}H \to t\bar{t}\tau^+\tau^- \to b\ell\bar{\nu}_\ell\bar{b}jj\tau_j\bar{\nu}_\tau\ell\bar{\nu}_\ell\nu_\tau$. *$S/B$ and $S/\sqrt{B}$ are also given.*

m_H (GeV)	Signal	Background	S/B	$S/\sqrt{B}$
110	6.21	7.40	0.84	2.28
120	5.26	7.21	0.73	1.96
130	2.94	6.89	0.42	1.12

Table 5.24: *The number of expected events for the signal and the background for* 300 fb^{-1} *for the combined two channels under consideration. S/B and $S/\sqrt{B}$ are also given.*

trigger requirements, and ∼25% for the events passing additional analysis cuts.

We also compared $t\bar{t}$ events generated with PYTHIA with two different masses of the t-quark, $m_{top} = 175$ GeV (that was the default m_{top} throughout our analysis) and $m_{top} = 178$ GeV. The obtained uncertainty after topology and trigger requirements was ∼5.8%, and after additional analysis cuts ∼11%.

- **Reconstruction and simulation uncertainties.**
  In order to estimate uncertainties due to the reconstruction of the fully simulated events, we changed the tagging[70] of b-jets, τ-jets and electrons, and the isolation criteria for the electrons and muons by moving the cut value by ±5%. We also rescaled the energies of the electrons, muons and jets by a factor (100 ± 5)%. The results are given in a Table 5.25 for the events passing the topology requirement, and those passing several other cuts[71]. Statistical uncertainties are given in the last row of the Table. The overall uncertainty is 3.3% after the topology requirement, and 14.1% after several cuts, and they are within the statistical uncertainties.

- **Analysis uncertainties.**
  In order to determine uncertainties due to the analysis, we rescaled all input variables for the final likelihood L_H[72]. The results after lose cuts are shown in a Table 5.26.

[70] We slightly changed the cut values used for the tagging of different objects as described in section 5.4.4.
[71] All cuts given in Table 5.12 except $q_{lep} \cdot q_{lep} > 0$ were applied.
[72] For the input variables to the likelihood we use *probability density functions* of the corresponding histograms. In order to estimate the uncertainties we have changed the coefficients of the functions by rescaling such that the *pdf*s get closer, and then get further away from each other.

Source	systematic uncertainty after reconstruction (in %)	systematic uncertainty after several cuts (in %)
b-tag	2.47	3.83
τ-tag	1.63	0
e-tag	1.31	0
e isolation	0.46	0
μ isolation	0	0
e energy	0	5.75
μ energy	0	5.75
jet energy	0	10.81
Total systematics	3.27	14.06
Statistical uncertainty	6.7	19.25

Table 5.25: *Systematic uncertainties due to the reconstruction of the fully simulated events, from the sources given in column 1 (see text). The statistical uncertainty is given in the last row. The uncertainties are given after the topology requirement (column 2) and after the cuts given in Table 5.12 except* $q_{lep} \cdot q_{lep} > 0$ *(column 3).*

It can be seen that the systematic uncertainties, 4.2% for the signal and 2.1% for the $t\bar{t}$ background are within statistical uncertainties.

	Signal	$t\bar{t} \to b\ell\bar{\nu}_\ell\bar{b}jj$	$t\bar{t} \to b\ell\bar{\nu}_\ell\bar{b}\ell\nu_\ell$	total $t\bar{t}$
N of events	1.74	6.60	0.9	7.54
Total systematics (in %)	4.20	2.94	7.08	2.05
Statistical uncertainty (in %)	7.69	17.15	31.62	15.33

Table 5.26: *Systematic uncertainties due to the analysis. The statistical uncertainty is given in the last row.*

5.4.8 Background normalization

In order to reduce the dependence of the analysis on the theoretical calculations[73] it is necessary to define *Control samples*, i.e. *Signal free regions*, to estimate the normalization of the most influential backgrounds. The basic procedure is:

1. Extract the ratio of the number of events in the *Signal region* and *Signal free region* from the simulated events (MC data in the following).

2. Measure the number of events in the *Signal free region* from the real data.

[73] We have shown that the uncertainties on the $t\bar{t}$ production can be as high as $\sim$25%.

3. From the measured number of events in the *Signal free region* (real data), and the obtained ratio (MC data), estimate the number of events in the *Signal region* in the real data.

The detailed description will be given in the following.

5.4.8.1 Channel 2

For channel 2, $t\bar{t}H \to t\bar{t}\tau^+\tau^- \to bjj\bar{b}jj\tau_j\bar{\nu}_\tau\ell\bar{\nu}_\ell\nu_\tau$, the *Signal region* comprises the events that pass the final selection as described in section 5.4.5.1. The *Signal free region* is defined with the following changes:

1. In the preselection cuts, the cut on the reconstructed mass[74] of the Higgs boson is set to $0 < m_H < 350$ GeV.

2. The reconstructed mass of the Higgs boson is removed from the calculation of the final likelihood.

3. Events are counted if the $\ln(L_H) < 0$, and $m_H < 95$ GeV or $m_H > 170$ GeV.

The ratio of the background events in the *Signal free region* and the *Signal region* is

$$r_{tt} = \frac{\sigma^{Signal}}{\sigma^{Signal\ free}} \tag{5.17}$$

The expected number of events in the *Signal region* and the *Signal free region* is given in Table 5.27.

		Signal	$t\bar{t}$
Signal region	N of events	0.93	0.67
	Statistical uncertainty (in %)	11%	58%
Signal free	N of events	0.04	10.13
	Statistical uncertainty (in %)	58%	14%
	Systematics (in %)	40%	18%

Table 5.27: *The expected number of the signal and $t\bar{t}$ events in the Signal region and Signal free region (see text). Uncertainties are also given.*

[74] Using the collinear approximation.

5.4.8.2 Channel 5

For channel 5, $t\bar{t}H \rightarrow t\bar{t}\tau^+\tau^- \rightarrow b\ell\bar{\nu}_\ell\bar{b}jj\tau_j\bar{\nu}_\tau\ell\bar{\nu}_\ell\nu_\tau$, the *Signal region* comprises the events that pass the final selection as described in section 5.4.5.3. The control samples are defined as:

- *Signal free region without the same lepton charge cut (Sample 1)*
  For this sample we make the following changes:

  1. In the preselection cuts, the cut on the p_T of the second lepton is lowered from 15 GeV to 10 GeV.
  2. The $\Delta\phi_{HE^{miss}}$ is removed from the likelihood calculation.
  3. The cut on the invariant mass of the τ-jet and the lepton originated from the second τ is dropped.
  4. We do not require that both leptons have the same charge.

  This control sample is then defined requiring that $\ln(L_H) < 0$ and $\Delta\phi_{HE^{miss}} > 2$. Figure 5.77 (a) shows $\Delta\phi_{HE^{miss}}$ distribution for the signal (enhanced by factor 5) on top of the $t\bar{t}$ background for *Sample 1*. Only the signal distribution is shown in Figure 5.77 (b).

- *Signal free region with the same lepton charge cut (Sample 2)*
  This sample is identical as the previous one, except the requirement 4. In this sample we do require that both leptons have the same charge. Figure 5.78 (a) shows $\Delta\phi_{HE^{miss}}$ distribution for the signal on top of the $t\bar{t}$ background for *Sample 2*. Only the signal distribution is shown in Figure 5.78 (b).

As shown in Table 5.28 the first sample contains $t\bar{t}$ events with both t-quarks decaying semileptonically (dominates this sample), and with one t-quark decaying semileptonically and the other one hadronically. The second sample contains only $t\bar{t}$ events with one t-quark decaying semileptonically and the other one hadronically.

In order to determine the total number of the $t\bar{t}$ events in the *Signal region*, we follow the prescription given in [129]. We define three quantities:

1. The ratio of the $t\bar{t} \rightarrow b\ell\bar{\nu}_\ell\bar{b}\ell\nu_\ell$ cross-section in the *Signal region* and *Sample 1*:

$$r_{tt_{sl}} = \frac{\sigma_{tt_{sl}}^{signal\ region}}{\sigma_{tt_{sl}}^{Sample\ 1}}. \tag{5.18}$$

2. The ratio of the $t\bar{t} \rightarrow b\ell\bar{\nu}_\ell\bar{b}jj$ cross-section in the *Signal region* and *Sample 2*:

$$r_{tt_{slh}} = \frac{\sigma_{tt_{slh}}^{signal\ region}}{\sigma_{tt_{slh}}^{Sample\ 2}}. \tag{5.19}$$

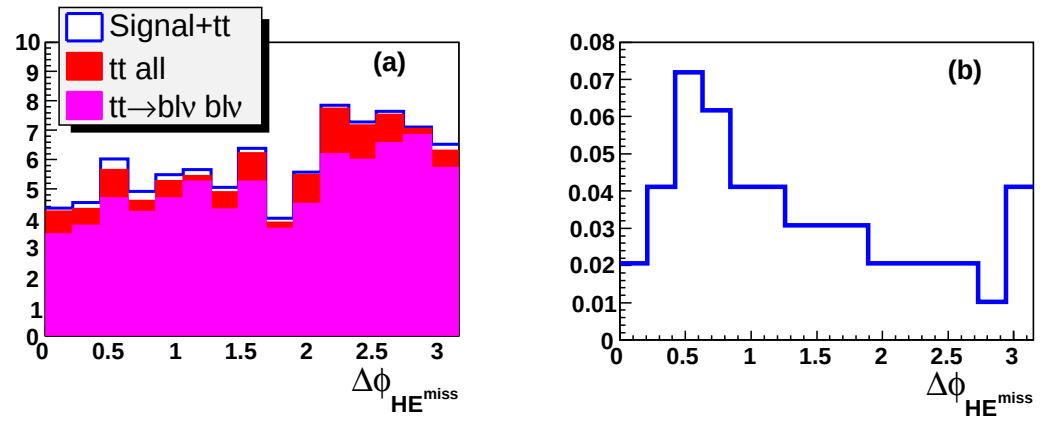

Figure 5.77: *The $\Delta\phi_{HE^{miss}}$ distribution for the signal (enhanced by factor 5) on top of the $t\bar{t}$ background for Sample 1 (a) and only the signal distribution (b).*

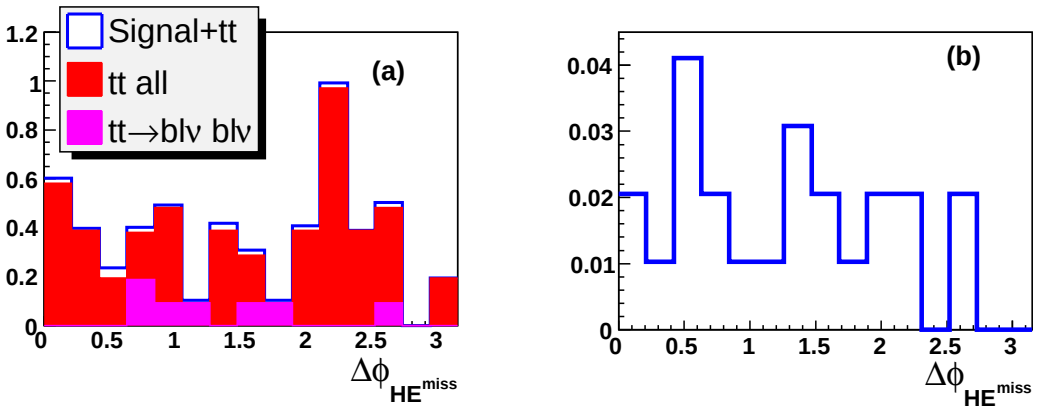

Figure 5.78: *The $\Delta\phi_{HE^{miss}}$ distribution for the signal on top of the $t\bar{t}$ background for Sample 2 (requiring that both leptons have the same charge) (a) and only the signal distribution (b).*

		Signal	$t\bar{t} \to b\ell\bar{\nu}_\ell\bar{b}jj$	$t\bar{t} \to b\ell\bar{\nu}_\ell\bar{b}\ell\nu_\ell$
Signal region	N of events	1.01	0.19	0.09
	Statistical uncertainty (in %)	10%	100%	100%
Signal free w/o the same charge lepton cut	N of events	0.11	5.05	33.81
	Statistical uncertainty (in %)	30%	20%	5.3%
	Systematics (in %)	24%	29.5%	7.6%
Signal free with the same charge lepton cut	N of events	0.04	2.14	0.09
	Statistical uncertainty (in %)	50%	30%	100%
	Systematics (in %)	25%	23%	100%

Table 5.28: *The expected number of the signal and $t\bar{t}$ events in the Signal region and two Control Samples (see text). Uncertainties are also given.*

3. The ratio of the $t\bar{t} \to b\ell\bar{\nu}_\ell\bar{b}jj$ cross-section in *Sample 1* and *Sample 2*:

$$r_{S2}^{S1} = \frac{\sigma_{tt_{slh}}^{Sample\ 1}}{\sigma_{tt_{slh}}^{Sample\ 2}}. \tag{5.20}$$

To determine the number of the $t\bar{t}$ events in the *Signal region*, the number of events in the two control samples should be measured (real data). Let us denote the number of the events in *Sample 1* N_{total}^{S1}, and number of the events in *Sample 2* N_{total}^{S2}. The number of $t\bar{t} \to b\ell\bar{\nu}_\ell\bar{b}jj$ events in the *Signal region* is then:

$$N_{tt_{slh}}^{Signal\ region} = N_{total}^{S2} \cdot r_{tt_{slh}}. \tag{5.21}$$

The number of $t\bar{t} \to b\ell\bar{\nu}_\ell\bar{b}jj$ events in *Sample 1* is:

$$N_{tt_{slh}}^{S1} = N_{total}^{S2} \cdot r_{S2}^{S1}. \tag{5.22}$$

The number of $t\bar{t} \to b\ell\bar{\nu}_\ell\bar{b}\ell\nu_\ell$ events in the *Signal region*:

$$N_{tt_{sl}}^{Signal\ region} = r_{tt_{sl}} \cdot \left(N_{total}^{S1} - N_{tt_{slh}}^{S1}\right) \tag{5.23}$$

For the estimation of the systematic uncertainties given in Table 5.28 we use the analysis uncertainties as described in section 5.4.7.

5.4.9 Conclusions

We performed a feasibility study of the $t\bar{t}H \to t\bar{t}\tau^+\tau^-$ channel. The signal events were reconstructed using the full and the fast simulation of the ATLAS detector. It is shown that both the distributions and the number of expected events after the same cuts agree, and that the fast simulation can be used to further develop the analysis.

We obtained a significance of 1.6σ for the low luminosity condition (30 fb^{-1}) and $m_H = 120$ GeV, and 2.0σ for the high luminosity condition (300 fb^{-1}) and $m_H = 120$ GeV.

We conclude that this channel can only be used as a corroborative channel to $t\bar{t}H \to t\bar{t}b\bar{b}$ for the determination of the top Yukawa coupling, but not as a main or discovery channel.

Chapter 6

Conclusions

Some aspects of the searches for the SM and MSSM Higgs boson at LEP, and prospects for such searches at the LHC and the ILC were presented in this thesis.

The search at LEP was motivated by the fact that the Standard Model fails to provide enough CP-violation to explain the cosmological matter-antimatter asymmetry. The CP-violating effects in the Higgs sector of SUSY may reduce this disturbing discrepancy. In this thesis we searched for hints of neutral Higgs bosons in the MSSM framework in which the Higgs sector is CP violated. The search was done using the OPAL detector at LEP. This search was based on data collected during 2000, at energies between 200 and 209 GeV (LEP2 phase). The corresponding integrated luminosity was $\sim 207\,\mathrm{pb}^{-1}$.

The work presented here described the search for these Higgs bosons in the channel $e^+e^- \to H_2Z^0 \to H_1H_1Z^0 \to b\bar{b}b\bar{b}\nu\bar{\nu}$ and $e^+e^- \to H_2Z^0 \to b\bar{b}\nu\bar{\nu}$. No significant excess of data over the expected background was found.

The results from this channel were combined with other possible experimental signatures of the same origin. In the case of the "CPX" benchmark scenario, designed to maximize the phenomenological differences in the Higgs sector with CP violation with respect to the CP-conserving scenarios, the region of $\tan\beta < 2.8$ was excluded at the 95% confidence level. However, no universal limit was obtained for either of the Higgs boson masses. However, for $\tan\beta < 3.3$, the limit $m_{H_1} > 112$ GeV was set for the mass of the lightest neutral Higgs boson (within this model) with the OPAL experiment only.

When the results from similar searches conducted by all the four LEP experiments were combined, $\tan\beta < 2.9$ was completely excluded in this scenario. Other scenarios gave less restrictive results.

If only one Higgs boson is found at the Large Hadron Collider (LHC), it would be important to determine its nature. The combined information of mass parameters from the LHC and the International Linear Collider (ILC), and the Higgs boson branching ratio measurements at the ILC can be used to obtain bounds on the deviation of the observed Higgs boson properties from those predicted by the Standard Model. Consequently one will be able to set indirect bounds on the mass of the CP-odd Higgs boson, M_A.

In this thesis, we have investigated indirect constraints on the MSSM Higgs sector

from various measurements at LHC and ILC in the SPS 1a benchmark scenario. We have shown that taking all experimental and theoretical uncertainties into account, an indirect determination of M_A with an accuracy of about 20% (30%) seems to be feasible for $M_A =$ 600 (800) GeV. In order to achieve this, a precise measurement of the branching ratios BR($h \to b\bar{b}$) and BR($h \to WW^*$) at the ILC and information on the parameters of the scalar top and bottom sector from the combined LHC / ILC analyses is crucial.

The ATLAS experiment at the LHC is expected to start its operation in 2007. The Higgs boson, if exists, will probably be found with the ATLAS and CMS detectors after a year or two of run.

The Higgs boson Branching ratio to τ-leptons pair, which is the second highest will play a crucial role in establishing the Higgs boson signal and in measuring the Higgs boson properties. Different SUSY models also contain events rich in τ-leptons. Hence, τ identification comes high on the ATLAS priority list. Electrons and muons from τ-decays cannot be efficiently discerned from those coming from other sources, and one way to identify a τ-lepton is to observe the jet formed from its hadronic products, i.e. τ_j.

In this thesis we introduced a new algorithmic method for τ identification within the framework of the fast simulation of the ATLAS detector. In principle there is no substitute for full simulation. However, often one finds it impossible to fully simulate all needed signal and background events and the practical solution, in such case, is to use the fast simulation. While comparing the performance of our algorithm with the results of the full simulation we found out that the Algorithmic method is superior to the parametrization one. Both methods do reproduce the acceptance as computed by the full simulation, however, the rejection curve that is produced by the Algorithmic method is much closer to the one obtained from full simulation than the curve obtained from the parametrization method.

The prescription for algorithmic τ identification given here is providing a reliable and accurate fast alternative.

One of the main goals of the ATLAS experiment is to measure various Higgs boson couplings as accurate as possible. Such a measurement is mandatory for a full understanding of the Higgs sector. The most challenging measurement of the Higgs boson properties is the determination of it's Yukawa coupling to the top quark.

To complement the $t\bar{t}H \to t\bar{t}b\bar{b}$ channel, which is the main discovery channel in the low Higgs mass region ($m_H \sim 120$ GeV), we performed feasibility study of the $t\bar{t}H$ channel with the Higgs decaying into a pair of τ leptons. The signal events were reconstructed using the full and the fast simulation of the ATLAS detector. It was shown that the two methods are in good agreement and that we can use the fast simulation to further develop the analysis.

For the most intresting case of $m_H = 120$ GeV we obtained a significance of 1.6σ for the low luminosity condition (30 fb^{-1}), and 2.0σ for the high luminosity condition

(300 fb^{-1}).

We concluded that this channel can only be used as a corroborative channel to $t\bar{t}H \to t\bar{t}b\bar{b}$ for the determination of the top Yukawa coupling, but not as a main or discovery channel.

Bibliography

[1] C.C.W. Taylor, *The Atomists: Leucippus and Democritus. Fragments, A Text and Translation with Commentary*, Toronto 1999.

[2] S. L. Glashow, Nucl. Phys. **22**, 579 (1961). (spires)
A. Salam, *Weak and electromagnetic interactions, Proceedings of the Nobel Symposium*, held 1968 at Lerum, Sweden
S. Weinberg, Phys. Rev. Lett. **19**, 1264 (1967). (Article)

[3] S. Weinberg, Eur. Phys. J. C **34**, 5 (2004) [arXiv:hep-ph/0401010] and references therein.
G. 't Hooft, *The glorious days of physics: Renormalization of gauge theories*, arXiv:hep-th/9812203, and references therein.

[4] P. W. Higgs, Phys. Lett. **12**, 132 (1964). (spires)
P. W. Higgs, Phys. Rev. Lett. **13**, 508 (1964). (spires)
P. W. Higgs, Phys. Rev. **145**, 1156 (1966). (spires)
F. Englert and R. Brout, Phys. Rev. Lett. **13**, 321 (1964). (spires)
G. S. Guralnik, C. R. Hagen and T. W. B. Kibble, Phys. Rev. Lett. **13**, 585 (1964). (spires)
T. W. B. Kibble, Phys. Rev. **155**, 1554 (1967). (spires)

[5] R. Barate *et al.* [LEP Working Group for Higgs boson searches], Phys. Lett. B **565**, 61 (2003) [arXiv:hep-ex/0306033].

[6] M. W. Grünewald, *Precision Tests of the Standard Model*, arXiv:hep-ex/0511018
LEP Electroweak Working Group. LEPEWWG/2005-01, arXiv:hep-ex/0511027.

[7] J. Wess and B. Zumino, Nucl. Phys. B **70**, 39 (1974). (spires)
J. Wess and J. Bagger, *Supersymmetry and supergravity*, Princeton, USA: Univ. Pr. (1992). (spires)

[8] S. Heinemeyer, W. Hollik and G. Weiglein, Eur. Phys. J. C **9** (1999) 343, [arXiv:hep-ph/9812472].

[9] G. Degrassi, S. Heinemeyer, W. Hollik, P. Slavich and G. Weiglein, Eur. Phys. J. C **28** (2003) 133, [arXiv:hep-ph/0212020].

[10] G. Abbiendi *et al.* [OPAL Collaboration], *Interpretation of the Search for Neutral Higgs Bosons from $\sqrt{s}$=91 GeV to $\sqrt{s}$=209 GeV in a CP Violating MSSM Scenario*, OPAL Physics Note PN505, 2002.
G. Abbiendi *et al.* [OPAL Collaboration], *Update Search for Neutral Higgs Bosons in a CP-Violating MSSM Scenario in e^+e^- collisions*, OPAL Physics Note PN517, 2003.
G. Abbiendi *et al.* [OPAL Collaboration], *Search for Neutral Higgs Bosons Predicted by CP Conserving and CP Violating MSSM Scenarios with the OPAL detector at LEP*, OPAL Physics Note PN524, 2003.

[11] G. Abbiendi *et al.* [OPAL Collaboration], Eur. Phys. J. C **37**, 49 (2004), (Article). [arXiv:hep-ex/0406057].

[12] ALEPH, DELPHI, L3, and OPAL Collaboration, The LEP Working Group for Higgs Boson Searches, *Search for Neutral MSSM Higgs Bosons at LEP*, LHWG-Note 2005-01

[13] K. Desch, E. Gross, S. Heinemeyer, G. Weiglein and L. Živković, JHEP **0409**, 062 (2004) [arXiv:hep-ph/0406322].

[14] G. Weiglein *et al.* [LHC/LC Study Group], *Physics interplay of the LHC and the ILC*, [arXiv:hep-ph/0410364], accepted for publication in Physics Reports.
see also LHC/ILC Study Group.

[15] L. Živković *et al.*, *LHC/LC Interplay in the MSSM Higgs Sector*, International Conference on Linear Colliders, (LCWS04), Volume 1, page 189, Paris, 2004.

[16] Eilam Gross and Lidija Živković, *An Alternative Algorithm for Fast Tau Identification within ATLAS*, ATL-PHYS-INT-2005-003;

[17] L. Živković, Czech. J. Phys. **54**, A73 (2004). ATL-PHYS-2004-023

[18] G. Arnison *et al.* [UA1 Collaboration], Phys. Lett. B **122**, 103 (1983). (spires)
G. Arnison *et al.* [UA1 Collaboration], Phys. Lett. B **126**, 398 (1983). (spires)

[19] D. P. Barber *et al.*, Phys. Rev. Lett. **43**, 830 (1979). (Article)

[20] Y. Nir *The Standard Model - Course Notes*

[21] J. F. Gunion, H. E. Haber, G. L. Kane and S. Dawson, *The Higgs Hunter's Guide*, SCIPP-89/13. (spires)

[22] M. Spira and P. M. Zerwas, *Electroweak symmetry breaking and Higgs physics* arXiv:hep-ph/9803257.

[23] A. Djouadi, J. Kalinowski and M. Spira, Comput. Phys. Commun. **108**, 56 (1998) [arXiv:hep-ph/9704448].

[24] T. Hambye and K. Riesselmann, Phys. Rev. D **55**, 7255 (1997). [arXiv:hep-ph/9610272].

[25] M. C. Gonzalez-Garcia and Y. Nir, Rev. Mod. Phys. **75**, 345 (2003), [arXiv:hep-ph/0202058].

[26] Y. Fukuda *et al.*, Nucl. Instrum. Meth. A **501**, 418 (2003). (spires)
see also: SuperKamiokande
A. Suzuki *et al.* [K2K Collaboration], Nucl. Instrum. Meth. A **453**, 165 (2000) [arXiv:hep-ex/0004024].
see also: K2K
A. Suzuki *et al.* [K2K Collaboration], Nucl. Instrum. Meth. A **453**, 165 (2000) [arXiv:hep-ex/0004024].
see also: SNO
A. Piepke [KamLAND Collaboration], Nucl. Phys. Proc. Suppl. **91**, 99 (2001). (spires)
see also: KamLAND

[27] E. W. Kolb and M. S. Turner, *The Early universe*, Addison-Wesley, Redwood City, USA (1990), Frontiers in physics, 69.

[28] A. D. Sakharov, Pisma Zh. Eksp. Teor. Fiz. **5**, 32 (1967) [JETP Lett. **5**, 24 (1967 SOPUA,34,392-393.1991 UFNAA,161,61-64.1991)] (spires).

[29] N. Cabibbo, Phys. Rev. Lett. **10**, 531 (1963). (spires)

[30] C. L. Bennett *et al.*, Astrophys. J. Suppl. **148**, 1 (2003). [arXiv:astro-ph/0302207].
D. N. Spergel *et al.* [WMAP Collaboration], Astrophys. J. Suppl. **148**, 175 (2003) [arXiv:astro-ph/0302209].

[31] E. Witten, Nucl. Phys. B **188**, 513 (1981). (spires)
S. Dimopoulos, S. Raby and F. Wilczek, Phys. Rev. D **24**, 1681 (1981). (spires)
S. Dimopoulos and H. Georgi, Nucl. Phys. B **193**, 150 (1981). (spires)

[32] J. Louis, I. Brunner and S. J. Huber, *The supersymmetric standard model*, arXiv:hep-ph/9811341.

[33] H. E. Haber and R. Hempfling, Phys. Rev. Lett. **66** (1991) 1815;(Article);
J. Ellis, G. Ridolfi and F. Zwirner, Phys. Lett. B **257** (1991) 83; (spires)
J. Ellis, G. Ridolfi, and F. Zwirner, Phys. Lett. B **262** (1991) 477;(spires);
Y. Okada, M. Yamaguchi and T. Yanagida, Prog. Theor. Phys. **85** (1991) 1; (Article]
M. Carena, J. R. Espinosa, M. Quiros, and C. E. M. Wagner, Phys.Lett. B **335** (1995) 209 [arXiv:hep-ph/9504316].

[34] M. Carena, J. Ellis, A. Pilaftsis, and C.E.M. Wagner, Phys. Lett. B **495** (2000) 155 [arXiv:hep-ph/0009212];
M. Carena, J. Ellis, A. Pilaftsis and C.E.M. Wagner, Nucl. Phys. B **586** (2000) 92 [arXiv:hep-ph/0003180];
A. Pilaftsis, *Radiative Higgs-Sector CP Violation in the MSSM*, arXiv:hep-ph/0003232.

[35] E. D. Commins, S. B. Ross, D. DeMille and B. C. Regan, Phys. Rev. A **50**, 2960 (1994). (spires).
P. G. Harris *et al.*, Phys. Rev. Lett. **82**, 904 (1999). (spires).

[36] S. Myers, *The LEP collider, from design to approval and commissioning*, Nov 26, 1990, CERN-91-08. Presented at CERN Accelerator School: The LEP Collider from Design to Approval and Commissioning, Geneva, Switzerland, Nov 26, 1990, CAS: CERN accelerator school, 6th John Adams Memorial lecture.

[37] K. Ahmet *et al.*, Nucl. Instr. and Meth. A **305** (1991) 275 [spires].
see also: `http://opal.web.cern.ch/Opal/welcome.html`

[38] P. P. Allport *et al.*, [OPAL Collaboration], Nucl. Instrum. Meth. A **324** (1993) 34 (spires).
P. P. Allport *et al.* [OPAL Collaboration], Nucl. Instrum. Meth. A **346**, 476 (1994) (spires).
S. Anderson *et al.* [OPAL Collaboration], Nucl. Instrum. Meth. A **403**, 326 (1998) (spires).

[39] R. D. Heuer and A. Wagner, Nucl. Instrum. Meth. A **265**, 11 (1988) (spires).

[40] M. Vincter, *A Study of the Momentum and ECAL Energy Resolution of the OPAL Detector*, OPAL Internal Technical Note TN274, 1995.

[41] S. Dado *et al.* [ISRAEL OPAL Collaboration], Nucl. Instrum. Meth. A **252**, 511 (1986) (spires).
G. Mikenberg, Nucl. Instr. and Meth., A **265** (1988) 223 (spires).
C. Beard *et al.*, Nucl. Instrum. Meth. A **286**, 117 (1990) (spires).

[42] G. Aguillion *et al.*, Nucl. Instrum. Meth. A **417**, 266 (1998). (spires)

[43] G. Abbiendi *et al.* [OPAL Collaboration], Eur. Phys. J. C **14**, 373 (2000) [arXiv:hep-ex/9910066].

[44] T. Sjostrand, *PYTHIA 5.7 and JETSET 7.4: Physics and manual*, arXiv:hep-ph/9508391.

[45] T. Sjostrand, P. Eden, C. Friberg, L. Lonnblad, G. Miu, S. Mrenna and E. Norrbin, Comput. Phys. Commun. **135**, 238 (2001) [arXiv:hep-ph/0010017].
see also http://www.thep.lu.se/∼torbjorn/Pythia.html

[46] J. Allison *et al.* [OPAL Collaboration], Nucl. Instrum. Meth. A **317**, 47 (1992) (spires).

[47] G. Abbiendi *et al.* [OPAL Collaboration], Eur. Phys. J. C **26** (2003) 479. [hep-ex/0209078].

[48] S. Mihara, S. Yamashita, *MT 3.00 a new algorithm to calculate energy flow based on MT package*, OPAL Internal Technical Note TN575, 1998.

[49] N. Brown and W. J. Stirling, Phys. Lett. B **252**, 657 (1990) (spires).

[50] E. Gross, G. Wolf and B. A. Kniehl, Z. Phys. C **63**, 417 (1994) [Erratum-ibid. C **66**, 321 (1995)] [arXiv:hep-ph/9404220].

[51] M. L. Mangano *et al.*, *Event generators for discovery physics*, arXiv:hep-ph/9602203.

[52] R. Engel and J. Ranft, Phys. Rev. D **54**, 4244 (1996) [arXiv:hep-ph/9509373].
see also: `http://www-ik.fzk.de/%7Eengel/phojet.html`

[53] S. Jadach, B. F. L. Ward and Z. Was, Phys. Lett. B **449**, 97 (1999) [arXiv:hep-ph/9905453].
S. Jadach, B. F. L. Ward and Z. Was, Comput. Phys. Commun. **130**, 260 (2000) [arXiv:hep-ph/9912214].

[54] J. Fujimoto *et al.*, Comput. Phys. Commun. **100**, 128 (1997) [arXiv:hep-ph/9605312].

[55] V. Ben-Hamo, E. Duchovni, E. Gross, and D. Hochman, *CONFIT A General purpose constrined fit program*, OPAL Technical Note TN286

[56] K. Ackerstaff *et al.* [OPAL Collaboration], Eur. Phys. J. C **2**, 441 (1998) [arXiv:hep-ex/9708024].

[57] The LEP Electroweak Heavy Flavour Working Group, *Final input parameters for the LEP/SLD heavy flavour analyses*, LEPHF 2001-01, 2001.

[58] G. Corcella *et al.*, JHEP **0101**, 010 (2001) [arXiv:hep-ph/0011363]; also: arXiv:hep-ph/0210213.

[59] M. W. Grünewald *et al.*, *Four-fermion production in electron positron collisions*, arXiv:hep-ph/0005309.

[60] S. Heinemeyer, W. Hollik and G. Weiglein, Eur. Phys. J. C **16** (2000) 139, [arXiv:hep-ph/0003022];
S. Heinemeyer, W. Hollik and G. Weiglein, Comp. Phys. Comm. **124** (2000) 76, [arXiv:hep-ph/9812320],
see `www.feynhiggs.de`.

[61] M. Frank, S. Heinemeyer, W. Hollik and G. Weiglein, *The Higgs boson masses of the complex MSSM: A complete one-loop calculation*, arXiv:hep-ph/0212037.

[62] S. Heinemeyer, W. Hollik and G. Weiglein, Phys. Lett. B **440**, 296 (1998) [arXiv:hep-ph/9807423].
S. Heinemeyer, W. Hollik and G. Weiglein, Phys. Rev. D **58**, 091701 (1998) [arXiv:hep-ph/9803277].
S. Heinemeyer, W. Hollik and G. Weiglein, JHEP **0006**, 009 (2000) [arXiv:hep-ph/9909540].

[63] M. Carena, M. Quiros and C. E. M. Wagner, Nucl. Phys. B **461**, 407 (1996) [arXiv:hep-ph/9508343].

[64] M. Carena, S. Mrenna and C. E. M. Wagner, Phys. Rev. D **60**, 075010 (1999) [arXiv:hep-ph/9808312].

[65] M. Carena, H. E. Haber, S. Heinemeyer, W. Hollik, C. E. M. Wagner and G. Weiglein, Nucl. Phys. B **580**, 29 (2000) [arXiv:hep-ph/0001002].

[66] J. R. Espinosa and R. J. Zhang, JHEP **0003**, 026 (2000) [arXiv:hep-ph/9912236].

[67] A. Heister *et al.* [ALEPH Collaboration], Phys. Lett. B **526**, 191 (2002) [arXiv:hep-ex/0201014].

[68] J. Abdallah *et al.* [DELPHI Collaboration], Eur. Phys. J. C **32**, 145 (2004) [arXiv:hep-ex/0303013].

[69] P. Achard *et al.* [L3 Collaboration], Phys. Lett. B **545**, 30 (2002) [arXiv:hep-ex/0208042].

[70] J. Aguilar-Saavedra *et al.*, TESLA TDR Part 3: *Physics at an e^+e^- Linear Collider*, [arXiv:hep-ph/0106315],
see: `tesla.desy.de/tdr` .

T. Abe *et al.* [American Linear Collider Working Group Collaboration], *Linear collider physics resource book for Snowmass 2001*, [arXiv:hep-ex/0106056].
K. Abe *et al.* [ACFA Linear Collider Working Group Collaboration], *Particle physics experiments at JLC*, [arXiv:hep-ph/0109166],
see: `lcdev.kek.jp/RMdraft`.

[71] A. Hoang *et al.*, Eur. Phys. J. C **3** (2000) 1, [arXiv:hep-ph/0001286].

[72] S. Heinemeyer, S. Kraml, W. Porod and G. Weiglein, JHEP **0309** (2003) 075, [arXiv:hep-ph/0306181].

[73] B. C. Allanach *et al.*, Eur. Phys. J. C **25** (2002) 113, [arXiv:hep-ph/0202233].
see: `www.ippp.dur.ac.uk/~georg/sps`.

[74] J. Guasch, W. Hollik and S. Peñaranda, Phys. Lett. B **515** (2001) 367, [arXiv:hep-ph/0106027];
M. Carena, H. Haber, H. Logan and S. Mrenna, Phys. Rev. D **65** (2002) 055005, E: *ibid* **D 65** (2002) 099902, [arXiv:hep-ph/0106116];
D. Asner et al., Eur. Phys. J. C **28** (2003) 27, [arXiv:hep-ex/0111056].

[75] M. Schumacher, *Investigation of the discovery potential for Higgs bosons of the minimal supersymmetric extension of the standard model (MSSM) with ATLAS*, arXiv:hep-ph/0410112.
M. Schumacher, *Investigation of the Discovery Potential for Higgs Bosons in the CP-Conserving MSSM with the ATLAS Detector at the LHC*, ATL-COM-PHYS-2004-070.

[76] J. Erler, S. Heinemeyer, W. Hollik, G. Weiglein and P.M. Zerwas, Phys. Lett. B **486** (2000) 125, [arXiv:hep-ph/0005024];
J. Erler and S. Heinemeyer, in *Proc. of the 5th International Symposium on Radiative Corrections (RADCOR 2000)* ed. Howard E. Haber, [arXiv:hep-ph/0102083].

[77] K. Desch, J. Kalinowski, G. Moortgat-Pick, M. M. Nojiri and G. Polesello, JHEP **0402** (2004) 035, [arXiv:hep-ph/0312069].

[78] H. E. Haber, M. J. Herrero, H. E. Logan, S. Peñaranda, S. Rigolin and D. Temes, Phys. Rev. D **63** (2001) 055004, [arXiv:hep-ph/0007006].

[79] J. C. Brient, *Measurement of the Higgs decays into WW* at FLC*, LC-PHSM-2004-002, (Article).

[80] T. L. Barklow, *Higgs coupling measurements at a 1-TeV linear collider*, [arXiv:hep-ph/0312268].

[81] LHC Design Report
see also: http://lhc.web.cern.ch/lhc

[82] ATLAS Collaboration, *Detector and Physics Performance Technical Design Report - Volume I*, CERN-LHCC-99-14 (1999).

[83] ATLAS Collaboration, *Detector and Physics Performance Technical Design Report-Volume II* CERN-LHCC-99-15 (1999).

[84] M. Della Negra *et al.* [CMS Collaboration], *CMS: The Compact Muon Solenoid: Letter of intent for a general purpose detector at the LHC*, CERN-LHCC-92-3
see also: http://cmsinfo.cern.ch/cmsinfo/Welcome.html

[85] S. Amato *et al.* [LHCb Collaboration], *LHCb technical proposal*, CERN-LHCC-98-4.
see also: http://lhcb.web.cern.ch/lhcb/

[86] P. Giubellino [ALICE Collaboration.], *The ALICE detector at LHC*, Nucl. Instrum. Meth. A **344**, 27 (1994). see also: http://aliceinfo.cern.ch/

[87] ATLAS Collaboration, *ATLAS calorimeter performance* CERN-LHCC-96-40.
ATLAS Collaboration, *ATLAS liquid argon calorimeter: Technical design report*, CERN-LHCC-96-41
ATLAS Collaboration, *ATLAS tile calorimeter: Technical design report*, CERN-LHCC-96-42
ATLAS Collaboration, *ATLAS inner detector: Technical design report. Vol. 1,*, CERN-LHCC-97-16
ATLAS Collaboration, *ATLAS inner detector: Technical design report. Vol. 2*, CERN-LHCC-97-17.
ATLAS Collaboration, *ATLAS magnet system: Technical design report*, CERN-LHCC-97-18-21
ATLAS Collaboration, *ATLAS first-level trigger: Technical design report*, CERN-LHCC-98-14
ATLAS Collaboration, *The ATLAS HLT, DAQ and DCS Technical Design Report*, CERN-LHCC-03-22

[88] ATLAS Collaboration, *ATLAS muon spectrometer: Technical design report*, CERN-LHCC-97-22

[89] ATLAS Collaboration, *Computing Technical Design Report - TDR*, CERN-LHCC-2005-022 and references therein.

[90] G. Barrand *et al.*, Comput. Phys. Commun. **140** (2001) 45. (spires)

[91] F. E. Paige, S. D. Protopescu, H. Baer and X. Tata, *ISAJET 7.69: A Monte Carlo event generator for p p, anti-p p, and e+ e- reactions*, arXiv:hep-ph/0312045, and references therein;
see also: http://www.phy.bnl.gov/%7Eisajet/

[92] M. Gyulassy and X. N. Wang, *HIJING 1.0: A Monte Carlo program for parton and particle production in high-energy hadronic and nuclear collisions*, Comput. Phys. Commun. **83**, 307 (1994) [arXiv:nucl-th/9502021].
see also: http://www-nsdth.lbl.gov/%7Exnwang/hijing/

[93] B. P. Kersevan and E. Richter-Was, Comput. Phys. Commun. **149**, 142 (2003) [arXiv:hep-ph/0201302].
B. P. Kersevan and E. Richter-Was, *The Monte Carlo event generator AcerMC version 2.0 with interfaces to PYTHIA 6.2 and HERWIG 6.5*, arXiv:hep-ph/0405247.
see also: http://borut.home.cern.ch/borut

[94] E. Boos *et al.* [CompHEP Collaboration], Nucl. Instrum. Meth. A **534**, 250 (2004) [arXiv:hep-ph/0403113].
A. Pukhov *et al.*, *CompHEP: A package for evaluation of Feynman diagrams and integration over multi-particle phase space. User's manual for version 33*, arXiv:hep-ph/9908288.
see also: http://theory.sinp.msu.ru/comphep

[95] M. L. Mangano, M. Moretti, F. Piccinini, R. Pittau and A. D. Polosa, JHEP **0307**, 001 (2003) [arXiv:hep-ph/0206293].
see also: http://mlm.home.cern.ch/mlm/alpgen

[96] Z. Was and P. Golonka, Nucl. Phys. Proc. Suppl. **144**, 88 (2005) [arXiv:hep-ph/0411377], and references therein.
see also: http://wasm.home.cern.ch/wasm/goodies.html

[97] W. Seligman, *ParticleGenerator*.

[98] S. Agostinelli *et al.* [GEANT4 Collaboration], Nucl. Instrum. Meth. A **506**, 250 (2003). (Article)
see also: http://wwwasd.web.cern.ch/wwwasd/geant4/geant4.html

[99] C. Iglesias, *Clustering of very low energy particles* ATL-CAL-INT-2005-001.
R. Mehdiyev, Z. V. Metreveli, P Nevski, D Salihagic, *Test of Sliding Window Algorithm fir Jets Reconstruction in ATLAS Hadronic Calorimeters* ATL-CAL-99-002.

[100] C. Cojocaru *et al.* [ATLAS Liquid Argon EMEC/HEC Collaboration], Nucl. Instrum. Meth. A **531** (2004) 481 [arXiv:physics/0407009].
see also: TopologicalClustering

[101] F. Derue, C. Serfon, *Electron/jet separation with DC1 data* ATL-PHYS-PUB-2005-016; see also: EgammaATLASRecoPerformance

[102] S. Tarem, N. Panikashvili, *Low PT Muon Identification in the ATLAS Detector at the LHC* ATL-SOFT-2004-003 Prepared for 2004 IEEE Nuclear Science Symposium And Medical Imaging Conference NSS-MIC 2004, Rome, Italy , 16 - 22 Oct 2004.
S. Tarem, N. Panikashvili, *A Method for Low PT Muon Identification with the ATLAS Detector at the LHC*, ATL-COM-MUON-2004-022.

[103] G. C. Blazey *et al.*, *Run II jet physics*, arXiv:hep-ex/0005012.

[104] J. M. Butterworth, J. P. Couchman, B. E. Cox and B. M. Waugh, Comput. Phys. Commun. **153**, 85 (2003) [arXiv:hep-ph/0210022]. see: `http://hepforge.cedar.ac.uk/ktjet/`
S. Catani, Y. L. Dokshitzer, M. H. Seymour and B. R. Webber, Nucl. Phys. B **406**, 187 (1993). (spires)

[105] F. E. Paige and S. Padhi, *Rome Jet Calibration Based on Athena 9.0.4* Note.

[106] E. Richter-Was, D. Froidevaux, L. Poggioli, *ATLFAST 2.0, ATLAS internal note*, 13 Nov 1998. ATL-PHYS-98-131.
see also: `http://www.hep.ucl.ac.uk/ATLAS/atlfast`

[107] K. Jakobs, and K. Mahboubi, *A fast parametrization of electromagnetic and hadronic calorimeter showers* ATL-SOFT-PUB-2006-001.

[108] S. Weinberg, Phys. Rev. D **19**, 1277 (1979). (Article)
L. Susskind, Phys. Rev. D **20** (1979) 2619. (Article)

[109] J. C. Pati and A. Salam, Phys. Rev. D **10**, 275 (1974). (Article)
W. Buchmuller and D. Wyler, Phys. Lett. B **177**, 377 (1986). (spires)
E. Eichten, K. D. Lane and M. E. Peskin, Phys. Rev. Lett. **50**, 811 (1983). (Article)
H. Georgi and S. L. Glashow, Phys. Rev. Lett. **32**, 438 (1974). (Article)

[110] M. Smizanska, Eur. Phys. J. C **34** (2004) S385. (spires)

[111] M. Spira, *Higgs boson production and decay at future machines*, arXiv:hep-ph/9711394, and references therein.

[112] S. Asai *et al.*, Eur. Phys. J. C **32S2**, 19 (2004) [arXiv:hep-ph/0402254].

[113] M. Hohlfeld, *On the determination of Higgs parameters in the ATLAS experiment at the LHC*, ATL-PHYS-2001-004.

[114] M. Dührssen, *Prospects for the measurement of Higgs boson coupling parameters in the mass range from 110 - 190 GeV*, ATL-PHYS-2003-030.

[115] M. Dührssen, S. Heinemeyer, H. Logan, D. Rainwater, G. Weiglein and D. Zeppenfeld, Phys. Rev. D **70**, 113009 (2004) [arXiv:hep-ph/0406323].

[116] C. P. Buszello, I. Fleck, P. Marquard and J. J. van der Bij, Eur. Phys. J. C **32**, 209 (2004) [arXiv:hep-ph/0212396].

[117] J. Cammin and M. Schumacher, *The ATLAS discovery potential for the channel ttH, H to bb*, ATL-PHYS-2003-024.

[118] M.Kupper, *Pulse Test System for TGC production*, 2002.

[119] Gage Applied Sciences Inc., CompuScope, SDK Manual, Volumes I-III.
http://www.gage-applied.com/index.htm

[120] D. Cavalli and S. Resconi, *τ-jet separation in ATLAS detector*, ATL-PHYS-98-118.

[121] M. Heldmann, *Taus id from DC1 events without and with noise: towards a new parametrisation for Atlfast*, see: Slides
M. Heldmann, *Tau Reconstruction and Physics*.

[122] D. Zeppendeld et al. The home page of the madcup project.
http://pheno.physics.wisc.edu/Software/MadCUP.
K.S. Cranmer, B. Mellado, B. Quayle, *MadCUP: Parton-level Monte Carlo*. ATLAS Week Feb. 2002,
see: http://www-wisconsin.cern.ch/physics/files/Kyle_25.02.02.pdf.

[123] H. Ma, F.Paige, and S. Rajagopalan, *τ Reconstruction in Athena*, can be found on: TAUREC
R. Tanaka, H. Nomoto, S. Asai, *Study of Identification of Hadronic Tau Decays for VBF Higgs $\rightarrow \tau\tau$ in ATLAS*, ATL-COM-PHYS-2004-069.
E. Richter-Was, H. Przysiezniak, F. Tarrade, *Exploring hadronic tau identification with DC1 datat samples : a track based approach*, ATL-PHYS-2004-030.
E. Richter-Was, T. Szymocha, *Hadronic tau identification with track based approach : the $Z \rightarrow \tau\tau, W \rightarrow \tau\nu$ and dijet events from DC1 data samples*, ATL-PHYS-PUB-2005-005.

[124] A. Belyaev and L. Reina, JHEP **0208**, 041 (2002) [arXiv:hep-ph/0205270].
L. Reina and A. Belyaev, private comunication.

[125] S. Frixione and B. R. Webber, JHEP **0206** (2002) 029 [arXiv:hep-ph/0204244].

[126] K. Benslama, private comunication.

[127] S. Correard, V. Kostyukhin, J Lévêque, A. Rozanov, J. B. De Vivie de Régie, *b-tagging with DC1 data*, ATL-PHYS-2004-006.

[128] M. Heldmann and D. Cavalli, *An improved tau-Identification for the ATLAS experiment*, ATL-PHYS-PUB-2006-008.

[129] B. Mellado, W. Quayle, and Sau Lan Wu; *Prospects for a Higgs discovery in the channel $H \to WW \to l\nu l\nu$ with no hard jets*, ATL-COM-PHYS-2005-074.

[130] S. Eidelman *et al.* [Particle Data Group], Phys. Lett. B **592**, 1 (2004). (spires)
see also: http://pdg.lbl.gov/pdg.html

[131] C. Peterson and T. Rognvaldsson, *An Introduction to artificial neural networks*, LU-TP-91-23 (spires)
Lectures given at 1991 CERN School of Computing, Ystad, Sweden, Aug 23 - Sep 2, 1991
see also: http://neuralnets.web.cern.ch/NeuralNets/nnwInHep.html

[132] C. Peterson, T. Rognvaldsson and L. Lonnblad, Comput. Phys. Commun. **81**, 185 (1994). (spires)

[133] E. Gross and A. Klier, *Higgs statistics for pedestrians*, arXiv:hep-ex/0211058.

[134] T. Junk, Nucl. Instrum. Meth. A **434**, 435 (1999) [arXiv:hep-ex/9902006].

Appendix A

Standard Model Parameters

The Standard Model has eighteen independent parameters. One possible choice of these parameters is listed bellow [130].

Gauge Sector

$$\begin{aligned} \alpha_{EM}^{-1}(m_e^2) &= 137.0359896(61) \\ \alpha_s(m_Z) &= 0.1187(20) \\ \sin^2\theta_W &= 0.23210(15) \end{aligned}$$

Lepton Sector

$$\begin{aligned} m_e &= 0.510998918 \pm 0.000000044\ MeV \\ m_\mu &= 105.6583692 \pm 0.0000094\ MeV \\ m_\tau &= 1776.9 \pm 0.3\ MeV \end{aligned}$$

Quark Sector Masses:

$$\begin{aligned} m_u &= 1.5 - 4.0\ MeV \\ m_d &= 4 - 8\ MeV \\ m_s &= 80 - 130\ MeV \\ m_c &= 1.15 - 1.35\ GeV \\ m_b &= 4.1 - 4.4\ GeV \\ m_t &= 172.7 \pm 2.9\ GeV \end{aligned}$$

CKM Parameters:

$$\begin{aligned} |V_{us}| &= 0.2196 \pm 0.0023 \\ |V_{cb}| &= (41.3 \pm 1.5) \cdot 10^{-3} \end{aligned}$$

$$
\begin{aligned}
|V_{ub}/V_{cb}| &= 0.08 \pm 0.02 \\
J &= (2.88 \pm 0.33) \cdot 10^{-5}
\end{aligned}
$$

Higgs Sector

$$
\begin{aligned}
G_F &= 1.16639(2) \cdot 10^{-5}\ GeV^{-2} \\
m_H &\geq 114.4\ GeV
\end{aligned}
$$

In addition $m_Z = 91.188 \pm 0.0021$ GeV and $m_W = 80.425 \pm 0.038$ GeV.

Appendix B

An Artificial Neural Network

B.1 Basic Principle

An Artificial Neural Network (ANN) is an information processing paradigm that is inspired by the way biological nervous systems, such as the brain, process information. It is composed of a large number of highly interconnected processing elements (neurons in biology, nodes in physics) working in unison to solve specific problems. An ANN is configured for a specific application, such as pattern recognition or data classification, through a learning process [131].

ANN differs from other methods in some aspects:

- Learning: an ANN have the ability to learn based on the so called learning stage.
- Auto organization: an ANN creates its own representation of the input given in the learning process.
- Tolerance to faults: because ANN stores redundant information, partial destruction of the neural network does not damage completely the network response.
- Flexibility: The responce of the ANN is appropriate, though somewhat less accurate, in the case when the input data is noisy. An ANN also can be easily ported to fit any problem from a particular problem area.
- Real Time: ANNs are parallel structures; if they are implemented in this way using computers or special hardware, fast response (enough for real-time applications) can be achieved.

As an application to the high energy physics, ANN achieves usually better results than simple cuts.

Basic elements of the ANNs, nodes, can exchange information between themselves through synapses. Nodes are grouped into three types of layers: input, hidden and output. In this thesis, we used feedforward network (Figure B.1), where the information travels one way only - from the input to the output layer. The input layer does no processing -

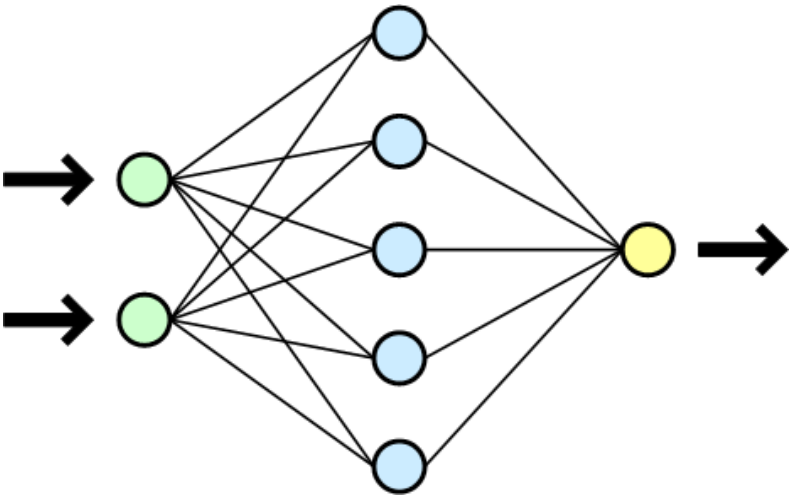

Figure B.1: *Diagram illustrating ANN.*

it is simply where the data vector (one dimensional data array) is fed into the network. The input layer then feeds the information to the hidden layer(s). Finally, the info is collected by the output layer. The actual processing in the network occurs in the nodes of the hidden layer(s) and the output layer. The network can be trained, i.e. given a specific task to solve and a class of functions F, network searches for the specific function $f \epsilon F$ which solves the task in an optimal sense. Feedforward networks, in particular, are very useful, when trained appropriately, to do intelligent classification or identification type tasks on unfamiliar data.

In the input layer each node is fed with a real value between zero and one. For the application to the analysis described in this thesis, these values are read from scaled characteristic variables. Output of the ANN is again number between zero and one, and can be interpreted as a signal probability of the given event.

Each node calculates its output value from the input values according to a nonlinear activation function. In our case this function is

$$g(x) = \frac{1}{2}(1 + \tanh x) = \frac{1}{1 + e^{-2x}}. \tag{B.1}$$

Then, the value of the node i is

$$F_i = g\left(\frac{1}{T}\sum_j \omega_{ij} F_j\right) \tag{B.2}$$

where j runs over the nodes of precedent layer, and ω_{ij} is the weight of corresponding connection[1]. The normalization factor T depends on the number of incoming connections. These are free parameters of the network.

[1]Every connection has a weight.

The weights are set[2] during the learning process. Test patterns with known target output[3] are fed into the ANN. In case of an ANN with one output node, the desired target output is one for a signal event, and zero for a background event. Starting with random weights, the ANN calculates the actual outputs for the training patterns and compares them with the target. During this process, weights are adjusted in order to get closer to the desired behaviour. The distance to the ideal ANN is expressed by the error function

$$E = \frac{1}{2N_p} \sum_{p=1}^{N_p} \sum_i \left(F_i(p) - T_i(P)\right)^2, \tag{B.3}$$

where i runs over the output nodes of the ANN and p over the training patterns. The target outputs for a pattern p are $T_i(p)$, and the actual ones are $F_i(p)$. The ANN is trying to minimize the error function by readjusting the weights.

The back propagation algorithm is the most widely used method for determining the error function. In the training step, the weight is shifted to

$$\begin{aligned} \omega(t+1) &= \omega(t) + \Delta\omega(t) \\ \Delta\omega(t) &= -\eta \frac{\partial E(t)}{\partial \omega} + \alpha \Delta\omega(t-1). \end{aligned} \tag{B.4}$$

The momentum term, governed by $\alpha < 1$, stabilizes the learning process by increasing the tendency of a weight to keep its value. The learning term η starts from a big value, and then decreases after each training period to allow quick improvement steps in the beginning and fine tuning at the end of the process.

The neural networks used in scope of these thesis have been created with the program JETNET [132].

B.2 Application: The search for CPV Higgs bosons

The neural networks used in this search have three layers, namely, a single hidden layer. The number of input nodes depends on the analysis as described in section 3.2, while the number of hidden nodes is twice the number of the input nodes.

As explained above, all the input variables have been scaled to fit the [0,1] interval. Some of the inputs were transformed logarithmically to give a flatter distributions. The actual (scaled) input variables are given in a Table B.1. As in the section 3.2, the nine common variables are listed first.

[2] This setting defines performance of the ANN.
[3] Monte Carlo signal and background events.

Input node	2-jet analysis	4-jet analysis
1	$\frac{\sqrt{s'} - 0.6\sqrt{s}}{0.4\sqrt{s}}$	
2	$\frac{M_{miss} - 50\ GeV}{(130 - 50)\ GeV}$	
3	$\frac{\lvert\cos\theta_{P_{miss}}\rvert}{0.95}$	
4	$\mathcal{B}_1$	
5	$\mathcal{B}_2$	
6	$\frac{\ln(50 \cdot (1 - \cos\sphericalangle(\vec{j}_1, \vec{P}_{miss})) + 1)}{\ln 101}$	
7	$\frac{1 + \cos\sphericalangle(\vec{j}_2, \vec{P}_{miss})}{2}$	
8	$\frac{\ln(200 \cdot \chi/20 + 1)}{\ln 201}$	$\frac{\ln(800 \cdot \chi/35 + 1)}{\ln 801}$
9	$\frac{-P_{miss} + 0.45\sqrt{s}}{0.45\sqrt{s}}$	
10	$\frac{\lvert\cos\theta_{P_{thr}}\rvert}{0.95}$	$\mathcal{B}_3$
11	$\frac{\ln(25 \cdot (\phi_{acop} - 3)/97 + 1)}{\ln 26}$	$\mathcal{B}_4$
12	$\frac{\ln(1 + 0.1 \cdot \lvert E_1 - E_2\rvert)}{\ln 11}$	

Table B.1: *The scaled inputs of the ANN for the analysis described in section 3.2. The final results are not sensitive to the details of the way the distributions have been flattened.*

Appendix C

Definition of Confidence Levels

The sensitivity of the searches for the Higgs boson is increased by combining the results of various topological searches [133]. In order to compute confidence levels, a test statistics Q is defined [134]. The test statistics is used to quantify the compatibility of the data with the two hypotheses: the background hypothesis and the signal+background hypothesis. Confidence levels are computed by comparing the observed data configuration with the expectations for these two hypotheses. For LEP analysis the ratio $Q = \mathcal{L}_{s+b}/\mathcal{L}_b$, where $\mathcal{L}_i$ is likelihood for the hypothesis i (i is background or signal+background), is often used as the test statistics.

In order to distinguish a background-like from a signal+background-like result it is necessary to construct a discriminator $\mathcal{D}$. Such a discriminator could be for example the reconstructed mass, or a 2D discriminator calculated from the reconstructed mass and the ANN output as in the present analysis (illustrated in Figure C.1). The discriminator is distributed and binned. For each bin i, three numbers are calculated: n_i - the number of observed events, s_i - the number of expected signal events for a given set of model parameters (obtained by MC), and b_i - the number of expected background events (obtained by MC). Each bin is considered to be statistically independent counting experiment obeying Poisson statistics (single event can produce only one entry). According to Poisson statistics, the probability to observe n events when b is expected is:

$$P_{Poisson}(Data|b) = \frac{1}{n!}e^{-b}b^n \tag{C.1}$$

and, similarly, when $s+b$ is expected:

$$P_{Poisson}(Data|s+b) = \frac{1}{n!}e^{-(s+b)}(s+b)^n \tag{C.2}$$

Then, the test statistics is given by:

$$Q = \frac{P_{Poisson}(Data|s+b)}{P_{Poisson}(Data|b)} = \frac{exp(-(s_{TOT}+b_{TOT}))}{exp(-b_{TOT})}\prod_{i=1}^{N_{bin}}\left(\frac{s_i+b_i}{b_i}\right)^{N_i} \tag{C.3}$$

and is often used in its logarithmic form:

$$-2\ln Q = -2s_{TOT} - 2\sum_{i=1}^{N_{bin}} n_i \left(1 + \frac{s_i}{b_i}\right) \tag{C.4}$$

where $s_{TOT} = \sum_i s_i$ and $b_{TOT} = \sum_i b_i$. Then, the confidence levels for the background and signal+background hypotheses, respectively, are defined as probabilities to obtain values of Q smaller then the observed value Q_{obs} from a large number of hypothetical experiments with background or signal+background processes, respectively, only:

$$CL_b = P(Q \leq Q_{obs}|background) \tag{C.5}$$

$$CL_{s+b} = P(Q \leq Q_{obs}|signal + background) \tag{C.6}$$

In principle, CL_{s+b} can be used to exclude the signal+background hypothesis, but in such a case, a downward fluctuation of the background might lead to an exclusion of the signal even though the experiment has no sensitivity. In order to avoid such a thing, LEP experiments use CL_s defined as a ratio:

$$CL_s = \frac{CL_{s+b}}{CL_b}. \tag{C.7}$$

By definition, signal hypothesis is considered excluded at 95% level if CL_s is less than 0.05. There is some loss of sensitivity by using CL_s rather than CL_{s+b}, and the limit obtained in this way will be conservative.

The expected confidence levels are obtained by replacing the observed data configuration by a large number of simulated experiment configurations for the background and signal+background hypotheses.

The effect of systematic uncertainties of the individual channels and their correlations has been calculated using a Monte Carlo technique. The signal and background estimations are varied within the bounds of the systematic uncertainties, taking correlations into account and assuming Gaussian distribution of the uncertainties. These variations are added to the Poisson statistical variations of the assumed signal and background rates in the confidence level calculation. The effect of systematic uncertainties turns out to be small for the excluded regions in parameter space.

If the different search channels do not overlap, the procedure described above is simply extended - test statistics are multiplied, i.e. their logarithms are added.

In a case of overlapping channels, i.e. channels sharing the events, the expected CL_s is calculated for each of the overlapping channels, but the channel that yields the smaller expected CL_s is retained. The procedure is repeated for each signal hypothesis.

The same procedure is applied if two signal processes can contribute to the same signal topology. One example is $H_2 \to b\bar{b}$ and $H_2 \to H_1 H_1 \to b\bar{b}b\bar{b}$ in a case of two-jet like

analysis. The data and background might contain some overlapping events. Therefore, only the hypothesis that yields the lower expected CL_s is retained.

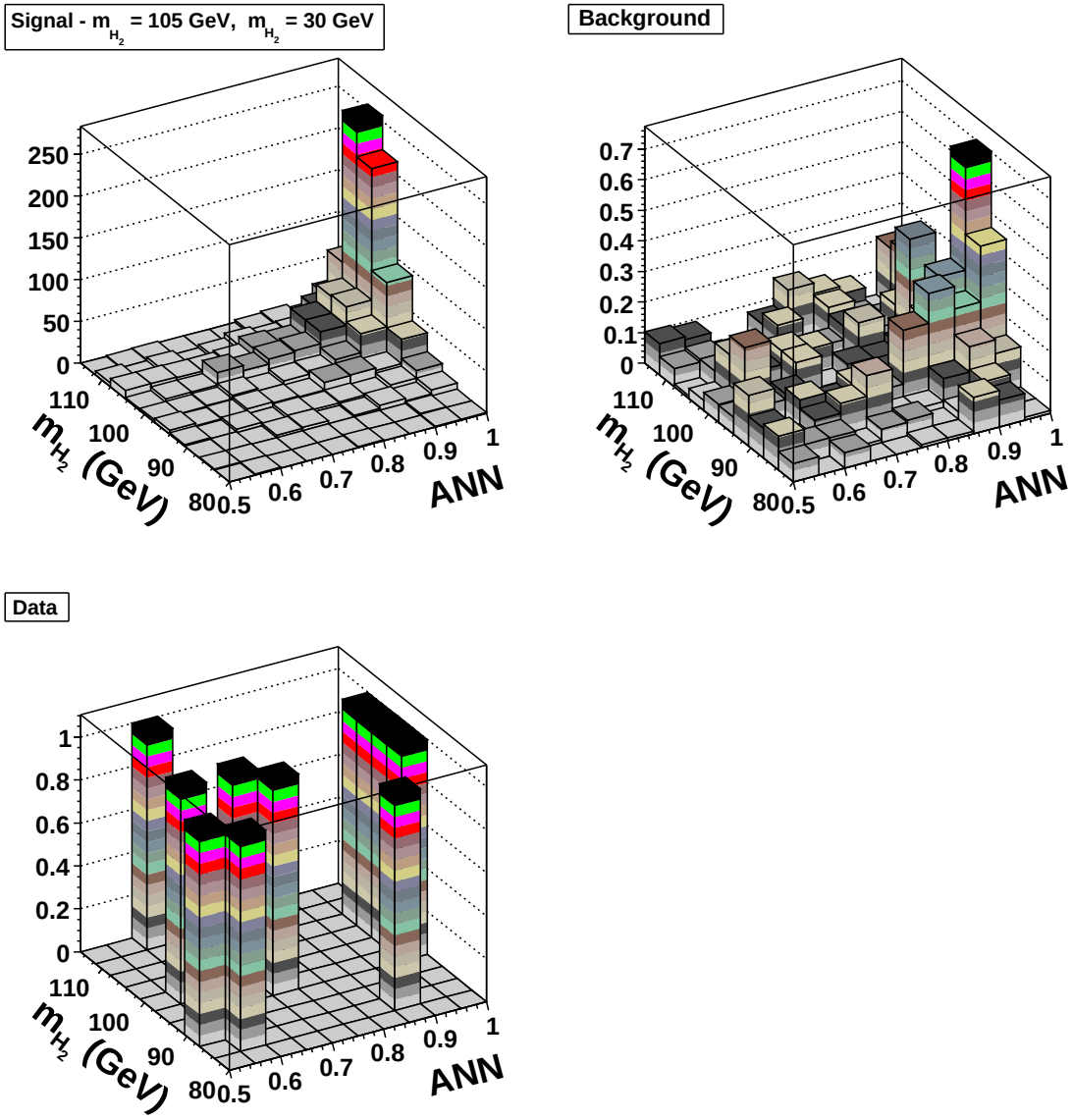

Figure C.1: *The two dimensional histogram that contain the distribution of the ANN output and reconstructed mass of the Higgs, m_{H_2}, is used to calculate the discriminator $\mathcal{D}$.*

Appendix D

SPS 1a

Our numerical evaluation in section 4.2 is based on the SPS 1a benchmark scenario that has been defined in Ref. [73]. The relevant parameters of the benchmark scenario are given below (more details can be found in Ref. [73]) in the $\overline{\text{DR}}$ scheme at the top squark mass scale. $m_{\tilde{t}_{L,R}}$ and $m_{\tilde{b}_{L,R}}$ denote the diagonal soft SUSY-breaking parameters in the $\tilde{t}$ and $\tilde{b}$ mass matrices, respectively.

$$
\begin{aligned}
m_{\tilde{t}_L} &= 495.9 \text{ GeV}, && \text{(D.1)}\\
m_{\tilde{t}_R} &= 424.8 \text{ GeV}, && \text{(D.2)}\\
A_t &= -510.0 \text{ GeV}, && \text{(D.3)}\\
m_{\tilde{b}_L} &= m_{\tilde{t}_L}, && \text{(D.4)}\\
m_{\tilde{b}_R} &= 516.9 \text{ GeV}, && \text{(D.5)}\\
A_b &= -772.7 \text{ GeV}, && \text{(D.6)}\\
m_{\tilde{g}} &= 595.2 \text{ GeV}, && \text{(D.7)}\\
M_2 &= 192.7 \text{ GeV}, && \text{(D.8)}\\
M_1 &= 99.1 \text{ GeV}, && \text{(D.9)}\\
\mu &= 352.4 \text{ GeV}, && \text{(D.10)}\\
M_A &= 393.6 \text{ GeV}, && \text{(D.11)}\\
\tan\beta &= 10. && \text{(D.12)}
\end{aligned}
$$

Appendix E

Electron Identification Likelihood and Artificial Neural Network

To construct Electron Identification using Likelihood and Artificial Neural Network in the full simulation framework, the following variables are used [126]:

1. The fraction of the total energy measured in the presampler, E_0/E;
2. The fraction of the total energy measured in the first sampling of the EM Calorimeter, E_1/E;
3. The fraction of the total energy measured in the second sampling of the EM Calorimeter, E_2/E;
4. The fraction of the total energy measured in the third sampling of the EM Calorimeter, E_3/E;
5. The ratio of the energy leakage into the first sampling of the Hadronic Calorimeter, E_{ha}/E;
6. The ratio of the uncorrected energies in a rectangular shape measuring 3×3 and 3×7 cells in the second sampling of the EM Calorimeter, E_{33}/E_{37};
7. The ratio of the uncorrected energies in 3×7 and 7×7 cells in the second sampling of the EM Calorimeter, E_{37}/E_{77};
8. The ratio of the transverse energy measured in the Calorimeter and the momentum measured by the Inner detector (from tracking), E/p_T.

In addition, we use the following track-matching quantities in the analysis described in this thesis:

- $|\Delta\eta| = |\eta_{strips} - \eta_{ID}|$, where η_{strips} is the position in the first sampling of the EM Calorimeter, i.e. strips, and η_{ID} is the position in the Inner Detector.

- $|\Delta\phi| = |\phi_2 - \phi_{ID}|$, where ϕ_2 is the position in the second sampling of the EM Calorimeter and ϕ_{ID} is the position in the Inner Detector.

Appendix F

τ Identification Likelihood

To construct τ Identification Likelihood in the full simulation, the following variables are used [128]:

1. Electormagnetic Radius given by:

$$R_{EM} = \frac{\Sigma_{i=1}^{n} E_{Ti} \Delta R_i}{\Sigma_{i=1}^{n} E_{Ti}}, \tag{F.1}$$

   where sum runs over all cells in the EM Calorimeter. E_{Ti} is the transverse energy deposited in the i^{th} cell and ΔR_i is the distance between the i^{th} cell and τ-candidate axis;

2. The Isolation Fraction defined as the fraction of transverse momentum within an annulus of $0.1 < \Delta R < 0.2$:

$$F_{Iso} = \frac{p_T(0.2) - p_T(0.1)}{p_T(0.4)}; \tag{F.2}$$

3. Number of associated tracks;

4. Total charge of the τ-candidate;

5. Number of hits in the first sampling of the EM Calorimeter, i.e. $\eta - strips$;

6. The weighted strip width:

$$\Delta\eta = \sqrt{\frac{\Sigma_{i=1}^{n} E_{Ti} \Delta\eta_i^2}{\Sigma_{i=1}^{n} E_{Ti}}} \tag{F.3}$$

7. Lifetime signed impact parameter significance defined as:

$$\sigma_{1P} = \frac{d_0}{\sigma_{d_0}} \cdot sign(\sin(\phi_{cl} - \phi_{track})) \tag{F.4}$$

   where d_0 is the impact parameter in the transverse plane, σ_{d_0} the corresponding error, and ϕ_{cl} and ϕ_{track} the position of the τ-candidate axis and the highest p_T track at the point of the closest approach of the track;

8. The ratio of the transverse momentum of the τ-candidate and the track with the highest p_T.

Appendix G

The Collinear Approximation

When the τ-lepton has a high momentum, one can approximate the direction of the neutrinos to be collinear with the visible τ decay products[1]. Then, the conservation of the total transverse momentum leads to:

$$(\vec{p}_T^{\,\tau_1} + \vec{p}_T^{\,\tau_2}) = \frac{\vec{p}_T^{\,l}}{x_l} + \frac{\vec{p}_T^{\,h}}{x_h} = \vec{p}_T^{\,l} + \vec{p}_T^{\,h} + \vec{\not{p}}_T, \tag{G.1}$$

where

$$\begin{aligned} x_l &= \frac{p_x^h p_y^l - p_y^h p_x^l}{p_x^h p_y^l - p_y^h p_x^l - p_y^h \not{p}_x + p_x^h \not{p}_y} \\ x_h &= \frac{p_x^h p_y^l - p_y^h p_x^l}{p_x^h p_y^l - p_y^h p_x^l - p_y^l \not{p}_x + p_x^l \not{p}_y} \end{aligned} \tag{G.2}$$

are the fractions of the parent τ-momentum carried by the lepton-daughter or τ-jet-daughter. $\vec{p}_T^{\,l}$ is the transverse momentum of the lepton-daughter, $\vec{p}_T^{\,h}$ is the transverse momentum of the τ-jet-daughter, and $\vec{\not{p}}_T$ is the missing transverse momentum. Both x_l and x_h are required to be positive[2]. Following these equations, the $\tau\tau$ invariant mass is:

$$m_{\tau\tau}^2 = 2(E_l + E_{\nu_l})(E_h + E_{\nu_h})(1 - \cos\theta) = \frac{m_{lh}^2}{x_l x_h}, \tag{G.3}$$

where m_{lh} is invariant mass of the lepton-daughter and τ-jet-daughter.

[1] The case when one τ-lepton decays hadronically (index h), and the other leptonically (index l) is described.

[2] Negative values are non-physical.